Instrumentation, Sequences and Applications for Magnetic Particles in Imaging and Spectroscopy

Vom Promotionsausschuss der
Technischen Universität Hamburg

zur Erlangung des akademischen Grades

Doktor-Ingenieur (Dr.-Ing.)

genehmigte Dissertation (kumulativ)

von
Fabian Mohn

aus
Hamburg

2024

Erstgutachter: Prof. Dr.-Ing. Tobias Knopp
Zweitgutachter: Prof. Dr.-Ing. habil. Alexander Kölpin
Tag der mündlichen Prüfung: 15.11.2024

Author’s ORCID : 0000-0002-9151-9929
Document’s DOI : 10.15480/882.13690

Institute for Biomedical Imaging, Hamburg University of Technology (TUHH)
Section for Biomedical Imaging, University Medical Center Hamburg-Eppendorf (UKE)

Abstract

As an emerging medical imaging modality, magnetic particle imaging (MPI) has demonstrated considerable potential in imaging scenarios where established techniques are limited or have adverse effects. However, it still faces several challenges for future clinical integration and for achieving theoretical predictions of performance. MPI is a quantitative, tracer-based, and indirect imaging technique, that measures the non-linear response of magnetic nanoparticles (MNPs) at high temporal and spatial resolution with very high sensitivity. Major milestones such as the in vivo measurement of a beating mouse heart in 2009 or the first MPI-tailored MNPs in the same year, have been complemented by progress in various disciplines that constitute the research field of MPI. These include image reconstruction, signal encoding, MNP synthesis, applications and hardware instrumentation as main categories. Today, real-time reconstructions are feasible for perfusion imaging, as well as simultaneous measurement and signal separation of different MNP systems, and intentional interaction of MNPs with their immediate environment by mechanical activation, hyperthermia or targeted drug delivery.

Initial progress toward the development of a full-scale, human-sized system by the Philips research division in Hamburg, Germany, in 2015 was accompanied by a number of challenges. The enormous engineering effort included the development of instrumentation needed to generate strong alternating and static magnetic fields in a cost-effective and maintainable manner, with a complexity similar to that of a magnetic resonance imaging (MRI) system. Ultimately, the project struggled to maintain funding. At the Institute of Biomedical Imaging, Hamburg University of Technology, the challenge in instrumentation was addressed on a smaller scale, but still within the range of human proportions. A human-sized head scanner was introduced in 2019 that incorporated numerous straightforward solutions to previous difficulties, benefiting from smaller components and lower electrical specifications. A significant aspect of this thesis is the comprehensive redesign of this head-sized imaging system to align with clinical standards in terms of 3D acquisition speed, safety, and resolution. The design process incorporates both feasibility and clinical trial requirements, and achievable results are highlighted for an approved, but inferior, Ferucarbotran-based tracer. One part of this thesis is devoted to an in-depth examination of the transmit-receive signal chain of the device, accompanied by a comprehensive account of the development and design process of a high current linear toroidal transformer. The high-gain transformer can also be utilized in applications beyond medical imaging, operating in the kHz range, such as wireless power transmission. Another section in the present thesis investigates the suitability of a novel Ferucarbotran tracer, its MPI signal quality, composition, and performance in comparison to other MNPs.

In the fields of neurology and interventional radiology, a head-sized imaging system can be employed for the prompt diagnosis of various types of stroke, including ischemic stroke, which represents a significant cause of mortality in the context of cardiovascular disease. Intracerebral hemorrhage represents the second most common type of stroke for which perfusion imaging serves as an invaluable diagnostic tool. Our head-sized imaging system may facilitate long-term monitoring of such patients. In this study, we propose a negative contrast perfusion imaging technique based on a long-circulating tracer and a saline bolus, which enables the repeated generation of trackable dynamic changes in MNP concentration without increasing the total administered iron dose. It leverages several significant advantages of MPI over other modalities, including its sensitivity, linearity, and high temporal resolution for 3D volume tracking, enabling not only concentration changes but also the rate of these processes to be monitored. Given the limited iron uptake by the liver and spleen, reducing the administered dose is a crucial aspect to consider for repeated monitoring of an individual patient.

MNP spectrometry is a highly valuable tool during the preclinical stage of MPI, as it allows for the assessment and evaluation of the non-linear response and relaxation behavior of MNPs with high signal quality and low noise in homogeneous fields. Concerning the instrumentation of MNP spectrometry, we develop and calibrate an arbitrary waveform magnetic particle spectrometer (MPS) for the purpose of measuring and emulating MPI excitation sequences. In particular, the device can operate at different excitation waveforms and offset fields, which can be utilized to emulate an arbitrary waveform MPI scanner, assess MPI signal encoding, saturation behavior, and the magnetization behavior of nanoparticles on a small scale with short measuring times, typically below one minute.

Kurzfassung

Als aufstrebende medizinische Bildgebungsmodalität hat die Magnet Partikel Bildgebung (MPI) ein beträchtliches Potenzial in Bildgebungsszenarien gezeigt, in denen etablierte Techniken begrenzt sind oder nachteilige Auswirkungen haben. Sie steht jedoch noch vor mehreren Herausforderungen, wenn es um die künftige klinische Integration und das Erreichen theoretischer Leistungsvorhersagen geht. MPI ist ein quantitatives, tracerbasiertes und indirektes Bildgebungsverfahren, das die nichtlineare Reaktion von magnetischen nanopartikeln (MNPs) mit hoher zeitlicher und räumlicher Auflösung und sehr hoher Empfindlichkeit misst. Wichtige Meilensteine wie die In-vivo-Messung eines schlagenden Mäuseherzens im Jahr 2009 oder die ersten auf MPI zugeschnittenen MNPs im selben Jahr wurden durch Fortschritte in verschiedenen Disziplinen ergänzt, die das Forschungsgebiet der MPI ausmachen. Dazu gehören die Bildrekonstruktion, Signalkodierung, Synthese von MNPs, medizinische Anwendungen und Hardware-Instrumentierung als Hauptkategorien. Heute sind Rekonstruktionen in Echtzeit für die Perfusionsbildgebung möglich, ebenso wie die gleichzeitige Messung und Signaltrennung verschiedener Partikelsysteme und die gezielte Interaktion von MNPs mit ihrer unmittelbaren Umgebung durch mechanische Aktivierung, Hyperthermie oder gezielte Medikamentengabe.

Die ersten Fortschritte bei der Entwicklung eines menschengroßen Systems durch die Philips-Forschungsabteilung in Hamburg, Deutschland, im Jahr 2015 wurde von einer Reihe von Herausforderungen begleitet. Der enorme technische Aufwand umfasste die Entwicklung von Feldgeneratoren, um starke magnetische Wechselfelder und statische Magnetfelder auf kosteneffiziente und wartbare Weise zu erzeugen. Das Gerät ist mit der Komplexität eines MRT-Systems zu vergleichen und hatte letztendlich Schwierigkeiten die Finanzierung aufrechtzuerhalten. Am Institut für Biomedizinische Bildgebung der Technischen Universität Hamburg wurde die Herausforderung der Instrumentierung in kleinerem Maßstab, aber immer noch im Bereich von menschlichen Proportionen, angegangen. Im Jahr 2019 wurde eine erste Version eines Kopfscanners in menschlicher Größe vorgestellt, der zahlreiche unkomplizierte Lösungen für frühere Schwierigkeiten enthielt und von kleineren Komponenten und geringeren elektrischen Anforderungen profitierte. Ein wichtiger Aspekt dieser Arbeit ist die umfassende Neugestaltung dieses kopfgroßen Bildgebungssystems, um es in Bezug auf 3D-Erfassungsgeschwindigkeit, Sicherheit und Auflösung an klinische Standards anzupassen. Der Entwurfsprozess berücksichtigt sowohl die Machbarkeit als auch die Anforderungen für klinische Studien. Es wird außerdem aufgezeigt, welche Ergebnisse mit einem zugelassenen, aber minderwertigen Tracer auf Ferucarbotran-Basis erzielt werden können. Ein eigenständiger Teil dieser Arbeit ist einer genauen Untersuchung der Sende-Empfangs-Signalkette des Geräts gewidmet, begleitet von einer umfassenden Darstellung des Entwicklungs- und Konstruktionsprozesses eines linearen Hochstrom-Ringkerntransformators. Der toroidale Transformator kann auch in Anwendungen außerhalb der medizinischen Bildgebung eingesetzt

werden, die im kHz-Bereich arbeiten, z.B. in der drahtlosen Energieübertragung. In einem weiteren Teil der vorliegenden Arbeit werden die Eignung des neuartigen Ferucarbotran-Tracers, seine MPI-Signalqualität, Zusammensetzung und Leistung im Vergleich zu anderen MNPs untersucht.

In der Neurologie und der interventionellen Radiologie kann ein kopfgroßes Bildgebungssystem zur schnellen Diagnose verschiedener Arten von Schlaganfällen eingesetzt werden, einschließlich des ischämischen Schlaganfalls, der im Zusammenhang mit kardiovaskulären Erkrankungen eine der führenden Todesursache darstellt. Die intrazerebrale Gerhinblutung ist die zweithäufigste Schlaganfallart, bei der die Perfusionsbildgebung ein unschätzbares diagnostisches Instrument darstellt. Unser kopfgroßes Bildgebungssystem kann die langfristige Überwachung solcher Patienten erleichtern. In einer eigenständigen Studie schlagen wir eine Perfusionsbildgebungstechnik mit negativen Konrast vor, die auf einem lang zirkulierenden Tracer und einem Bolus aus Kochsalzlösung basiert, der die wiederholte Erzeugung dynamischer Veränderungen der MNP-Konzentration ermöglicht, ohne die verabreichte Gesamtdosis an Eisen zu erhöhen. Dabei werden mehrere wesentliche Vorteile von MPI gegenüber anderen Modalitäten genutzt, darunter die Empfindlichkeit, Linearität und hohe zeitliche Auflösung für die 3D-Volumentomographie, so dass nicht nur Konzentrationsänderungen, sondern auch die Geschwindigkeit dieser Prozesse überwacht werden können. Angesichts der begrenzten Eisenaufnahme durch Leber und Milz ist die Verringerung der verabreichten Dosis ein entscheidender Aspekt, der bei der wiederholten und dauerhaften Überwachung eines einzelnen Patienten zu berücksichtigen ist.

Die MNP-Spektrometrie ist ein äußerst wertvolles Instrument in der präklinischen Phase von MPI, da sie die Beurteilung und Bewertung der nichtlinearen Reaktion und des Relaxationsverhaltens von MNPs mit hoher Signalqualität und geringem Rauschen in homogenen Feldern ermöglicht. Bezüglich der Instrumentierung der MNP-Spektrometrie, entwickeln und kalibrieren wir ein MPS mit beliebiger Wellenformanregung für die Messung und Emulation von MPI-Anregungssequenzen. Insbesondere kann das Gerät mit verschiedenen Anregungswellenformen und Offset-Feldern arbeiten, die zur Emulation eines MPI-Scanners mit beliebiger Wellenform, zur Bewertung der MPI-Signalkodierung, des Sättigungsverhaltens und des Magnetisierungsverhaltens von Nanopartikeln in kleinem Maßstab mit kurzen Messzeiten, typischerweise unter einer Minute, verwendet werden können.

Contents

Glossary

Nomenclature

Notations	
$\hat{a}$	hat: Fourier transform of signal a
a^*	asterisk: complex conjugate of signal a
$\boldsymbol{a}$	boldsymbol: vector or matrix
$\mathbf{e}_{a}$	unit vector: points in direction of $\boldsymbol{a}$

Name	*Unit*	*Description*
$\boldsymbol{B}$	T = Vs/m^2	Magnetic flux density
$\boldsymbol{B}_\text{DF}$	T	Magnetic drive field
$\boldsymbol{B}_\text{SF}$	T	Magnetic selection field
$\boldsymbol{c}$	g$_\text{Fe}$ / m^3	MPI particle concentration
C	F = As/V	Capacitance
$\boldsymbol{D}$	As/m^2	Electric displacement field
$\boldsymbol{E}$	V/m	Electric field
f	Hz	Frequency (see also ω)
Δf	Hz	Bandwidth
f_r	Hz	Resonance frequency
f_1	Hz	Fundamental frequency, first harmonic
f_s	Hz	Sampling frequency (ADC)
$\boldsymbol{G}$	T	Magnetic gradient field
$\boldsymbol{H}$	A/m	Magnetic field
j		Imaginary unit, $j^2 = -1$
k		Frequency index (harmonics)
k_B	J/K	Boltzmann constant, $k_\text{B} \approx 1.381 \cdot 10^{-23}$ J/K
k_c		Coupling coefficient (transformer)
K		Number of frequencies k
l		Channel index
L_ch		Number of channels l
L	H = Vs/A	Inductance
L_1	H	Primary inductance of transformer
L_2	H	Secondary inductance of transformer
L_M	H	Mutual inductance, also: L_{21} acting on 2 from 1 (reciprocal)
L_σ	H	Stray inductance of transformer
$\boldsymbol{m}$	Am^2	Magnetic moment ($\boldsymbol{m} = \int \boldsymbol{M} \, \mathrm{d}V$)
$\boldsymbol{M}$	A/m	Magnetization

$\boldsymbol{J}$	A/m^2	Free current density
$\boldsymbol{P}$	As/m^2	Polarization density
P	W	Power
Q_c	C = As	Charge
Q_f		Quality factor of resonance
$\boldsymbol{r}$	m	Location vector, $\boldsymbol{r} \in \mathbb{R}$
$\boldsymbol{S}$	V m^3/g$_\mathrm{Fe}$	System matrix
SNR	dB	Signal-to-noise ratio
t	s	Time
t_0	s	Initial time, e.g. of bolus
T	s	Period
T_g	s	Group period
$\boldsymbol{u}$	V	Receive signal
Z	Ω	Impedance, complex resistance
δ_s	m	Skin depth
$\boldsymbol{\epsilon}$	As/Vm	Permittivity (tensor)
ϵ_0	As/Vm	Permittivity of free space ($\epsilon_0 \approx 8.854 \cdot 10^{-12}$ As/Vm)
ϵ_r		Relative permittivity
Θ	m^3	Field of view
λ_r		Regularization parameter (Kaczmarz solver)
$\boldsymbol{\mu}$	Vs/Am	Permeability (tensor)
μ_0	Vs/Am	Permeability of free space ($\mu_0 \approx 4\pi \cdot 10^{-7}$ Vs/Am)
μ_r		Relative permeability
ρ	As/m^3	Free charge density
$\boldsymbol{\sigma}$	S/m	Electrical conductivity (tensor)
σ_d		Statistical standard deviation
τ_B	s	Brownian relaxation time
τ_N	s	Néel relaxation time
$\boldsymbol{\Phi}$	Vs	Magnetic flux
ω	rad/s	Angular frequency
$\Delta\omega$	rad/s	Bandwidth
ω_0	rad/s	Angular resonance frequency

Abbreviations

ADC analog-to-digital converter
CT computed tomography
DAC digital-to-analog converter
DFG drive field generator
DFT discrete Fourier transform
DLS dynamic light scattering
ECD equivalent circuit diagram
ESL equivalent series inductance
ESR equivalent series resistance
FFL field-free-line
FFP field-free-point
FFR field-free-region
FFT fast Fourier transform
FNOs Fourier neural operators
FOV field-of-view
FWHM full width at half maximum
GI gastrointestinal
GUI graphic user interface
HCR high current resonator
ICN inductive coupling network
ICU intensive care unit
ISI integrated signal intensity
JFET junction field-effect transistor
lcm least common multiple
LFR low-field-region
LNA low noise amplifier
MNP magnetic nanoparticle
MoM method of moments
MPI magnetic particle imaging
MPS magnetic particle spectrometer
MRI magnetic resonance imaging
MTT mean-transit-time
NF noise figure
NWA network analyzer
PA power amplifier
PCB printed circuit board
PDE partial differential equation
PET positron emission tomography
PNS peripheral nerve stimulation
PSF point spread function
PTT pulmonary transit time
PWM pulse width modulation
RBCs red blood cells
rBF relative blood-flow
rBV relative blood-volume
rCBF relative cerebral-blood-flow
rCBV relative cerebral-blood-volume
RFFT right-sided fast Fourier transform
RMS root mean square
ROI region of interest
RP RedPitaya *Stemlab 125-14*
RSS root sum-of-squares
SAR specific absorption rate
SFG selection field generator
SPECT single-photon emission CT
SR slew rate
SU surveillance unit
TDD targeted drug delivery
TEM transmission emission microscopy
TF transfer function
THD total harmonic distortion
TTP time-to-peak
TxRx transmit-receive
VNA vector network analyzer
VOI volume of interest
VSM vibrating sample magnetometry

1

Introduction

Medical imaging plays a pivotal role in modern healthcare and describes the process of obtaining an internal image of the body that can be used for diagnosis and treatment. It is largely based on the ability to non-invasively analyze, prepare for, and guide medical procedures using one or several imaging modalities. Historically, medical imaging has been a tool used primarily for diagnosis. Treatment was a separate process and imaging was used as a pre- and post-evaluation of the surgical intervention. Over the years, this distinction has faded and medical imaging has begun to play an important role during interventions, e.g. for minimally invasive surgery via catheters [216]. Additional requirements for medical device design, such as patient accessibility and acquisition speed, became important for surgical integration. Today, medical imaging is an integral part of many therapies, providing feedback for monitoring and combining therapy and diagnostics into theranostics. At its essence, the interdisciplinary field of medical imaging combines principles from physics, engineering, mathematics, computer science, and medicine to devise new methodologies for the visualization of internal structures, organ functionality, and physiological processes within the human body.

Since the introduction of clinical X-ray imaging and its refinement over the last century, a large number of other techniques have been invented, each with different purposes and advantages that determine its specific clinical application [55, 206]. There is no single imaging modality suited for an all-embracing evaluation, but each method has distinct advantages, is suitable for different imaging aspects, and has adverse effects. Advances in the instrumentation of individual modalities improve their capabilities, such as spatial resolution or sensitivity, which in turn enable new applications. These two main pillars of instrumentation and application form a progressive interplay in advancing modern imaging modalities. We loosely differentiate two groups of non-invasive methods: The class of direct or morphological techniques and the class of indirect imaging methods [40]. The former is based on physical parameters that are directly coupled to the imaging signal, as in computed tomography (CT), magnetic resonance imaging (MRI), or sonography. The latter involves the injection of a tracer material with specific properties that enables its detection, such as in positron emission tomography (PET), single-photon emission CT (SPECT) and magnetic particle imaging (MPI). A basic comparison and overview of these non-invasive modalities is given in Table 1.1. The wide range of requirements for modern modalities includes, but is not limited to, high spatial resolution, fast acquisition times, high sensitivity, strong image contrast and low risk to patients and staff, at best in demanding environments such as an intensive care unit (ICU) with free access to conduct surgery. Moreover, engineering effort and system cost are important factors in ensuring a widespread availability. There are also invasive imaging techniques, such as optical coherence tomography angiography or endoscopy, which will not be the focus of this work.

1.1 Motivation

This dissertation focuses on MPI, which is the only aforementioned imaging modality that is not yet established in clinical practice. It was first patented in 2001 [68] and subsequently published in 2005 by Gleich et al. [70] during their tenure at the Philips Research Laboratories in Hamburg. The first in vivo images of a beating mouse heart where presented in 2009 by Weizenecker et al. [309]. As an indirect imaging modality, MPI requires a tracer, more specifically magnetic nanoparticles (MNPs), which are typically introduced into the bloodstream by intravenous injection. Based on different static and varying magnetic fields in the kHz range, the nonlinear response of the MNPs is measured without employing ionizing radiation. Associated risks are therefore bound to heating, peripheral nerve stimulation (PNS) and tracer toxicity. MPI is capable of yielding real-time, background-free images with excellent contrast and sensitivity, making it a promising technology that has already shown significant potential in preclinical studies [27, 130, 194, 319].

In an effort to enhance current medical imaging capabilities for patients and clinical staff, research conducted on MPI aims to complement and refine medical imaging rather than replace existing modalities. Key objectives for future patients include reducing radiation exposure, combining diagnosis and therapy, and reducing scan times for fast and effective diagnosis, e.g. through the use of hybrid devices [37, 63, 290, 291]. MPI is a driver for the aforementioned interplay of instrumentation and application, as advances in instrumentation enable new applications that may become feasible in the near future, providing new imaging aspects, physiological information, tailored monitoring and unprecedented resolution [95]. Current efforts are directed toward the creation of clinical-grade systems for use in human applications, where five major areas of study can be loosely distinguished: research on MNPs, reconstruction, signal encoding, instrumentation, and application. In an effort to validate the safe and useful future use of MPI, this work aims to contribute primarily to instrumentation, signal encoding, and suited applications of MPI.

Advances of MPI. Present capabilities of MPI include real-time reconstructions providing live feedback of ongoing 3D measurements [132, 289], which can then be dissected into cross-sectional images or used for volume rendering. MPI can be classified as a tomographic imaging technique that employs algorithms to reconstruct the detailed 3D spatial distribution of the MNPs by solving a linear inverse problem. The underlying signal-model assumes a linear model [70, 130, 163], that is usually solved either in the time-domain [74] or using a system matrix approach in the frequency domain [70, 215]. Current bore-sizes of preclinical imaging systems are restricted to around 20 to 30 cm and commercial human-sized system do not yet exist, however different groups are committed to path the way by investigating different human-scale designs [76, 174, 213, 233, 255, 287] or independent hand-held devices [43, 105, 175, 228, 231].

Table 1.1: Overview and comparison of different non-invasive imaging techniques [95, 137]. Measurement times refer to slices or small volumes and increase for full 3D (body) scans. The contrast resolution of CT, MRI, and sonography can be increased using suitable tracers [162].

	CT	MRI	sonography	PET	SPECT	MPI
spatial resolution	0.5 mm	1 mm	1 mm	4 mm	8 mm	0.5 mm
measurement time	1 s	1 s to 10 min	<0.1 s	1 min	1 min	<0.1 s
sensitivity	low	low	low	high	high	high
quantitativity	yes	no	no	yes	yes	yes
contrast resolution	low	moderate	low	high	high	high
tracer	optional	optional	optional	yes	yes	yes
anatomical info.	yes	yes	yes	no	no	no
risks	ionizing	heating	heating	β/γ-rad.	γ-rad.	heating

An important step for MPI has been the invention of the magnetic particle spectrometer (MPS) [26, 300], which not only resembles a low-power model of the signal chain and thus refines and shapes the requirements for the instrumentation of larger devices, but it is also fundamental for the development of tailored tracers. The performance of MNPs can be measured at high SNR and the effects on the signal spectrum of changing the MNPs environment can be determined [219]. This is important to quantify the future image resolution and sensitivity of MPI. An MPS can also be used for highly sensitive medical diagnosis [218, 293] or as a continuous flow apparatus to optimize and monitor particle synthesis [172].

It is also possible to gather information about the immediate environment of MNPs, as long as a calibration is performed beforehand [209]. Such a functionalization includes, but is not limited to, evaluating viscosity [51, 186, 219, 280], temperature [217, 226, 253, 281, 312], particle core size [247], and binding state [185, 285] or several simultaneously [331]. The use of multi-contrast reconstructions allows the simultaneous visualization of different properties in different colors or images (channels). The combination of imaging, targeted therapy (theranostics) and feedback is a unique feature of MPI and motivates further development. For example, during hyperthermia treatment, the MNPs can be simultaneously tracked for imaging, actuated to induce cellular apoptosis, and used for thermometry via multi-contrast imaging [37, 222].

Examples for future diagnostic MPI applications are stroke imaging [76, 262, 313], angiography [156, 187], perfusion imaging [79, 120, 164, 165, 187, 332], cardiovascular and periinterventional imaging [17, 91–93, 104, 305, 309]. The transition to theranostics is manifested in cell tracking [11, 27, 221, 244, 245, 251, 267, 329], cancer detection [14, 59, 60, 96, 122, 168, 226, 282, 325], hyperthermia [6, 24, 41, 113, 188, 266], and targeted drug delivery [38, 81, 155, 158, 169, 284, 327]. Moreover, MPI has the ability to assist during clinical procedures, like vascular interventions [5, 82, 93, 103, 211, 227, 287, 304, 311] or potentially by actuation of micro-robots (magnetic force navigation) [18, 19, 38, 39, 213, 212], i.e. to treat cerebral aneurysms. Preclinical MPI devices exist in a variety of configurations, like cylindrical bore [70–72] single sided scanner [232], or Halbach configuration (permanent magnets) [16, 303], which rely on different approaches towards signal encoding, like an field-free-point (FFP) [70, 292], or an field-free-line (FFL) [25, 54, 74, 129, 176, 256].

Potential and Limitations of MPI. Established modalities such as CT for cerebral angiography [160] or MRI for imaging stroke or intracranial hemorrhage [124] outclass current MPI capabilities. However, MPI does not need to replace current imaging modalities, but can be used to compensate for drawbacks and limitations of established modalities. It has many clear advantages in terms of sensitivity, resolution, speed and low risk, especially for applications in perfusion imaging or hyperthermia treatment. Among disadvantages of MRI are the long acquisition times and low temporal resolution for dynamic processes with low tracer contrast. CT, PET, and SPECT use harmful radiation that causes adverse effects for tissue health. Although MPI measures no anatomical background information, a single CT or MRI reference image could provide the necessary co-registration and subsequently MPI provides sensitive tracer based images at high temporal resolution. Overall the radiation dose is reduced for the patient and more diversity is added the established modalities. Combined CT/MPI or MRI/MPI systems can help to bridge the gap to healthcare [27, 63, 290], together with theranostic platforms [37, 222].

Current concerns and limitations of MPI include the lack of commercially available hardware and approved MNPs, as well as risks to humans in the form of tracer biocompatibility and toxicity [27, 259], heating and PNS [34, 229, 243]. Limits of the specific absorption rate (SAR) for tissue are not expected to be a problem below 150 kHz [35, 241, 306]. However, the medical approval of suited tracers constitutes a causality dilemma, because clinical approval is a costly endeavor and the broad market for tailored MPI tracers does not yet exist that justifies such an investment. Preclinical tailored MNPs for MPI are available since 2009 [58], and some approved contrast agents from MRI like Ferucarbotran also exhibit a measurable, but low, MPI signal contrast [70, 121, 166, 323]. Nevertheless, MPI has great potential as a non-invasive, real-time imaging modality that can permeate the human body without attenuation and with low risk to patients and staff [35]. The benefit of combining diagnosis and therapy, along with its robustness to be integrable to demanding environments like an ICU, makes it a valuable candidate in neuroimaging, hyperthermia treatment and cardiovascular interventions. To enable a wider range of applications and to expand the tools available in medical imaging, the assessment of new applications and the upscaling of instrumentation to human dimensions is a major motivation for further research in MPI.

1.2 Publications and Contributions

In order to contribute to overcoming current limitations, the first part of this work concerns the **instrumentation** of MPI over the course of three publications. We commence with a hybrid simulation framework based on a custom designed arbitrary waveform MPS that enables the investigation of different excitation waveforms and offsets [O1]. Most notably, different types of imaging sequences can be modeled in 2D using arbitrary waveforms to characterize the signal response and the potential of future scanner designs and the eligibility of tracers (chapter 5). Stepping from spectroscopy to the instrumentation of an imaging device, a highly linear transformer with a high gain, called inductive coupling network (ICN), is simulated and designed in the second work [O2]. As a resonant passive component, this toroidal transformer is optimized and integrated as one essential part of a human-sized head scanner for MPI (chapter 6). Lastly, the head scanner is the subject of the third work, which encompasses the full development and system characterization of a 3D real-time human-sized head scanner, intended for diagnosis like cerebral imaging [O3]. A variety of phantom imaging experiments are conducted to determine resolution and sensitivity, as well as to calculate perfusion maps using a medically approved MRI tracer (chapter 7).

The second part of this thesis addresses the extension of future **applications** of MPI, again over the course of three publications. Firstly, we connect to our work of chapter 7 [O3] with a discourse and detailed analysis of the mentioned approved MNPs (Ferucarbotran) for MRI which are both, suitable for MPI and currently approved for human injection [O4]. In addition to our arbitrary waveform MPS, various methods and instruments such as vibrating sample magnetometry, dynamic light scattering, transmission emission microscopy, and preclinical MPI are used to evaluate spectral signal quality, magnetization, imaging performance, and composition (chapter 8). Secondly, we further pursue enhancements to perfusion imaging, a prospective area for MPI, as evidenced by our development of a human-sized system for cerebral applications. A new way to utilize the MPI signal is proposed by exploiting a negative contrast in the concentration based on long circulating MNPs [O5]. We demonstrated the successful deduction of medical parameters in the context of perfusion imaging using a negative-contrast-saline bolus (chapter 9). Finally, we present an application for interventional radiology that improves the future detection of gastrointestinal bleeding in humans using two tracers and multi-contrast real-time imaging in [O6] (chapter 10).

Teamwork. The construction of the first version of a human-sized head scanner in 2019 [76] and its advancement towards a safe clinical prototype [O3] from 2020 to 2024 was a major interdisciplinary team effort at our institute, spanning across all research fields of MPI. Essential to a running imaging device is the data acquisition system [90], a graphic user interface (GUI) [138], and the data processing [89], developed over time with a suitable data format [144, 147]. The reconstruction of images requires not only a versatile software package [O16, 132, 148], but also detailed knowledge on artifact suppression [29, 192, 235] and on parameter tuning and balancing [30, 33, 190, 237, 279]. Prerequisite for an MPI system evaluation is the exact determination of its magnetic fields [28, 32, O15, 238, 274], an excitation sequence [76, 261, 314] and the tools to calibrate the system correctly [31, 276]. Our group also contributed research on background signal reduction [131, 139, 143], on the long-term stability of a running system [273, O20], on hardware components [79, O3, O21], and on channel decoupling [O2, 275]. Lastly, a significant amount of effort was dedicated to the development, simulation, and prototyping of a flexible selection field generator with low power consumption [61, 62, O14, O13], aimed to be integrated in a future upgrade of the head scanner. The sum of these publications and preliminary work, their interlinking and their parallel progress have helped to achieve iterative improvements at our institute.

Concerning the work of the author, parts of this thesis were published in peer-reviewed scientific journals [O1] to [O6], and presented at conferences [O7] to [O11]. Furthermore, several publications were published and/or presented at conferences with the author's participation [O12] to [O22].

1.3 Structure of this Work

The introduction is followed by two preliminary chapters, one on the fundamentals of MPI (chapter 2) and one with a focus on electromagnetic fields in MPI (chapter 3). The purpose is to explain the basic physics of MPI and provide the reader with an understanding of instrumentation and signal processing first, before moving on to an encompassing description of all works in chapter 4. Here, a detailed outline and motivation of the six journal publications that attend to this dissertation is provided, including their relation with each other. The focus is on details that were omitted in published articles and to motivate our approach, without duplicating the findings or discussion of the self-contained works.

Chapters 5, 6, and 7 treat the instrumentation, characterization, and optimization of hardware components and imaging systems, as well as hybrid sequence modeling. Chapters 8, 9, and 10 are focused on applications that are self-contained works, using primarily an established preclinical MPI scanner for measurements. The corresponding studies are included in their respective chapters in the journal style. Finally, the overall conclusion, discussion, and outlook are given in chapter 11.

2

Fundamentals of Magnetic Particle Imaging

This chapter provides an introduction to MPI, outlining the necessary steps involved in obtaining an image. The image acquisition process in this thesis can be broadly categorized into four essential components:
Measurand: MPI measures MNPs, which convey information from the subject to the scanner. As a quantitative imaging method, MPI primarily measures the MNP concentration, which consists mainly of superparamagnetic nanoparticles. Although intrinsic information on tissue or bones is not recorded in MPI, the nanoparticles are influenced by their surroundings and also encode information about their environment, viscosity and binding state.
Signal encoding: In order to excite the MNPs to evoke a measurement signal, MPI uses magnetic excitation fields in the low kHz range and detects the particles non-linear magnetization response via induction. Due to the quick relaxation of the MNPs, the receive signal is recorded simultaneously during the ongoing excitation. The relaxation delay and non-linearity in the magnetization response is then visible in the induced receive signal.
Spatial encoding: An image requires distinguishable spatial information on the exact origin of the particles that cause the receive signal. Typically, a gradient field for spatial selection is applied to reduce the signal origin to a small selective low-field-region (LFR). The desired field-of-view (FOV) of the image is then sampled by a trajectory, that continuously shifts the LFR. The location of the LFR over time is thus known and encoded in the receive signal.
Reconstruction: A reconstruction algorithm is used to solve the underlying inverse problem of MPI in the frequency domain. The solver utilizes the spatially dependent features in the recorded signal to match the spatial particle concentration distribution to a prior calibration measurement. The FOV can be a 3D volume and each voxel is then ascribed a concentration dependent value.

The following sections elaborate on each step and present the process of obtaining an MPI image from data acquisition to image reconstruction.

2.1 Magnetic Nanoparticles

The essential measurand in MPI are small magnetic iron oxide particles, i.e. magnetite Fe_3O_4 and maghemite Fe_2O_3, which are coated to improve biocompatibility and influence hydrodynamic behavior [154]. They vary in shape and core-size, ranging from a few nanometers to several micrometers which determines the governing physics and thus their behavior in an oscillating magnetic field [23]. The coating is often dextran-based or PEG-based (polyethylene glycol) to ensure and design biocompatible properties [57, 157] and avoid particle agglomeration. Agglomeration and aggregation into particle clusters, as well as long particle chains, greatly affect the particle response [53, 271, 322]. To understand the non-linear magnetization behavior of MNPs, we will first consider magnetic permeability, which describes the measure of internal magnetization $\boldsymbol{M}$ that a material obtains in response to an externally applied magnetic field $\boldsymbol{H}$ [111]. The magnetic flux density $\boldsymbol{B}$ can then be expressed as

$$\boldsymbol{B} = \mu_0(\boldsymbol{H} + \boldsymbol{M}) = \boldsymbol{\mu}\boldsymbol{H}. \tag{2.1}$$

Non-magnetic materials do not interact with $\boldsymbol{H}$ and therefore $\boldsymbol{B}$ aligns with $\boldsymbol{H}$ and the permeability tensor $\boldsymbol{\mu}$ becomes a scalar material constant as expressed in

$$\boldsymbol{B} = \mu_0\mu_\mathrm{r}\boldsymbol{H} \tag{2.2}$$

with a relative permeability $\mu_\mathrm{r} = 1$ in vacuum [111] and a vacuum permeability $\mu_0 \approx 4\pi \cdot 10^{-7}\,\mathrm{H\,m^{-1}}$. The μ_r can be regarded as a neutral threshold line and is drawn in Figure 2.1 (a). Materials that reduce the overall magnetization by internally opposing the external magnetic field, are called diamagnetic and are positioned below μ_0 with an $\mu_\mathrm{r} < 1$. Substances above this line interact with an external field by aligning internally with the field, which increases the overall magnetic flux density ($\mu_\mathrm{r} > 1$) [326]. In the case of ferromagnetic materials, this intensification greatly increases $\boldsymbol{B}$ until the majority of magnetic domains are aligned and consequently saturation occurs above a certain external field strength ($\mu_\mathrm{r} \gg 1$).

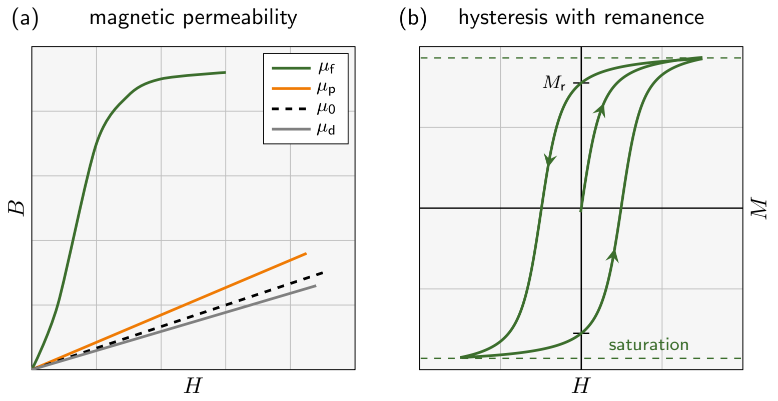

Figure 2.1: Permeability and hysteresis. Different types of magnetic permeability are shown in (a) and their reaction in terms of magnetic flux density to an applied 1D external field: ferromagnetism μ_f, paramagnetism μ_p and diamagnetism μ_d. The hysteresis loop depicted in (b) corresponds to a ferromagnetic material, whereby the magnetization curve exhibits a non-zero residual magnetization M_r, also known as remanence.

When ferromagnetic materials are reduced in size, they eventually become a single magnetic domain and paramagnetic behavior can be evoked. If the particles are considered in isolation, thermal fluctuations cause the magnetization to flip, resulting in a net magnetization of zero in the absence of an external field [44, 67]. However, when an external field is applied to the considered superparamagnetic iron nanoparticles, the resulting net magnetization is much larger than that of typical paramagnetic materials and is thus called superparamagnetism.

One typical ferromagnetic characteristic at macroscale is remanence, where the material retains a non-zero residual magnetization M_r after the external magnetic field is removed [326]. This effect arises due to the persistence of magnetic domain alignment, causing the magnetization to deviate from the demagnetization curve. If exposed to an oscillating magnetic field, a hysteresis loop is created that does not pass through the origin of the H-M-field plot, as shown in Figure 2.1 (b).

In the case of MPI, remanence is an undesired property. However, a steep magnetization curve is desired for effective signal encoding. Beside the magnetic core material, the design of a suitable coating is very important to improve biocompatibility with the human body and to influences particle agglomeration [99, 195]. The coating creates a hull around the particle (or a cluster of particles) and a spatial separation of these is achieved that reduces magnetic particle-particle-interactions between individually coated particles. Specific applications can thus be conceived by changing the shape and size of the particle shell, although the core material is identical [24, 52, 66, 154, 322].

2.1.1 Brownian and Néel Relaxation

The size of the magnetic core and its shell can be roughly modeled by diameters d_c and d_h, respectively. The latter describes the hydro-dynamic particle diameter, which determines aqueous particle behavior when suspended in a fluid like water or blood, illustrated in Figure 2.2 (a). In the following subsection, we will regard two different relaxation types, which together govern the particle dynamics at the nanometer range.

Brownian and Néel relaxation are two fundamental phenomena that are observed in a wide range of physical systems. In the MPI context they pertain to the process of particle relaxation, and they are characterized by the time required for the particles to align with an applied field, which we call relaxation. Of the two, the relaxation time that is shorter dominates the measured signal response, due to the time dependence of signal induction (see Equation (3.6c) of section 3.1).

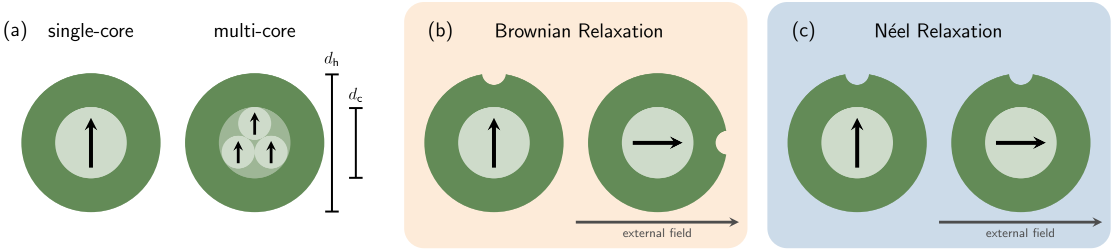

Figure 2.2: Particle diameters and relaxation. In (a), diameters and different particle cores (bright green) in a coating/hull (dark green) are shown. Relaxation relates to the time it takes a particle to align with an external field or revert back to its easy-axis. Brownian relaxation in a fluid is shown in (b), where the entire particle rotates (marked by a dent) and Néel relaxation is shown in (c) where only the magnetization turns internally.

Brownian relaxation can be used to describe a mechanism by which small particles suspended in a fluid undergo hydrodynamic motion caused by external forces such as molecular collisions or magnetic fields, if susceptible. The internal magnetization remains fixed with respect to the crystalline lattice and the whole particle rotates, as shown in Figure 2.2 (b). A rotational motion is influenced by e.g. viscosity η and temperature T and can be simplified to the zero-field Brownian relaxation time τ_B as

$$\tau_\mathrm{B} = \frac{\eta \pi d_\mathrm{h}^3}{2 k_\mathrm{B} T}\,, \tag{2.3}$$

where k_B is Boltzmann's constant [49].

Néel relaxation, on the other hand, is a mechanism by which the magnetization of a magnetic material turns internally with respect to the surrounding crystalline lattice [193], shown in Figure 2.2 (c). An immobilized particle (e.g. frozen or cemented) would only undergo Néel relaxation and Brownian motion is suppressed. This is a tool to methodically analyze the contributions of both relaxations [317]. The underlying mathematical model is more complex and depends on material parameters like the gyromagnetic ratio, saturation magnetization and anisotropy [49, 127], which makes τ_N in general sensitive to the magnetic field strength. A simplified zero-field expression is found with

$$\tau_\mathrm{N} = \tau_0 \,\exp\left(\frac{K_\mathrm{i} V}{k_\mathrm{B} T}\right) = \tau_0 \,\exp\left(\frac{K_\mathrm{i} \pi d_c^3}{6 k_\mathrm{B} T}\right)\,, \tag{2.4}$$

where $K_\mathrm{i} V$ describes the energy barrier and τ_0 denotes a material-specific constant (Ki is the anisotropy constant). However, this expression fails to express field strength dependence and phase delay in an oscillating field. In addition, τ_B and τ_N are coupled and cannot be treated independently [49, 223, 248].

The simulated individual sensitivity of τ_B and τ_N with respect to the excitation field amplitude is plotted in Figure 2.3 (a) for a step input. The green line highlights the τ that dominates the induced signal response for MPI. Brownian relaxation dominates at lower amplitudes, but is outrun by Néel relaxation at high amplitudes for this simulated particle [49] (simulation parameters can be found in the figure description). This exemplifies that a precise prediction of particle relaxation in a fluid is difficult and complex, as well as identified the dominating physical mechanism. However, accurate particle models are an active research field and have many applications in MPI [7, 127, 139], which will be explained in detail in subsection 2.5.1.

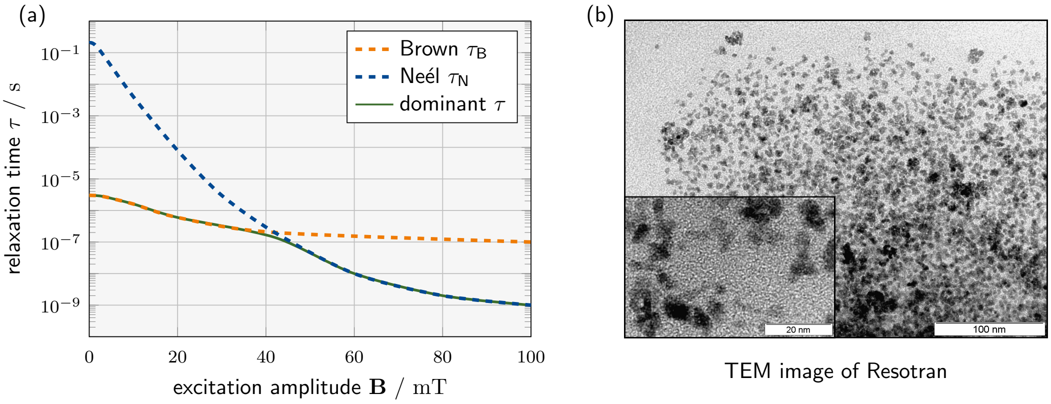

TEM image of Resotran

Figure 2.3: Relaxation times and TEM images. In (a), the simulated step response for different amplitudes is shown, demonstrating the amplitude dependence of a single particle. Data and simulation from Deissler et al. [49]. Parameter selection: $d_\mathrm{h} = d_\mathrm{c} = 20\,\mathrm{nm}$, $T = 300\,\mathrm{K}$, $\eta = 1.0049\,\mathrm{mPa\,s}$, $K = 20\,000\,\mathrm{J/m^3}$. In (b), transmission emission microscopy (TEM) images of Resotran are shown, where particles agglomerate and form clusters that change their relaxation time [O4].

To visualize the magnetic core and particle clusters and how particles agglomerate and aggregate, a TEM image is shown in Figure 2.3 (b) of the tracer Resotran (b.e. imaging, Baden-Baden, Germany).

2.1.2 Langevin Model and Signal Generation

After introducing the basics for particle magnetization and relaxation, this section focuses on a model to express the non-linear signal generation of MNPs. Under the assumption that $\boldsymbol{M}$ adiabatically follows an externally applied field $\boldsymbol{B} = B\mathbf{e}_{\boldsymbol{B}}$, a simplified model for the 1D magnetization M can be expressed using the Langevin function

$$M(\xi) = M_0 \coth \xi - \frac{1}{\xi}, \quad \text{with} \quad \xi = \frac{mB}{k_{\mathrm{B}} T}. \tag{2.5}$$

Here, m stands for the mean magnetic moment of a single particle in a 1D excitation field B [214]. This approximation is valid for ideal paramagnetic materials at the thermodynamic limit [125], and it ignores effects of dynamic excitation, remanence or coercivity, which explains the single magnetization curve for both magnetization directions seen in Figure 2.4 (a). The advantage of this simplistic model is its ability to demonstrate the basic principle of signal generation, shown by the point spread function (PSF) in (b): Plotted are the changes in magnetization $\frac{\mathrm{d}M}{\mathrm{d}t}$ for different particle core sizes. One insight is that a larger core size corresponds to a steeper, non-linear magnetization curve, resulting in a higher change of $\frac{\mathrm{d}M}{\mathrm{d}t}$, which is directly related to the voltage induction in MPI receive coils. A desirable property of particles for MPI is therefore a high and narrow PSF to obtain a strong receive signal [46].

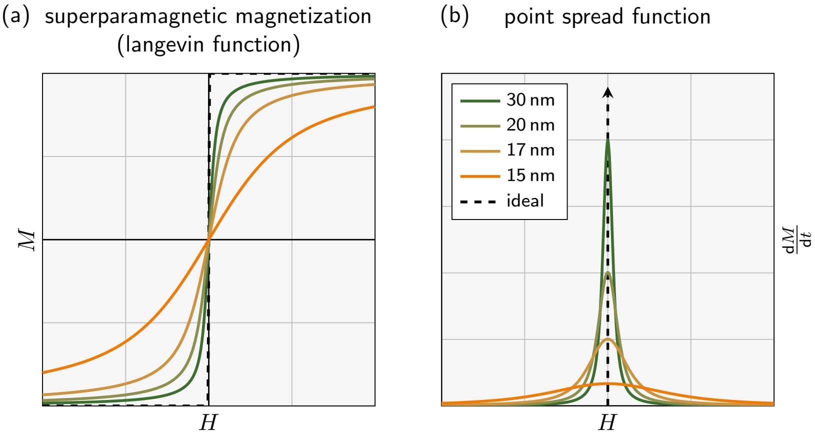

Figure 2.4: Langevin function and PSF. Langevin function simulation of magnetization (a) and the associated point spread function (b) for different particle core sizes. An ideal magnetization flips instantaneously and thus produces a Dirac-like induced signal.

A review of empirical data on particle measurements reveals that superparamagnetic nanoparticles exhibit some hysteresis and that the PSF is asymmetrically broadened, shown in Figure 2.5 along with different types of PSFs. Reason for this include the mainly the dynamic excitation instead of a ferromagnetic remanence, as studied in more detail in chapter 8. One typical model used to estimate spatial resolution is shown in Figure 2.5 (b), the static PSF [46]. During a constant 1D excitation of $B_{\mathrm{DF}} = 20\,\mathrm{mT}$, a sweep of different offset fields B_{Off} is performed, similar to moving a sample from one end to the other through the FOV of an MPI scanner. The result is an offset-field dependent PSF that is typically characterized by its full width at half maximum (FWHM) in mT [268]. This value can easily be converted to a distance in mm for a specific gradient field $\boldsymbol{G}$ and relates to the maximum achievable spatial resolution, which will be explained in section 2.3.

A more straight-forward consideration is shown in the plot of Figure 2.5 (c), which can be understood as a dynamic PSF where $\frac{\mathrm{d}M}{\mathrm{d}t} \propto \frac{\mathrm{d}m}{\mathrm{d}t}$ is plotted against a single period of the sinusoidal excitation field. At maximum amplitude ($\pm 20\,\mathrm{mT}$) the change in magnetization is zero, which corresponds to the change to the other half-wave. The highest slew rate of a sinusoid is located at its zero-crossing, as evidenced by the plot, which reveals the delay by particle relaxation as a shifted maximum in its direction, either positive or negative. The plots in Figure 2.1 permit the assessment of tracer performance for the MPI by evaluating shape, size, and FWHM. They demonstrate the fundamental principles underlying 1D signal generation: the significance of the nonlinear particle response that identifies them as distinct from the excitation field.

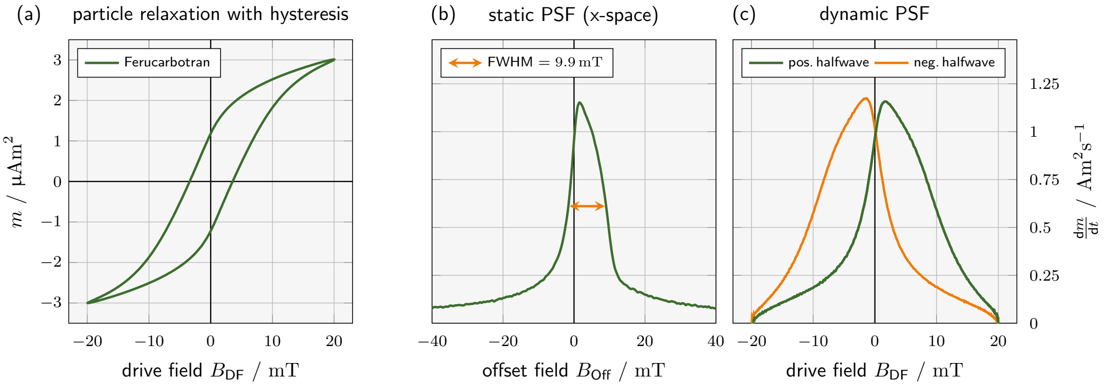

Figure 2.5: Measured hysteresis and PSF of MNPs. Spectroscopy measurements of Resotran [O19]. The magnetization curve in (a) deviates from the Langevin model (broadening) and a relaxation delay is introduced, which shifts the PSF and causes asymmetry. In (b), the change in magnetization is plotted against an offset in excitation direction, and in (c) against the drive field.

2.2 Signal Encoding

With the introduction of modeled and measured particle signals, we commence with a detailed description of the MPI signal and the methodology employed to obtain it. The objective of signal encoding is to acquire a response from the measurand that inherently carries information about both the measurand itself and its immediate environment. This information mainly provides the particle concentration, but it depends on characteristics such as size, binding state, easy axis alignment, and temperature, which influence the recorded signal as well.

The 1D response of a particle ensemble refers to the non-linear magnetization $M(t)$ that MNPs exhibit when exposed to an external sinusoidal field $B_{\mathrm{DF}} = A\sin(2\pi f_1 t)$ with amplitude A, time t and fundamental frequency f_1. The particle's response can be quantified by measuring the time derivative of the magnetization $\frac{dM}{dt} \propto u$, which is proportional to the voltage induced in a nearby receive coil. This voltage is known as the receive signal and it is typically converted to frequency space [70, 214], denoted by a hat as in $\hat{u}$, for signal processing and image reconstruction.

The MPI signal encoding principle is illustrated in Figure 2.6 for a low amplitude A_1 and a high excitation amplitude $A_2 = 5A_1$, based on a Langevin function particle model. The smaller amplitude (orange) barely leaves the linear region of the magnetization curve in (b), which results in a weak receive signal u in (d) and in steeply declining harmonics of the magnitude of $\hat{u}$ in (e). The high amplitude (green) yields a much stronger and more distorted signal u, resulting in numerous and larger harmonics. A magnetization curve with a steeper slope would also result in a stronger signal induction and the creation of more harmonics when the particles are driven in their saturation region [214]. The first harmonic of $\hat{u}$ is called the fundamental with frequency f_1 and higher-order harmonics are referred to by their indices $f_k = kf_1$ with $k \in \mathbb{N}^+$, which are integer multiples of the fundamental.

It should be noted that the unfiltered receive signal also contains the fundamental of the excitation field itself, either due to coil coupling between receive and transmit coils or because a single transmit-receive coil is shared. The coupled signal fundamental is approximately eight orders of magnitude higher than the particle's response, if not suppressed or filtered [214, 308]. For this reason, two types of filters are typically employed: transmit filters to minimize the total harmonic distortion (THD) of the excitation field, thereby ensuring the presence of only particle harmonics suitable for imaging; and receive filters to suppress the fundamental feedthrough, thus maintaining the dynamic range of the low noise amplifier (LNA) at the end of the receive chain. A homogeneous sinusoidal excitation, as illustrated in Figure 2.6, results in the generation of only odd harmonics for a punctual Langevin magnetization [214]. In superposition with other fields, such as a selection field or an offset field, will result in the generation of different harmonic patterns in amplitude and phase. These patterns are crucial for spatial encoding, as they represent unique spatial locations that can be matched to the signal origin.

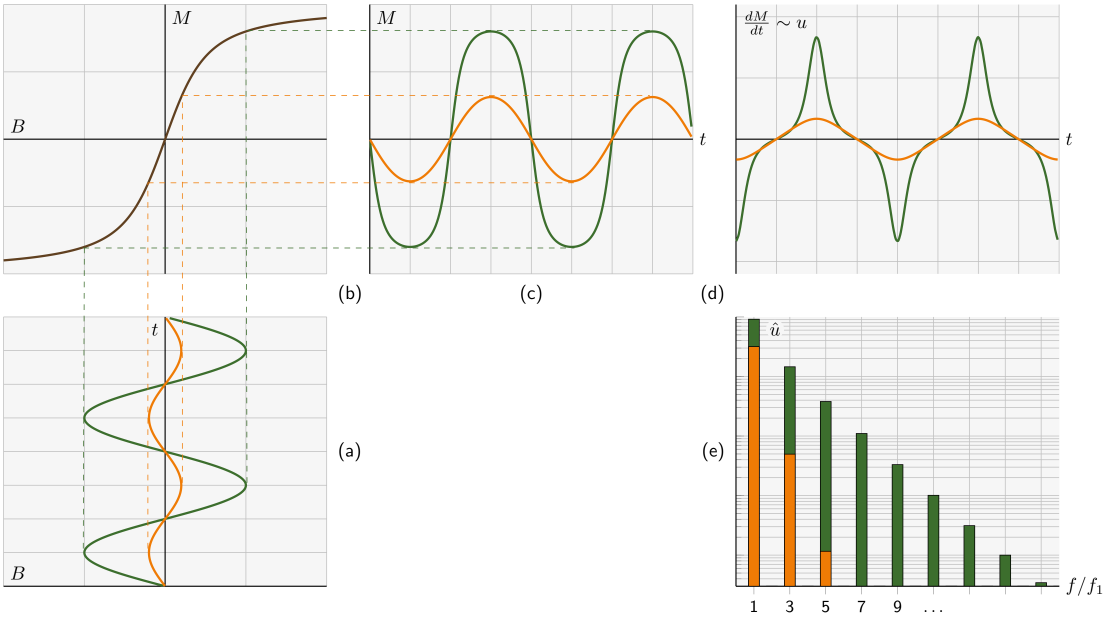

Figure 2.6: Signal encoding for two different signal amplitudes. In order: (a) excitation from an externally applied field, (b) Langevin particle magnetization, (c) resulting magnetization M, (d) the derivative $\frac{dM}{dt}$ which relates to the induced voltage u, (e) the Fourier transform $\hat{u}$ of u, plotted on a logarithmic y-axis. The smaller amplitude (orange) creates a weaker and more linear voltage u, whereas a larger amplitude (green) drives the particles into the non-linear saturation region which creates a stronger particle response and thus more harmonics.

2.3 Spatial Encoding

We have just observed the emergence of harmonic patterns while exciting individual particles in signal encoding, and it has been determined that these patterns are influenced by the excitation field and the particle's magnetic properties. The subsequent stage of spatial encoding is designed to intentionally generate a distinctive signal for various locations, enabling the reconstruction of the signal's origin. One approach involves the utilization of a second field, the selection field $\boldsymbol{B}_{\mathsf{SF}}(\boldsymbol{r})$, which is spatially dependent and thus the magnetization vector of particles varies with the FOV. Taking a magnetic field with a linear gradient, such as

$$\boldsymbol{G} = \begin{pmatrix} G_x & 0 & 0 \\ 0 & G_y & 0 \\ 0 & 0 & G_z \end{pmatrix} = g \begin{pmatrix} 1 & 0 & 0 \\ 0 & -\frac{1}{2} & 0 \\ 0 & 0 & -\frac{1}{2} \end{pmatrix} , \tag{2.6}$$

with a gradient strength g in $\mathrm{T\,m^{-1}}$, creates a location depend offset field. G_x, G_y and G_z are chosen in this way in order to satisfy Gauss's law for magnetism

$$\nabla \cdot \boldsymbol{B} = \frac{\partial B_x}{\partial x} + \frac{\partial B_y}{\partial y} + \frac{\partial B_z}{\partial z} = \mathsf{trace}(G) = 0 \, , \tag{2.7}$$

which states that magnetic field lines are always closed and magnetic monopoles do not exist. This is a natural restriction to the amplitude and direction of selection fields that can be used. In superposition of a 1D drive field and the selection field, the local flux density at a point $\boldsymbol{r} \in \mathbb{R}^3$ in the FOV is given by

$$\boldsymbol{B}(\boldsymbol{r}, t) = \boldsymbol{B}_{\mathsf{DF}}(t) + \boldsymbol{B}_{\mathsf{SF}}(\boldsymbol{r}) = \boldsymbol{A} \sin(2\pi f_1 t) + \boldsymbol{G}\boldsymbol{r} \, . \tag{2.8}$$

With $\boldsymbol{B}_{\mathsf{SF}}(\boldsymbol{r})$, a spatial selection is achieved that has a field-free-region (FFR) around an FFP, or more precisely a low-field-region (LFR) in its center, where the particles are responsive, while surrounding particle responses are gradually silenced by a dominating saturation magnetization. These particles in saturation do not contribute to the receive signal and are not flipped by $\boldsymbol{B}_{\mathsf{DF}}$, thus achieving spatial selection.

2.3.1 Field Free Point (FFP)

In the following, we will consider a one dimensional example with $\boldsymbol{r} = (x, 0, 0)^\top$ where a linear gradient $G(x)$ is zero at $x = 0$, called the FFP. At all other locations $x \neq 0$ along this line, the gradient field creates a different offset, which is shown in Figure 2.7 for 4 different positions (1-4). It should be noted that either the sample can be moved through the field or vice versa, the field can be shifted relative to a stationary sample. The amplitude A_x of $B_{\mathsf{DF}}(t)$ is constant and superimposed with the linear offset from $G(x)$. Together they span a 1D FOV in x-direction (green area). At positions $x = \pm A_x/g$, the offset becomes larger than the amplitude and therefore the particles cease to flip. Here, particle saturation is achieved. The signal contribution from outside the FOV is strongly dampened with distance, but it depends on the slope of the magnetization and particles still contribute to the recorded response in close proximity of FOV borders. The response falloff is gradual, as shown in (1) of Figure 2.7, and stronger for steep particle magnetization. Nevertheless, $\hat{u}$ is dominated by contributions from inside the FOV as illustrated by (2) and (3).

Therefore, 1D spatial encoding is achieved: each location induces a slightly different voltage which corresponds to the unique combination of excitation and offset field along x. Consequently, $\hat{u}$ has a different complex spectral pattern for all positions of x throughout the

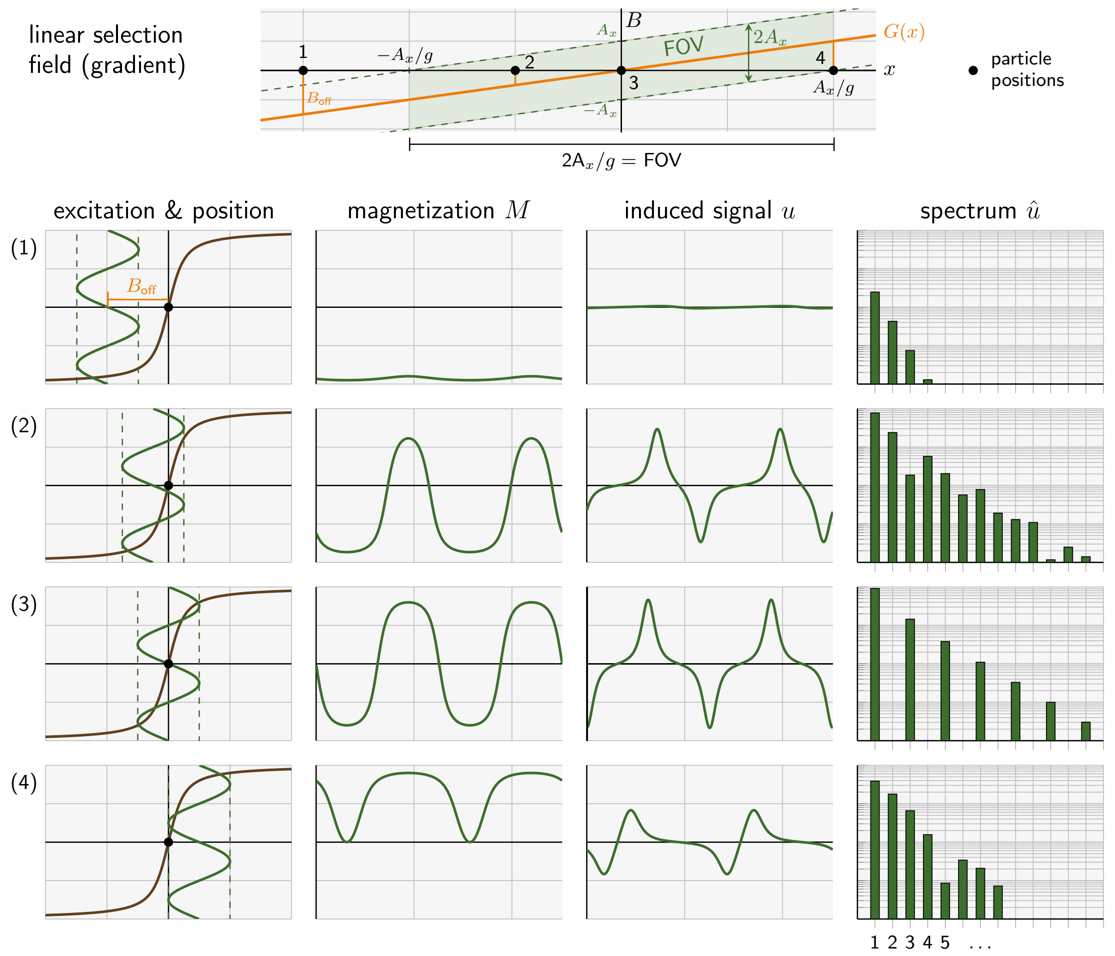

Figure 2.7: 1D spatial encoding. Simulation of different relations of particle responses and offset fields. Shown are magnetization, receive signal and spectrum for four different particle locations in a linear gradient field $G(x)$ of strength g, at a constant excitation $B_{\mathrm{DF}}(t) = A\sin(2\pi f_1 t)$. Note that moving the sample through the field is equivalent to shifting the field relative to a stationary sample. A spans the 1D FOV with a distance of $2A/g$. Characteristic patterns of $\hat{u}$ indicate that different locations can be spatially separated. The MNP response outside the FOV is strongly suppressed.

FOV, also called a spectral fingerprint. If the spectral fingerprints of all locations are known, a system of linear equations can be solved to reconstruct position and concentration (see section 2.5). This example can be transferred to 2D or 3D excitations and the challenge becomes to encode large areas while maintaining a high resolution, which is a fundamental challenge for MPI that requires a careful trade-off.

Resolution and FOV Size: A significant observation is that the spatial position of the LFR undergoes a shift due to the presence of the drive field, which is relative to the ratio of the drive-field amplitude vector $\boldsymbol{A}$ and the selection field gradient $\boldsymbol{G}$. This is the fundamental mechanism that simultaneously creates a trajectory to sample different positions within the scanner, determines the FOV size, and causes the MNPs to flip. For each spatial direction, the component-ratio A/G defines the deflection that is caused by each drive-field cycle and results in the boundaries of the 2D or 3D FOV. Large amplitudes in the presence of a low selection field gradient yield a large FOV as stated in Equation (2.8). It can be postulated intuitively that the size of the LFR should be reduced with a high $\boldsymbol{G}$ in order to create a smaller area of responsive particles that guarantees high spatial selectivity. However, for a constant $\boldsymbol{A}$ this is coupled to a reduction of the FOV size and forces a trade-off.

2D and 3D MPI: The creation of an LFR with a single Maxwell coil pair and its displacement by current variations in the same coils via $\boldsymbol{B}_{\mathsf{DF}}$ is illustrated in Figure 2.8. For a 2D scenario with two sinusoids and a second coil pair, the LFR follows a Lissajous trajectory, if slightly different frequencies f_x, f_y are used for each channel. This is shown in Figure 2.8 (c), where a full trajectory is completed with the group period T_{g}. The same principle can be expanded to 3D, shown in (d), where T_{g} is determined by the least common multiple (lcm) of all involved periods, required a third coil pair. The base frequency

$$f_{\mathsf{base}} = f_x K_x = f_y K_y = f_z K_z \tag{2.9}$$

expresses the relation of the individual frequencies, which can be used to determine the sampling density and the group period of one full drive field cycle

$$T_g = \frac{\mathsf{lcm}(K_x, K_y, K_z)}{f_{\mathsf{base}}} \, . \tag{2.10}$$

One characteristic of Lissajous trajectories is the dense sampling of edge regions and a sparse sampling towards the center due to the higher velocity, caused by the high slew rate at the

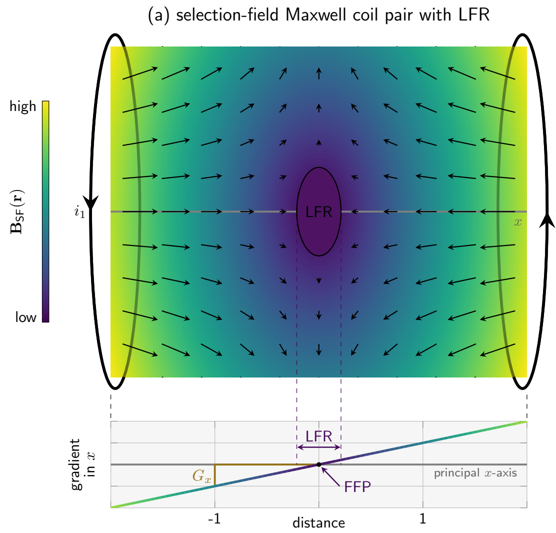
(a) selection-field Maxwell coil pair with LFR

(b) moving the LFR along the principal x-axis

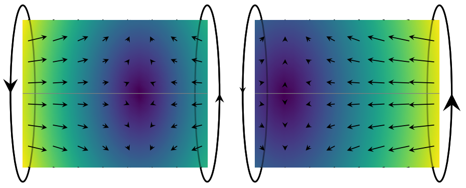

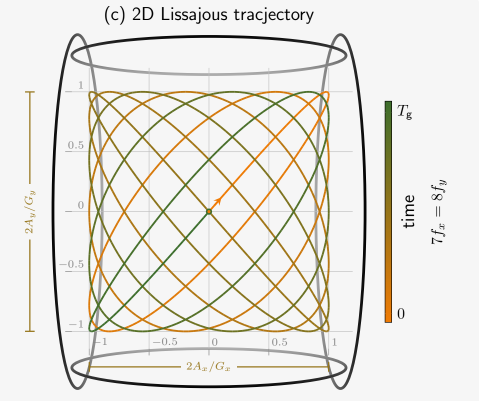
(c) 2D Lissajous tracjectory

(d) 3D Lissajous tracjectory

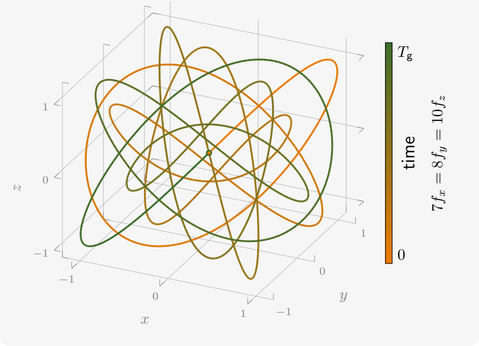

Figure 2.8: Selection field, LFR and Lissajous trajectory. A linear selection field that satisfies Equation (2.7) is shown in (a), with $2G_x = G_y = G_z$, which yields an ellipsoidal LFR shape. By varying currents i_1 and i_2, the LFR is shifted in (b) along a single axis. On the right side, a 2D (c) and a 3D (d) Lissajous trajectory with the group period T_{g} are shown, based on a combination of sinusoidal oscillations. These offer the possibility to shift the LFR around the FOV, but require additional coils.

zero-crossing of sinusoids. Examples of common trajectories exhibit a meandering shape (Cartesian) or a combination of harmonic oscillations (Lissajous, spiral, radial) [128]. It should be noted that the sequence trajectory exerts a direct influence on the image quality and the types of artifacts that occur.

We have now described and illustrated the fundamentals of spatial encoding in MPI using an FFP and a technique to simultaneously excite a small selection of particles along a specific trajectory. It should be noted that a genuine field-free point is neither achieved nor strictly required. LFRs often have an ellipsoid shape or fields are distorted by coil geometry or excitation [36], especially towards the edges of the imaging bore.

Before embarking on a short discourse on advanced concepts for dynamic selection fields in section 2.4, we will briefly examine a specific type of LFR in the following subsection. The last part of this chapter will explain the reconstruction of acquired data in section 2.5.

2.3.2 Field Free Line (FFL)

As mentioned in the previous section, a minimization of the LFR incurs high spatial selectivity and seems desirable. However, the amount of responsive nanoparticles is also reduced if a homogeneous distribution is assumed and their combined response constitutes the overall receive signal strength. Thus, the sensitivity is diminished for a higher gradient field.

In an effort to increase the sensitivity, other spatial encoding techniques feature different concepts for the shape of the LFR, such as the FFL. Here, the responsive region of particles is larger and the system becomes more sensitive, but the spatial encoding requires a mechanism to recover the lost information along the principal axis of the line [141, 310]. A classic approach is to rotate the FFL to achieve volumetric sampling [25, 134, 151, 310], as known from Radon-space sampling where the receive signal equals the integral along the projected line [129]. The FFL gradient can be described using a gradient field such as

$$\boldsymbol{G} = g \begin{pmatrix} 1 & 0 & 0 \\ 0 & -1 & 0 \\ 0 & 0 & 0 \end{pmatrix} , \tag{2.11}$$

which creates a field-free-line in z-direction. A filtered back-projection can be used for image reconstruction, which is well known from CT [134, 208, 310].

The advantage of an FFLis the boost in sensitivity due to a larger responsive area. The trade-off is that it requires more complex dynamic selection field generation and sequencing. FFL scanners pose an active field of research and the development in the community also focuses on flexible selection field generators (SFGs) [O14, 80, 176, 256, 278, 303].

2.4 Dynamic Selections Fields

So far, the size and shape of the FOV relies on the component-wise ratio of $\boldsymbol{B}_{\mathsf{DF}}$ and the static $\boldsymbol{B}_{\mathsf{SF}}$. The FOV is thus limited by the drive field amplitude that deflects the LFR. Due to limitations of the drive-field amplitude concerning instrumentation and safety, the size of the FOV needs to be increased by other means [69].

To maintain high spatial selectivity for large scanned volumes, the introduction of a third field component is necessary, mutating the static selection field $\boldsymbol{B}_{\mathsf{SF}}(\boldsymbol{r})$ into a dynamic selection field $\boldsymbol{B}_{\mathsf{SF}}(\boldsymbol{r}, t)$. Consequently, the LFR can be gradually shifted to other areas within the scanner bore, and the overall field can be expressed as

$$\boldsymbol{B}(\boldsymbol{r},t) = \boldsymbol{B}_{\mathsf{DF}}(\boldsymbol{r},t) + \boldsymbol{B}_{\mathsf{SF}}(\boldsymbol{r},t) = \boldsymbol{B}_{\mathsf{DF}}(\boldsymbol{r},t) + \boldsymbol{G}(\boldsymbol{r}) + \boldsymbol{B}_{\mathsf{SF,dyn}}(\boldsymbol{r},t)\ . \tag{2.12}$$

The LFR typically undergoes a slower displacement induced by the dynamic selection field compared to the fast drive field, and gradually follows a sampling trajectory to scan the FOV, which may have arbitrary geometry. This increases the FOV for an unchanged drive-field slew rate. This can be adapted to the type of excitation, e.g. to bring orthogonal motion to an excitation plane, and such fields usually require additional coils to cover the remaining spatial dimensions [145, O3]. This imposes additional constraints on positioning, current efficiency, and bore accessibility [142, 145, 146].

In conclusion, the incorporation of a dynamic component to $\boldsymbol{B}_{\mathsf{SF}}(\boldsymbol{r},t)$ allows for the spatiotemporal adjustment of the LFR, thereby enhancing the overall flexibility of the MPI scanner. If the objective is to expand the image FOV, multi-patch reconstructions are an effective tool. Further important use cases of a dynamic selection field besides imaging are its deployment in force experiments and hyperthermia applications.

2.4.1 Multi-Patch Imaging

The term "multi-patch" refers to enlarging the overall image FOV by sequentially shifting an enclosed drive field FOV, using the dynamic selection field to include multiple, neighboring 2D or 3D patches [69]. This sequential technique is particularly useful to exploit the high resolution of small drive field FOVs, covering large volumes in the range of the human body. Typical gradients strengths lie in the region of 0.5 to 7 T m^{-1} [152, 261] and drive field amplitudes are limited around 4 to 7 mT [200, 242]. Restrictions by PNS are often more important for MPI than SAR limits [229, 230, 243]. A typical drive field FOV remains for example at $10 \times 10 \times 5\,\mathrm{mm}^3$ for $A_x = A_y = A_z = 5\,\mathrm{mT}$ and $\boldsymbol{G} = \mathrm{diag}(-1,-1,2)\mathrm{T\,m}^{-1}$. In multi-patch imaging, multiple drive field FOVs are connected to form a much larger overall volume. The resulting individual sections are called patches and may overlap slightly, are imaged on a continuous trajectory in order to reduce boundary artifacts [4, 33, 136, 235, 261]. The comparably slow movement of the temporal component in $\boldsymbol{B}_{\mathsf{SF}}$ causes no intensification in terms of PNS or SAR, compared to the duration and effects of the drive field. Multi-patch sequences imply a major leap towards human scale MPI and its clinical application and feasibility.

2.4.2 Torque, Force and Actuation

Another aspect of dynamic selection fields is their ability to manipulate the focus gradient to exert a magnetic force on MNPs [169, 320]. This concept allows particles to be navigated to a desired position and their target position simultaneously verified by imaging using a time division multiplexing scheme [48, 169, 197]. Such a combination of actuation and imaging is particularly useful for targeted drug delivery (TDD) [155, 158, 169] and for steering magnetic devices such as magnetically coated swimmers or magnetic drills [18, 19, 213]. MNPs in combination with a tissue plasminogen activator could dissolve blood clots in the future and can be controlled in the presence of blood flow of 1.36 mL s^{-1} to reach a 100% stenosis [81]. The advantage of TDD is manifold, it delivers the drug more precisely to the target site (less dispersed), which reduces side effects and the duration at the target location is longer. Consequently, with TDD the total dose administered can be reduced, which is a major benefit for many therapies.

The technique behind magnetic actuation relies on the torque and force originating in a magnetic field gradient [2]. The force on a particle in a given direction is defined by the dot product of the magnetic field derivative in that direction and its magnetization. Therefore, the force has no upper limit, unlike the torque, which has an upper bound as a function of the particle geometry and its saturation magnetization [2]. A strong and flexible selection field can therefore steer and visualize untethered magnetic micromachines at a distance and would be a valuable tool in a broad range of clinical applications [213, 212].

2.4.3 Hyperthermia

By deliberately leveraging the mechanism that particles convert some part of the excitation field energy into heat due to their reorientation and remagnetization, magnetic particles or magnetic fluids can be used in hyperthermia applications [37, 113, 114, 170]. In hyperthermia treatment, the objective is to destroy carcinogenic cells by increasing local tissue temperature to induce cytoclasis and apoptosis, or to sensitize cells to other treatments [100]. The selection field is used to spatially focus the treatment, and heating is caused by energy absorption in magnetic or conductive materials induced by an alternating field in the frequency range of 100 to 300 kHz [100, 266]. The potential benefit to patients lies in combined theranostic MPI devices capable of hyperthermia treatment, simultaneous imaging, precise temperature feedback, all with high spatiotemporal control [41, 100]. Recent studies promise a successful combination of imaging, hyperthermia treatment and thermometry [37, 222].

In case of implants or metals used in osteosynthesis, the effect is reversed and heat becomes an undesired side-effect for MPI, due to eddy currents in conductive materials and the power absorption of magnetic materials [252].

2.5 Image Reconstruction

With the previously outlined fundamentals in MPI signal encoding and spatial encoding, this section treats the method to calculate a medical image from the acquired raw data. The image reconstruction in MPI determines the spatial concentration of particles based on the measured receive voltage and assigns them to corresponding voxels. Unlike projection data in modalities like CT, raw MPI data cannot be directly interpreted in a visual manner without undergoing the reconstruction process.

Spatial encoding makes the particle's response dependent on its location, allowing identification of the signal's origin. To this end, an inverse problem needs to be solved, which can be approached either in the frequency domain (subsection 2.5.1) [70] or in the time domain (subsection 2.5.2) [72]. The inverse problem involves the measured receive signal and a system function that accurately describes the particle relaxation for different positions to recover their spatial concentration.

The key assumption to this type of MPI reconstruction is the linear relationship between the measured receive signal $u(t)$ and the particle concentration $c(\boldsymbol{r})$ [70], expressed by the integral equation over the FOV Θ

$$u_l(t) = \int_{\Theta} s_l(\boldsymbol{r}, t)\, c(\boldsymbol{r})\, \mathrm{d}^3 r\,. \tag{2.13}$$

l refers to the channel index of $l \in \{0, ..., L_{\mathrm{ch}} - 1\}$, with $L_{\mathrm{ch}} \in \mathbb{N}$ receive coils. The mapping and physical relation between particle concentration and voltage is embodied by the integral kernel $s_l(\boldsymbol{r}, t)$, which represents the system function in time domain. An expansion into a

Fourier series (subsection 3.5.1), yields the Fourier coefficients

$$\hat{u}_{l,k} = \int_{\Theta} \hat{s}_{l,k}(\boldsymbol{r})\, c(\boldsymbol{r})\, \mathrm{d}^3 r\,, \tag{2.14}$$

of the receive signal with indices $k \in \{0, ..., K-1\}$ for $K \in \mathbb{N}$ frequency components. Usually, K is determined by a maximum frequency or the bandwidth of the receive chain, e.g. the LNA or analog-to-digital converter (ADC) sampling. For algebraic reconstruction, the system function $\hat{s}_{l,k}$ is discretized on a grid covering Θ with $N \in \mathbb{N}$ integration points $\boldsymbol{r}_n$ with indices $n \in \{0, ..., N-1\}$, determining the resolution of the final image. The integral of Equation (2.14) is approximated by the discrete imaging equation

$$\hat{\boldsymbol{u}}_j = \sum_{n=0}^{N-1} \hat{s}_{j,n}\, c_n\,, \tag{2.15}$$

where $\hat{s}_{j,n} := w_n \hat{s}_{j,n}(\boldsymbol{r}_n)$ are the sampled system function and $c_n := c(\boldsymbol{r}_n)$ are the sampled particle concentration [130]. If a non-regular grid is sampled, the quadrature weights w_n will also be not constant [117]. The row index $j = k + lK \in \{0, ..., M\}$ is introduced for convenience to enumerate all channels l and frequency components k linearly, with a maximum number of $M = L_{\mathrm{ch}}K$ frequency components in the system function.

Consequently, the system function encodes the relationship between the particle concentration and the measurement signal, and can be obtained using different approaches: calibration-based, model-based, learning-based, or hybrid.

Calibration-based system functions rely on measurements conducted within the MPI scanner, utilizing a delta sample of the tracer and a robot to position it along a grid. The unique particle responses from the known positions along the grid are recorded and stored. Usually these calibration measurements require a long time and need to be repeated if parts of the hardware change, but they are very accurate and track the entire receive path information from particle until the ADC. Compressed sensing approaches from MRI [167] significantly reduce the acquisition time [150] by exploiting spatial symmetries in the system matrix [302] and suitable sparsity transformations [161, 189, 301]. These methods can be combined and provide results for high undersampling factors even for multi-patch system matrices [85].

Model-based system functions require precise mathematical models and computing time. They are broadly categorized in equilibrium and nonequilibrium models with varying degrees of idealized and realistic field shapes and particle dynamics [87, 127, 246]. Realistic nonequilibrium models are numerically expensive [126], e.g. the Fokker-Planck equation is a partial differential equation, which is usually translated into a set of stiff ordinary differential equations for the solver.

Learning-based system functions form a third approach, based on neural networks [279, 298]. Recent works indicate that machine learning significantly accelerates the calculation of system matrices and accuracy approaches that of a Fokker-Planck model, e.g. by using Fourier neural operators (FNOs) [139]. To improve accuracy, measurements can be included (e.g. magnetic fields or the transfer function (TF)) [8, 75].

The **hybrid system function** is a fourth approach, a combination of model- and calibration-based or learning- and calibration-based representations. Measurements are conducted in an MPS [26] with high SNR for a parameter set of excitation and offset fields. The delta sample does not need to be moved by a robot and the measured responses are combined or interpolated to a hybrid system matrix by a processing step. The basic principle is that each point of the field in the MPI scanner can be represented by the correct superposition of static offset and excitation fields in the MPS, providing an accurate response at a fraction of the robot-based calibration time [86, 94, 294].

In this thesis, we use the calibration-based and the hybrid approach by solving the system of linear equations in frequency space to obtain the reconstructed image as shown in Figure 2.9. A convenient matrix notation that can be implemented in a programming language is introduced in the following section.

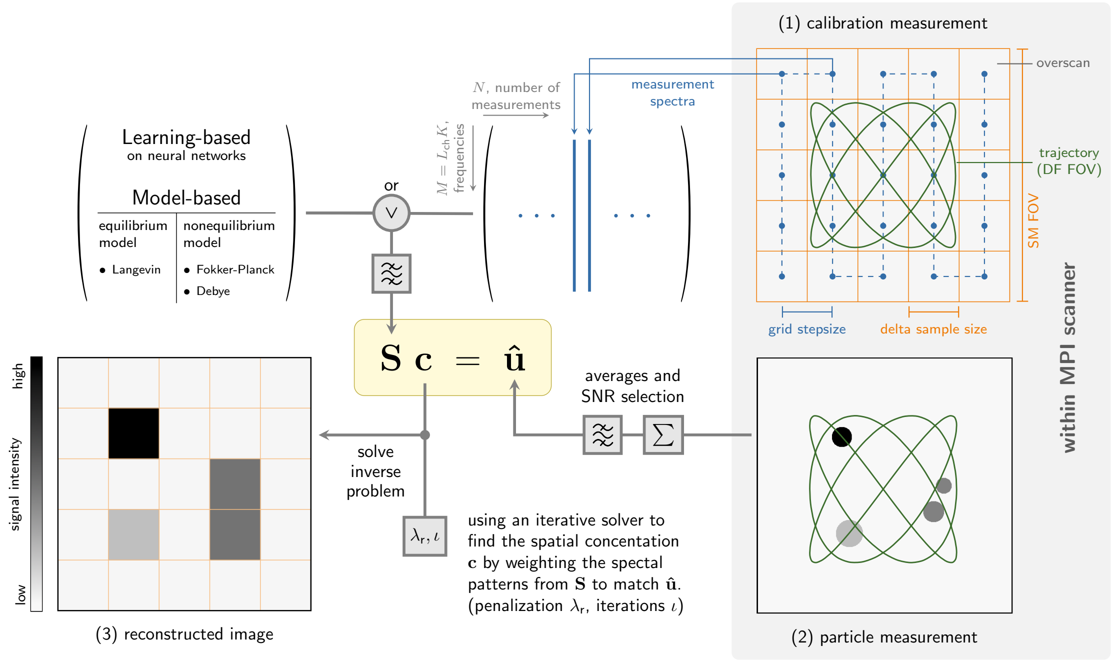

Figure 2.9: System matrix image reconstruction. At the center of image reconstruction is the image equation in matrix form. The system matrix $\boldsymbol{S}$ can be calibration-based (1) or model-based, the former requires lengthy, time consuming measurements and the latter elaborate simulations for the non-linear particle behavior. The blue dots mark the N positions where a delta sample is imaged to store each spectrum in a new column of $\boldsymbol{S}$, prior to particle measurements. If distributed particles are measured (2), the receive voltage $\boldsymbol{u}$ is Fourier transformed and $\hat{\boldsymbol{u}}$ equals the product of $\boldsymbol{S}$ and $\boldsymbol{c}$. The solution of the spatial concentration $\boldsymbol{c}$ can be found by solving the inverse problem (3). If $\boldsymbol{S}$ contains the spectral fingerprints for all positions of a grid, these can be used to match the spectrum of $\hat{\boldsymbol{u}}$ using a linear combination. The grid of the calibration measurement (SM FOV) directly determines the image resolution of $\boldsymbol{c}$. The quality of the image is influenced by many factors, for example the solver, its reconstruction parameters, the SNR and the sequence trajectory.

2.5.1 System Matrix Reconstruction

If the discretized Equation (2.15) is expressed in matrix vector notation, the system matrix $\boldsymbol{S} \in \mathbb{C}^{M \times N}$ is obtained and the rewritten equation becomes

$$\hat{\boldsymbol{u}} = \boldsymbol{S}\boldsymbol{c}\ . \tag{2.16}$$

This system of linear equations can now be inverted and the Fourier transformed receive signal components $\hat{\boldsymbol{u}} \in \mathbb{C}^M$ are utilized to solve for the unknown particle distribution $\boldsymbol{c} \in \mathbb{C}^N$. An overview of the entire reconstruction process is shown in Figure 2.9. Since different positions are recorded and stored in the columns of $\boldsymbol{S}$ during calibration (1), their unique spectral fingerprints can be used to find an appropriate linear combination of $\boldsymbol{c}$ (3) that best represents the measured receive voltage (2) and thus the actual spatial particle distribution.

Different types of approaches and solvers can be used in system matrix reconstruction, but the gold standard in system matrix reconstruction is to solve the Tikhonov regularized optimization problem

$$\underset{\boldsymbol{c}}{\operatorname{argmin}} \|\boldsymbol{S}\boldsymbol{c} - \hat{\boldsymbol{u}}\|_2^2 + \lambda_{\mathrm{r}} \|\boldsymbol{c}\|_2^2 \,. \tag{2.17}$$

This approach adds the penalty term $\|\boldsymbol{c}\|_2^2$ to the least squares approach, which penalizes oscillatory solutions with a large L_2 norm. The Tikhonov regularization is suitable for the ill-conditioned system matrix $\boldsymbol{S}$ due to its robustness against noise in the measured data [140]. The regularization parameter $\lambda_{\mathrm{r}} \in \mathbb{R}^+$ can be used to weigh data and penalty terms and thus it has a strong influence on the final image quality. Choosing λ_{r} too small results in a corroded and noisy image, choosing λ_{r} too large results in smoothing the data at the expense of spatial resolution. Typically, λ_{r} and the number of iterations ι are determined empirically, but ideas for a model representation and fully automated reconstructions have recently been proposed [236, 237]. Equation (2.17) can be complemented by another term based on the L_1 norm $\alpha\|\boldsymbol{c}\|_1$ to reduce image blurring [161, 257], motivated by the sparsity of the data [130]. For real-time reconstructions, however, minimizing a non-smooth optimization function is difficult, and small adjustments can have a large impact on the solution.

One solver that is often used in practice is the Kaczmarz method, which is an iterative method that converges rapidly and is implemented in a wide range of publications [O16, 115, 133]. A significant advantage of approaches that solve the imaging equation using the system matrix is that it is a generic approach. Consequently, the transition from 1D to 2D and 3D imaging is facilitated because the underlying particle physics is already included in the generic model. This facilitates the transition from small-scale prototypes in the early stages of development to human-sized bore diameters and 3D imaging, as the system matrix simply increases in size, but the technique remains identical. Finally, the total particle concentration, measured within the FOV $\Theta \in \mathbb{R}^3$, is given by the integral

$$\mathrm{C_p} = \int_{\Theta} c(\boldsymbol{r}) \, \mathrm{d}^3 r \,. \tag{2.18}$$

2.5.2 X-Space Reconstruction

An alternative approach to image reconstruction in MPI is x-space reconstruction, which is a fast technique in the time domain and straightforward in a 1D or 2D conception [72]. It is based on the assumption that particles relax instantaneously and that their relaxation curve is well represented by an analytical model [46]. Thus, the signal origin and intensity can be mapped because the position and motion of the FFP is known at all times during the excitation. If the excitation field is assumed to be homogeneous and the coil current of the assumed linear selection field is known, the FFP positions can be calculated. This is usually done for Cartesian trajectories as a grid, line by line, and sequentially for different excitation directions if more than one is used. In general, three steps are necessary to obtain a reconstruction image in x-space:

- velocity compensation by normalizing the speed of the sinusoidal drive field
- match spatial information by gridding data on the sampling trajectory
- optional deconvolution with the PSF of the particle (image kernel)

The inaccuracies from the mentioned presumptions pose a challenge for x-space reconstruction and may cause image artifacts, especially near the edges of the FOV where velocity compensations fails (division by zero, results in amplification of noise). Particles do not relax infinitely fast, which causes an positioning error, however, an additional term in the signal model with an exponential relaxation function may compensate the offset [46] and field inhomogeneities can be partly addressed by calibration [265]. Generalization to multi-dimensional excitation [73] and different trajectories is complicated due to complex particle relaxation effects for 2D and 3D excitations and the shortcomings of the model assumptions. Due to the simplicity of the approach, tailored particles for 1D excitation, and the computationally easy implementation, many advantages outweigh the drawbacks and x-space has produced great reconstruction results [13, 199, 269, 325]. Although acquisition can be fast, typical scan times are long [324] and cartesian sampling of 3D volumes requires several minutes [173].

2.5.3 Multi-Contrast MPI

The term "multi-contrast" refers to the ability to distinguish and map multiple particle systems or environmental states onto distinct reconstruction channels [209]. These contrasts can be visualized separately or together using different colors after the reconstruction process. The discrimination of channels can be achieved by exploiting the amplitude and phase information of slightly different relaxations, as particles exhibit different responses to excitation due to factors such as core size or hydrodynamic diameter [209, 247]. Additionally, it is also possible to discriminate between physical parameters in the vicinity of the particle environment, such as viscosity [186], temperature [253, 281], or binding state (easy-axis alignment) [185, 285], as already explained in section 1.1. Alterations in temperature or the (partial) immobilization of particles within a gel or by means of cementation induce variations in the effects of anisotropic energy and the dominant relaxation processes, as highlighted in subsection 2.1.1 [217, 219]. By generalizing Equation (2.16), we obtain the following signal model for multi-contrast MPI

$$\begin{bmatrix} \boldsymbol{S}_1 & \boldsymbol{S}_2 & \cdots & \boldsymbol{S}_R \end{bmatrix} \begin{bmatrix} \boldsymbol{c}_1 \\ \boldsymbol{c}_2 \\ \vdots \\ \boldsymbol{c}_R \end{bmatrix} = \sum_{i=1}^{R} \boldsymbol{S}_i \, \boldsymbol{c}_i = \hat{\boldsymbol{u}} \ . \tag{2.19}$$

Here, $R \in \mathbb{N}$ sub system matrices contain different complex valued spectral patterns. In other words, multi-contrast is obtained by using multiple system matrices that differ in phase and amplitude information and that allow the separation of the measured signal into R reconstruction channels $\boldsymbol{c}_i, i \in \{1, ..., R\}$. After reconstruction, the result is R different images, one for each reconstruction channel. The Kaczmarz method typically requires a higher number of iterations to clearly distinguish the channels compared to single channel reconstructions.

Multi-contrast is a valuable tool in the future clinical application of MPI: it can help in tracking, orienting and positioning surgical instruments by marking the tip [93] or during the inflation of a balloon-catheter [227], to differentiate the tools from surrounding liquid particles. Furthermore, the timescale of a brain hemorrhage can be quantified [262] and in hyperthermia applications the particles themselves can provide the necessary temperature feedback [226]. An isolation of different particles was also shown for x-space reconstructions, based on the physical relaxation model [102]. Multi-contrast reconstructions are used in this work in chapter 7 and chapter 10.

3

Electromagnetic Perspective on MPI

Alternating electromagnetic fields and currents are fundamental to MPI signal encoding, where they are used to obtain information about the measurand from a distance, as discussed in the previous chapter. Here we present the underlying equations that govern electromagnetic fields, their relationships, and how they can be combined to provide resonances and filters. In addition, signal amplification, reception, digitization, and processing are discussed to complete the picture of the physical background required for MPI signal acquisition and processing. Finally, an overview of a generic MPI system schematic is provided to guide the reader to the published works that follow.

3.1 Maxwell's Equations

In analogy to the magnetic flux density $\boldsymbol{B}$ in Equation (2.1), the electric displacement field $\boldsymbol{D}$ (flux density) is linked to the electric field $\boldsymbol{E}$ by the permittivity tensor $\boldsymbol{\epsilon}$, as in

$$\boldsymbol{D} = \boldsymbol{\epsilon}\boldsymbol{E} = \epsilon_0\boldsymbol{E} + \boldsymbol{P}\,. \tag{3.1}$$

In the presence of an electric field, the displacement field accounts for the effect by free and bound charges within dielectric materials that influence the internal electric field [111]. $\boldsymbol{E}$ can be separated from the polarization density $\boldsymbol{P}$, using the vacuum permittivity $\epsilon_0 \approx 8.854 \cdot 10^{-12}\,\mathrm{A\,s\,V^{-1}\,m^{-1}}$. For linear materials with symmetric tensors (isotropic), ϵ becomes a simple material constant

$$\boldsymbol{D} = \epsilon_r\epsilon_0\boldsymbol{E}\,. \tag{3.2}$$

In general, the relative permittivity ϵ_r can be understood as the factor by which the electric field inside a dielectric material is reduced compared to vacuum, and measures the ability of the material to store electric energy [111]. The polarization inside a material opposes the external electric field and can be considered analogous to the magnetization $\boldsymbol{M}$. The polarization cannot change instantaneously in response to an applied electric field, which introduces a phase lag (relaxation and resonance effects) and causes losses. Consequently, ϵ becomes a complex and frequency dependent quantity, which is embodied by the introduction of $\boldsymbol{P}$.

A major difference between magnetic and electric fields is the existence of electric charges, so called electric monopoles, which give rise to the electric field and can be positively or negatively charged. Considering a closed surface interval of $\boldsymbol{D}$, the total enclosed charge Q_c is expressed by Gauss's law

$$Q_\mathrm{c} = \oint_S \boldsymbol{D}\,\mathrm{d}\boldsymbol{A}\,. \tag{3.3}$$

Using the divergence theorem, this can be rewritten as the *first* of Maxwell's equations (Equation (3.6a)). In other words, field lines emanate from the location of a localized charge density ρ of a given volume. In the case of magnetic fields, there are no monopoles, and magnetic fields of particles arise due to the magnetic dipole moment. This is expressed by the *second* of Maxwell's equations, Gauss's law of magnetism, which states that a closed surface integral always equals zero, as in

$$\boldsymbol{\Phi} = \oint_S \boldsymbol{B}\,\mathrm{d}\boldsymbol{A} = 0\,. \tag{3.4}$$

The magnetic flux $\boldsymbol{\Phi}$ through a closed surface is zero, which means that a magnetic field has no individual sources or sinks. Therefore, magnetic field lines are always closed, which can be expressed in terms of a divergence operator, as in Equation (3.6b).

So far, Equation (2.1) and (3.1) establish a connection between the magnetic and electric fields and their respective flux densities. A third important equation, that links the free current density $\boldsymbol{J}$ within a material to the electric field is given by Ohm's law (for vectors)

$$\boldsymbol{J} = \sigma \boldsymbol{E}\,. \tag{3.5}$$

Note that the electrical conductivity σ is also a complex, frequency-dependent rank-2 tensor in general, which becomes a material constant for linear isotropic materials.

The first two of Maxwell's equations on field densities $\boldsymbol{D}$ and $\boldsymbol{B}$ are complemented by Faraday's law of induction and Ampère's circuital law, based on the vector rotation of the electric and magnetic fields. All 4 equations are given by [111, 180, 179]:

$$\nabla \cdot \boldsymbol{D} = \rho \qquad \text{Gauss's law} \tag{3.6a}$$

$$\nabla \cdot \boldsymbol{B} = 0 \qquad \text{Gauss's law for magnetism} \tag{3.6b}$$

$$\nabla \times \boldsymbol{E} = -\frac{\partial \boldsymbol{B}}{\partial t} \qquad \text{Faraday's law of induction} \tag{3.6c}$$

$$\nabla \times \boldsymbol{H} = \boldsymbol{J} + \frac{\partial \boldsymbol{D}}{\partial t} \qquad \text{Ampère's circuital law} \tag{3.6d}$$

Faraday's law (or the Maxwell-Faraday equation) states that changing magnetic fields cause a rotating electric field and vice versa, which is called electromagnetic induction. The induced quantity opposes the direction of its origin, hence the negative sign (Lenz's law). Induction is the key player in signal reception for many imaging modalities, such as MRI or MPI, which allows to pick up receive voltages at a distance in coils due to dynamic magnetic fields. Lastly, Ampère's Circular Law relates rotational magnetic fields to a constant current density and a dynamically changing displacement field. This law is famous as an example of the right-hand rule that symbolizes directions of cause and effect.

The presented form of Maxwell's equation are given for the general case, but different written forms and approximations exist that allow simplifications, depending on e.g. materials (vacuum), dimensions or frequency ranges. In this work, the quasi-stationary approximation for harmonic oscillations is often applied, based on the condition

$$\frac{1}{\omega} \gg \frac{\epsilon_0}{\sigma}, \tag{3.7}$$

which conveys the idea of neglecting the displacement current $\boldsymbol{J}_\mathrm{D} = \frac{\partial \boldsymbol{D}}{\partial t}$ at low angular frequencies ω. It also depends on device and circuitry dimensions, which should be small compared to the wavelength. The typical transmit fields of MPI are in the low kHz range of 10 to 150 kHz [130] (wavelength of 2 to 30 km) and thus comply with the quasi-stationary condition for conductors like copper with $\sigma_\mathrm{copper} = 5.8 \cdot 10^7\,\mathrm{S\,m^{-1}}$. For receive circuits, especially at high harmonic indices, the approximation may not hold, when the dimensions of the coil length of a receive coil approach that of the wavelength. For gradiometric receive coils, this effect is discussed in subsection 3.6.2. Two important phenomena concerning the current distribution in electrical conductors are the skin effect and proximity effect, which motivate the deployment of stranded litz wires in MPI transmit and receive circuitry.

3.1.1 Skin Effect

The skin effect describes an increase of losses of a solid conductor at high frequencies, when internal induction causes a rotating magnetic field within the conductor, according to Equation (3.6d) [111]. A circular (longitudinal) current is induced with opposing orientation as stated by Equation (3.6c), called *eddy current*, consequently reducing the primary current at the center and amplifying it at the surface. The result is a high current density towards the surface, where the majority of the total current forms like a "skin" of the conductor. Due to the reduction to a fraction of the cross-section compared to a DC current, the energy dissipation increases. A common approximation of the skin depth δ_s is

$$\delta_\mathrm{s} \approx \sqrt{\frac{2}{\sigma \mu \omega}}, \tag{3.8}$$

showing that the skin depth decreases with rising frequency [116]. For copper the skin depth at 25 kHz is already below 500 µm. Materials with a high relative permeability μ_r like iron are a bad conductor for alternating currents, due to enhancing the internal rotating magnetic fields, reducing the skin depth significantly with high eddy currents.

3.1.2 Proximity Effect

The proximity effect causes non-uniform current distributions in parallel neighboring conductors due to induced eddy currents. It is similar to the skin effect, however, the phenomenon is caused by the penetration of magnetic fields from currents in close proximity, independent of galvanic connections. The resulting changes in $\boldsymbol{J}$ depend on the specific layout and arrangement of all contributing wires and are neither symmetric nor homogeneous. The proximity effect can be caused by two different types of internal magnetic fields: Either by neighboring wire-bound currents or by the presence of a strong magnetic field that acts on the entire wire bundle [258], e.g. for the windings of a transformer. The results is that eddy currents cause local non-uniform current densities.

In MPI, skin effect and proximity effect play an important role in both the transmit and receive chains. They cause significant losses in signal generation, filtering, and transmission, as well as thermal noise in the receive chain. To mitigate these effects during transmission, litz wires are used with up to 2000 individual strands of insulated wire, each only 50 µm thick. In the receive chain, a thickness of 20 µm is common to further reduce the skin effect. A Rutherford wire configuration is used to counteract the proximity effect, which refers to the winding of the strands as a helix. The helical pitch provides a more homogeneous effect on individual parallel wires by interchanging all positions throughout the litz wire, which compensates for the penetrating flux by transposition. This technique can be used on multiple layers (sub-strands) or by winding multiple litz wires in parallel [116, 258].

3.2 Resonance and Filters

Resonance is a fundamental physical phenomenon, that occurs in many forms and variations in nature. Typically, it has a periodic character that stores and transfers energy easily between different storage modes. Cyclic losses will dampen the oscillation and are expressed by the quality factor Q_f (subsection 3.2.2) for electromagnetic fields. In electrodynamics, resonance is determined by harmonic oscillations with a sinusoidal waveform and their natural frequency is called resonance frequency f_r. Two fundamental storage modes are the energies of the electric and magnetic fields, which are represented by capacitor and inductor in electrical engineering. The dampening of such oscillations occurs due to resistive elements, which means that power is dissipated and lost to the environment [111].

In MPI, resonances are primarily, but not exclusively, found in transformers, filters and to generate the drive field. Before elaborating on resonance circuits and their characteristics, we quickly review the transient response of capacitor and inductor. These are determined by their first order differential equations of capacitor voltage v_C and coil current i_L

$$i_C(t) = C\,\frac{\mathrm{d}\,v_C(t)}{\mathrm{d}t}\,, \qquad (3.9a) \qquad\qquad v_L(t) = L\,\frac{\mathrm{d}\,i_L(t)}{\mathrm{d}t}\,. \qquad (3.9b)$$

They can be rewritten to express the complex impedances

$$Z_C(\omega) = \frac{1}{j\,\omega\,C} = j\,X_C\,, \qquad (3.10a) \qquad\qquad Z_t u L(\omega) = j\,\omega\,L = j\,X_L\,, \qquad (3.10b)$$

for an easier assessment and visualization in the complex plane.

The capacitance depends on the amount of charge on the capacitors plates and on the polarization density of the dielectric. A dielectric with a high ϵ_r reduces the electric field between the electrodes, due to the anti-parallel alignment of charges to the applied field, which corresponds to a high capacitance. Losses due to dipole (re-)polarization are generally lower than conduction losses for alternating currents in MPI.

A large inductance refers to a strong reluctance to a change in the current of the inductor, and hence in its magnetic field. The effect can be understood by the opposing voltage induced by the self-inductance across the inductor if its field is changed, which cancels the potential energy of the charges flowing through it. Materials with a high μ_r increase the magnetic flux density for a constant current and therefore the inductance, if placed within the magnetic field of an inductor.

Compared to mechanical oscillators, typical inductors and capacitors in circuits can only store small amounts of energy. One way to integrate a mechanical oscillation into an electrical circuit is the quartz crystal, which changes shape under an electric field, known as inverse piezoelectricity. It has a much higher quality factor, described in subsection 3.2.2, and is thus a tool for increasing the total energy stored in a circuit [182].

3.2.1 Series and Parallel Resonance

The unification of a capacitor C and an inductor L creates a resonant circuit with losses R, called RLC circuit. A voltage source can be integrated inline as a series RLC circuit or in parallel to both elements, which defines two fundamental resonance behaviors. A series RLC has a minimum impedance ("acceptor") and a parallel RLC a maximum impedance ("rejector"), during frequency analysis. An overview of both types is given in Figure 3.1.

The minimum impedance of a **series RLC** appears at resonance and corresponds to a maximum current in the circuit limited only by R, when the imaginary part of Z becomes zero. In many cases, R is equal to the dominant equivalent series resistance (ESR) R_L of L, and is defined by the copper losses of L and the connectors. Considering the Nyquist plot at the bottom of Figure 3.1 (a), the locus curve resembles a vertical line that goes to positive infinity for high frequencies. The overall circuit impedance Z can be derived, which becomes the minimum real resistance $Z = R_L$ at the resonance frequency

$$f_\mathrm{r} = \frac{\omega_r}{2\pi} = \frac{1}{2\pi\sqrt{LC}}\,, \tag{3.11}$$

which is the frequency at which the imaginary parts of L and C are equal and cancel each other out: $X_L = X_C$. This is typically denoted by f_0, for zero phase. Note, that for the considered series RLC $f_0 = f_\mathrm{r}$, however, for a parallel resonance a $f_0 \neq f_\mathrm{r}$ is possible. At frequencies $f > f_\mathrm{r}$ the capacitor becomes irrelevant for the series RLC and the inductor dominates with $\sim \omega L$. Below f_r, the capacitor dominates with $\sim \frac{1}{\omega C}$ and determines the behavior of the circuit. When implementing a series RLC circuit, component ratings should be heeded, as high voltages will occur internally across L and C, although they cancel out for the overall circuit.

The **parallel RLC** is inversely analogous to many general characteristics of the series RLC, such as its frequency response, which has a maximum impedance at resonance. However, closer inspection reveals that the resonance of a parallel RLC has two distinct frequencies that play an important role: First, f_0, where the imaginary parts cancel and $Z = R_0$ (zero phase). Second, the resonance frequency f_r, where Z is maximum (Z_r) and a small imaginary part remains. This shift between f_0 and f_r is caused by the ESR R_L, which does not affect the phase shift at f_0 when the imaginary part is zero, but causes a peak impedance at a slightly higher frequency when the parallel voltage reaches its maximum. The Nyquist diagram at the bottom of Figure 3.1 (b), resembles a circle for small $R_\mathrm{p} = R||R_L$, but becomes increasingly distorted for high R_L or when other losses like the ESR of C are included. The $||$ symbolizes a parallel connection. The point where the locus curve crosses the real axis gives f_0. The maximum distance of R_p from the circulation defines f_r and Z_r. The parallel RLC is dominated by $X_C \sim \frac{1}{\omega C}$ at high frequencies, approaching a short for $f \to \infty$ (or the ESR of C, if included). At frequencies $f < f_\mathrm{r}$, inductance dominates first, eventually being replaced by R_p at low frequencies, resembling the positive arc of the locus curve, or a plateau of magnitude and zero phase in the magnitude plot of Figure 3.1 (b). When implementing a parallel RLC circuit, it is important to choose components with minimum ESR due to the high internal currents that occur at resonance as energy is transferred back and forth from the electric field of C to the magnetic field of L, effectively creating a high impedance to the supply voltage source.

Passive Filters. Frequency analysis of series and parallel RLC circuits provides two insights that bridge the gap between resonant circuits and passive filters: single lumped elements provide simple high/low pass filters, and resonances can be combined to achieve band-

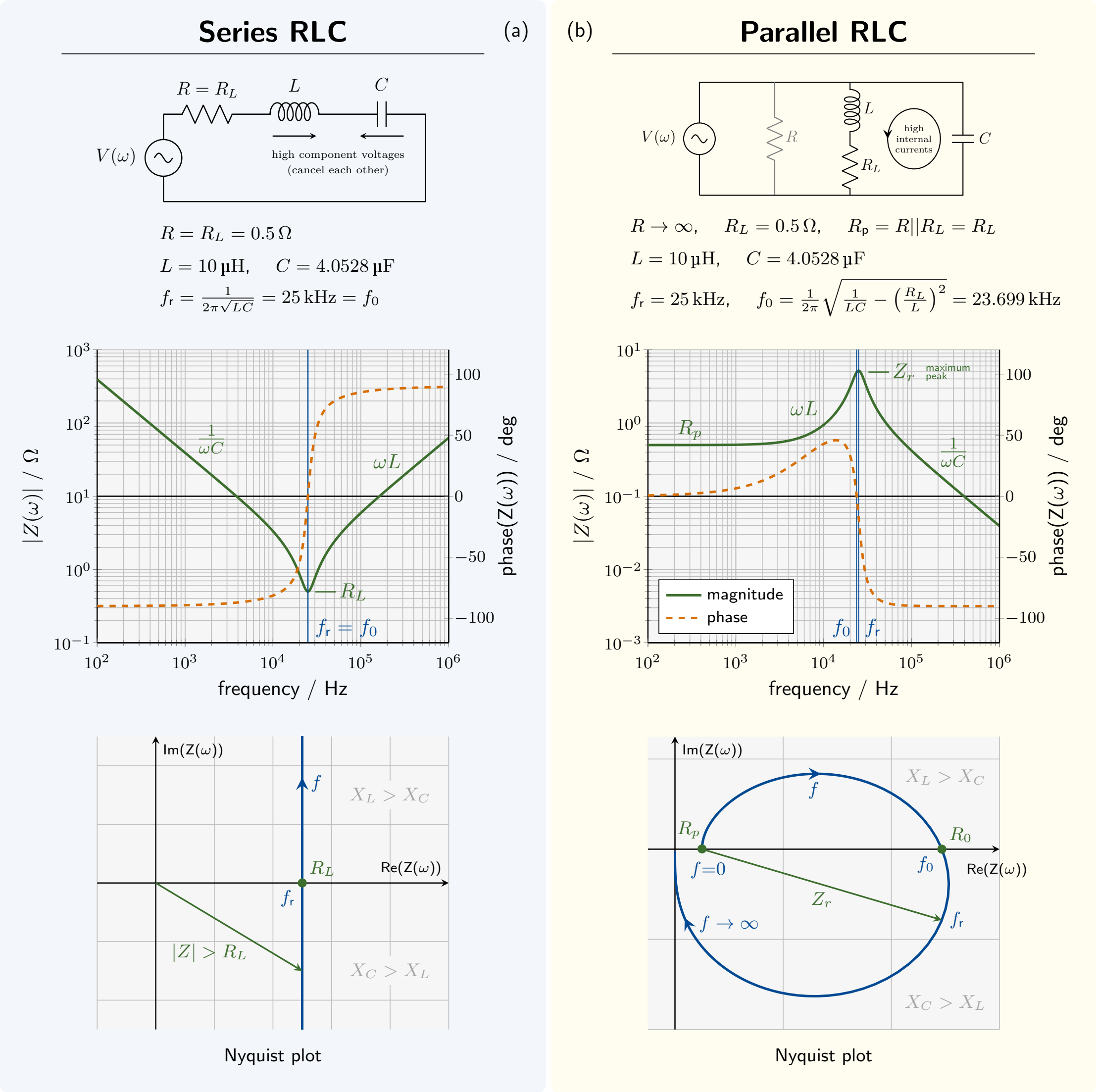

Figure 3.1: RLC series and parallel resonance. For each RLC type, an equivalent circuit diagram (ECD) is shown along with the component values for the simulation. In the middle, a magnitude/phase plot shows the frequency response of the two RLC circuits in the kHz range, and at the bottom, the corresponding Nyquist plot shows the frequency-dependent locus curve. Note that the parallel RLC has two different frequencies, f_0 where the imaginary part is zero (phase turn) and f_r with maximum impedance. Series and parallel RLCs are a simple example of passive bandpass and bandstop filters, respectively, and reflect (inverse) mutual characteristics.

pass/stop behavior or higher order filters. For example, a fifth-order bandpass filter can be designed by cascading several RLC circuits to provide higher rejection of signals outside the passband [177, O21]. Common filter types, such as the Buttherworth or Chebyshev filters, differ in the flatness of the passband as a trade-off for the roll-off steepness after their cutoff frequency. During MPI signal reception, a bandstop filter is typically implemented to filter the fundamental frequency and mitigate feedthrough. The reader is referred to [110, 315] for further reading on active and passive filter design.

3.2.2 The Quality Factor

The quality factor or Q_f is a dimensionless quantity that relates the stored energy of an oscillating physical system to the dissipated energy per cycle. It is a measure of the merit of a resonance and is used to assess the damping of the oscillation, hence a low Q_f marks a strongly damped system [110, 111]. We consider the stored energy W_s and the losses W_loss *per cycle* in

$$Q_\mathrm{f} = 2\pi \frac{W_\mathrm{s}}{W_\mathrm{loss}} \tag{3.12}$$

with $W_\mathrm{loss} = W_\mathrm{radiation} + W_\mathrm{conduction}$, that refer to the radiated energy and the dissipated energy by ohmic resistance, respectively. The series and parallel RLC circuits have inverse Q_f factors, which can be derived from the ECDs and Equation (3.11) to yield

$$Q_\mathrm{f,series} = \frac{1}{R}\sqrt{\frac{L}{C}} = \frac{\omega_\mathrm{r} L}{R} = \frac{1}{R\,\omega_\mathrm{r} C}\,, \tag{3.13}$$

$$Q_\mathrm{f,parallel} = R\sqrt{\frac{C}{L}} = \frac{R}{\omega_\mathrm{r} L} = \omega_\mathrm{r}\, RC\,. \tag{3.14}$$

Multiple definitions for Q_f exist, that provide similar results and one other alternative expression is to measure the $-3\,\mathrm{dB}$ FWHM of a resonance [110]. This approach is visualized in Figure 3.2 for three different quality factors of the same resonance and based on

$$\tilde{Q}_\mathrm{f} = \frac{\omega_r}{\omega_\mathrm{3dB}}\,. \tag{3.15}$$

The cutoff frequencies that define the bandwidth ω_3dB are given by an amplitude reduction of $\frac{1}{\sqrt{2}}$, which equals $20\log_{10}\frac{1}{\sqrt{2}} = -3.01\,\mathrm{dB}$ on a logarithmic scale. The FWHM is therefore measured at $-3\,\mathrm{dB}$ from the maximum or $+3\,\mathrm{dB}$ from the minimum of the resonance, depending on the measured parameter. Typically, the values for the Q_f based on ω_3dB are lower than the estimates given in (3.13) and (3.14).

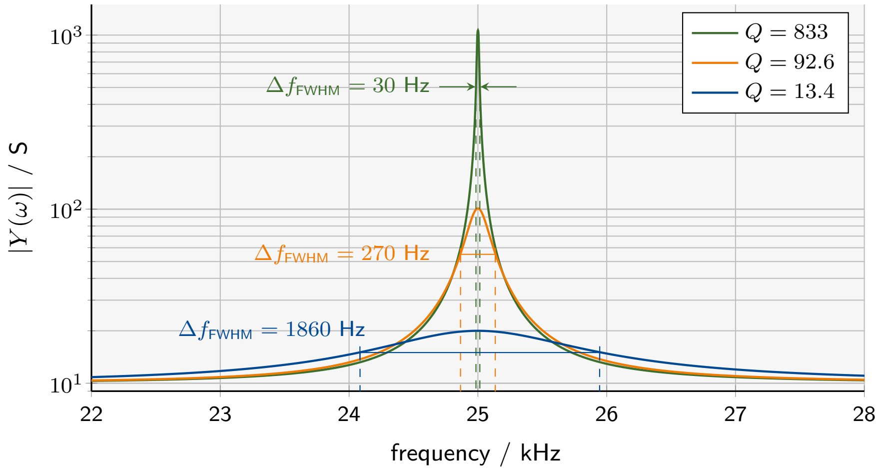

Figure 3.2: Different Q-factors. Three Q_f of a series resonance are plotted on a logrithmic y scale and evaluated using their 3 dB FWHM. A Q_f above 100 indicates a high quality resonance in the kHz range, which forms a sharp peak.

3.3 Electromagnetic Coupling

Line voltages and wire-bound currents in close proximity affect each other by coupling via electromagnetic fields. In particular, resonant circuits that are sensitive to impedance changes and carry high currents are susceptible. Coupling in general can refer to inductive coupling via magnetic fields or to capacitive coupling via the displacement current of electric fields. The term crosstalk refers to unintended coupling, that should be suppressed. Although inductive coupling is dominant in MPI, a combination of both is most commonly encountered and is quantified by the coupling coefficient k_c [326]. Different strategies for decoupling to avoid unwanted interference are presented in subsection 3.3.2 and in chapter 6. Desired coupling can occur when using transformers, filters, decoupling, motors, or eddy currents in breaks or heating.

An example of unintended inductive coupling occurs between two or more resonant circuits tuned to very similar frequencies and located in close proximity. In MPI, this is the case for orthogonal drive-field coils operating at different but very similar frequencies. With field imperfections, manufacturing variations, and coil geometry limitations, residual coupling becomes an unwanted side effect that greatly affects system performance. Amplifiers experience varying loads and undesired beat frequencies can occur in the transmit chain. The higher the Q_f of a resonator, the more sensitive it is to coupling at f_r.

Two coupled resonant circuits are shown in Figure 3.3 and described in the caption. Peak splitting creates a new minimum current at the desired position of the target resonance instead of the intended maximum. At high Q_f, two slightly shifted modes appear, the anti-phase mode and the in-phase mode, which are analyzed in the ECD on the left in Figure 3.3. When the currents in both loops oscillate in phase, the overall circuit has a lower inductance because the voltages across L_M have opposite signs, effectively canceling each other out. This results in an upward shift of the resonance, as well as a slightly higher Q_f due to the

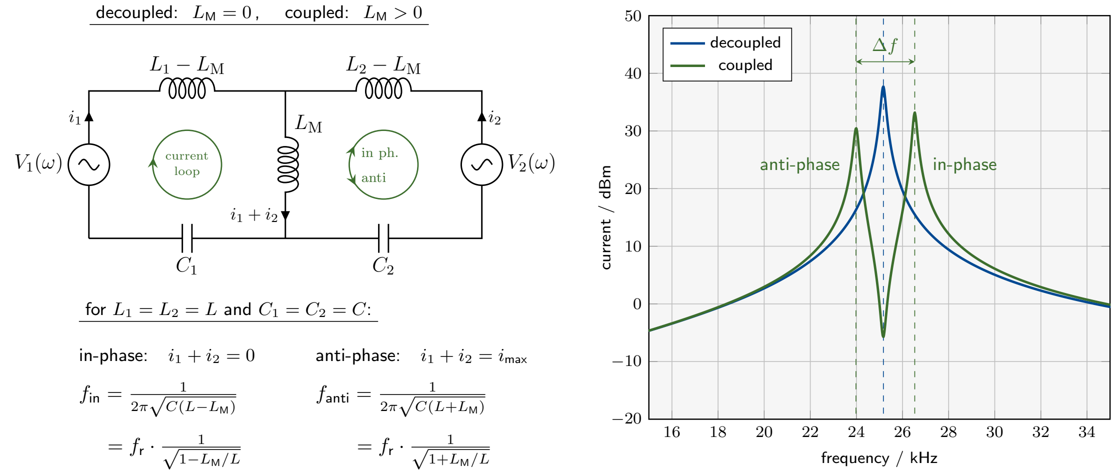

Figure 3.3: Mutual inductance and mode-splitting. The ECD on the left represents two separate resonance circuits, both individually tuned to f_r, which can be galvanically disconnected, but experience inductive coupling. This is expressed by the shared mutual inductance L_M, with $L_\mathrm{M} < L_1$ and $L_\mathrm{M} < L_2$. A consequence is the split of the original frequency f_r, with an unsymmetrical shift into an anti-phase and an in-phase mode. The new frequencies both modes can be calculated by accounting for the contribution of L_M, that carries no current for the in-phase mode and both currents for the anti-phase mode. At f_r the currents oppose each other, which creates a minimum.

bypassing of the series resistance R_s of L_M (specific to this example). For the anti-phase mode, the frequency shift is downwards, because twice the current is carried by the mutual circuit branch.

Different techniques to counter cross-talk by inductive coupling will be discussed in the upcoming subsection 3.3.2. This type of coupling is typical for phased arrays in MRI [159], but due to the close proximity of drive field frequencies (often less than 3 % apart [130]) it can affect MPI as well, depending on the quality factor of involved resonances.

3.3.1 Transformers

An example of intentional coupling is the transformer, where the coupling coefficient k_c is typically maximized by guiding, bundling and intensifying the magnetic flux $\mathbf{\Phi}$ between two coils. Typically, iron cores are used to achieve fully linked flux $\Phi_{11} = \Phi_{22}$, when $k_\mathsf{c} \to 1$, for the ideal transformer. In this case the stray inductance L_σ becomes zero, which describes the part of the coil that is not coupled to the other side of the transformer. This can be visualized as stray field lines, which pass through only one side but are not enclosed by the other side. With regard to Figure 2.1 above, the hysteresis of a magnetic transformer core material means that the transformer has limited energy storage. This causes a non-linear distortion of the signal when the material is driven into and above its saturation region. Air cores are better suited for applications that require highly linear behavior, although the stray inductance is typically much higher. A toroidal transformer with optimal cross-section for high currents is developed in chapter 6.

3.3.2 Resonant Decoupling Strategies

To avoid electromagnetic coupling and unwanted crosstalk, several strategies exist to suppress the influence of nearby alternating fields and charges in medical imaging [159]. In MPI, these include inductive decoupling, capacitive decoupling, and active cancellation [O2]. Broadly speaking, they can be divided into narrowband and broadband solutions, referring to the bandwidth for which decoupling is achieved.

For formal analysis, an l-port network model can be used [326] that takes on the shape of an impedance matrix and which can be simplified for zero capacitance as

$$\begin{bmatrix} Z_{11} & \dots & Z_{1,l} \\ \vdots & \ddots & \vdots \\ Z_{l,1} & \dots & Z_{l,l} \end{bmatrix}, \text{ for } L_\mathsf{ch} = 2 \text{ to } \begin{bmatrix} R_{11} + j\omega L_{11} & j\omega L_\mathsf{M} \\ j\omega L_\mathsf{M} & R_{22} + j\omega L_{22} \end{bmatrix}. \tag{3.16}$$

In the case of two channels $L_\mathsf{ch} = 2$ and neglected capacitances, the mutual inductance L_M is the sole contribution to coupling $k_\mathsf{c} = L_\mathsf{M}(\sqrt{L_1 L_2})^{-\frac{1}{2}}$ [O2, 326]. The goal of decoupling is to reduce k_c, including the initial geometric arrangement of the channels (orthogonal field directions). If orthogonality is unachievable, overlap decoupling can be used, such as in the case of coil arrays. This is often used in MRI, e.g. for phased arrays, that have the same resonant frequency and are located in close proximity of each other [159, 224]. The advantage of these strategies is that they do not introduce additional resistance that lowers Q_f, which is the case when additional loops or transformers are used for decoupling. However, complete (perfect) decoupling is unattainable in real-world applications, which is why decoupling schemes are necessary. Even very small coupling factors can contribute to significant undesired currents in the coupled channel [O2, O3]. This topic is the subject of an in-depth analysis and discussion in chapter 6.

3.4 Amplifiers

Different types of amplifiers are used in MPI, ranging from small-signal and low-noise amplifiers to power amplifiers with several kW. The reader is referred to [45] for a detailed overview of amplifier classes and their design.

Power Amplifier: Power amplifiers (PAs) are used to generate strong alternating magnetic fields in MPI, like the drive-field or dynamic selection field. If selection fields are not entirely based on permanent magnets, they also require PAs to create the gradient or to adjust FFR positioning. Proper impedance matching aims to terminate the PA with an appropriate load to guarantee stability and best performance, which is typically slightly inductive with a dominating resistive part.

An important figure of merit is the THD, given by the sum of all voltage root mean square (RMS)-amplitudes of the signal harmonics, divided by the fundamental

$$\mathrm{THD} = \frac{\sqrt{\sum_{k=2}^{K} |\hat{u}_k^2|}}{|\hat{u}_1^{\mathrm{rms}}|}, \tag{3.17}$$

with K measured harmonics [249]. Another important characteristic of amplifiers is the slew rate (SR), which is given by the maximum change of the output voltage per unit time

$$\mathrm{SR} = \max \left| \frac{\mathrm{d}v_{\mathrm{out}}(t)}{\mathrm{d}t} \right|, \tag{3.18}$$

and typically expressed in $\mathrm{V\,\mu s^{-1}}$. Especially at high frequencies, or when generating rectangular waveforms and step inputs, amplifier performance is limited by the SR.

Previously, class-D amplifiers were avoided in MPI due to their higher THD compared to linear gain amplifiers (class-A/B/AB). However, modern class-D amplifiers reach a THD of $-110\,\mathrm{dB}$ [178] and should not be categorically excluded. They score on a compact design, high efficiency and low heat dissipation, but require an actively controlled pulse width modulation (PWM) unit to shape their output waveform.

PAs can be operated in voltage or current mode, although the voltage mode is more widely used. The current mode requires a specific adaptation to the load, by tuning a small feedback control circuit, i.e. a PID controller, that the amplifier uses to control the output current. This can reduce the bandwidth of the amplifier, which may become unstable at high frequencies. However, the current mode is of advantage for MPS devices that control the drive-field directly via the coil current at different excitation frequencies and waveforms [O12, O1], due to the direct relation of the magnetic field and coil current of (3.6d).

Operational Amplifier: The input signal to a power amplifier is often amplified by a small operational amplifier (5 to 10 times) for simple step-up voltage conversion. The operational amplifier usually provides a single-ended output, and they can be configured with much higher gain and very low noise, such as the ADA-4898 from Analog Devices, MA, USA [9]. Their simple circuitry makes them an alternative for many applications that do not require the more complex design of an LNA.

Low Noise Amplifier: The LNA is a special type of amplifier for very low signal amplitudes, designed to amplify weak signals without (significantly) decreasing the SNR. Every amplifier introduces additional noise, with regard to the noise level at its input, and LNAs are built to minimize this undesired influence while providing a high gain [239]. In a typical MPI receive chain, one or several LNAs are used to amplify the weak receive signal prior to ADC sampling and after the signal was filtered to suppress the dominant fundamental signal, which would exceed the dynamic range of a sensitive LNA. In this work, we use a custom LNA consisting of highly parallelized ultra-low-noise JFETs, cascaded with an operational amplifier as a second stage for high gain [78].

To compare different LNA models, typically the noise figure (NF) is used, defined by the ratio of SNR at in- and output, given with

$$\mathsf{NF} = 10\log_{10}\left(\frac{\mathsf{SNR}_{\mathsf{in}}}{\mathsf{SNR}_{\mathsf{out}}}\right) . \tag{3.19}$$

The Friis formula [239] identifies the first amplifier in a cascade as the most critical, having the greatest influence on the overall NF. This criterion can be met by using the amplifier with the lowest NF first and then, for example, an operational amplifier with a significantly higher gain.

Due to the input capacitance of an LNA, a receive coil connected to the input will always form a resonance and therefore a non-linear frequency response. This can be exploited to increase sensitivity in a limited frequency range that can be selected by shifting this resonance to a desired point.

3.5 Signal Processing

After the introduction of resonances, coupling, and amplifiers, the picture of the MPI signal chain is gradually completed with the basics of signal processing. To this end, an ADC is used to digitize analog signals for further processing like the image reconstruction. An overview of the complete send and receive chain is given at the end of this chapter in section 3.7. Fundamental to the system matrix approach is the Fourier transform, which is the key topic of this section.

Two important variables that determine the digitization of an analog signal are the sampling rate f_{s} in Hz and the amplitude resolution in $\mathsf{V\,bit}^{-1}$. The sampling rate limits the highest frequency that can be recorded, with

$$f_{\mathsf{s}} > 2\,f_{\mathsf{max}} , \tag{3.20}$$

which is referred to as the Whittaker–Nyquist–Shannon theorem [198]. If it is not satisfied, the sampling points of higher frequencies might be interpreted as lower frequencies, causing aliasing. The maximum bandwidth of an ADC is called the receive bandwidth, which is often an integer division of its main clock frequency. The receive bandwidth Δf and the amplitude or ADC resolution determine the amount of data produced for each sample point. The product of f_{s} and the ADC resolution determine the data rate required to store the received data.

3.5.1 The Fourier Series

A primary tool in frequency analysis is the Fourier transform and the expansion of periodic signals into a Fourier series within the frequency domain. The Fourier transform is a linear map, that transforms a time-domain signal into a frequency-domain signal [254] with commutative and associative properties.

For a T-periodic voltage $u(t)$ of a single channel ($L_{\mathsf{ch}} = 1$), the Fourier coefficients can be calculated with

$$\hat{u}_k = \frac{1}{T}\int_0^T u(t)\,\mathrm{e}^{-j2\pi kt/T}\mathrm{d}t . \tag{3.21}$$

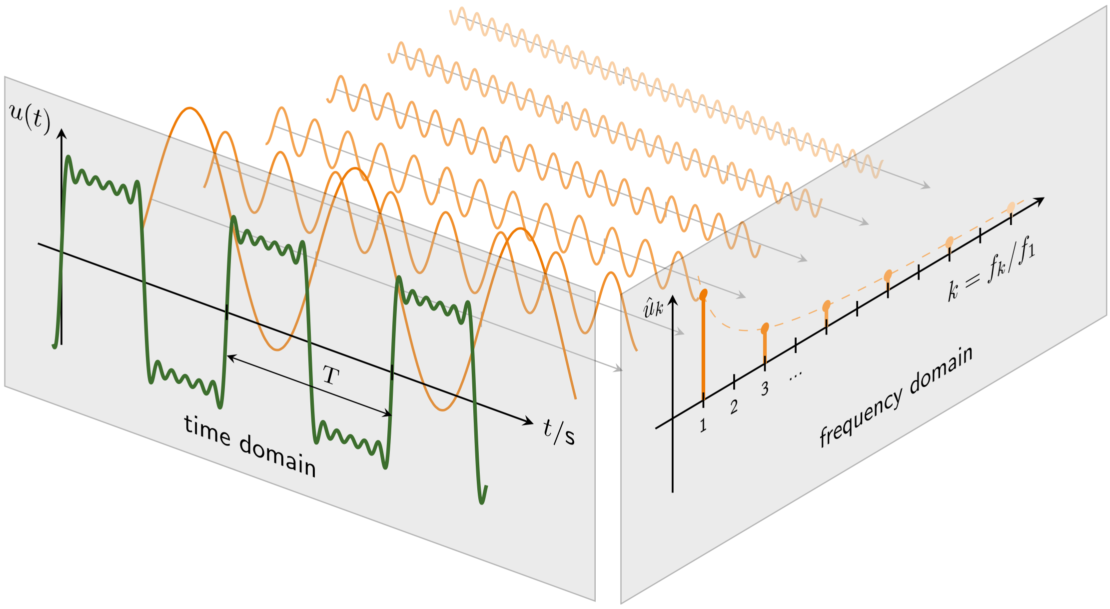

Figure 3.4: Fourier series expansion. A signal $u(t)$ is shown in the time domain and it's Fourier components $\hat{u}(f)$ in the frequency domain, arranged on two orthogonal planes. The original signal (green) can be expanded into individual components f_k (orange), shown in 3D space, and both 2D projections fully represent the periodic signal.

As mentioned in section 2.5, the index k denotes the frequency components with a total of K frequencies, which mainly depends on the chosen receive bandwidth of the ADC. These coefficients represent the original signal as a superposition of sinusoidal waves in the time domain

$$u(t) \sim \sum_{k=-\infty}^{+\infty} \hat{u}_k \, \mathrm{e}^{j2\pi kt/T}, \tag{3.22}$$

which converges for 2π periodic signals, although general convergence is a multifaceted problem [254]. The representations in the time and frequency domain are illustrated as projections in Figure 3.4. Due to symmetry, the complex conjugate of the negative frequency coefficients equal the positive coefficients, as stated by

$$(\hat{u}_{-k})^* = \hat{u}_k \, . \tag{3.23}$$

This holds for all real signals, which is the case for the MPI measurement signal. Note that the above definitions use continuous signals. However, after signal acquisition and ADC sampling, $u(t)$ becomes the discrete signal u_t for digital signal processing. Therefore, the Fourier series is usually performed with a right-sided fast Fourier transform (RFFT), which calculates only the positive coefficients of the fast Fourier transform (FFT), which in itself is a fast implementation of the discrete Fourier transform (DFT).

The FFT is based on the principle of interlaced decomposition that calculates a spectra for each pair of sample points and then re-combines them step-wise into the full spectrum of the signal, effectively reducing the number of complex multiplications to $\mathcal{O}(n \log n)$ instead of $\mathcal{O}(n^2)$ for the DFT [101]. Thus, a rapid implementation on computers is feasible, but also on low complexity microcontrollers with low computing power like the 8-bit AVR ATmega328P.

Spectral Leakage: A challenge in digital signal processing arises when the sampling time window does not exactly cover a full 2π-period (or an integer number of T). Depending on how the discrete time points are spaced, the selected window may not represent an exact period, causing the DFT to interpret and repeat the window with discontinuities. This causes new frequency components to appear as side bands, that are not part of the original function, which may result in a continuous spectrum instead of individual frequencies. This is called spectral leakage, and usually the unwanted frequency bins are highest closest to the original components and follow an exponential decay. For example, the RFFT of a single real cosine signal should have only a single frequency component, but multiple non-zero components appear near the original component if periodicity is violated. The problem is intensified when the sampling becomes sparse, which is typically not the case with MPI, except for high harmonics, compressed sensing or arbitrary waveforms with high slew rates. Window functions that differ from the rectangular window like e.g. Gaussian, Hann, Hamming, Blackman or Nutell windows can be used to suppress side-lobes and to influence the shape of the main lobe [97]. An efficient workaround is to synchronize ADC sampling with the digital-to-analog converter (DAC) clock, resulting in the special case of zero spectral leakage. To this end, the channel frequencies in subsection 3.5.3 are chosen as integer divisors to match the clock and sampling frequency f_s. Consequently, the DAC and the ADC use a single global clock.

Zero Padding: Zero padding refers to adding trailing zeros to a windowed signal in order to increase the sampling time window size. If this is done to obtain a total number of samples as a power of 2, the DFT operation can be sped up significantly using radix-2 FFTs. Another strategy is to add as many zeros as necessary to obtain an integer multiple of the expected signal frequency component(s) if the sampling and signal frequencies cannot be synchronized. Such operations require prior knowledge and can mitigate spectral leakage by matching the sample spacing to the expected frequencies to resolve those frequencies.

Gibbs Phenomenon: The Gibbs phenomenon describes oscillating behavior of the Fourier series in proximity to a jump discontinuity. For a rectangular signal, the signal representation given by Equation (3.22), has an over- or undershoot error of roughly 9 % of the jump height [254]. Even if a large number of frequency components K are included, a jump cannot be fully represented using finite orders of sine waves. The Gibbs phenomenon is also visualized in time domain representation of the signal in Figure 3.4, visible before and after the zero-crossings of the green signal.

3.5.2 Intermodulation

Frequency multiplication or frequency mixing results in a certain number of amplitude modulated sidebands that depend on the sum and difference of the multiplied frequencies, called intermodulation products [225]. This phenomenon is exploited in high-frequency engineering in applications such as broadcasting, satellite, or cellular devices, and plays a role in the MPI received signal, where sidebands contain valuable information about particles [215, 260]. Intentional intermodulation is for example achieved with a known nonlinear element, while unintentional intermodulation can be caused by unwanted nonlinearities or time-varying systems.

To perform intermodulation, a signal f_a is multiplied with a carrier signal f_b of higher frequency ($f_\mathrm{b} \gg f_\mathrm{a}$), resulting in two bands at $f_\mathrm{b} \pm f_\mathrm{a}$, symmetrically spaced around f_b. Magnetic particles are in principle a magnetic mixer, which relies on a non-linearity to perform the frequency multiplication [153, 196]. Consequently, at least two distinct drive-field frequencies need to be utilized, causing intermodulation of the particle signal at the channel frequencies themselves and again, between resulting mixing products. The result is side bands around all harmonics of the drive field frequencies that are rich in different frequency components and include higher mixing orders of the particle signal (higher order intermodulation). These side bands are not masked by the harmonics of the fundamentals of the direct excitation feedthrough and contain spatial information on the particles, hence they are easier to detect and isolate than the k harmonics.

3.5.3 Data Acquisition System

To complete this section on signal processing and before continuing with the MPI receive chain, a specific input-output-card is introduced: The RedPitaya *Stemlab 125-14* (RP) is a flexible low-cost open-source hardware solution that integrates DAC and ADC into a single device for precise real-time signal handling. The advantage of unifying DAC and ADC within a single device is the synchronous system clock, effectively avoiding spectral leakage and the software can administer both data streams clock-synchronously. Multiple RPs can be combined to form a synchronous stack, using one identical system clock, and are coordinated by a collection of open-source software in this work [89, 90]. The RP is clocked at 125 MHz, has an amplitude resolution of 14 bit and typically we use ADC-dividers of 8, 16, 32 or 64, resulting in a receive bandwidth of 7.8125 MHz, 3.906 25 MHz, 1.953 125 MHz or 976.5625 kHz, respectively. Typical transmit frequencies are also the product of integer dividers and the clock frequency, for example

$$f_{\mathrm{ch1}} = \frac{125 \cdot 10^6}{64 \cdot 76} = 25699.013...\mathrm{Hz} \quad \text{and} \quad f_{\mathrm{ch2}} = \frac{125 \cdot 10^6}{64 \cdot 75} = 26041.666...\mathrm{Hz}\,. \qquad (3.24)$$

These frequencies are implemented across many devices in MPI, from MPS and head-scanner [O3] to the preclinical Bruker MPI 25/20 FF (Bruker BioSpin, Ettlingen, Germany). The custom open-source software is also capable of handling arbitrary signal waveforms and tracking feedback signals for drive field control, while real-time operations are handled on the Xilinx Zynq 7010 FPGA. The signal data in this work is stored in the open MPI data format (MDF) [149] and all custom build devices are based on the RP [O14, O13, O1, O3].

3.6 MPI Signal Reception and Calibration

So far, we have introduced the fundamental equations, theory and phenomena needed to understand signal generation and transmission in MPI, as well as specific details on the equipment and circuitry necessary to generate the required field strengths. This section addresses the process of signal reception and the theory behind it, using signal processing tools such as the Fourier transform to interpret and analyze the received signals in the frequency domain.

A general representation of the MPI receive signal for channel l in the time domain is separable into three components, as in

$$u_l(t) = u_l^{\mathrm{EF}}(t) + u_l^{\mathrm{P}}(t) + u_l^{\mathrm{N}}(t)\,. \qquad (3.25)$$

EF refer to the direct excitation feedthrough of the drive-field excitation, P denotes the particle signal and N summarizes different noise sources. The particle signal is typically about 6 to 10 orders of magnitude below the excitation signal, exceeding the dynamic range of ADCs and requiring separation prior to signal acquisition [77]. One approach implements filters to fully suppress the fundamental and another typical design uses a gradiometer, explained in the upcoming subsection 3.6.2.

In an ideal scenario, the particle signal can be isolated by separating the different signal contributions using the following steps:

1. background measurement of $u_l^{\mathsf{BG}}(t) = u_l^{\mathsf{EF}}(t) + u_l^{\mathsf{N}}(t)$, without particles
2. foreground measurement of $u_l(t)$, including the particles
3. measurement subtraction of $u_l(t) - u_l^{\mathsf{BG}}(t) = u_l^{\mathsf{P}}(t)$

Unfortunately, the noise floor itself and other non-deterministic signals cannot be fully subtracted and are prone to time-shifts and spontaneous fluctuations or channel cross-talk [203]. Thus the real signal after background subtraction becomes

$$u_l(t) = u_l^{\mathsf{P}}(t) + u_l^{\mathsf{res}}(t)\,. \tag{3.26}$$

The residual component u^{res} includes thermal noise from the coils, patient noise [240], acquisition noise from the LNA and ADC, cross-talk signals, random distortions [203], as well as a residual drive-field feedthrough despite filtering and compensation. Imperfect background cancellation poses a challenge and u^{BG} represents only a snapshot in time, that is prone to drift and change, especially during long measurements [143]. Excitation harmonics, caused by nonlinearities of bad connections or eddy currents, leave standing harmonics at the precise frequency positions where the weak particle signals are located and, in the worst case, mask them. Mitigating the residual component by combined analog and digital signal processing methods is therefore important to increase the sensitivity of MPI.

Before focusing on a receive coil configuration for feedthrough cancellation and the exact calibration of the receive path, the MPI signal equation is analyzed in the following.

3.6.1 Signal equation

Using Faraday's law of induction (3.6c), the receive coil voltage signal in the l-th channel is given by

$$u_l(t) = -\mu_0 \int_{\Theta} \frac{\partial}{\partial t}\boldsymbol{M}(\boldsymbol{r},t) \cdot \underbrace{\frac{\mu_0}{4\pi}\oint_{\partial S} \mathrm{d}\boldsymbol{l} \times \frac{\boldsymbol{r}-\boldsymbol{r}'}{\|\boldsymbol{r}-\boldsymbol{r}'\|_2^3}}_{\boldsymbol{p}_l(\boldsymbol{r})} \,\mathrm{d}^3 r\,, \tag{3.27}$$

where $\boldsymbol{p}_l(\boldsymbol{r})$ is the receive coil's sensitivity profile and $\mathrm{d}\boldsymbol{l}$ a vector along the path on the boundary ∂S. The sensitivity profile is determined by the coil's geometry and the generated flux density per unit current in it's wire at position $\boldsymbol{r}'$, acting on the (evaluation) point $\boldsymbol{r}$, via the Biot-Savart law. Reciprocity states that the relation of an oscillating current in a coil with sensitivity $\boldsymbol{p}_l$ and the resulting electromagnetic field generated at $\boldsymbol{r}$ is unchanged, if source and effect are exchanged: The same electromagnetic field will induce a voltage in the coil, causing the identical current. This is very helpful, because we can measure the sensitivity profile for a known current and thus conclude on the origin and strength of a signal. The receive signal of (3.27) is Fourier transformed and further supplemented with coefficients $\hat{a}_{l,k}$ that denote the TF to give the general expression

$$\hat{u}_{l,k} = -\hat{a}_{l,k}\,\frac{\mu_0}{T}\int_0^T \int_{\Theta} \frac{\partial}{\partial t}\boldsymbol{M}(\boldsymbol{r},t)\cdot \boldsymbol{p}_l(\boldsymbol{r})\,\mathrm{e}^{-j2\pi k t/T}\,\mathrm{d}^3 r\,\mathrm{d}t\,, \tag{3.28}$$

for particles located in the FOV Θ. The TF of the MPI system characterizes the frequency response and it is used to calibrate the receive signal to account for the signal chain influence and its components such as filters and LNA. Using such a calibration, the magnetic moment of the particles can be derived from $\hat{u}_{l,k}$, independent of the device that measured the response [276], as will be shown in subsection 3.6.3.

We already stated an expression for $\hat{u}_{l,k}$ that includes the system function $\hat{s}_{l,k}(\boldsymbol{r})$ and the spatial particle distribution $c(\boldsymbol{r})$ in Equation (2.14). Using (2.14) and (3.28), as well as the linear relationship of the magnetic field $\boldsymbol{H}$ and the magnetization $\boldsymbol{M}$, we can derive an expression for the Fourier coefficients of the system function with

$$\hat{s}_{l,k} = -\hat{a}_{l,k}\,\frac{\mu_0}{T}\int_0^T \frac{\partial}{\partial t}\boldsymbol{m}(\boldsymbol{r},t)\cdot\boldsymbol{p}_l(\boldsymbol{r})\,\mathrm{e}^{-j2\pi kt/T}\,\mathrm{d}t\,. \tag{3.29}$$

The changing spatial magnetization $\boldsymbol{M}(\boldsymbol{r},t) = \boldsymbol{m}(\boldsymbol{r},t)\,c(\boldsymbol{r})$ is therefore linked to the particle distribution via the mean magnetic moment $\boldsymbol{m}$.

The general expression of the system function in (3.29) completes the picture of the MPI imaging equation. The correlation of measured receive voltage, system function and particle concentration form the backbone of the MPI image reconstruction in section 2.5.

3.6.2 Gradiometer Receive Coil

After discussing various signal contributions within u_l and the theory of signal induction by particles based on $\boldsymbol{m}$ and $\boldsymbol{p}_l$, we continue to complete the receive chain by introducing the gradiometer receive coil [119].

To suppress direct feedthrough, a gradiometric coil winding technique is commonly used in MPI: the receive coil is duplicated and the second coil captures the same amount of magnetic flux $\boldsymbol{B}$ as the primary receive coil, but in reverse orientation. This requires the second coil to be sensitive only to the transmit field and not to the particle signal. The technique is very similar to the methods described in subsection 3.3.2 (reverse induction), but the goal is not to decouple two drive field channels, but to decouple the transmit and receive channels. As a result, the sensitivity of the receive channel to the particle signal is increased and the feedthrough is suppressed. The strong advantage of this technique is that it is broadband, in the sense that is is not tuned to a specific frequency and also suppresses distortions from within the transmit chain [204], and its flexibility to adapt to changes during excitation. Gradiometers have been shown to provide excellent sensitivity [78, 79, 204, 207, 256].

The explanation of the principle is as follows: The exact same excitation field, including unwanted distortions, induces two identical voltages of opposite sign, which cancel each other out in the gradiometer coil. Ideally, only the signal harmonics of the nonlinear response of the magnetic particles remain in the receive coil after cancellation. Two factors are important at this point: the amplitudes of the receive and cancellation voltages must match, and the phase difference should be as close to 180° as possible. The amplitude can be adjusted by placing the coils in different areas of the $\boldsymbol{B}_{\mathrm{DF}}$ and the number of turns. In contrast, the phase is affected by coil topology, wire length (frequency), and parasitic elements (capacitance and series resistance), reducing the efficiency of the gradiometer. Residual signal contributions become part of the background measurement $u_l^{\mathrm{BG}}(t)$, especially for large field generators and at high frequencies.

The influence of the wire length can be exemplified if a fundamental frequency of 26 kHz as given in Equation (3.24) is considered and a head-sized cylindrical coil is used: for a diameter of 24 cm and $N = 30$ windings for each coil, receive and cancellation coil each, the total wire length is approximately 45 m. This is approximately equal to 2 % of the wavelength at the 5th harmonic, which causes a significant phase shift and the cancellation signal does not match the receive signal. For higher harmonics, this effects scales linearly.

A prerequisite for the gradiometer is that the length of the excitation coil exceeds the FOV, so that one set of turns is sensitive to particles in the FOV, while the other set of turns is away from the FOV and does not pick up the particle signal. Especially for multiple nested coils or saddle coil designs, this becomes a major challenge due to the limited space available (with orthogonal fields). In addition, a gradiometer adds additional windings to the receive coil, increasing the total inductance and resistance, which is usually not a problem due to the high impedance input of the LNA, but must be considered because it changes the resonance with the input capacitance of the LNA.

A variation of the gradiometer uses a full duplicate field generator for decoupling, which has advantages when space is limited and multiple (orthogonal) channels are implemented [77]. It also ensures that the particles are only in the intended FOV and separated from the duplicate gradiometer [77]. However, especially for large MPI systems, the power consumption is significantly increased, and the wire lengths for the receive path are extended and prone to distortion [177]. The particle excitation field is not the same as the field used for decoupling, further reducing effectiveness. All of the above are passive compensation techniques that can be supplemented with active feedthrough suppression [106, 264, 321, 330], such as using a low-loss injection transformer to add an actively controlled compensation signal [202].

3.6.3 Receive Path Calibration

As mentioned at the beginning of section 3.6, a receive path calibration method called TF correction can be derived for the entire receive chain [276]. Based on the knowledge of the signal model of Equation (3.28), the frequency response is measured, which depends on the receive path characteristics such as $\boldsymbol{p}_l(\boldsymbol{r})$, LNA and receive filter. This measurement can be used to transfer $\hat{u}_l$ into the domain of the magnetic moment, making it independent of specific device characteristics and comparable.

To this end, we use a small and known transmit coil (calibration coil) placed in the center of the FOV to generate a known magnetic field corresponding to the magnetic moment of the particles. The setup can be viewed as a two-port network and measured with a network analyzer (NWA), using a frequency sweep to determine the joint frequency response of the receive coil, filter, connections, and LNA. If performed by the DAC/ADC itself, even the frequency behavior of this stage can be considered (e.g. using the RP as a virtual NWA). For each scanned frequency bin, a coefficient is determined that can be used to correct and calibrate the receive signal in amplitude and phase (weighting bins). The reader is referred to [276] for a general discourse on this topic, where the authors elaborate on the implementation, limitations, and accuracy of this method. An important finding is that coil positioning has a large influence on the method, along with the radius of the calibration coil, which enters quadratically into the equation. It is critical to know the exact dimensions of the coil and to position it closely to the measured spatial dimensions [275]. This method is also used to confirm and calibrate model-based field predictions [O22].

To derive the TF, first we assume homogeneous coil sensitivity profiles inside the FOV, so $\boldsymbol{p}_l(\boldsymbol{r})$ becomes a constant $\boldsymbol{p}_l$. Moreover, a constant tracer sample distribution and a homogeneous applied magnetic field in the FOV allow to simplify $\boldsymbol{m}(\boldsymbol{r},t)$ to $\boldsymbol{m}(t)$ with the Fourier coefficients $\hat{\boldsymbol{m}}_{l,k}$. A channel-wise evaluation projects $\hat{\boldsymbol{m}}_{l,k}$ on to the directions of the receive coil sensitivity, resulting in $\hat{m}_{l,k}$ and p_l, if calibration coils and receive coils align for each channel. Using these assumptions, (3.28) simplifies to

$$\hat{u}_{l,k} = -\hat{a}_{l,k}\,(\mu_0 \frac{j2\pi k}{T} p_l)\,\hat{m}_{l,k} = \hat{g}_{l,k}\,\hat{m}_{l,k}\,, \tag{3.30}$$

which is accurate for an MPS setting. However, for large MPI systems the deviations may increase and further restrictions apply [276]. The missing knowledge on the generated calibration field of a TF can be explained by considering the magnetic moment

$$\hat{m}_{l,k} = N \cdot \hat{\imath} \cdot A_l\,, \tag{3.31}$$

generated by a calibration coil with a number of turns N, current $\hat{\imath}$ and a cross-sectional area A_l for each considered channel [111]. The current is typically determined by the voltage across a large series resistance that dominates the R_s of the coil channel. With all constituents known, the intended magnetic moment $\hat{m}_{l,k}$ is generated by the NWA, consecutively for each channel l, while the receive voltage $\hat{u}_{l,k}$ is measured using a frequency sweep. The known and measured spectra are used to determine $\mathsf{TF}_l(\omega)$ by interpolating the calculated weights

$$\mathsf{TF}_{l,k} = \frac{\hat{u}_{l,k}}{\hat{m}_{l,k}} = \hat{g}_{l,k}\,. \tag{3.32}$$

As mentioned above, the dimension of the coil enters quadratically into A_l via πr^2 and small deviations lead to a significant error in $\hat{m}_{l,k}$, which is amplified by positioning or rotation offsets and field inhomogeneities of the FOV [O22, 275, 276].

Given the aforementioned assumption that the coil sensitivity is homogeneous within the specified FOV, it is not possible to apply an exact TF correction to obtain the magnetic moment in a generalized manner in the case of a measurement of distributed particles using a large MPI scanner. However, the inversion is feasible for calibration measurements (system matrix) where the delta sample position is known. Also, MPS measurements can be calibrated very precisely, where the entire FOV is excited homogeneously [276].

3.7 MPI System Composition

Throughout this chapter, all fundamental equations, physical effects, processing steps and hardware components were introduced that play a part in the construction and implementation of an MPI system. Finally, we present a generic assembly of a typical MPI system with an overview of common components and their interactions in Figure 3.5. All constructed systems described later are based on this generic DAC/ADC system model. It should be noted that a system can also be designed differently and the complexity varies depending on the size of the imaging or spectroscopic device.

Central to all MPI systems are the DAC/ADC stages, power amplifier, field generator and low-noise-amplifier, as illustrated in Figure 3.5 when moving on a circle from the top left to the right and back to the bottom left. Some devices do not use a selection field, such as the MPS, and others achieve it either by permanent magnets and mechanical motion [15, 16], by driving currents in coils [25, 71, 76, 213], or by a hybrid form of permanent magnets combined with coils [3, 176, 292]. Most systems with harmonic drive fields employ filter stages to reduce the THD and improve feedthrough cancellation, although this is not feasible for arbitrary waveform devices [O1, 202, 268].

A compensation or cancellation technique is required by all systems, due to the fast relaxation process coherent with the excitation, as mentioned in the previous chapters. Some passive

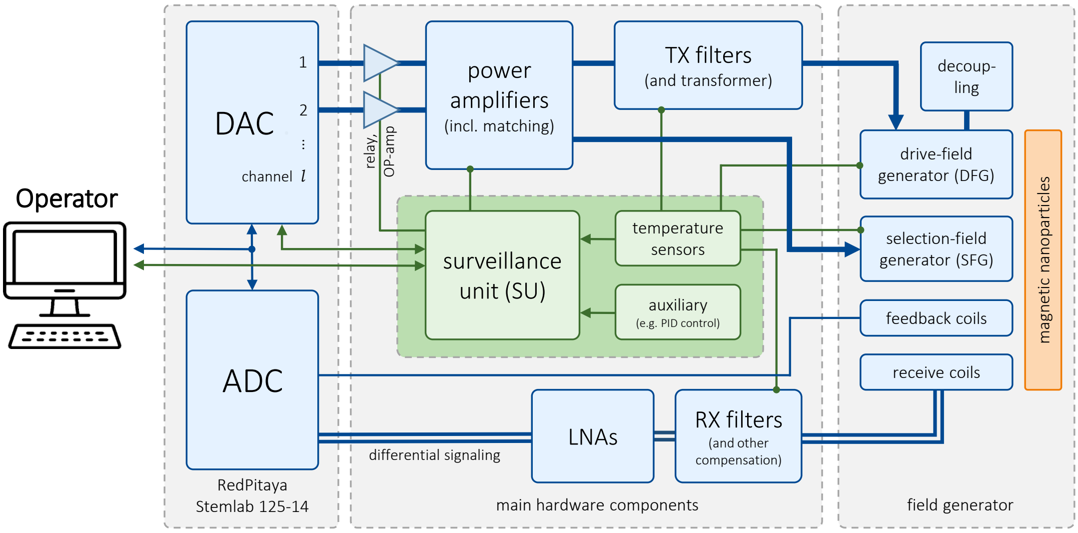

Figure 3.5: MPI system overview with a generic DAC/ADC model. We use a synchronized DAC/ADC device (RedPitaya *Stemlab 125-14*) for signal generation and acquisition, that is connected to a computer. Here, the operator can initiate, abort, supervise and analyze measurements, as well as perform the (live) reconstruction. Depending on the specific system topology and number of channels, some components may be omitted, amended or customized.

techniques were already introduced, like the gradiometer (subsection 3.6.2), using a signal-tap in a symmetric circuit [233, O3], duplicating the entire drive field generator (DFG) [77], or using inductive coupling transformers [77]. In principal, these can be combined with active control signaling using an injection transformer [106, 202, 330] and additional filtering to improve overall signal quality [77].

We conclude this chapter with the transition to clinical safety, which will play a key role in most of the upcoming chapters and individual publications in this thesis. When human trials are planned, it is beneficial to use a type of surveillance unit (SU) that collects sensor data to monitor the ongoing measurements for increased component protection and patient safety. Various failure states can be categorized to decide if automatic transmission interruption is necessary, to inform the operator, and to write meaningful log files [O3]. The system design can also include panic buttons and limit the hardware to a maximum operating field strength that is safe for humans [242].

4

From Instrumentation to Application

The following chapter offers a comprehensive motivation of the works included in this dissertation, providing additional information of the works, explaining their interrelationships and contributions to the field of MPI. Figure 4.1 below presents an overview of the active research fields of MPI, along with a positioning of the contributions of this dissertation.

The outline of this thesis is oriented along the indices: [O1] refers to chapter 5, [O2] refers to chapter 6, [O3] refers to chapter 7, [O4] refers to chapter 8, [O5] refers to chapter 9 and [O6] refers to chapter 10.

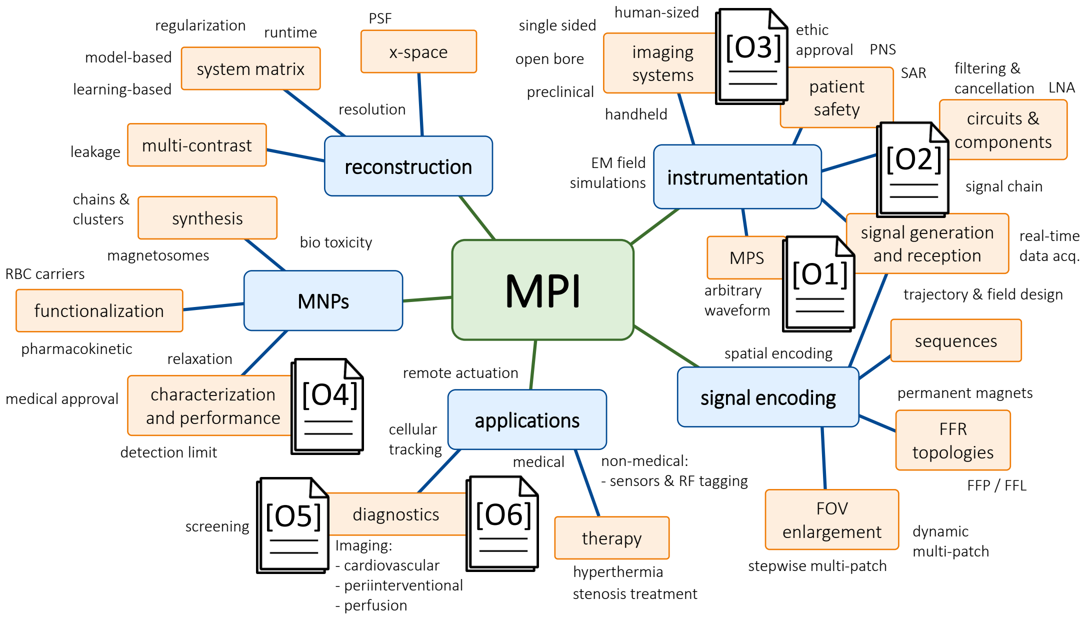

Figure 4.1: MPI research fields overview. The index number [#] refers to the journal publications [O1] to [O6], and chapters 5 to 10, respectively. This overview does not explicitly mention software development, although it is the underlying and required element of most research fields.

4.1 Instrumentation

With the fundamentals of MPI in chapter 2 and the outlined electromagnetic perspectives on resonance, coupling, signal processing, reception, and calibration in chapter 3, the previous section concludes with a generic MPI system composition. On this basis, we first motivate and describe the construction of an arbitrary waveform MPS and its components. This device is not new to the instrumentation of MPI, but the additional orthogonal offset channel that we will introduce allows for a novel way of emulating 2D sequences. We begin by exploring a hypothesis about pulsed excitation and its influence on particle relaxation, and analyze our device and method in general. The complete study is then documented in chapter 5.

As a second and third contribution to the instrumentation, the process and motivation to refine and advance a human-sized head scanner, including the development and construction of an ICN, is elucidated from a general perspective. Since a detailed description of methods and their discussion is included in chapter 6 [O2] and in chapter 7 [O3], we will focus on specific issues, challenges, and simulations for insight that were omitted from the original manuscript. These will be addressed together in a single section before transitioning and connecting these to the applications within this thesis.

4.1.1 Pulsed Magnetic Particle Imaging

Motivation. The utilization of non-sinusoidal waveforms to drive the MNPs into saturation, referred to as pulsed excitation, originated in the context of x-space MPI, where researchers encountered a resolution limit in 2017, referred to as the relaxation wall [270]. The researchers analyzed sinusoidal data of varying amplitudes and frequencies obtained from an x-space MPI scanner [47] and from an arbitrary waveform MPS that was constructed in 2016 [268]. The Langevin model for particles predicts a cubic improvement in spatial resolution with increasing particle core diameter, however, this was only observed up to a certain size of approximately 25 nm [270] for single-core particles, coated with carboxylic acid. Beyond this size, blurring of x-space reconstructions hinders any further expected improvement in resolution. The team determined that relaxation effects were the cause and that their model did not account for them when using deconvolution in the time domain. To address this, they used a low amplitude and very short rise times, namely a rectangular waveform at 5 kHz. This resulted in a better resolution that seemed to follow the expected trajectory for increasing core size [269].

Pulsed excitation promises an improvement in resolution for large particles (narrower PSF), but it comes with two major constraints: (1) a broad-band excitation, and (2) PNS / SAR limits. A broad-band excitation impedes the use of resonators, i.e. filters and LC tanks for amplification gain in drive-field coils. This represents a significant drawback that necessitates a rethinking of the signal chain and the direct feeding of the required current drive-field coils. In order to scale to human size, this places high demands on amplifier specifications in terms of slew rate and maximum voltage, and requires a relatively low-inductance DFG. With regard to PNS, it is highly probable that a pulse of several mT amplitude with a high slew rate in the kHz region will stimulate nerves, which will result in an unpleasant sensation and/or pain [229, 230, 243, 269]. An orientation for limits can be derived from MRI gradient fields [263]. PNS tests with a head-sized cylinder coil found a $\boldsymbol{B}_{\mathrm{DF}}$ amplitude limit of around 3.5 to 4 mT at 24 kHz [200], which is rather a low threshold. For extremities such as the arms and legs, this threshold is higher, due to the differing orientation of nerves and tissue composition [230]. Concerns on the SAR for body tissue arises if a threshold of $4\,\mathrm{W\,kg^{-1}}$ is exceed within 6 minutes, which was found to be not an issue for a sinusoidal drive-field at

150 kHz with 3 simultaneous (orthogonal) excitation channels with 11 mT amplitude [242]. This threshold is a lot higher compared to PNS limitations and therefore of lower concern for the drive field parameters of most MPI systems. Awareness of these limitations is of higher concern when scaling arbitrary excitation to human-sized scanners. This work researches the possible benefits of pulsed excitation over a broad range of parameters for a potential small bore system and spectroscopy.

Hypothesis. An open question at this point is the usefulness of pulsed excitation for system matrix-based reconstructions. Here, the problem of blurring (relaxation wall) is different than in x-space, because the measured response of the particles to the excitation is used instead of a model with assumptions. Yet, large particles with a slow relaxation may not have sufficient time during a sinusoidal half-wave to follow the excitation, resulting in a partial loss of their response at the moment the magnetization changes sign. However, in principle large particle are desirable, because the magnetic moment of large particles is higher, which would increase the MPI signal. A pulsed excitation offers the advantage of a high slew rate and a sufficient hold time to observe the full relaxation of the MNPs [268].

A further question is whether the phase information is partially or completely lost if the change in magnetization of small MNPs to a step input is *instantaneous* [O1, O8]. If only amplitude information remains, is a Radon-based reconstruction with a filtered back-projection a viable approach that necessitates a rotating excitation to supplement the missing information [129]?

Hardware Setup. To investigate these questions, we constructed an arbitrary waveform MPS, which is capable of producing pulsed waveforms with an optional DC offset in the x-channel [O1], shown in Figure 4.2. Concurrently, another DC offset channel can drive the particles into saturation from an orthogonal direction in the y-channel. This enables the measurement of a 2D grid of arbitrary waveforms for a small MNP sample of 5 to 20 µL, including a reference signal of the coil current. Such measurements contain data for a 2D PSF, the static x-space PSF and the dynamic PSF. For the required flexibility, a low-inductance drive-field coil is necessary which is not resonant, reducing the overall complexity by omitting a resonant drive-field circuit and the TX filter (see Figure 3.5). Due to the small inductance, a 3 Ω resistor is connected in series to stabilize the amplifier operation and increase temperature stability for long measurements due to the changing resistance of a heated coil. The power amplifier Hubert A 1110-40-QE-100 with a slew rate of 70 V µs^{-1} is used for the x-channel drive-field. Gained insights to different amplifier operation modes are used to derive a voltage-mode model with feedback in contrast to a current-mode operated amplifier, presented in [O12].

A stack of two RPs are used as a ADC/DAC stage, with a receive bandwidth of 7.8125 MHz that are operated with the open source software RedPitayaDAQServer [90] and MPIMeasurements.jl [89]. The RP stack is shown in Figure 4.2 (a), along with other hardware components such as the LNA, a filtered linear voltage supply and both, measurement chamber and decoupling unit for signal feedthrough compensation. A custom GUI developed by software developers of our institute shown in Figure 4.2 (b) is used to execute and record measurements. It does not provide post-processing or sequence simulation, but raw data can be displayed with several options like background subtraction or transfer function correction. One typical pulsed sequence is outlined in Figure 4.2 (c) for a combination of different xy-offsets. Each blue cross marks a patch where a fixed number of repeated periods of a given x-channel amplitude and freely configured waveform is executed. Device calibration is achieved by DC field calibration of the drive-field coil sensitivity and a transfer function

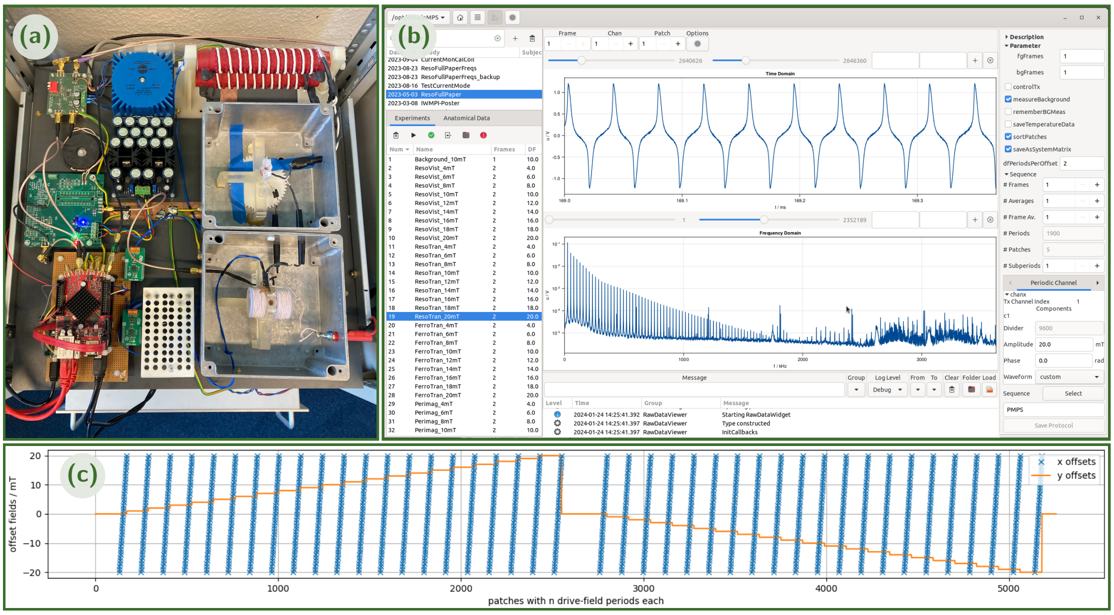

Figure 4.2: Overview of pulsed MPS system. In (a), a picture of the main electric components of the arbitrary waveform MPS is shown. The top aluminum box is the compensation chamber, the bottom one the measurement chamber (both are closed during operation). The RP stack [90] is on the bottom left, the LNA in the center left. Amplifiers, network hub, measurement computer and voltage sources are located underneath. The measurement GUI can be seen in (b), where measurements are configured, saved and displayed [89]. A typical pulsed sequence with different x- and y-offsets is shown in (c). See chapter 5 for more details on coil arrangement.

measurement using a known small calibration coil [276]. Thus, the entire receive chain is calibrated and device-independent measurements can be performed that are particle specific using the net magnetic moment m of the sample.

Framework. We developed a custom, versatile software framework in the programming language `Julia`, aiming to process measurement data with the following requirements [O1]:

- data handling: selection, cropping, calibration and storage (.h5)
- data processing: sample interpolation to create and concatenate time sequences
- reconstruction: using emulated sequences to calculate phantom spectra and images
- variability: adaptation to different forms of scanners, sequences and excitation types

Using these features, the framework interprets the recorded pulsed data as a 2D grid of offset combinations with a chosen excitation waveform and amplitude that can be shaped into a time sequence that is e.g. meandering, rotating, shifting, or a combination of these. It works by selecting a sub-set of the measured 2D grid with a spatial interpretation based on the offset amplitudes and uses temporal concatenation to create a time sequence. Noise and measured background signals are added to mask the repeated use of identical parts of the measurement data. The Fourier transform of this sequence yields a spectrum, which can be used either as phantom data or as input vector for image reconstruction. The versatility of the developed framework is emphasized by the work of Niebel et al. [O17], where a trajectory analysis is conducted for an FFL scanner [303].

Wrap up. To follow up on the above stated hypotheses that motivated the construction of the arbitrary waveform MPS, we initially analyze the well-known tracer Perimag. The measured signal for Perimag is presented in Figure 4.3 for sinusoidal and pulsed excitation with different offsets in the x-direction. As anticipated for small particles, they are capable of following the excitation slope, with no loss of phase information. Consequently, for a Radon-based reconstruction, other particles need to be measured, such as large single-core particles, as motivated in the hypothesis paragraph above. In this case, spatial information would be lost, if relaxation and signal response are identical from all positions within the FOV, hence no phase-shift occurs between different signal positions. We would not expect a Dirac-like response due to the strong Brownian relaxation component (compare to pulsed excitation in Figure 4.3), but that the signal response is shaped identically for all offsets (colored crosses) with the same starting point. As reasoned above, for the measured small particles, we can discern a separation along x-offsets and therefore within the FOV. However, the Perimag data can be used to validate the sequence generation approach: offsets in two directions with constant excitation amplitude provide a 2D grid of piecewise measurements. A selection and temporal concatenation of a subset of the measured 2D grid is used to emulate sequence motion and excitation direction. To avoid inverse crime, we overlay the data with measured noise floors and use two different grids, namely 1/3 mT and 1/2 mT steps [O1]. Two system matrices are computed, one for each measured grid, which are then utilized separately for phantom spectrum computation and image reconstruction.

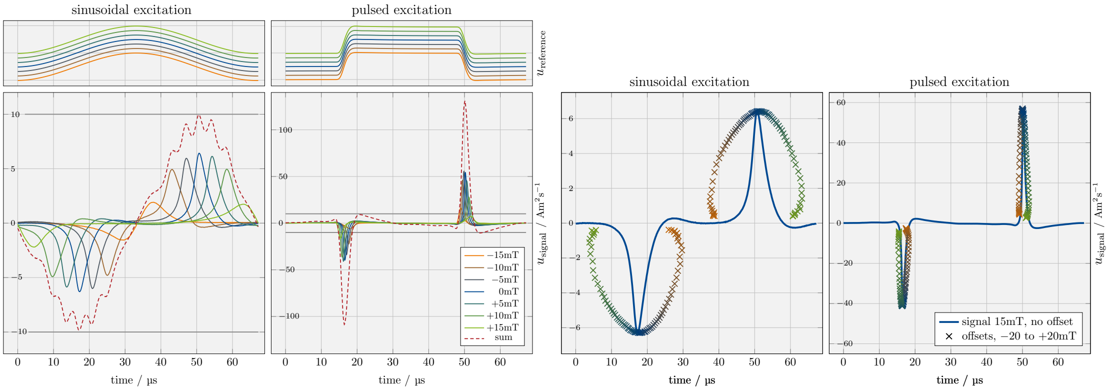

Figure 4.3: Measured sinusoidal and pulsed excitation for various offsets [O8]. Offsets are aligned in excitation direction and non-overlapping crosses indicate that a pulsed excitation with a high slew rate does provide residual phase information. The color coded lines and crosses indicate negative offsets (orange), fading to positive offsets (green).

The detailed methodology and outcomes for distinct waveforms and different sequences are elucidated in depth in chapter 5 [O1]. This works contributes to the instrumentation of MPI by providing a platform and an approach to compare sequences and flexible excitations in a realistic emulation based on measurement data. Insights on possible enhancements for MPI and on the small-scale signal chain with low power assist in the identification of challenges prior to the construction of a full-scale arbitrary waveform device.

4.1.2 Towards a Safe Human-Sized Head Scanner

The following section will examine the connection and relationship between the works [O2] and [O3] of chapters 6 and 7 of this thesis, and the individual design decisions that are stated but not explained in detail in the published papers. Both works concern the instrumentation of MPI, where [O2] provides a detailed account of the development of a portion of the signal chain that is part of the head-sized human MPI scanner described in [O3].

Motivation. Prior to our work, the first human-sized head scanner was presented by Graeser et al. [76] in 2019. The design is effective and straightforward, similar to upscaling the signal chain of a resonant MPS device. This scanner was designed with high sensitivity and low power consumption in mind, and it featured a custom receive chain, including an LNA, similar to the receive chain presented in [78]. Despite its satisfactory performance, the scanner was deemed unsuitable for human trials due to its prototype status and potential safety concerns. These include exposed and uninsulated wires but also regard high voltages, as well as the design for discharge- and leakage currents. A complete redesign is motivated by three main aspects, which can be expressed as follows:

- motivation 1: electrical patient safety & future clinical trials
- motivation 2: fast, volumetric imaging in real-time
- motivation 3: a 2D transmit-receive (TxRx) drive-field signal chain

Key characteristics, overview and comparison between the original head scanner version (2019, [76]) and our redesign (2023, [O3]) are shown in Table 4.1.

First, a direct ground connection of the DFG may expose a patient to a life-threatening current in the case of a first fault. The version by Graeser et al. [76] was designed as a

Table 4.1: Overview of both head sized imaging systems. A selection of parameters for performance and safety are considered. For the 2023 version, a sagittal slice requires a closed Lissajous frequency of both drive fields with $f_x = 25.699\,\mathrm{kHz}$ and $f_z = 26.042\,\mathrm{kHz}$, which is then shifted by perpendicular focus fields [O3]. The redesign required more than 3 years (2020 to 2023).

		version 2019 [76]	version 2023 [O3]
imaging performance	drive field channels	x	x, z
	receive channels (gradiometric)	x, y	x, y
	receive channels (TxRx)	none	x, z
	2D slice coronal xy	2 Hz	4 Hz
	2D slice sagittal xz	robot-shifted	342.6 Hz
	2D slice transversal yz	robot-shifted	4 Hz
	3D volume	robot-shifted	4 Hz
	$\boldsymbol{B}_{\mathrm{SF}}$ type and gradient	FFP, 0.2 T m^{-1}	FFP, 0.24 T m^{-1}
	$\boldsymbol{B}_{\mathrm{SF}}$ sequence	sinusoidal	triangular
	$\boldsymbol{B}_{\mathrm{DF}}$ amplitude	x: 6 mT	x: 5 mT / z: 4 mT
safety considerations	DFG voltage at max. $\boldsymbol{B}_{\mathrm{DF}}$	1000 V	565 V / 485 V
	DFG inductance	186 µH	14.4 µH / 9.74 µH
	DFG resistance	125 mΩ	17.2 mΩ / 10.9 mΩ
	floating potentials	no	yes
	conducting surfaces	yes	no
	control unit	no	yes
	panic button	no	yes
	surveillance unit	yes	yes

proof-of-concept prototype, without the intention of measuring humans and the design did not consider leakage or discharge current specifications. A single point of contact is sufficient for a life threatening electric shock, considering the high voltage in the unprotected DFG. The redesign uses floating potentials for the entire drive field signal chain, which requires contact at to separate points of the circuit. Furthermore, due the lower inductance, the total voltage in the vicinity of the DFG is also reduced [O21]. To deliver the same power to the field, high currents and a low loss DFG design are required. In addition, this design avoids single-ended signaling and prevents long ground loops that can cause unwanted signal distortions [112]. The redesigned scanner is expected to be suitable for human trials after documentation and approval by the local ethics committee.

The second motivation is driven by imaging performance to increase the usability in a clinical setting, effectively reducing scan times, and having accessibility to a volumetric scan, including the important transversal slice of the brain. Cerebral imaging is important to diagnose different types of stroke and to provide rapid imaging of the relevant slices.

The third motivation pertains to the topology of the signal chain and the implementation of the capability for rapid volumetric imaging. We use two nested coils for the two drive-field channels, one of which is a cylindrical coil in x-direction and the other a saddle coil for an orthogonal field profile in z-direction. With regard to the topology of the signal chain, the decision was made to employ a TxRx design, despite the proven excellent performance of dedicated receive coils [78, 204, 207]. Reasons for this include the reduced complexity of the receive chain, which saves valuable space within the DFG, the possibility of lowering resistive coil noise due to large copper-cross sections in pursuit of a patient-noise-dominated system [240, 328], the low inductance DFG with a reduced voltage to increase safety, and the available receive channel in the z-direction. Due to its position on the surface of a cylindrical bore, a saddle coil is used for which no gradiometer has yet been developed, which will be explained in paragraph "Fields and Receive Coils" below. Although a full duplicate setup can be used for compensation [77], the increases in system complexity and power consumption [177] is larger compared to a TxRx design.

The following paragraphs will present a methodology for the balanced evaluation of these decisions. Despite the identification of certain trade-offs during the development process [O11] and the avoidance of numerous setbacks through the introduction of new conceptualizations [O20], several decisions were ultimately irrevocable and deeper knowledge only acquired afterwards which will be discussed in section 11.2.

Implementation. For the implementation of the TxRx signal chain, an ICN is chosen as the central element for the realization of a TxRx concept, however, a backup solution of a dedicated x-receive coil is prepared as an insert [O11, O3], reducing the available free bore size. The ICN itself is shown in Figure 4.4 and part to the signal chain shown in Figure 4.5 (b) and (c). Each ICN feeds the high current resonator (HCR) of one drive field channel. The DFG and its resonance capacitors are effectively mirrored vertically and horizontally inside the HCR. This symmetric topology brings the advantage of a built-in f_1 filter: the potential v_{TxRx} can be used as a receive signal tap [233] without feedthrough of the excitation fundamental. As previously stated, a significant current of approximately 300 A oscillates within the HCR, necessitating the optimization of all electrical components with a large copper cross-section to minimize losses. The complete design process of the ICN is explained in depth in chapter 6 [O2], encompassing all design decisions, requirements, and conflicting design goals that necessitate meticulous trade-offs. In principle, the design can be adapted for other applications, e.g. in wireless power transfer [183, 283, 318].

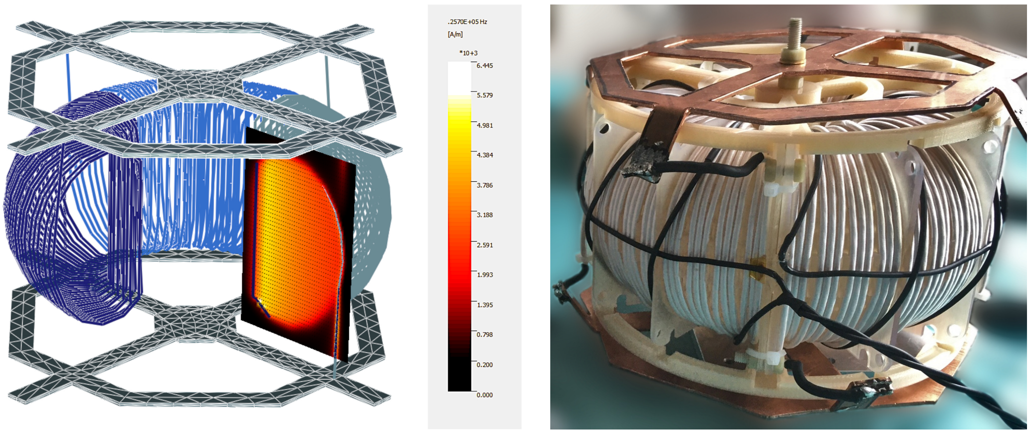

Figure 4.4: The inductive coupling network. A low loss and highly linear toroid with an optimized cross-section shape and parallel segmentation for high signal gain is shown [O2]. The figure on the left depicts the secondary side of a single ICN, where only 3 of 4 parallel segments (dark blue to gray) are displayed. The copper crosses at the top and bottom are thick copper connections to equalize the current distribution to the parallel segments. The $\boldsymbol{H}$ magnitude of is shown for the D-shaped cross section, simulated in CONCEPT-II [108]. On the right, a picture of the constructed ICN is shown, including its primary toroid (black). A compensation turn, akin to the Rogowski coil, reduces leakage field by reversing one turn along the circumference.

One unexpected challenge during the construction of the head scanner is the frequency detuning of the resonant circuit by thermal drift. Due to the required current rating and the high internal voltages driven by the series resonance, capacitors of type CELEM CSM 150/200 are used, rated with up to 200 kVA, which form the 4 capacitor banks in Figure 4.5 (c). Their housings are mainly made of copper, and the capacitance drifts considerably due to heat dissipation, especially during extended measurements. To prevent resonator detuning and to ensure stability during long system matrix calibration measurements, a heating control unit is designed and evaluated in [O20]. The concept here is counter-intuitive: rather than cooling, the capacitors are heated to a preset individual temperature within the range of 35 to 55 °C. This process reduces but stabilizes the value of the capacitance. To this end, the capacitors are mounted on rails that support heating cartridges and sensors, which are driven by a PID controller. If the limitations of capacitor current at elevated temperatures are adhered to, there are two advantages to be gained. Firstly, water- or oil-based cooling is effective, but requires an unacceptable amount of auxiliary equipment and modifications to the HCR. Secondly, air-based cooling is not fast or effective enough because a small and sudden change of 2 to 5 °C already causes a significant rise in power consumption due to detuning of the resonator [O20]. Another combined effect is a pronounced increase in drive field coupling, which, due to the meticulously calibrated single decoupling capacitor between both channels, results in a rising beat frequency and a steep increase in power consumption [O2, O3].

As previously visualized for a generic ADC/DAC model in Figure 3.5, the entire head-sized imaging system is controlled through a stack of 3 RPs [90] for signal acquisition and signal encoding. The synchronization, communication and storage of measurements is done with MPIMeasurements.jl [89] and controlled with a custom GUI.

Fields and Receive Coils. The drive field of the head scanner consists our of two superimposed fields in x-direction (cylindrical coil, 25.699 kHz) and in z-direction (saddle coil, 26.042 kHz). Although measured field plots are shown in Fig. 2 of [O3], these are restricted

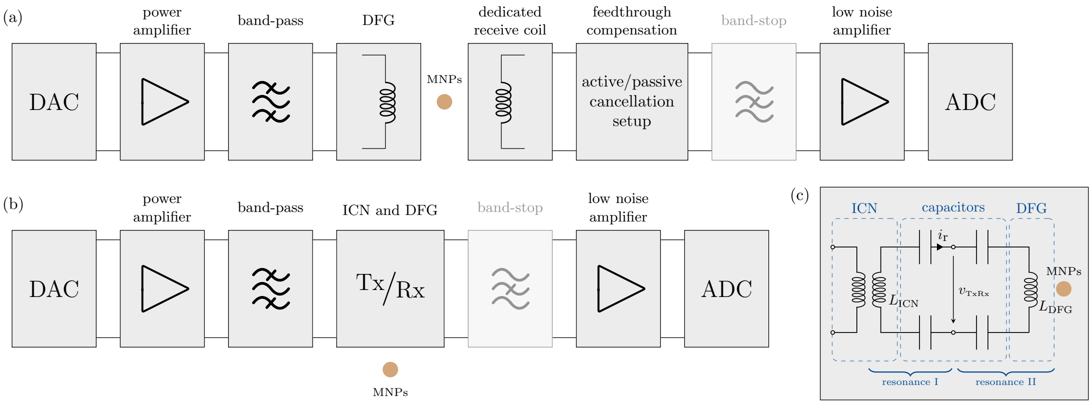

Figure 4.5: Overview of different MPI signal chains. A topology with a dedicated receive-only coil is shown in (a) that is fully coupled to the transmit coil and requires feedthrough compensation to unmask the MNPs signal. In (b), a TxRx circuit is shown that uses the DFG for signal generation and acquisition. In (c), the symmetric circuit within the Tx/Rx box is shown, which is composed of the ICN, 4 (split) capacitor symmetric banks and the DFG on the right side [O11].

to a spherical area within the DFG, about the size and position of the FOV, forward of the geometrical DFG center [O3]. Shown in Figure 4.6 is a complete simulation setup of both DFG coils and the copper shielding that encapsulates the SFG. Here, a larger area of the simulated drive-field profiles are shown in Figure 4.6 (d) and (e), as influenced by their coil design and proximity to the copper housing. Eddy currents are induced on the copper surface of the SFG, especially on the back plane behind the DFG along the principal x-axis of the coils and on the bottom in front of the DFG, as shown in Figure 4.6 (c). These eddy currents create magnetic fields, that oppose their origin and thus distort the field towards its edges. Such an analysis of eddy currents in shielding and their influence on field homogeneity was not included in our article [O3]. The simulation in CONCEPT-II is confirmed by measured field values and field profile, which showed good agreement with a Cartesian and a spherical harmonics-based field measurement method [32, 36, 274]. Field plots and the resulting shape of the Lissajous trajectory are shown and evaluated in detail in chapter 7.

The simulated results for surface currents and field plots are of significant interest when constructing a dedicated gradiometer receive coil. Given the prevalence of signal distortions in the TxRx chain, a high base harmonic content and a high noise floor [O3], we decided to include a gradiometer receive coil in the x- and z-direction[1]. While the field distortion due to eddy currents is more readily observable in the x-DFG in Figure 4.6 (d), it is more straightforward to construct a gradiometer in this direction. This becomes evident, when considering Figure 4.6 (d) and (e), due to two main conditions: a gradiometer requires a large homogeneous region where the same field can be encompassed twice, once with a set of turns with broad sensitivity of the FOV and with a second set of turns for cancellation, away from the influence of MNPs. Additionally, the gradiometer cancellation should be insensitive to the other drive field channel to mitigate crosstalk between receive channels (decoupled).

For the cylindrical coil in Figure 4.6 (d), the approach is obvious, as a specific number of windings with high sensitivity can be applied around the FOV (green) and a dense region towards the back plane (negative x-direction) for cancellation, which is sufficiently distant

---

[1] The y-channel is already equipped with a dedicated receive coil, due to its orthogonal orientation to all transmit channels. It is not necessary to use a gradiometer if the coil is positioned carefully.

from the FOV. The field of the saddle coil in Figure 4.6 (e) is not nearly as homogeneous and a closer look reveals a rhombus-shaped area in the center where the field is roughly unidirectional. Due to the narrow center cavity of each saddle-coil pair, only a small vertical column is truly unidirectional. A solution that involved moving the two parts of the gradiometer to different locations with the same field vectors was not found to be viable, despite the intuitive suggestion that symmetry would permit such a solution. Either both coils are sensitive to the same area or coupling to the x-field is stronger than to z. Hence, the signal quality of a z-gradiometer prototype was not sufficient, and the effort was abandoned in favor of the x- and y-receive coils utilized in chapter 7 [O3]. The loss in spatial resolution due to the loss of the z-channel is expected to be in the range of 12 to 22 % [260]. Possible alternative approaches are proposed in section 11.4.

Wrap up. The full system characterization within safe PNS limits for humans [200, 229] is treated and presented in chapter 7. A safe and MRI approved tracer is used to resemble feasible future human imaging capabilities and results are not artificially enhanced by tailored MNPs [O2]. Various experiments aim to characterize field homogeneity, the 3D measurement sequence, spatial resolution, sensitivity, dynamic perfusion and multi-contrast imaging. A direct comparison of spatial resolution or sensitivity to the earlier version before our redesign is difficult for several reasons, such as the use of different tracers, experiments, imaging sequence, drive-field strengths and receive coils [O3]. Refer to Table 4.1 for a comparison

(a) simulation setup of head scanner in CONCEPT-II

(b) rendering of DFG and SFG, without copper housing

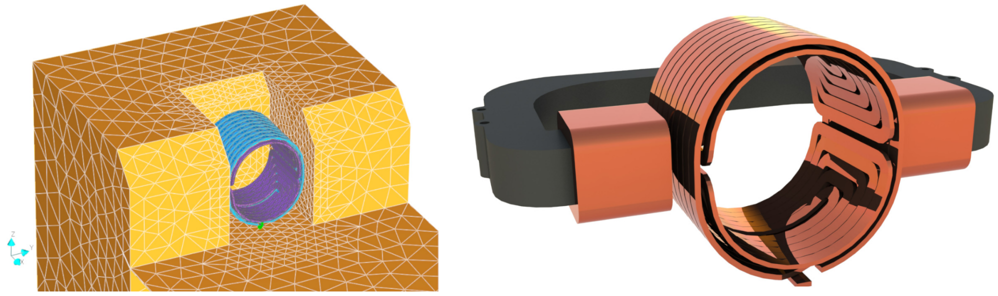

(c) surface eddy currents, log-scale

(d) xz-plane of x-DFG H-field, linear

(e) xz-plane of z-DFG H-field, log-scale

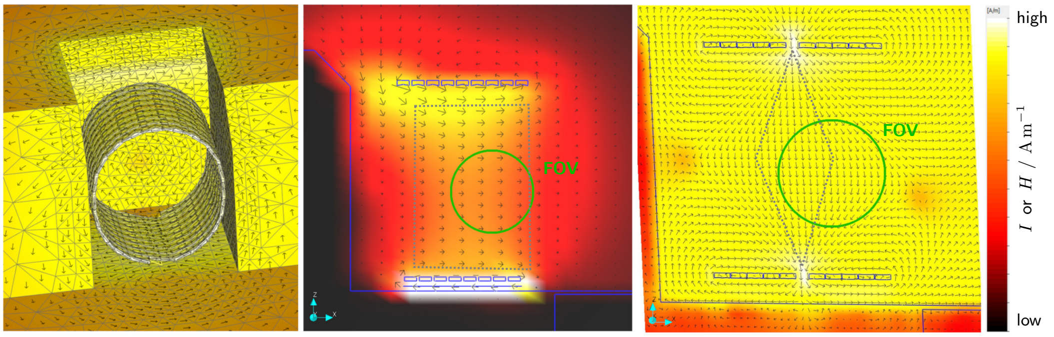

Figure 4.6: Simulation setup for head scanner. (a) A discretized model using surface currents is developed in CONCEPT-II [108] and both DFG coils are simulated independently. (b) Rendering of SFG with iron yoke and both DFG coils, without dedicated receive coils. (c) Simulation results of surface currents, showing two pronounced eddy current nodes. (d) Results for the cylindrical x-DFG show a smooth, but slightly distorted field plot due to the proximity of the copper shielding where eddy currents occur. Gray dashed lines indicate a sufficiently homogeneous field region for decoupling gradiometer coils. (e) Results for the saddle coil z-DFG indicate a narrow center line with homogeneous z-field. A central rhombus-shaped unidirectional field region occurs.

of the instrumentation and safety considerations between the original head scanner [76] and our redesign [O3]. The used Ferucarbotran tracer is the link to the following application part of this thesis, which initially features a detailed analysis and comparison of different MNPs.

4.2 Applications of MPI

Within the experimental part of [O3], we do not use a high performance MPI tailored tracer to enhance and maximize the MPI specific signal [58], but intentionally conduct all experiments using the MRI approved tracer Resotran (b.e.imaging GmbH, Baden-Baden, Germany). It has a signal performance akin to the well-studied tracer Resovist (formerly Bayer Schering Pharma, Berlin, Germany) [98, O4, O19], which is expected because both consist of Ferucarbotran, mainly a mix of maghemite and magnetite. We conduct this study in order to predict the realistically achievable resolution and sensitivity for the first human trials. Possible medical applications, such as perfusion imaging, are conducted and analyzed, demonstrating the current ability and limitations of head-sized scanners for human trials in the near future.

Perfusion imaging is a valuable diagnostic tool for identifying different types of stroke and its severity. This motivates the investigation of potential improvements for likely scenarios where MPI can be utilized in the future. Further research on the applications of MPI within chapter 9 concerns reducing the amount of administered MNP material for long-term monitoring scenarios, such as perfusion imaging of a stroke patient [O5]. Moreover, the viability of multi-contrast MPI for real-time gastrointestinal bleeding detection [O6] is investigated in chapter 10 using a preclinical MPI system. Here, MPI has the potential to reduce X-ray radiation exposure and to be integrated to interventional medicine in the future.

4.2.1 Resotran and the Dilemma of Tailored MNPs

Tailored MNPs like Perimag (micromod Partikeltechnologie, Rostock, Germany) [52], Synomag (micromod Partikeltechnologie, Rostock, Germany) [64, 286], VivoTrax+ (Magnetic Insight Inc., Alameda, United States) [66], PrecisionMRX (Imagion Biosystems Ltd, Melbourne, Australia) [270], LS-008 (LodeSpin Labs, Seattle, USA) [288], or magnetosomes [171, 277] have shown significant potential for MPI and superior magnetic properties compared to Ferucarbotran (Resotran, Resovist, VivoTrax), of which only around 3 % of the total iron mass were reported to be MPI active [70, 322]. However, the requirements for a medical approval are a costly endeavor, justified only for a well defined business case and far exceeding the budget of most research divisions. This contributes to the dilemma that without suitable clinical scanners, there will be no approved tailored MNPs in the near future and vice versa, that the performance of prototype (human-sized) scanners will not be fully exploited due to unsuitable MNPs or lack of diversity.

Our work in chapter 8 focuses on the characterization of Resotran, Resovist, Perimag and Ferrotran (b.e.imaging GmbH, Baden-Baden, Germany) to draw a conclusion on performance and eligibility for MPI based on comparison. Next to magnetic properties and imaging performance, an evaluation of size and shape concludes that Resotran is very similar to the well-understood MNPs Resovist. This is expected, because both consist of Ferucarbotran and the article forms a basis and reference for experiments conducted with MPI-tailored MNPs and the medically approved Ferucarbotran in the future. Calibrations are used to derive general magnetic properties via vibrating sample magnetometry (VSM) and MPS that are displayed device-independent. Along TEM images and size distributions obtained by dynamic light scattering (DLS), the data in [O4] (chapter 8) provide a reference for the investigated MNPs beyond the scope of medical imaging.

4.2.2 Reducing Tracer Dosage: Saline Bolus

Many envisioned applications of MPI include perfusion imaging [79, 120, 164, 165, 187, O3, 332], which aims to capture the transient process of fluids that pass through the lymphatic or vascular system within the human body. As a non-invasive, radiation-free modality with high temporal resolution, MPI is a promising candidate for such a tool and could become an alternative in the diagnosis of ischemic stroke and intracerebral hemorrhage.

In pursuit of optimizing perfusion imaging for devices like the head scanner of chapter 7, our work in chapter 9 is based on the idea that a negative change in signal can provide the same information as a positive change. Because the derivation of perfusion parameters is based on the curve's gradient, shape, area, or time differences between two points, it does not matter if the bolus introduces an signal intensity maximum or minimum [22]. However, so far only the positive bolus application has been investigated in MPI. Negative contrast is known from MRI perfusion imaging, where the MNPs influence the regional magnetic susceptibility linearly and thus changes the measured signal relaxation time [22].

For a successful implementation of this technique, a long-circulating tracer with a strong MPI signal response is required. Here, the design of the MNP surface coating [27, 118] plays a key role. Other research suggests to load red blood cells with MNPs [12]. In this case, the MNPs circulate within the blood stream for several hours and are not taken up by the liver or spleen, so imaging at regular intervals can be performed, i.e. for a monitored stroke patient. Effectively, the overall dose of MNPs could be reduced because a fresh bolus of tracer is not required for every image. We show that negative contrast using a saline bolus is possible and that equal perfusion-maps of the time-to-peak (TTP), the mean-transit-time (MTT), the relative blood-flow (rBF) and the relative blood-volume (rBV) can be calculated. To this end, a circulatory pump setup and a rat-sized heart-phantom are used in chapter 9 [O5]. The main advantage of neutral saline is that vast amounts with regard to bolus sizes in the µL to mL range can be given, where recommendations exceed $100\,\mathrm{mL\,h^{-1}}$ to treat dehydration, and that its composition is approximately isotonic to the human blood serum with a 0.90 % mass concentration of sodium chloride [205].

4.2.3 Real-Time Multi-Contrast MPI for Gastrointestinal Bleeding

As a potential tool for interventional medicine, MPI also aims to improve the diagnosis of occult or overt gastrointestinal (GI) bleeding, which in severe cases can be a life-threatening condition [123]. Endoscopic evaluation of the upper and lower abdomen is an invasive treatment and if inconclusive, further modalities such as CT are required. The middle GI tract can be difficult to access by endoscopy and clinically important lesions may be missed [65]. Real-time MPI could be used to image the entire GI tract without sedating the patient and providing high spatiotemporal information on MNP passage at the source of the bleeding.

The study in chapter 10 focuses on the deployment of single- and multi-contrast MPI to detect GI bleeding in human-sized bowels by performing two types of experiments [O6]. These include 3D printed phantoms with and without a perforation and ex vivo porcine small bowel specimen, which are similar in size to the human bowel. We also focus on a real-time aspect, for acute bleeding that requires prompt intervention. Single-contrast MPI was previously used to detect GI in rodents by Yu et al. [325], but in their work, pictures are taken at time intervals of 20 s, prone to long averaging times and a slow acquisition with a high gradient field. We use the preclinical MPI scanner Bruker MPI 25/20 FF with a repetition time of 21.54 ms per 3D FOV to be able to provide real-time online reconstruction [132] and the system matrix approach is used to apply single- and multi-contrast MPI.

The main advantage of using multi-contrast is that a signal threshold can be applied to each channel individually: if two tracers occupy separate volumes, a region with signal overlap of both tracers can be identified as bleeding. For this purpose, one tracer is administered orally and the other via the bloodstream. This helps to achieve independence from the anatomical reference, in the sense that any cluster of voxels containing a fraction of both tracers will identify a nearby perforation. In the case of single contrast, a hemorrhage is identified only by using an anatomical reference, such as a CT image, to determine if the signal location is within an area that should be perfused. Even with anatomical reference information, a referenced and tracked voxel, e.g. located in the vascular structure around the bowel lumen, remains very sensitive to motion such as breathing and displacement. Misdiagnosis is more likely and more CT reference images are required as opposed to the multi-contrast approach where a single reference may suffice.

In our study, stomach acid may pose a challenge to coated MNPs particles and a tracer that can survive hostile environments is therefore required for human applications. However, the general principle is applicable to other separated volumes and gains in accuracy for two tracers with high separability and low channel leakage.

5

System Matrix based Reconstruction for Pulsed Sequences in MPI

In this chapter, a hybrid system matrix approach is combined with a sequence simulation framework that allows the computation of system matrices based on arbitrary waveform excitation measurements with one offset channel [O1]. Our framework is generic and can be used for different types of data to evaluate the performance of different trajectories, such as for a trajectory analysis of an FFL type scanner [O17].

Parts of this work were presented at the BMT 2021 conference in Hannover [O7] and at the IWMPI 2022 online conference [O8]. During waveform optimization and value calibration of the arbitrary waveform MPS, gained insights helped to contribute to deriving an iterative voltage-mode amplifier model, presented by Ackers et al. [O12] at the IWMPI conference 2023. Also presented on the same conference was the work by Niebel et al. [O17]. Measurements using the arbitrary waveform MPS have also been used in other publications [O4].

Two Bachelor theses were conducted during the construction and optimization of the hardware for the arbitrary waveform MPS, the first by Lars Feyerabend "*Konstruktion eines Breitbandmagnetpartikelspektrometers für beliebige Signalformanregungen*", 29.01.2020, TUHH, concerning the construction and the second thesis by Lukas Hildebrandt "*Optimierung und Analyse der analogen Signalentkopplung eines Breitbandmagnetpartikelspektrometers*", 17.11.2020, TUHH, concerning the optimization of the transmit coil and decoupling unit.

5.1 IEEE - Transactions on Medical Imaging

Manuscript received August 9, 2021.
Revised January 26, 2022.
Accepted February 2, 2022.

Type: Open Access. CC-BY-4.0 license.
DOI: 10.1109/TMI.2022.3149583

System Matrix Based Reconstruction for Pulsed Sequences in Magnetic Particle Imaging

Fabian Mohn, Tobias Knopp, Marija Boberg, Florian Thieben,
Patryk Szwargulski, and Matthias Graeser

***Abstract*— Improving resolution and sensitivity will widen possible medical applications of magnetic particle imaging. Pulsed excitation promises such benefits, at the cost of more complex hardware solutions and restrictions on drive field amplitude and frequency. State-of-the-art systems utilize a sinusoidal excitation to drive superparamagnetic nanoparticles into the non-linear part of their magnetization curve, which creates a spectrum with a clear separation of direct feed-through and higher harmonics caused by the particles response. One challenge for rectangular excitation is the discrimination of particle and excitation signals, both broad-band. Another is the drive-field sequence itself, as particles that are not placed at the same spatial position, may react simultaneously and are not separable by their signal phase or shape. To overcome this potential loss of information in spatial encoding for high amplitudes, a superposition of shifting fields and drive-field rotations is proposed in this work. Upon close view, a system matrix approach is capable to maintain resolution, independent of the sequence, if the response to pulsed sequences still encodes information within the phase. Data from an Arbitrary Waveform Magnetic Particle Spectrometer with offsets in two spatial dimensions is measured and calibrated to guarantee device independence. Multiple sequence types and waveforms are compared, based on frequency space image reconstruction from emulated signals, that are derived from measured particle responses. A resolution of 1.0 mT (0.8 mm for a gradient of (-1.25, -1.25, 2.5) Tm^{-1}) in x- and y-direction was achieved and a superior sensitivity for pulsed sequences was detected on the basis of reference phantoms.**

***Index Terms*— Biomedical imaging, pulsed excitation, high amplitudes, sequence design, MPI.**

I. INTRODUCTION

IN MAGNETIC Particle Imaging (MPI) the spatial distribution of superparamagnetic iron oxide nanoparticles (SPIONs) is determined by a superposition of a static gradient field and one or several oscillating excitation fields [1]. The static gradient field, called selection field, generates a low-field-region (LFR) in its center, that includes a field-free-region (FFR), which could either be a field-free-point (FFP) or field-free-line (FFL), depending on its shape. On the one hand, the oscillating excitation field drives the SPIONs through their magnetization curve, causing higher harmonics due to their nonlinear characteristic. On the other hand, it drives the LFR through the imaging volume and creates a specific trajectory. Most scanner topologies use narrow-band sinusoidal signal shapes to excite the tracer material (see Table II in [2] for an overview). Due to the superposition of the oscillating fields and the selection field, these encoding schemes cause the SPIONs in the LFR to respond at a specific point in time with their maximal amplitude. In frequency domain this results in a spectral fingerprint depending on space, which can be used to reconstruct the image by solving a linear system of equations [1], [3]. Another advantage of narrow-band excitation is the discrimination of the frequency space in the two domains, the narrow-band excitation band and the higher receive band, which contains the harmonics caused by the particles nonlinearity. Due to this discrimination, a separation between the strong feed-through of the excitation field and the by 10^{-6} to 10^{-10} lower particle signal can be achieved, using resonant passive filtering [4]. Current developments show that such encoding schemes can provide sub-millimeter resolution [5], more than 46 volumes per second time resolution [6] and pico-gram sensitivity [7]. Developments in instrumentation now reach for clinical scale [8]–[10] to address specific needs, which are currently only partly addressed by conventional imaging systems. Possible medical applications reach from catheter imaging [11] in digital subtraction angiography, over stent quantification [12], stroke imaging [13]–[15] and many more. Using multi-contrast image reconstruction [16], it is also possible to distinguish between different particle systems [17] or physical parameters in the vicinity of the particle system

---

Manuscript received August 9, 2021; revised January 26, 2022; accepted February 2, 2022. Date of publication February 7, 2022; date of current version June 30, 2022. This work was supported in part by the German Research Foundation (DFG) under Grant GR 5287/2-1 and Grant KN 1108/7-1, in part by the Forschungszentrum Medizintechnik Hamburg (FMTHH) under Grant 01fmthh2018, and in part by the Fraunhofer Research Institution for Individualized and Cell-Based Medical Engineering (IMTE). The IMTE is supported in part by the European Regional Development Fund (EFRE) and in part by the State Schleswig-Holstein, Germany, through Project IMTE under Grant 124 20 002 and Grant LPW-E1.1.1/1536. Publishing fees supported by the Funding Programme Open Access Publishing of Hamburg University of Technology (TUHH). *(Corresponding author: Fabian Mohn.)*

Fabian Mohn, Tobias Knopp, Marija Boberg, Florian Thieben, and Patryk Szwargulski are with the Institute for Biomedical Imaging, Hamburg University of Technology, 21073 Hamburg, Germany, and also with the Section for Biomedical Imaging, University Medical Center Hamburg-Eppendorf, 20251 Hamburg, Germany (e-mail: fabian.mohn@tuhh.de; t.knopp@uke.de; m.boberg@uke.de; f.thieben@uke.de; p.szwargulski@uke.de).

Matthias Graeser is with the Institute for Biomedical Imaging, Hamburg University of Technology, 21073 Hamburg, Germany, also with the Section for Biomedical Imaging, University Medical Center Hamburg-Eppendorf, 20251 Hamburg, Germany, and also with the Fraunhofer Research Institute for Individualized and Cell-Based Medicine and the Institute for Medical Engineering, University of Lübeck, 23562 Lübeck, Germany (e-mail: matthias.graeser@imte.fraunhofer.de).

Digital Object Identifier 10.1109/TMI.2022.3149583

like temperature [18], viscosity [19], or binding state [20], [21]. With sinusoidal excitation, large single-core particles show a strong relaxation behaviour, which broadens the point spread function (PSF) and reduces the signal response, therefore reducing sensitivity and resolution [22]. Recently, Tay *et al.* proposed a rectangular excitation and showed that it has the potential to improve the achievable resolution by using large particles in combination with a new reconstruction approach [23]. They showed that the effect of broadening the PSF can be significantly reduced under certain conditions, using rectangular excitation with small amplitudes [23]. In idealized rectangular excitation sequences, a LFR would jump between two resting points in space, causing all particles in between to react simultaneously. Tay *et al.* proposed a reconstruction scheme, that integrates the receive signal, which in turn encodes the magnetic moment $\boldsymbol{m}$ of the area between the LFR locations before and after the pulse, as long as $\boldsymbol{m}$ reaches a steady state within the resting time between pulses. Consequently, this approach requires low field amplitudes (1 to 3 mT), such that the LFR remains within a single voxel and no loss in spatial resolution in the excitation direction is induced. Otherwise, the information of the particle distribution between two LFR positions would be lost. Furthermore, a low excitation frequency is required in order to let the particles fully relax to ensure their steady state [23].

In this paper, multiple sequences based on different excitation waveforms and amplitudes are compared in system matrix phantom reconstructions. A sequence for rectangular excitation shapes is proposed, that uses shifts and rotations simultaneously for better spatial encoding. In this proposed sequence, the rectangular excitation is rotated and shifted orthogonal to the excitation. Similar to a radon sampling scheme, this allows to reconstruct measured data with large amplitudes and an isotropic sampling trajectory in 2D, even if the phase information between the resting points is lost. If particles relax fast enough to follow the slew rate of the drive field, their phases within the signals become distinguishable which allows a system matrix approach to reconstruct images at high resolution. For pulsed sequences, the results show improved sensitivity while the proposed sequence has uniform and high resolution with short acquisition times.

II. MOTIVATION AND CONCEPT

All signals and reconstructions are emulated, meaning they are based on measurements of an arbitrary waveform magnetic particle spectrometer (AWMPS) [24]–[26], which are processed to resemble a specific particle response for a defined sequence. By exciting SPIONs, superimposed by a range of different DC-offsets in two spatial dimensions, their response is mapped on a 2D grid. This resembles the response to an overlaying 2D gradient field [27]. This approach has the benefit to deliver reliable results for a first evaluation, without the time consuming process of building an actual system that can produce the required fields on a large scale. Following conditions should be met to reproduce the data:

a) Hardware: A device that is capable of producing arbitrary waveform excitations, superimposed by two orthogonal spatial DC-offsets. See Section III-A for details on the AWMPS, which is used to measure a hybrid system matrix with 1D excitation and 2D offset fields [27]. This raw dataset is later processed to generate the sequence specific particle response.

b) Transfer function correction: To be able to compare the results with other imaging systems, the data needs to be handled in a comparable physical variable, in this case the domain of the magnetic moment $\boldsymbol{m}$ ($[\boldsymbol{m}] = \mathrm{Am}^2$), which is achieved by correcting the received signals with the transfer function (TF) of the system [28]. In this domain, the signal is independent of the receiver and individual properties of a given system, like receive coils or amplification [29]. This allows cross-platform comparison of the SPIONs response to a given excitation.

c) Sequence noise: To avoid correlation of intrinsic measurement noise by reusing a subset of the same dataset within the emulated sequence, the signal needs to be overlaid with dominant, digitally generated noise $\tilde{u}^s_{\text{noise}}(t)$.

d) Reconstruction noise: A model to accurately represent receive chain noise of a scaled MPI system, consisting of resonant coils, low noise amplifier (LNA) and analog-to-digital converter (ADC), based on reference measurements from a 40 mm receive coil, named $\tilde{u}^r_{\text{noise}}(t)$ [30]. Therefore, calculated images are comparable to those of a small scanner system.

e) Phantoms: In spite of correcting data by a TF, the measured data from the AWMPS has a high signal-to-noise ratio (SNR), due to the close proximity of the receive coils to the tracer and the large sample compared to a voxel volume of a system matrix calibration. While the close proximity is corrected by the TF, a realistic model for scaling the measured iron mass to the emulated voxel grid is needed.

f) Independent system matrices: Two sets of system matrices need to be acquired to avoid inverse crime, when the phantom spectrum stems from the identical dataset as the system matrix used for reconstruction. For each sequence that is investigated in this paper, two independent system matrices on different grids are calculated, which are based on separately measured datasets, to guarantee a realistic reconstruction.

g) Comparability across sequences: In a final condition, the total sequence measurement time is chosen as the common criterion to compare sequences of different design.

Following these criteria, the images reconstructed by this method represent realistic images, achievable by a well designed pulsed MPI system.

III. METHODS

Different sequences are generated on various sets of raw data, to compare and identify the effects that excitation waveform, amplitude or sampling trajectory have on the image SNR and resolution. This includes pulsed and sinusoidal excitation, as well as low and high excitation amplitudes. Individual sequences and their sampling trajectories are explained in Section III-C. Instead of depending on a narrow PSF for high resolution, the proposed method in this work uses higher excitation field strengths above 10 mT, as this benefits not only the sensitivity, but also reduces acquisition time in future imaging systems due to the capability of using less averages.

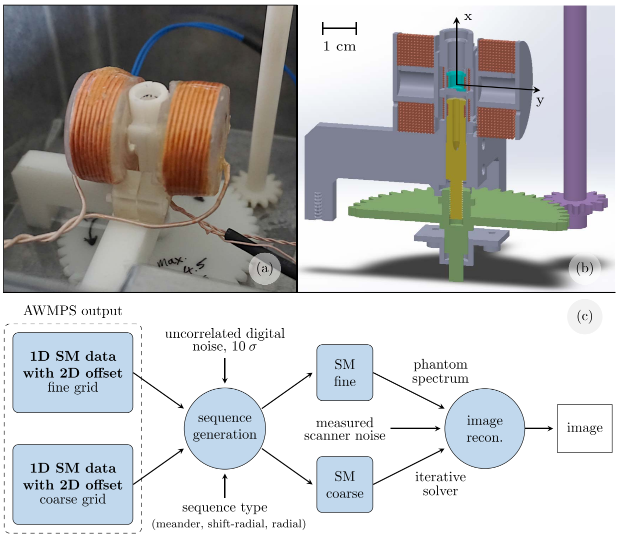

Fig. 1. **Sectional view of the AWMPS and flowchart of the entire process chain from raw data to image.** Using gradiometric receive coils, the receive signal can be isolated by suppressing direct excitation feed-through. Fine-tuning is achieved by turning the gear-wheel. A Helmholtz-coil creates an additional DC-offset field in another spatial dimension (y-direction). The general process of the methodology is shown in the block diagram.

To highlight the advantages and limitations between the different methods, the Cartesian sequence proposed in [23] is compared with the proposed method in this work. For a detailed comparison of the benefits of pulsed excitation, the proposed shift-radial sequence is run with both, rectangular excitation as well as sinusoidal excitation. A radial sine sequence is also included, as proposed by Knopp *et al.* in [31], which does not use the shift orthogonal to the excitation direction. The system matrix reconstruction approach is chosen for all sequences [3]. For an overview of the image reconstruction pipeline in this study, the process is depicted in Fig. 1 (c).

A. Arbitrary Waveform Magnetic Particle Spectrometer

A non-resonant AWMPS with two transmit coils was built to perform measurements that contain the one-dimensional excitation, superimposed by DC-offsets in two orthogonal spatial dimensions. The main transmit coil combines excitation signal and DC-offset in x-direction within a single cylindrical coil, whereas a second transmit coil in Helmholtz configuration is responsible for the orthogonal DC-offset in y-direction with up to ±50 mT. The AWMPS may measure any waveform up to 45 mT in amplitude and is limited for arbitrary pulse shapes by a final slew-rate due to load and amplifier characteristics, around 10 $\mathrm{mT\mu s^{-1}}$. Fig. 1 shows a picture and the cross-section of the design. The excitation and x-offset coil is connected to a 4-quadrant-amplifier (*Dr. Hubert GmbH, Bochum, Germany*). To avoid direct feed-through, two receive coils are arranged in opposite orientation for decoupling of the receive path from the transmission line. The position of one coil is adjustable by a gear wheel for fine-tuning of the feed-through cancellation. The signal is then amplified by a custom-build LNA. The data acquisition card *STEMLab 125-14, Red Pitaya* is used for signal generation on two transmit channels and records the receive signal, as well as the amplifiers reference current monitor for control purposes.

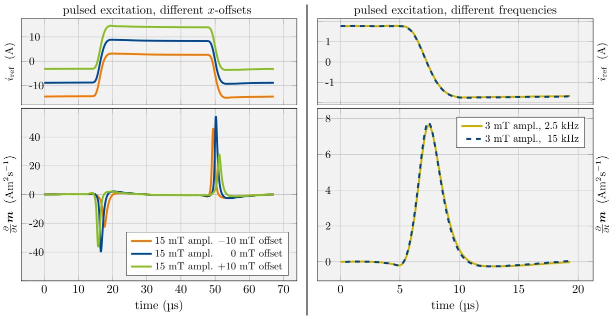

Fig. 2. **Pulsed excitation measurements with a 20 µL sample of Perimag 17 $\mathrm{\mu g_{Fe}\,\mu L^{-1}}$.** To the left, three offsets in excitation direction are plotted (14.88 kHz), the reference channel from the current monitor is on the top, the TF corrected receive signal on the bottom. Plots on the right show identical relaxation behavior of two overlaid signals at 2.5 kHz and 14.88 kHz. The slew rate of both frequencies is identical, only the hold time differs. Both signal curves are coinciding for Perimag.

B. Measurements

All measurements in this work are based on a multicore tracer, Perimag (*micromod Partikeltechnologie GmbH, Rostock, Germany*) with an undiluted iron concentration c_{meas} of 17 $\mathrm{mg_{Fe}\,mL^{-1}}$ (304.4 $\mathrm{mmolL^{-1}}$). The delta sample is filled with $V_{\mathrm{meas}} = 20\mathrm{\mu L}$ of undiluted tracer to guarantee high measurement SNR at low amplitudes. The excitation frequency is chosen to be 14.88 kHz, to ensure steep flanks of the rectangle excitation and avoid slew rate artifacts on the edges while keeping a good reception for induction sensors. This differs from the choice of 2.5 kHz in [23], however the rise time t_{r} of the pulsed excitation (square wave, $t_{\mathrm{r}} = 3\mathrm{\mu s}$) lies in a similar region (2 to 5 µs). On the right side in Fig. 2 these two frequencies are compared, to confirm the quick and identical relaxation behaviour of the used tracer for both frequencies. We note that Perimag is a tracer with low relaxation times, in contrast to the long relaxations times of the tracers used in [23]. Therefore, our frequency choice is only valid for fast relaxing particles and not a general choice for larger core SPIONs. Instead of averaging 25 times [23], datasets in this work are all recorded with 3 averages. Data is acquired sequentially, each y-offset is held constant during which a sweep of all x-offsets is performed. Frequency and excitation amplitude stay constant until a dataset acquisition is completed. Measurements are background corrected, TF corrected for device independence and arranged by time samples and spatial offsets. The two resulting raw data sets for each sequence type form the basis for the sequence generation process, yielding a low resolution system matrix ($\hat{\boldsymbol{S}}_{\mathrm{LR}}$ with 0.67 mT steps in x- and y-direction) and a high resolution system matrix ($\hat{\boldsymbol{S}}_{\mathrm{HR}}$ with 0.5 mT steps in x- and y-direction), respectively.

C. Sequence Generation

Three sequence types are presented in this paragraph, each based on two independent sets of measured raw data,

TABLE I
OVERVIEW OF SEQUENCE DETAILS AND MEASUREMENT PARAMETERS OF THE AWMPS RAW DATA

	drive field				sequence parameter		raw data matrix	
sequence name	amplitude	waveform	frequency	ISI shape	sequence specific values	periods J seq. time	FOV $x \times y$	grid low res. grid high res.
meander 3mT	$3\,\mathrm{mT}$	rectangular $t_\mathrm{r} = 3\,\mathrm{\mu s}$	$14.88\,\mathrm{kHz}$	small, localized	31 steps in x and y $1\,\mathrm{mT}$ step resolution	1920 $129\,\mathrm{ms}$	$80 \times 80\,\mathrm{mT}^2$	121×121 161×161
meander 15mT	$15\,\mathrm{mT}$	rectangular $t_\mathrm{r} = 3\,\mathrm{\mu s}$	$14.88\,\mathrm{kHz}$	broad area, circular	31 steps in x and y $7/31$ mT step res. in x $1\,\mathrm{mT}$ step res. in y	1920 $129\,\mathrm{ms}$	$80 \times 80\,\mathrm{mT}^2$	121×121 161×161
shift-radial	$15\,\mathrm{mT}$	rectangular $t_\mathrm{r} = 3\,\mathrm{\mu s}$	$14.88\,\mathrm{kHz}$	broad area, circular	15 mT amplitude of shifts 32 shifts per rotation J_SpR 31 pulses per shift J_PpS	1920 $129\,\mathrm{ms}$	$40 \times 80\,\mathrm{mT}^2$	61×121 81×161
shift-radial	$15\,\mathrm{mT}$	sinusoidal	$14.88\,\mathrm{kHz}$	broad area, elliptic	15 mT amplitude of shifts 32 shifts per rotation J_SpR 31 pulses per shift J_PpS	1920 $129\,\mathrm{ms}$	$40 \times 80\,\mathrm{mT}^2$	61×121 81×161
radial	$15\,\mathrm{mT}$	sinusoidal	$14.88\,\mathrm{kHz}$	broad area, elliptic	1920 pulses per rotation J_PpR	1920 $129\,\mathrm{ms}$	$40 \times 40\,\mathrm{mT}^2$	61×61 81×81

to compose $\hat{\boldsymbol{S}}_\mathrm{LR}$ and $\hat{\boldsymbol{S}}_\mathrm{HR}$ for reconstruction. The parameters for excitation amplitude and waveform depend on the sequence version, as detailed in Table I.

The sequence itself is built from the time series data $\tilde{u}(\boldsymbol{r}, t)$ in a way, that a subset of the dataset, like a virtual FOV, is continuously shifted over the raw dataset by the LFR sequence. If the sequence contains a rotation $\boldsymbol{R}(\vartheta(t))$, it is applied consecutively with the shifting $\boldsymbol{b}(t)$, as described by the rigid transformations

$$\mathcal{T}(\boldsymbol{r}, t) = \begin{cases} \boldsymbol{R}(\vartheta(t))\,(\boldsymbol{r} + \boldsymbol{b}(t)) & \text{seq. type } a) \\ \boldsymbol{R}(\vartheta(t))\,\boldsymbol{r} & \text{seq. type } b) \\ \boldsymbol{r} + \boldsymbol{b}(t) & \text{seq. type } c) \end{cases}$$

$$\text{for} \quad \boldsymbol{R}(\vartheta(t)) = \begin{pmatrix} \cos\vartheta(t) & -\sin\vartheta(t) \\ \sin\vartheta(t) & \cos\vartheta(t) \end{pmatrix}, \quad \boldsymbol{b}(t) = \begin{pmatrix} b_x(t) \\ b_y(t) \end{pmatrix}$$

where $\vartheta(t)$, $b_x(t)$ and $b_y(t)$ are piecewise constant functions for each period. The measurement noise within the transformed measurement voltage $\tilde{u}(\mathcal{T}(\boldsymbol{r}, t), t)$ from the AWMPS, would appear identically numerous times within the sequence, which can create reconstruction artifacts. To avoid correlation of measurement noise throughout the sequence, digitally generated noise is added with a higher noise level of

$$\tilde{u}^s_\mathrm{noise}(t) = 10\,\sigma_\mathrm{meas}\,\tilde{u}_{\mathrm{n},1/\mathrm{f}}(t) \tag{1}$$

which is crucial to mask the measurement noise floor of the raw dataset. σ_meas is the standard deviation of the measurement background noise and $\tilde{u}_{\mathrm{n},1/\mathrm{f}}$ is the digitally generated noise, that has been fitted to the shape of the measured background noise. The overall shape resembles 1/f noise, which is typical for integrated circuits in the low frequency region. The addition of the tenfold standard deviation is based on an analysis of the correlation coefficient versus the addition of $n \cdot \sigma_\mathrm{meas}$ with $n \in \mathbb{R}_+$, such that the noise in the generated sequence is dominated by uncorrelated noise. In general, $\tilde{u}$ is the unprocessed voltage signal whereas the TF corrected signal $u = a * \tilde{u}$ is in the domain of the magnetic moment.

Finally, the voltage signal is Fourier transformed (denoted by hat) and TF corrected, yielding the system function

$$\hat{s}(\boldsymbol{r}, k) = \frac{\hat{a}(k)}{T} \int_0^T \Big(\tilde{u}(\mathcal{T}(\boldsymbol{r}, t), t) + \tilde{u}^s_\mathrm{noise}(t)\Big) e^{\frac{-i2\pi kt}{T}}\,dt \tag{2}$$

where $\boldsymbol{r} \in \mathbb{R}^2$ is the position and $k \in \mathbb{N}_0$ the frequency component. Negative frequency components are omitted, due to the symmetry of Fourier coefficients of real signals. $T = Jt_\mathrm{max}$ is the sequence time length, J the number of appended periods and t_max the time length of a single period. Each voxel contains a time signal of J periods.

To visualize the sequence generation process, a magnitude plot is used in Fig. 3, 4 and 5. In this plot, the absolute value of the raw data $\tilde{u}(\boldsymbol{r}, t)$ is summed up over a whole period for each offset value. In other words, the signal intensity is integrated to quantify the system response for discrete, equally spaced measurement values $\tilde{u}_i = \tilde{u}(\boldsymbol{r}, t_i)$ as in

$$\|(\tilde{u}_i)_i\|_{\ell^p} = \left(\sum_{i=0}^{i_\mathrm{max}} |\tilde{u}_i|^p\right)^{1/p}. \tag{3}$$

In this work, the ℓ^1-norm with $p = 1$ is selected and referred to as the integrated signal intensity (ISI). Thus, the ISI is represented by bright yellow colors for positions of strong signal response and dark blue colors represent low signal response. It is noted that the ISI-plot is for visualization purposes only and the ℓ^1-norm is not implemented in the sequence calculation. Within the virtual FOV, the ISI-plot visualizes a moving (and rotating) system response. The final sequence is generated by appending all time signals. Noise addition, fast Fourier transform and TF correction are done equivalently for all sequences.

a) Shift-radial sequence: Proposed in this work is a sequence with the properties of combining a shift, orthogonal to its excitation direction, with a rotation of the excitation itself, referred to as shift-radial sequence. The excitation direction in the raw data is in x-direction and the shift is in y-direction. The shift-radial sequence requires twice the

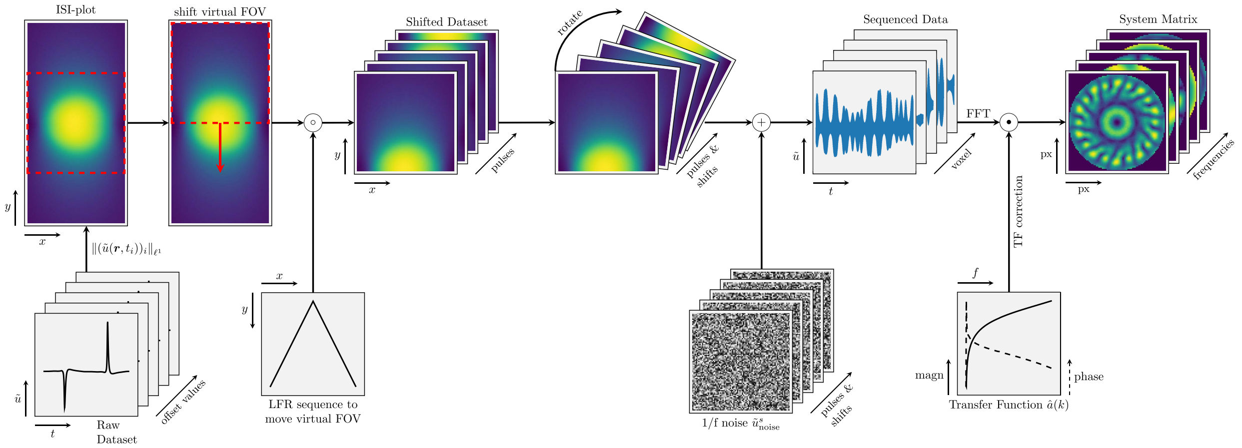

Fig. 3. **Sequence generation diagram of the proposed shift-radial sequence.** Raw data is recorded with twice the offset values in *y*-direction than in *x* (excitation direction) with pulsed excitation. The absolute values of $\tilde{u}(\boldsymbol{r}, t)$ are summed up for each offset value to represent an integrated signal intensity (ISI) plot. To generate a sequence, a virtual FOV is shifted from positive to negative *y*-offsets, mimicking an orthogonal shifting field. Simultaneously, it is continuously rotated to perform a rotation of the fields or the object. To avoid inverse crime, due to reusing the same dataset over and over, noise is added to mask repeating measurement background noise and prevent correlation from within the sequence. The sequenced data is fast Fourier transformed and TF corrected to yield a system matrix, which is used to reconstruct images or create phantom spectra. Refer to Table I for specific sequence parameter choices, excitation waveform and other measurement details.

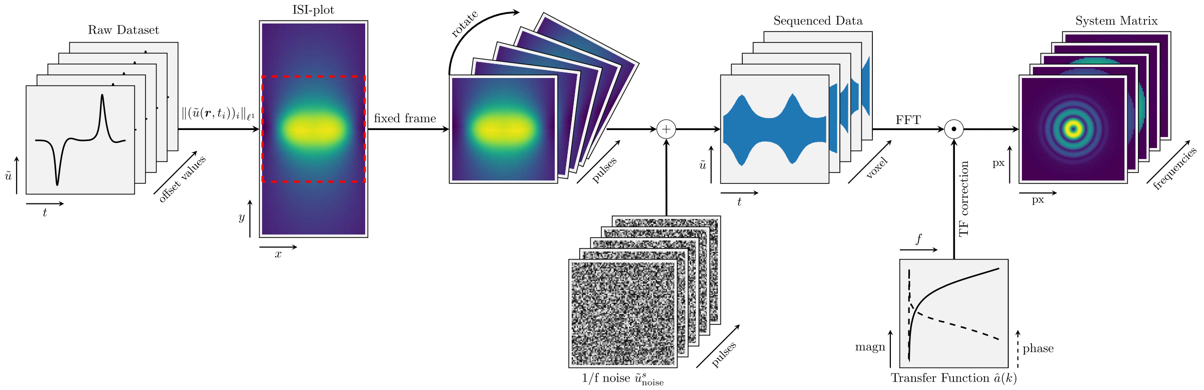

Fig. 4. **Sequence generation diagram of the radial sequence.** Similar to the shift-radial sequence, the radial sequence is a simplified version, without the FOV shifting component. A rectangular subset is solely rotated, as proposed by Knopp *et al.* in [31]. In contrast to Fig. 3 and Fig. 5, the ISI-plot shows the response to a sinusoidal excitation waveform (in *x*-direction). Otherwise, the system matrix is generated likewise, by noise addition, FFT and TF correction. Refer to Table I for specific sequence parameter choices, excitation waveform and other measurement details.

oversampling of raw data along the y-direction with ±40 mT than in x-direction with ±20 mT, to produce the necessary oversampling for the shift (see Fig. 3). A high excitation amplitude of 15 mT is chosen, which corresponds to a wide PSF spanning almost the entire FOV. An LFR sequence controls the virtual FOV shift over the raw data to produce a shifted dataset with a given number of pulses per shift J_{PpS}. These are rotated with a given number of shifts per rotation J_{SpR} with respect to their center. Subsequently, shifts and rotations are interweaved to generate a continuous acquisition of both in the time domain. In this work, $J_{\text{SpR}} = 32$ with $J_{\text{PpS}} = 31$ are chosen, amounting to $J = J_{\text{SpR}} \cdot (J_{\text{PpS}} \cdot 2 - 2) = 1920$ total periods. For each pulse the virtual FOV is shifted one step in y-direction, starting from -35 mT until $+35$ mT is covered, where the direction inverses without sampling the turning-point nor the start-end-point twice (15 mT amplitude of shifts, virtual FOV of 40×40 mT^2). This sequence is similar to sequences known from MPI-FFL encoding and Computed Tomography (CT) and restores the lost information caused by large amplitudes [32]. The trajectory is plotted in Fig. 6 (a). For a better understanding of the influence of the excitation waveform, this sequence is generated for both, a sinusoidal and a pulsed rectangular excitation.

b) Radial sequence: The radial sequence is an adaptation of the shift-radial sequence, which solely utilizes a rotation of the raw data, without the virtual FOV shift component. Hence, a square-shaped subset with ±20 mT offsets in x- and y-direction is rotated with a given number of pulses per rotation J_{PpR} around its center, imitating a rotating excitation as proposed in Knopp *et al.* [31]. The excitation amplitude is the same as the shift-radial sequence with 15 mT, but the waveform depicted in Fig. 4 differs, as the radial sequence is only generated on the base of sinusoidal raw data. The sequence trajectory is shown in Fig 6 (b).

c) Meander sequence: A Cartesian sequence is implemented with a discretization of 31 steps in a resolution of 1 mT per

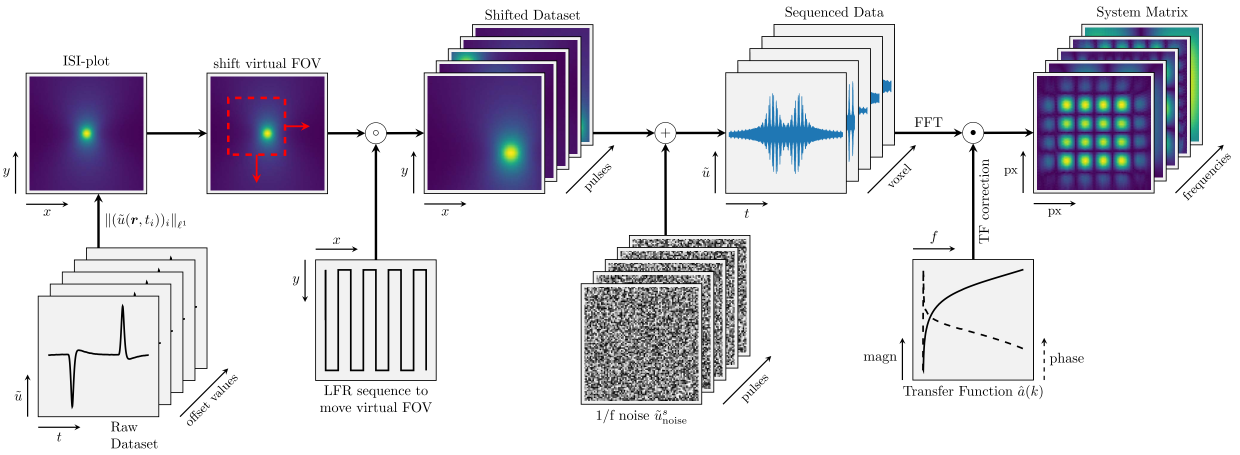

Fig. 5. **Sequence generation diagram of the meander sequence proposed in [23]**. Measured raw data of 3 mT amplitude, with offsets in two spatial dimension is over-sampled in order to be able to move a virtual FOV, which results in a smaller shifted dataset. The sequence name stems from the nature of this LFR movement and the excitation is in *x*-direction only. The system matrix is generated identically as for all other sequences, by noise addition, FFT and TF correction. Refer to Table I for specific parameter choices of the LFR sequence and other measurement details.

step in x- and y-direction, and is referred to as meander sequence due to its LFR movement. By over-scanning the required square-shaped FOV of ±20 mT, with a larger offset of ±40 mT, the initial measurement yields enough raw data to move the virtual FOV, as illustrated in Fig. 5. The virtual FOV is moved along the meandering sequence, resulting in a shifted dataset. The measurement data inside the shifted dataset has been moved along the trajectory and was sequentially appended to represent the particle response to the entire sequence. A version of the sequence is generated for each of the two drive field amplitudes, 3 mT and 15 mT (x-direction). The low excitation amplitude is chosen to be 3 mT, in a way to trade off SNR and spatial resolution as proposed by Tay et. al [23]. In order to keep the FOV boundaries identical between versions, the step resolution for 15 mT amplitude is reduced to 7/31 mT in x, as illustrated in Fig. 6 (d). Both sequences consist of 31 steps in x- and 31 steps in y-direction, tracing the same path backwards without sampling the turning-point nor the start-end-point twice, amounting to $J = 31 \cdot 31 \cdot 2 - 2 = 1920$ periods.

The sequence types differ in the shape of their FOV, depending on the fact if a rotation was applied. Rotating a rectangular dataset necessarily results in a circular sampled area (see Fig. 3 and Fig. 4, far right), whereas for the meander-sequence (Fig. 5) the FOV stays rectangular. To create common ground between different sequence types, the same time length to compare sequence types is chosen, as this reflects the acquisition time. For a generated sequence length of 129 ms at 14.88 kHz, this amounts to 1920 periods for each sequence in this work.

D. Phantoms

The intensity of the signal response of SPIONs scales linearly with the concentration of the tracer [1], [33]. Consequently, the system matrix signal based on the AWMPS needs to be scaled down. One option is to introduce a scaling factor α_s that scales the phantom concentration vector $\boldsymbol{c}_P \in [0,1]^N$ (N voxel), to a realistic value, in order to match the total iron mass within one voxel. α_s together with a noise addition from a real life receiver system, results in realistic signal spectra. In all undiluted tracer experiments, a targeted tracer concentration of $c_{\text{target}} = 5\ \text{mg}_{\text{Fe}}\,\text{mL}^{-1}$ was used throughout this work. The concentration vector $\boldsymbol{c}$, which is used to create the phantom spectrum voltage $\hat{\boldsymbol{u}}_P$ for reconstruction, is expressed by

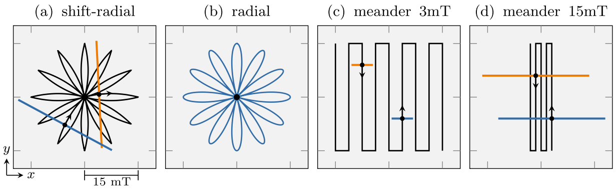

Fig. 6. **Sequence trajectory plot.** The black line typifies the focus-field trajectory of the LFR, as transformed by $\mathcal{T}(\boldsymbol{r},t)$. Orange and blue depict exemplary drive field excitations at individual time points, which then deflect the LFR from this trajectory. The length of these bars correlates with the excitation amplitude and ticks are drawn in 15 mT increments. One side length equals 40 mT. Type (b) is not exposed to any offsets. Type (c) and (d) have identical FOV boundaries. Image sizes and scales are consistent throughout this work. For demonstration purposes, the density of the trajectories is reduced.

$$\begin{aligned}\boldsymbol{c} &= \alpha_s\,\boldsymbol{c}_P\\ &= \frac{V_{\text{target}}\ c_{\text{target}}}{V_{\text{meas}}\ c_{\text{meas}}}\,\boldsymbol{c}_P\end{aligned} \tag{4}$$

where V_{meas} is the volume and c_{meas} the concentration of the measured delta sample in the AWMPS. An assumed linear gradient field $\boldsymbol{G}$, with $\det \boldsymbol{G} \neq 0$ in $\text{T}\,\text{m}^{-1}$, and a voxel grid vector $\boldsymbol{g}$ in mT with 3 dimensions, yield the target concentration V_{target} in

$$V_{\text{target}} = \prod_{i=1}^{3} \left|\boldsymbol{G}^{-1}\boldsymbol{g}\right|_i = 64\ \text{nL}, \quad \text{for}$$

$$\boldsymbol{G} = \begin{pmatrix}-1.25 & 0 & 0\\ 0 & -1.25 & 0\\ 0 & 0 & 2.5\end{pmatrix}, \quad \boldsymbol{g} = \begin{pmatrix}0.5\\ 0.5\\ 1\end{pmatrix} \tag{5}$$

where i denotes the i-th entry of the vector. This gradient field results in an exemplary scaling factor of $\alpha_\text{s} = 9.4 \cdot 10^{-4}$, for a volume of 20 µL and a concentration of 17 $\text{mg}_\text{Fe}\,\text{mL}^{-1}$ as described in Section III-B. Further experiments are performed with a lower phantom concentration $\boldsymbol{c}_\text{P}$ to create a dilution series for a sensitivity analysis of all sequences types. Due to α_s, the change in $\boldsymbol{m}$ contributed by a voxel with concentration $\boldsymbol{c}_\text{P}$ matches the real life magnetic moment change.

A second step involves a noise model to represent realistic MPI receiver noise during reconstruction. Real background noise measurements from a pre-clinical MPI scanner (*Bruker, Ettlingen, Germany*), utilizing an optimized 42 mm coil [30], are used to select a noise level of $n^r = 70 \cdot 10^{-15}\text{mA}^2$ for the highest frequency. Using a 1/f function to model the noise curve results in a higher noise for every frequency compared to the measured reference in [14], guaranteeing a realistic SNR scenario. The TF corrected noise level added during image reconstruction is

$$\hat{\boldsymbol{u}}^r_\text{noise} = \frac{n^r \zeta}{2\pi \;\, T_\text{f,max}} \boldsymbol{T} \;\; \in \mathbb{C}^K \tag{6}$$

with $\zeta \sim \mathcal{CN}(0, 1)$ a standard complex normal random variable with zero mean and variance of 1. $\boldsymbol{T} \in \mathbb{R}^K_+$ contains the period time for each of the K frequency components and $T_\text{f,max}$ is the period length of the highest frequency in the receive band. $\hat{\boldsymbol{u}}^r_\text{noise}$ will overlay the scaled phantom spectrum $\hat{\boldsymbol{u}}_\text{P}$, as visualized in Fig. 8, during the image reconstruction process. In Fig. 7, four phantoms are shown for original reference.

E. Image Reconstruction

Images are reconstructed using the iterative Kaczmarz method [34], which gives the calculated particle concentration $\boldsymbol{c} \in \mathbb{R}^N_+$ for N voxel, solving the linear system of equations

$$\hat{\boldsymbol{S}}\,\boldsymbol{c} = \hat{\boldsymbol{u}}_\text{SNR} \tag{7}$$

where $\hat{\boldsymbol{u}}_\text{SNR} \in \mathbb{C}^K$ is a filtered subset of the emulated complex phantom voltage $\hat{\boldsymbol{u}}_\text{P}$ with K frequency components and $\hat{\boldsymbol{S}} \in \mathbb{C}^{K\times N}$ is the system matrix in the frequency domain. For reconstruction the following least squares problem can be solved

$$\boldsymbol{c}^\lambda_\text{reco} = \underset{\boldsymbol{c}\in\mathbb{R}^N_+}{\text{argmin}} \left\| \hat{\boldsymbol{S}}\,\boldsymbol{c} - \hat{\boldsymbol{u}}_\text{SNR} \right\|_2^2 + \lambda \, \|\boldsymbol{c}\|_2^2 \tag{8}$$

where $\left\| \hat{\boldsymbol{S}}\,\boldsymbol{c} - \hat{\boldsymbol{u}}_\text{SNR} \right\|_2^2$ is the data discrepancy term and $\|\boldsymbol{c}\|_2^2$ is the penalization term used to dampen large oscillations in the solution. $\boldsymbol{c}^\lambda_\text{reco}$ is the solution of the concentration distribution, controlled by a relative regularization parameter $\lambda \in \mathbb{R}_+$, that blurs the image noise at the cost of spatial resolution. With increasing dilution, the SNR threshold is set higher and both, λ and the number of iterations, increase. Additionally, the SNR selection P_SNR is subjected to a minimal frequency threshold, acting as a high-pass, to filter out any signal before the first harmonic of the fundamental frequency. A reconstruction diagram is shown in Fig. 8, to visualize necessary steps. Handling noise amplification in images is described in detail in [35]. We note that the solution of (8) in practice leads to better spatial resolutions than the width of the derivative of the particle magnetization curve would predict [36].

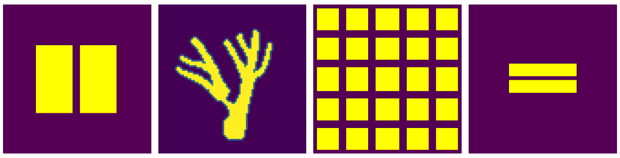

Fig. 7. **Phantoms used in this study.** Reference for original shape. Left to right: Gap phantom with 2.0 mT (1.6 mm) gap in *x*-direction, vessel phantom with stenosis in the left branch, large phantom to reveal borders of FOV and fine resolution phantom with 1.0 mT (0.8 mm) gap.

As this work contains emulated gradients only, distances in phantoms are best defined in mT. However, to give the reader a better classification of the results, the corresponding dimensions for a gradient as in (5) are given in brackets e.g. 2.0 mT (1.6 mm) in x- and y-direction. This same gradient is used for all emulations through-out this work. All phantoms are oriented in xy-plane. Resulting images are reconstructed with the low resolution system matrix $\hat{\boldsymbol{S}}_\text{LR}$, yielding an image resolution of 61 by 61 pixel, corresponding to a side length of 40.0 mT (24.4 mm). Assuming the gradient field from (5), the fine system matrix $\hat{\boldsymbol{S}}_\text{HR}$, that is used to constitute the phantom spectrum, accounts for an image resolution of $0.5\ \text{mT/pixel} \cdot (1.25\ \text{T/m})^{-1} = 0.4\ \text{mm/pixel}$. System matrices are denoised to reduce the impact of system matrix noise on the reconstructed image [37].

F. Implementation

Raw data measurements in the AWMPS are controlled by a system software implemented in the open source programming language *Julia* [38]. It controls the parameter sweep through the chosen x-offset range and gradually steps up the y-offset for each excitation combination. The raw data is stored in an extended version of the Magnetic Particle Imaging data format (MDF) [39] and the sequence is afterwards calculated within a custom simulation framework developed in *Julia*. System matrix reconstructions are based on the MPI reconstruction package developed in [40], accessible under [41].

IV. RESULTS

Results are summarized in two main figures with phantom image reconstructions, one focusing on sensitivity by means of a dilution series (Fig. 9), the other on resolution and FOV shapes (Fig. 10). Reconstruction parameters are individually determined to match the image noise across the different reconstructions.

Fig. 9 shows a dilution series of two phantoms to visually compare the results of different excitation waveforms, amplitudes and sequences, with an undiluted iron concentration of $\kappa_0 = 5\ \text{mg}_\text{Fe}\text{mL}^{-1}$. The left part of the figure depicts a simple two bar phantom (gap in x-direction), the right part a more intricate vessel phantom with a stenosis in the left branch (see Fig. 7 for originals). For undiluted reconstructions, the shift-radial sequences and the meander sequence with

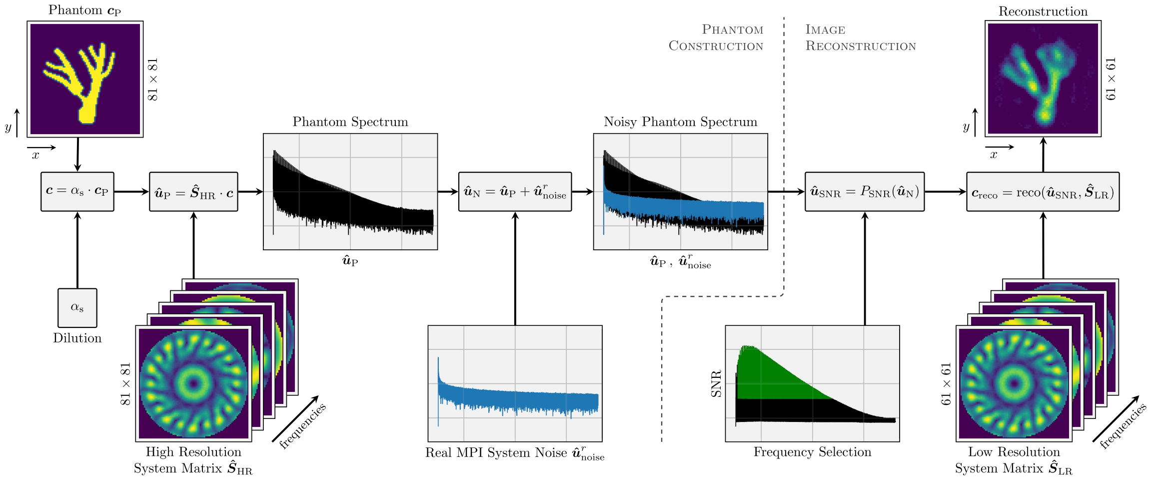

Fig. 8. **Diagram of the implemented reconstruction process.** A vessel phantom with a visible stenosis is scaled to represent a tracer distribution $\boldsymbol{c}$ with a concentration of 5 mg$_{\mathrm{Fe}}$ mL^{-1} and a selectable dilution. The high resolution system matrix $\hat{S}_{HR}$ multiplied by the phantom vector $\boldsymbol{c}$ results in the phantom spectrum $\hat{u}_P$, which is overlaid by a realistic measurement noise level $\hat{u}^r_{noise}$. After frequency selection (P_{SNR}), the low resolution matrix $\hat{S}_{LR}$ is used to reconstruct the image using the iterative Kaczmarz method with Tikhonov regularization. All images span 40 × 40 mT^2.

high excitation amplitude perform very similar, whereas the low amplitude meander sequence suffers from a low SNR. Fine structures are resolved independent of the excitation waveform. This effect becomes more visible with the intricacy of the vessel phantom on the right hand side in Fig. 9. In undiluted reconstructions of the radial sequence, significant blurring appears towards the edges of the FOV with the exception of a small region in the center, where resolution is excellent. At a dilution of 78 μg$_{\mathrm{Fe}}$mL^{-1} (1:64, κ_2), the pulsed 3 mT meander sequence starts to lose the ability to resolve any fine structures and for dilutions of 1.2 μg$_{\mathrm{Fe}}$mL^{-1} (1:4096, κ_3) it stops to resemble even the rough shape of the original phantom. However, the pulsed 15 mT meander sequence is able to display basic phantom features down to the highest dilution. The shift-radial sequence is able to depict phantom outlines of simple shapes at κ_3 for both, pulsed and sinusoidal excitation. The pulsed excitation for extremely high dilutions of 153 ng$_{\mathrm{Fe}}$mL^{-1} (1:32768, κ_4) seems to have a slight advantage over the sinusoidal excitation, being still able to marginally reconstruct a simple phantom whereas the sinusoidal excitation is entirely dominated by system noise. When comparing pulsed sequences with 15 mT amplitude, edges are traced more accurately by the pulsed shift-radial sequence than the meander sequence at dilution κ_3 for the left phantom (row 2 and 3). The sinusoidal radial sequence is able to resolve most structures at κ_2, especially around its center, however it becomes heavily distorted beyond κ_3.

In Fig. 10, the characteristic FOVs of all sequences are visualized using a phantom that extends over the full image width (40 mT). For the meander sequence, the FOV spans to the out-most LFR boundaries (36 × 30 mT^2). Shift-radial is confined with full resolution to the radius of its shift amplitude (inner circle, 15 mT), although this extends with $\sqrt{2}$ to a second region of slightly degraded reconstruction ability (dashed, white line). The shift in excitation, which can be described as a pulse line, results in a rectangular shaped sampling area. As this rectangle is rotated, only a circle with the diameter of one side length is fully covered. As shown in Fig. 10, the area in between the inner circle with diameter of a side length and a circle with a diameter of a diagonal length, is only occasionally covered by the corner of the rectangular sampling area. Thus, the resolution decreases as sampling becomes sparse. The radial sequence shows a very fine resolution in the center of the FOV, which deteriorates continuously with increasing radius. As the excitation is rotated without shifting, the center of the FOV is sampled by every pulse, which in turn results in a fine local resolution. This comes with the drawback of losing precision towards the edges of the FOV. A bar-phantom with a 1.0 mT (0.8 mm) gap in y-direction is shown in the center row of Fig. 10, with the associated intensity profile over y in the bottom row. An average of three pixel left and right of the center line is taken to calculate the intensity plot. The reconstruction based on the meander sequence is not able to resolve the two bars in both cases, whereas shift-radial and radial sequences are able to do so. This can be explained by the limitation of Cartesian sequences to be an-isotropic in their nature, as the excitation is oriented solely in one direction. In this work, x is chosen for excitation and therefore a better resolution in x is obtained than in y, as also apparent in the an-isotropic FOV plot in the top row for the meander sequence, independent of using small or large amplitude.

In Fig. 11 the impact of changing a sequence parameter is shown by comparing shift-radial sequences with different trajectory densities. On the left, the identical system matrix that was used throughout this work for sinusoidal shift-radial reconstructions with $J_{\mathrm{SpR}} = 32$ shifts per rotation was implemented. On the right side, a sequence was generated with $J_{\mathrm{SpR}} = 120$ that has 7200 periods instead of 1920. All other parameters and reconstructions are identical. Results indicate that for a good representation of edges and corners a high density is advantageous.

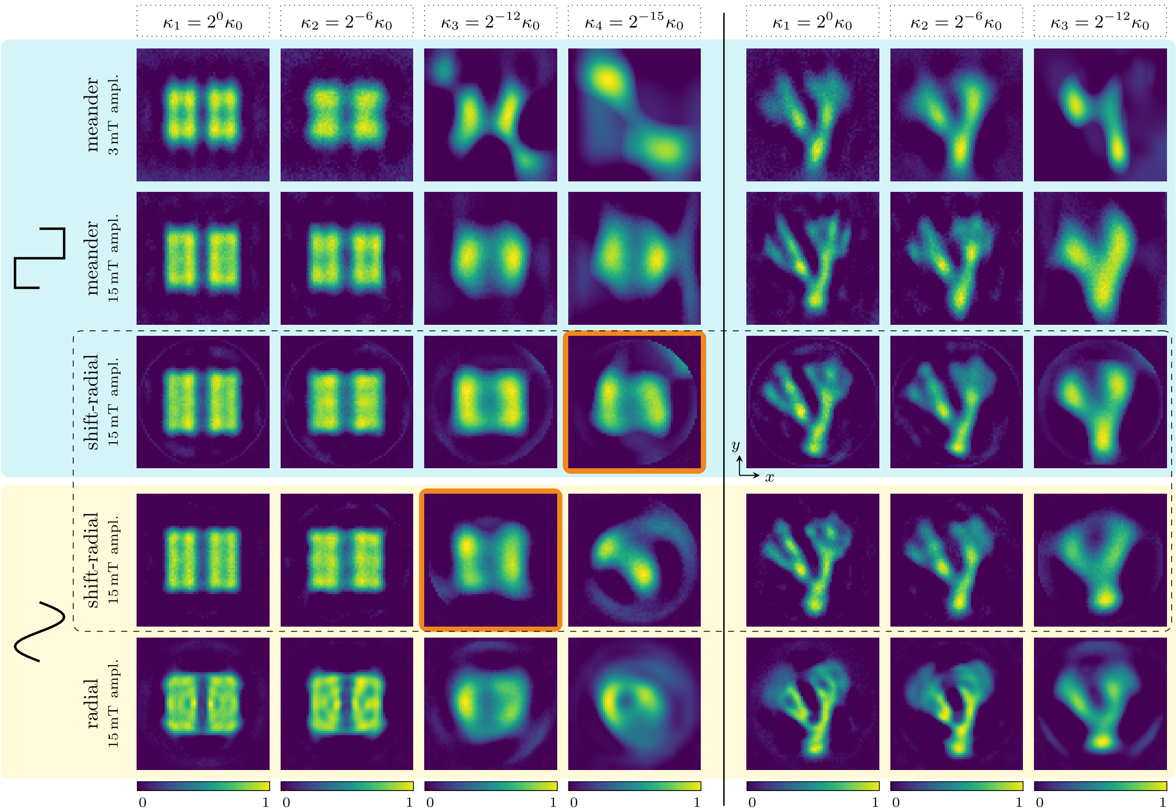

Fig. 9. **Dilution series emulation for two excitation waveforms and three different sequence types.** Iron concentration κ_0 of 5 mg$_{\text{Fe}}$ mL^{-1}, which is diluted from left to right, for two different phantoms. On the left, the phantom consists of two rectangles with a gap of 2.0 mT (1.6 mm) in x-direction, whereas the right side depicts a vessel phantom with a stenosis towards the left branch (originals in Fig. 7). Reconstruction parameters are individually determined, to yield comparable noise in the image domain. System matrices are denoised and the intensity is normalized to 1 within each image. Highlighted in orange are reconstructions of similar quality, produced by the identical sequence but differing in excitation waveform and dilution. All images span 40 × 40 mT^2 (24.4 × 24.4 mm^2), sequence trajectories are shown to scale in Fig. 6.

In a final result in Fig. 12, the effect that phase information from within our measured data has on resolution, is isolated by creating an immobile sequence without any shifted or rotated components in the trajectory. This can be done by setting the shift amplitude and step resolution to zero and the repetitions to 1920 periods, so the time length is identical to all other sequences. The lack of any focus-field movement implies that the LFR is solely moved by the excitation waveform along a single line in x, resulting in a 30 mT FOV line (dashed, white line). Shown in Fig. 12 are reconstructions based on pulsed and sinusoidal data, which are both capable of restoring a simple pattern in the FOV. The elliptic outline of this area is shaped similar to the outline of the ISI plots of raw data in Fig. 3 and 4 for pulsed and sinusoidal data respectively.

V. DISCUSSION

By combining a shifting focus field with a rotating drive field of large amplitude, the proposed shift-radial sequence overcomes previous limitations in amplitude and acquisition time for pulsed rectangular excitations. Shift-radial sequences provide an alternative to Cartesian sampling schemes, due to their ability to resolve 1.0 mT gaps (0.8 mm for a gradient of $(-1.25,\ -1.25,\ 2.5)$ Tm^{-1}) and their spatially isotropic sampling trajectory. Furthermore, pulsed excitation seems to bear a slight advantage in sensitivity compared to sinusoidal excitation for the identical shift-radial sequence, if the two images marked in orange in Fig. 9 are considered reconstructions of the same quality. Note that a factor of 10^3 distinguishes column 3 from 4. The basis of this advantage lies in the simultaneous response of many spatial positions, resulting in a better SNR. The magnitude of this advantage becomes visible at higher dilutions only, and it depends on the phantom or on the medical application. The more homogeneous the distribution of SPIONs (e.g. perfusion imaging), the higher seems the advantage of pulsed excitation in contrast to the accumulation of tracer material in a bulk (e.g. stem cell tracking).

The drive field frequency was chosen to be 14.88 kHz as this is the upper limitation of the amplifier to produce a clean waveform with rise-times around 3 µs. The relaxation behaviour of the used tracer (Perimag, Fig. 2) allows the use of 14.88 kHz in this work, due to its quick relaxation. Two points need to be clarified regarding this choice: First, tracers need to be asserted individually and measurement parameters such as frequency and rise time would need to be adapted for larger particles to match their relaxation. Tay *et al.* proposed the pulsed excitation scheme for large particles beyond a specific size of about 28 nm [23], [42]

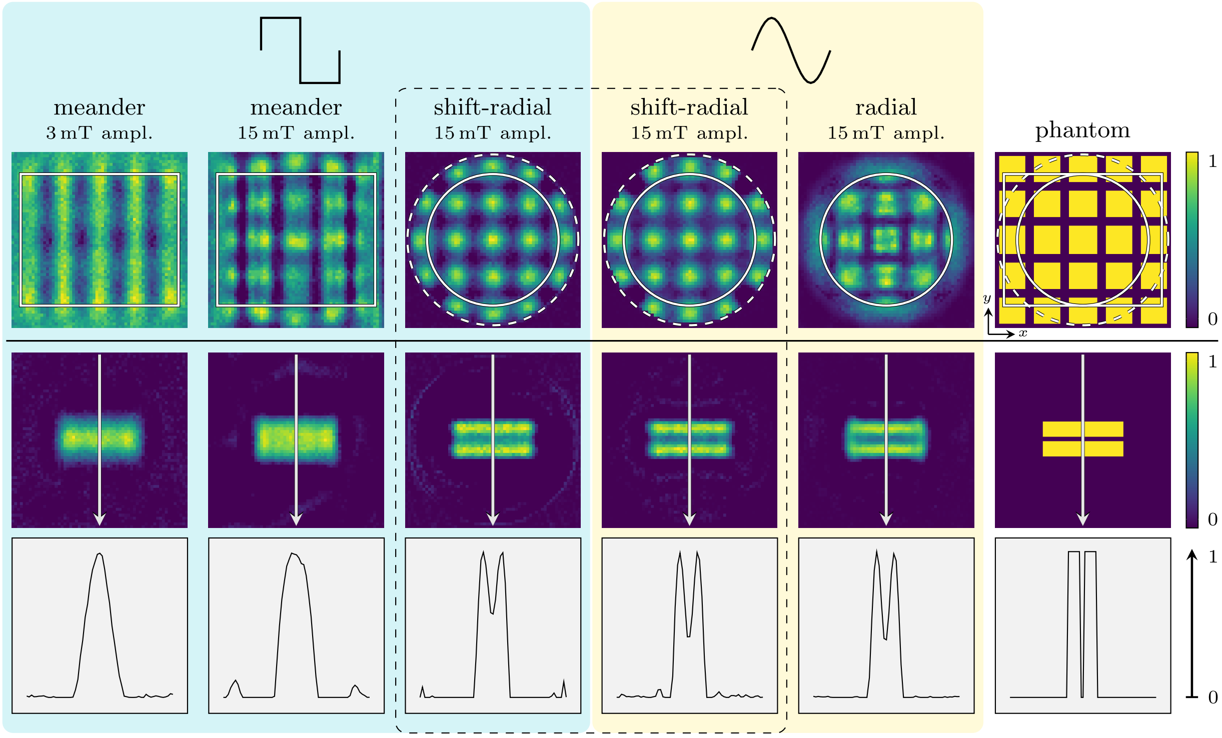

Fig. 10. **Resolution simulation and FOV comparison.** The top row compares the reconstruction of a 5 by 5 squares phantom, separated by 2.0 mT (1.6 mm) gaps to distinguish the boundaries of the respective FOVs (white lines). The phantom is shown in the rightmost column for reference. The shape of the FOV depends on the sequence, resulting in a circular FOV for radial sequence types. In the center row, a phantom with a 1.0 mT (0.8 mm) gap in *y*-direction is shown, with the corresponding intensity profile in the bottom row. The iron concentration is 5 $\mathrm{mg_{Fe}\,mL^{-1}}$ each and the images span 40 × 40 $\mathrm{mT^2}$ (24.4 × 24.4 $\mathrm{mm^2}$).

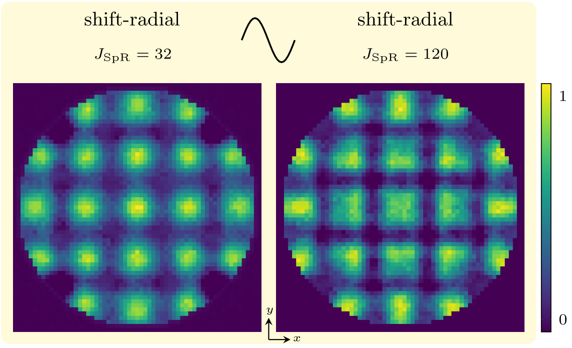

Fig. 11. **Trajectory density comparison.** The image to the left stems from the same system matrix for the sinusoidal shift-radial sequence throughout this work, with the sequence parameter of $J_{\mathrm{SpR}} = 32$ shifts per rotation. The image to the right has a denser trajectory with $J_{\mathrm{SpR}} = 120$, consequently the sequence is longer with 7200 periods instead of 1920. Image reconstruction parameters are identical.

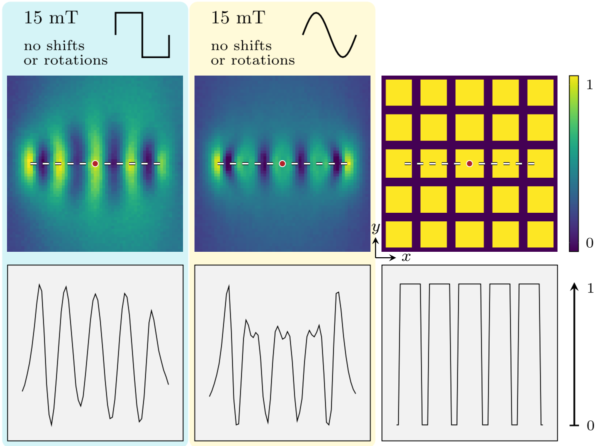

Fig. 12. **Comparison of pulsed and sinusoidal data without a sequence trajectory.** In order to reveal the effect of information encoded within the phase of the measured raw data for different excitation waveforms, an immobile sequence is generated that does not use shifts or rotations of any kind (also 1920 periods). Consequently, the LFR is only moved by the drive field (in *x*) and the resulting FOV is a single line with 15 mT amplitude (white, dashed). The images span 40 × 40 $\mathrm{mT^2}$. Below, the intensity profile along this line in *x* is plotted.

to circumvent limiting relaxation effects and improve resolution. The so called "relaxation wall" blurs the MPI image, as particles do not follow the Langevin model [22], and the optimum predicted resolution cannot be achieved [43], [44]. One precondition in order to reach optimum resolution for any particle system is to ensure that the particle magnetization is sufficiently saturated to generate a strong signal, which sets an upper limit to the excitation frequency. The second point is that due to the quick relaxation of Perimag and the sigmoid-shaped excitation, which differs from an idealized rectangle, a small time-shift is observable in the raw data, as shown in Fig. 2 on the left. Therefore, the phase information of the signal is distinguishable within the measured raw data, despite our assumption that all phase information is lost by pulsed excitation. Due to this fact, the following argument needs to be considered: Results in Fig. 9, 10 and 11 show the combined effect of pulsed excitation including phase and the effect of the sequence trajectory for system matrix reconstruction. A separation of individual contributions is not possible with our measurement data. Ultimately, system matrix reconstruction of pulsed sequences with high amplitude combine the benefit in the SNR and profit from any phase information within the particle response. This holds true for meander as well as shift-radial sequences and explains why a meander sequence with 15 mT amplitude performs similar compared to the pulsed shift-radial sequence (Fig. 9, rows 2 and 3) for our measurement data and using system matrix reconstruction. Shift-radial sequences profit from phase information, but they would be capable to restore basic phantom features even without any phase information, similar to a Radon transform [32]. For an ideal rectangular excitation (no phase discrimination) Cartesian meander sequences depend on a small excitation amplitude for achieving high resolution. For this reason a low amplitude (1 mT) was chosen in previous works [23] to guarantee a small sampling kernel and sustain high resolution, with the draw back of a low SNR.

The sole benefit due to phase information for pulsed and sinusoidal raw data can be identified in Fig. 12. Surprisingly, basic phantom features are resolved by the reconstruction based on pulsed raw data, which can only be attributed to phase information as there is no additional information provided by means of a sequence trajectory. Edges of the squares along the white FOV line are slightly better shaped for sinusoidal data, when the intensity profiles along the x-center line are compared. However, the pulsed reconstruction clearly separates all 5 squares, relying only on the small time-shift that is induced in the raw signal, as shown in Fig. 2 on the left. If this holds true for larger particle systems remains to be proven. As a consequence, system matrix reconstruction may be able to sustain basic resolution even for large single-core particles, if the Nyquist criterion is not violated during waveform slopes (rise-time). Resolution improvements of pulsed excitation compared to sinusoidal excitation were neither observed nor expected for the given tracer and measurement parameters. However, the proposed shift-radial imaging sequence and reconstruction method does not make any assumptions on the particle size and thus we predict that it generalizes to different relaxations and larger particles, if individual particle dynamics are heeded and an equilibrium state is reached.

Concerning our implemented methods, the noise added during sequence generation, as well as the noise added during image reconstruction, are overestimated and higher than in a well designed scanner system. While rectangular excitation can be superior for large particles, the results in this work could not assert a clear advantage for standard MPI tracers with a size lower than the relaxation wall. In fact, sinusoidal excitation seems superior at high concentrations, as it is less prone to artifacts at the edges of the FOV. The signal intensity for each spatial position is linked to the derivative of the excitation field at the time the LFR passes [45]. For sinusoidal excitation this leads to an attenuation of the signal at the FOV border, which is lower for pulsed sequences. This attenuation may help avoiding artifacts at the hard cut off at the end of the circular FOV for the presented radial-shift sequences. Sinusoidal drive fields performed equally in almost all regards throughout this study, hence the effort for a pulsed non-resonant scanner may only be reasonable for larger particle systems. Further research on the application of the proposed method to large single-core particles has to be done. Improvements may be limited by peripheral nerve stimulation and the specific absorption rate, reducing the advantage of high drive field amplitudes for in-vivo imaging in large animals or humans. Also, the optimum frequency-amplitude combination for shift-radial and the choice of sequence parameters to trade off resolution and acquisition speed need to be investigated.

Although rectangular excitation patterns did not outperform the sinusoidal ones for medium-sized MPI particles in this work, they certainly have the potential to improve MPI not only for large particles. By allowing to vary the excitation frequency as an adjustable hardware parameter, one can tailor the excitation pattern to the currently used particle system, giving maximum flexibility. Potentially, this allows optimizing the contrast in multi-contrast MPI applications, e.g. for discriminating different particle sizes [17].

REFERENCES

[1] B. Gleich and J. Weizenecker, “Tomographic imaging using the nonlinear response of magnetic particles,” *Nature*, vol. 435, no. 7046, pp. 1214–1217, 2005.

[2] N. Panagiotopoulos *et al.*, “Magnetic particle imaging: Current developments and future directions,” *Int. J. Nanomed.*, vol. 10, pp. 3097–3114, Apr. 2015.

[3] T. Knopp *et al.*, “Weighted iterative reconstruction for magnetic particle imaging,” *Phys. Med. Biol.*, vol. 55, no. 6, pp. 1577–1589, 2010.

[4] M. Graeser, T. Knopp, M. Grüttner, T. F. Sattel, and T. M. Buzug, “Analog receive signal processing for magnetic particle imaging,” *Med. Phys.*, vol. 40, no. 4, p. 42303, 2013.

[5] P. Vogel *et al.*, “Micro-traveling wave magnetic particle imaging—Sub-millimeter resolution with optimized tracer LS-008,” *IEEE Trans. Magn.*, vol. 55, no. 10, pp. 1–7, Oct. 2019.

[6] J. Weizenecker, B. Gleich, J. Rahmer, H. Dahnke, and J. Borgert, “Three-dimensional real-time *in vivo* magnetic particle imaging,” *Phys. Med. Biol.*, vol. 54, no. 5, pp. L1–L10, 2009.

[7] M. Graeser *et al.*, “Design of a head coil for high resolution mouse brain perfusion imaging using magnetic particle imaging,” *Phys. Med. Biol.*, vol. 65, no. 23, Dec. 2020, Art. no. 235007, doi: 10.1088/1361-6560/abc09e.

[8] M. Graeser *et al.*, “Human-sized magnetic particle imaging for brain applications,” *Nature Commun.*, vol. 10, no. 1, Dec. 2019, Art. no. 1936.

[9] E. E. Mason, C. Z. Cooley, S. F. Cauley, M. A. Griswold, S. M. Conolly, and L. L. Wald, “Design analysis of an MPI human functional brain scanner,” *Int. J. Magn. Part. Imag.*, vol. 3, no. 1, 2017, Art. no. 1703008.

[10] J. Rahmer, C. Stehning, and B. Gleich, “Remote magnetic actuation using a clinical scale system,” *PLoS ONE*, vol. 13, no. 3, Mar. 2018, Art. no. e0193546.

[11] J. Haegele *et al.*, “Toward cardiovascular interventions guided by magnetic particle imaging: First instrument characterization,” *Magn. Reson. Med.*, vol. 69, no. 6, pp. 1761–1767, Jun. 2013.

[12] F. Wegner *et al.*, “Magnetic particle imaging: Artifact-free metallic stent lumen imaging in a phantom study,” *CardioVascular Intervent. Radiol.*, vol. 43, no. 2, pp. 331–338, Oct. 2019.

[13] P. Szwargulski *et al.*, “Monitoring intracranial cerebral hemorrhage using multicontrast real-time magnetic particle imaging,” *ACS Nano*, vol. 14, no. 10, pp. 13913–13923, Oct. 2020, doi: 10.1021/acsnano.0c06326.

[14] M. Graeser *et al.*, “Design of a head coil for high resolution mouse brain perfusion imaging using magnetic particle imaging,” *Phys. Med. Biol.*, vol. 65, no. 23, Dec. 2020, Art. no. 235007, doi: 10.1088/1361-6560/abc09e.

[15] P. Ludewig *et al.*, "Magnetic particle imaging for real-time perfusion imaging in acute stroke," *ACS Nano*, vol. 11, no. 10, pp. 10480–10488, Oct. 2017.

[16] J. Rahmer, A. Halkola, B. Gleich, I. Schmale, and J. Borgert, "First experimental evidence of the feasibility of multi-color magnetic particle imaging," *Phys. Med. Biol.*, vol. 60, no. 5, p. 1775, 2015.

[17] C. Shasha, E. Teeman, K. M. Krishnan, P. Szwargulski, T. Knopp, and M. Möddel, "Discriminating nanoparticle core size using multi-contrast MPI," *Phys. Med. Biol.*, vol. 64, no. 7, p. 74001, 2019.

[18] C. Stehning, B. Gleich, and J. Rahmer, "Simultaneous magnetic particle imaging (MPI) and temperature mapping using multi-color MPI," *Int. J. Magn. Imag.*, vol. 2, no. 2, pp. 1–6, Dec. 2016.

[19] M. Möddel, C. Meins, J. Dieckhoff, and T. Knopp, "Viscosity quantification using multi-contrast magnetic particle imaging," *New J. Phys.*, vol. 20, no. 8, p. 83001, Aug. 2018.

[20] M. Möddel, F. Griese, T. Kluth, and T. Knopp, "Estimating orientation using multi-contrast MPI," *Int. J. Magn. Part. Imag.*, vol. 6, no. 2, pp. 1–3, 2020.

[21] T. Viereck, C. Kuhlmann, S. Draack, M. Schilling, and F. Ludwig, "Dual-frequency magnetic particle imaging of the Brownian particle contribution," *J. Magn. Magn. Mater*, vol. 427, pp. 156–161, Apr. 2017. [Online]. Available: http://www.sciencedirect.com/science/article/pii/S0304885316329031

[22] Z. W. Tay, D. W. Hensley, E. C. Vreeland, B. Zheng, and S. M. Conolly, "The relaxation wall: Experimental limits to improving MPI spatial resolution by increasing nanoparticle core size," *Biomed. Phys. Eng. Exp.*, vol. 3, no. 3, May 2017, Art. no. 035003, doi: 10.1088/2057-1976/aa6ab6.

[23] Z. W. Tay *et al.*, "Pulsed excitation in magnetic particle imaging," *IEEE Trans. Med. Imag.*, vol. 38, no. 10, pp. 2389–2399, Oct. 2019.

[24] Z. W. Tay, P. W. Goodwill, D. W. Hensley, L. A. Taylor, B. Zheng, and S. M. Conolly, "A high-throughput, arbitrary-waveform, MPI spectrometer and relaxometer for comprehensive magnetic particle optimization and characterization," *Sci. Rep.*, vol. 6, no. 1, Sep. 2016, Art. no. 34180.

[25] D. Pantke, N. Holle, A. Mogarkar, M. Straub, and V. Schulz, "Multifrequency magnetic particle imaging enabled by a combined passive and active drive field feed-through compensation approach," *Med. Phys.*, vol. 46, no. 9, pp. 4077–4086, Jul. 2019, doi: 10.1002/mp.13650.

[26] C. B. Top, "An arbitrary waveform magnetic nanoparticle relaxometer with an asymmetrical three-section gradiometric receive coil," *TURKISH J. Electr. Eng. Comput. Sci.*, vol. 28, no. 3, pp. 1344–1354, May 2020.

[27] A. von Gladiss, M. Graeser, P. Szwargulski, T. Knopp, and T. M. Buzug, "Hybrid system calibration for multidimensional magnetic particle imaging," *Phys. Med. Biol.*, vol. 62, no. 9, pp. 3392–3406, Apr. 2017.

[28] A. von Gladiss, M. Graeser, A. Behrends, X. Chen, and T. M. Buzug, "Efficient hybrid 3D system calibration for magnetic particle imaging systems using a dedicated device," *Sci. Rep.*, vol. 10, no. 1, pp. 1–12, Oct. 2020.

[29] T. Knopp *et al.*, "Model-based reconstruction for magnetic particle imaging," *IEEE Trans. Med. Imag.*, vol. 29, no. 1, pp. 12–18, May 2010.

[30] M. Graeser *et al.*, "Towards picogram detection of superparamagnetic iron-oxide particles using a gradiometric receive coil," *Sci. Rep.*, vol. 7, no. 1, p. 6872, Jul. 2017.

[31] T. Knopp *et al.*, "Trajectory analysis for magnetic particle imaging," *Phys. Med. Biol.*, vol. 54, no. 2, pp. 385–397, Dec. 2008.

[32] T. Knopp, M. Erbe, T. F. Sattel, S. Biederer, and T. M. Buzug, "A Fourier slice theorem for magnetic particle imaging using a field-free line," *Inverse Problems*, vol. 27, no. 9, p. 95004, 2011.

[33] K. Lu, P. W. Goodwill, E. U. Saritas, B. Zheng, and S. M. Conolly, "Linearity and shift invariance for quantitative magnetic particle imaging," *IEEE Trans. Med. Imag.*, vol. 32, no. 9, pp. 1565–1575, Sep. 2013.

[34] S. Kaczmarz, "Angenäherte Auflösung von systemen linearer Gleichungen," *Bull. Int. Academie Polonaise Sci. et des Lettres*, vol. 35, pp. 355–357, Oct. 1937.

[35] M. Boberg, N. Gdaniec, P. Szwargulski, F. Werner, M. Möddel, and T. Knopp, "Simultaneous imaging of widely differing particle concentrations in MPI: Problem statement and algorithmic proposal for improvement," *Phys. Med. Biol.*, vol. 66, no. 9, Apr. 2021, Art. no. 095004, doi: 10.1088/1361-6560/abf202.

[36] T. Knopp, S. Biederer, T. F. Sattel, M. Erbe, and T. M. Buzug, "Prediction of the spatial resolution of magnetic particle imaging using the modulation transfer function of the imaging process," *IEEE Trans. Med. Imag.*, vol. 30, no. 6, pp. 1284–1292, Jun. 2011.

[37] A. Weber, J. Weizenecker, U. Heinen, M. Heidenreich, and T. M. Buzug, "Reconstruction enhancement by denoising the magnetic particle imaging system matrix using frequency domain filter," *IEEE Trans. Magn.*, vol. 51, no. 2, pp. 1–5, Feb. 2015.

[38] J. Bezanson, A. Edelman, S. Karpinski, and V. B. Shah, "Julia: A fresh approach to numerical computing," *SIAM Rev.*, vol. 59, no. 1, pp. 65–98, 2017.

[39] T. Knopp *et al.*, "MDF: Magnetic particle imaging data format," 2016, p. 9, *arXiv:1602.06072*.

[40] T. Knopp, P. Szwargulski, F. Griese, M. Grosser, M. Boberg, and M. Möddel, "MPIReco.jl: Julia package for image reconstruction in MPI," *Int. J. Magn. Part. Imag.*, vol. 5, no. 1, 2019, Art. no. 1907001.

[41] *MPIReco.jl: Julia Package for Image Reconstruction in MPI*. Accessed: Jan. 10, 2021. [Online]. Available: https://github.com/MagneticParticleImaging/MPIReco.jl.git

[42] C. Shasha, E. Teeman, and K. M. Krishnan, "Nanoparticle core size optimization for magnetic particle imaging," *Biomed. Phys. Eng. Exp.*, vol. 5, no. 5, pp. 1548–1551, 2019.

[43] R. M. Ferguson, K. R. Minard, and K. M. Krishnan, "Optimization of nanoparticle core size for magnetic particle imaging," *J. Magn. Magn. Mater.*, vol. 321, no. 10, pp. 1548–1551, May 2009, doi: 10.1016/j.jmmm.2009.02.083.

[44] J. Weizenecker, B. Gleich, J. Rahmer, and J. Borgert, "Micro-magnetic simulation study on the magnetic particle imaging performance of anisotropic mono-domain particles," *Phys. Med. Biol.*, vol. 57, no. 22, pp. 7317–7327, Nov. 2012.

[45] P. W. Goodwill and S. M. Conolly, "The X-space formulation of the magnetic particle imaging process: 1-D signal, resolution, bandwidth, SNR, SAR, and magnetostimulation," *IEEE Trans. Med. Imag.*, vol. 29, no. 11, pp. 1851–1859, Nov. 2010.

6

Resonant Inductive Coupling Network for Human-Sized Magnetic Particle Imaging

Balancing safety considerations, performance and power consumption, this work goes into the details of design decisions and optimization of an ICN, as well as multi-channel decoupling in MPI [O2]. Two devices have been built and integrated into the human-sized head scanner [O3]. The underlying theory, the simulation process and the conceptualized design are presented in this chapter. The provided insights are not limited to this specific use case and might improve other application that require highly linear air-core transformers. It should be noted that the mutual induction L_{M} is denoted with M within [O2].

Parts of this chapter were presented at the IWMPI 2024 conference in Switzerland [O11].

6.1 AIP - Review of Scientific Instruments

Manuscript received December 20, 2023.
Revised March 1, 2024.
Accepted March 7, 2024.

DOI: 10.1063/5.0192784

Editor's Pick (EP) and featured as the front cover of Vol. 95, Issue 4, April 2024.

Review of
Scientific Instruments

ARTICLE

pubs.aip.org/aip/rsi

Resonant inductive coupling network for human-sized magnetic particle imaging

Cite as: Rev. Sci. Instrum. **95**, 044701 (2024); doi: 10.1063/5.0192784
Submitted: 20 December 2023 • Accepted: 7 March 2024 •
Published Online: 1 April 2024

View Online Export Citation CrossMark

Fabian Mohn,[1,2,a)] Fynn Förger,[1,2] Florian Thieben,[1,2] Martin Möddel,[1,2] Ingo Schmale,[3] Tobias Knopp,[1,2,4] and Matthias Graeser[4,5]

AFFILIATIONS

[1] Institute for Biomedical Imaging, Hamburg University of Technology, 21073 Hamburg, Germany
[2] Section for Biomedical Imaging, University Medical Center Hamburg-Eppendorf, 20251 Hamburg, Germany
[3] Philips GmbH Innovative Technologies, Research Laboratories, 22335 Hamburg, Germany
[4] Fraunhofer Research Institution for Individualized and Cell-based Medical Engineering, IMTE, 23562 Lübeck, Germany
[5] Institute of Medical Engineering, University of Lübeck, 23562 Lübeck, Germany

[a)] Author to whom correspondence should be addressed: fabian.mohn@tuhh.de

ABSTRACT

In magnetic particle imaging, a field-free region is maneuvered throughout the field of view using a time-varying magnetic field known as the drive-field. Human-sized systems operate the drive-field in the kHz range and generate it by utilizing strong currents that can rise to the kA range within a coil called the drive field generator. Matching and tuning between a power amplifier, a band-pass filter, and the drive-field generator is required. Here, for reasons of safety in future human scanners, a symmetrical topology and a transformer called an inductive coupling network are used. Our primary objectives are to achieve floating potentials to ensure patient safety while attaining high linearity and high gain for the resonant transformer. We present a novel systematic approach to the design of a loss-optimized resonant toroid with a D-shaped cross section, employing segmentation to adjust the inductance-to-resistance ratio while maintaining a constant quality factor. Simultaneously, we derive a specific matching condition for a symmetric transmit–receive circuit for magnetic particle imaging. The chosen setup filters the fundamental frequency and allows simultaneous signal transmission and reception. In addition, the decoupling of multiple drive field channels is discussed, and the primary side of the transformer is evaluated for maximum coupling and minimum stray field. Two prototypes were constructed, measured, decoupled, and compared to the derived theory and method-of-moment based simulations.

I. INTRODUCTION

Medical imaging modalities such as magnetic particle imaging (MPI) and magnetic resonance imaging (MRI) rely on alternating current to generate strong radio-frequency fields that form the backbone of signal generation and acquisition.[1,2] In the context of MPI, the frequency of the so called drive field does not depend on the Larmor precession of hydrogen atoms, nor is it correlated with a static B_0 field, as in MRI. The choice of this frequency is flexible, with the proviso that it should be above the human audible range but below frequencies where wave propagation effects begin to affect signal detection and below the limits for energy deployment due to the tissue's specific absorption rate (SAR).[3,4] Typically, this frequency falls in the range of 20–160 kHz,[3,5,6] where lower frequencies tend to cause more peripheral nerve stimulation (PNS).[7] In addition, the best non-linear signal response of the required magnetic nanoparticles (MNPs) that provide the image contrast in MPI falls into this range, depending on the particle's anisotropy.[8] Currents for a human torso system reach the kA range,[9,10] whereas head-sized systems require around 300–500 A.[11] While it is possible to perform MPI with non-sinusoidal excitation waveforms,[12,13] the benefit of using sinusoidal excitation lies in the ability to implement resonators such as passive filters. This study focuses primarily on MPI, while the basic concept has broader applicability to similar circuits and other frequencies. Such circuits can be found in the context of inductively coupled wireless power transmission,[14–17] power converters,[18,19] band-pass filters,[20–23] or other applications requiring high linearity and large currents. A prominent challenge in this context is the formulation of a resonant transformer, i.e., the primary side forms a resonance with the band-pass filter output stage, and the secondary side of the transformer is part of a high quality factor (Q) resonant transmit–receive circuit called the high current resonator (HCR).

Our purpose for the resonant transformer, referred to as the inductive coupling network (ICN), is to obtain a differential voltage system and a safe operating voltage. Ground loops and long, high-current cables can introduce undesired harmonics or disturbances into the received spectrum, i.e., induced by eddy currents in non-linear components such as unsoldered joints (screws). These distortions can dominate important particle harmonics, or sidebands, that are essential to the imaging process.[10,24] A differential design with balanced filters avoids a global ground node and is less susceptible to interference and noise.[25] Another strong advantage of a differential setup is floating signals with respect to the patient under examination, who is always capacitively coupled to the ground. A single-ended transmission chain entails the danger for humans if they come into contact with any single point in the system. As MPI systems strive for human trials,[6,11,26,27] this safety aspect cannot be ignored. Furthermore, reducing voltage levels in proximity to the patient requires a low inductance DFG, which in turn requires large currents to maintain the same field specifications.[9,11]

In this work, we design and implement a resonant toroidal inductive coupling network that encompasses safety concerns and incorporates a strictly linear and loss-optimized design. We elaborate on our design decisions and weigh different conditions and restrictions to present a new approach to finding suitable parameter choices, i.e., for inductors, cross section shape, parallel segments, gain, and dimensions. Our reasoning is intended to be transferable to other transformers under similar constraints using resonant loads for applications beyond medical imaging. Furthermore, we consider crosstalk by channel decoupling between multiple drive-field channels that each use an individual ICN and review multiple decoupling strategies. Based on a TxRx topology that was presented without details by Sattel *et al.*,[10] this study elaborates on the original implementation and optimization of an ICN and tailors the design parameters to a human-sized head scanner.[11]

II. MOTIVATION AND PURPOSE

Many current MPI systems use dedicated receive coils, often in a gradiometer configuration,[28–31] effectively suppressing feedthrough harmonics, interference, and systemic background.[24,32] However, receive coils take up valuable space and ultimately increase power consumption when signal generating coils have to be placed farther away, independent of the method of feedthrough suppression.[27] For preclinical systems with rodent-sized bores, power consumption can be managed; however, on the path to human-sized systems, this issue becomes a major challenge.[9,27] The advantage of choosing to combine the transmit and receive circuitry is that it reduces system complexity and overall space requirements by eliminating the need for a dedicated receive coil nested within the DFG and the receive band-stop filter.[33] One possible topology of a transmit–receive (TxRx) circuit is a symmetric HCR, as shown in Fig. 1(a), with a linear ICN, as shown in Fig. 1(b). A comprehensive characterization of the different noise and background contributions of TxRx and dedicated receive systems can be found in Ref. 24. However, there is currently no clear consensus in the community as to which system performs better on a human scale with manageable power consumption, although this may change in the future. The development of a TxRx system with an ICN is driven by various

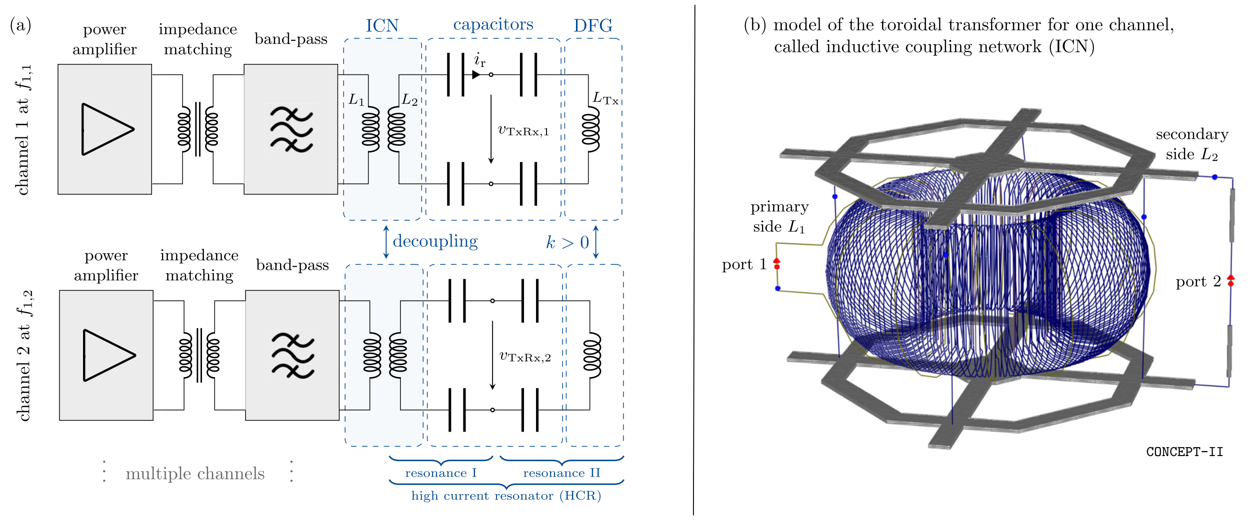

FIG. 1. Overview of the MPI transmit chain and the ICN. In (a), the power amplifier is connected to a ferrite-core transformer, a band-pass filter, and the primary side of the ICN. The secondary side of this transformer is part of a high-Q resonator, called a high current resonator (HCR), that includes the drive-field generator (DFG). Magnetic particles excited by the DFG induce signals via L_{Tx}, and the received signal is tapped within the symmetric HCR at v_{TxRx}. In (b), a four-fold segmented toroidal, D-shaped ICN is shown within a simulation setup of CONCEPT-II.[34]

design goals, including a. achieving floating potentials; b. ensuring linearity; c. attaining high current gain and high Q; d. designing circuit symmetry for excitation, filtering, and signal reception; and e. modularizing for impedance matching.

A. Floating potentials

The first design goal concerns patient safety and avoids ground loops that may negatively affect signal reception. A galvanically isolated high current resonator (HCR) with an overall low voltage and floating potential is achieved by many common transformer topologies. Floating potentials become relevant for a patient being examined in the scanner. Following the principle of the first fault case, the potential separation ensures that a patient is not exposed to a life-threatening current through single contact with the circuit. This would require contact at two separate points of the circuit, which drastically reduces the risk. In this unlikely event, we take the further precaution of reducing the overall voltage in the DFG and HCR by selecting low-inductance components.[11,35] A capacitive coupling network[36] would not provide real isolation at the drive-field frequency, although DC currents are blocked.

B. Linearity

A strictly linear air-core transformer is required because the ICN is located after the band-pass filter stage and must not increase the total harmonic distortion (THD) of the transmit or received signal. Harmonics generated directly within the HCR, where the received signal is tapped, would be unfiltered and, thus, mask and alter the particle's response. Harmonic generation by iron-core transformers is well known due to core saturation effects,[37,38] and the principle is demonstrated in Fig. 2(c). Here, we compare the THD after the band-pass filter with the THD generated by a ferrite-core transformer. Although an iron core would be preferable for its high permeability, effectively bundling magnetic field lines to achieve a high coupling coefficient k and low leakage inductance, it introduces distortion due to the saturation effects of the ferrite-core material. This constraint is so strong that a THD of 0.5% from a class-AB power amplifier in combination with our transmit filter results in a theoretical THD benchmark of below $5 \times 10^{-6}\%$, calculated using the fundamental definition of THD_F.[39] The typical THD of a linear power amplifier ranges from 0.1% to 1%,[40–43] and our filter achieves a measured 65 dB amplitude attenuation at the second harmonic f_2, 100 dB at f_3, and below 150 dB at f_4 and above.[11,23] Regarding a low-core loss iron powder material such as "−8" (Micrometals, Inc., CA, USA[44]) and neglecting any hysteresis effects, a maximum amplitude deflection of only 1% of the saturation field strength H_sat results in a THD of $3 \times 10^{-3}\%$, as shown in Fig. 2(c-4). Although this number is extremely low, it is about three orders of magnitude higher than the combined THD of the amplifier and band-pass filter. Similarly, an amplitude of about $0.14 \times H_\text{sat}$ would cause a THD of 0.5%, counteracting any achievements by the band-pass filter. Moreover, intermodulation of harmonics will occur, which further degrades the THD of an iron-core transformer, which was not modeled here. Consequently, an air-core transformer is preferred to achieve maximum linearity, and a toroidal shape is advantageous to enclose the majority of field lines within the toroid. This minimizes any coupling leakage flux and eddy current losses in the surrounding shielding and reduces the susceptibility to external disturbances to avoid spurious harmonics.

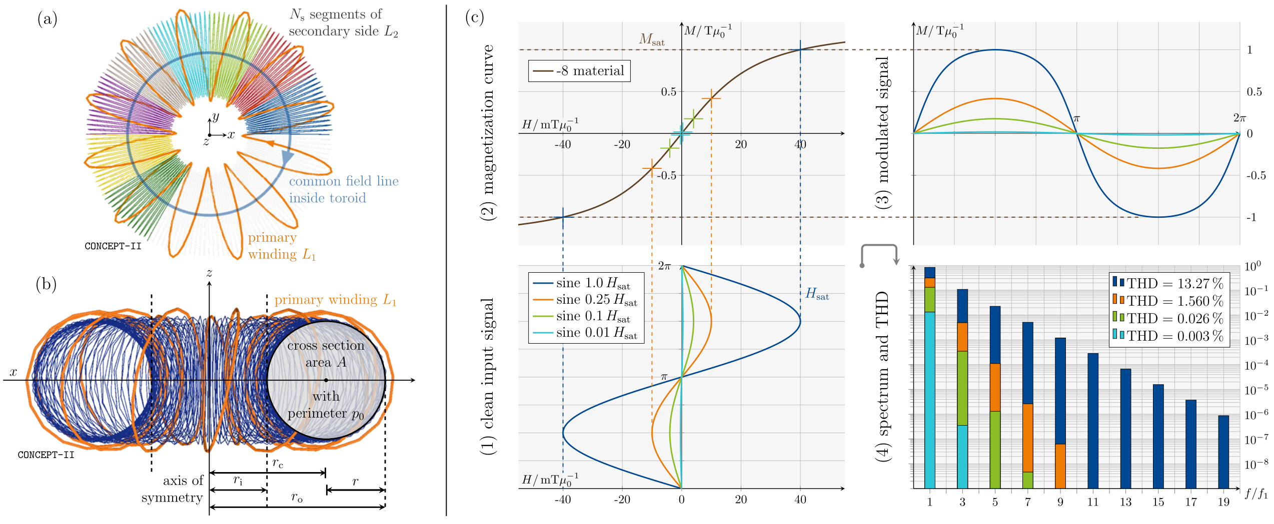

FIG. 2. Segmented toroidal air-core transformer and THD simulation of iron-core saturation without hysteresis. Shown in (a) is a toroid parallelized with $N_s = 12$ individual segments, of which eight are shown in different colors (four are hidden). The primary winding also forms a toroid, here with $N_1 = 12$ turns, whereas each secondary segment has $N_2 = 13$ turns. In (b), the circular cross section in the xz-plane is shown with characteristic parameters noted. On the right in (c), three sinusoidal input signals (1) are modulated by the magnetization curve in (2), which results in the output in (3) and its spectrum in (4). The magnetization curve is adapted from the "−8" iron powder core material,[44] but without hysteresis effects and modeled with a tanh-function.[45] A THD of 0.5%, typical for class-AB amplifiers, is caused by an amplitude of about 0.14 of H_sat.

C. High current gain and high *Q*

In order to maintain the same excitation field using low-inductance components, higher currents are required.[11] We are focusing on minimal conduction losses and an overall loss-optimized transformer design. The ICN is a resonant transformer, shown in Fig. 1(b), and the secondary side of the transformer is part of the HCR. Note that both voltage and current are amplified on the secondary side, unlike non-resonant transformers. This is based on a two-step process of having a tank LC with high impedance from the perspective of the primary side and the voltage scaling into a high Q load on the secondary side. However, amplification is due to resonance, and a change in the turns ratio still changes the voltage and current in opposite directions. A limiting factor in the gain is the structural size because it limits the overall achievable Q of the HCR.

Independent of the desired inductor values, the cross-sectional shape of the toroid is optimized to maximize the inductance L_2 for a given wire length, i.e., the perimeter p_0 of the toroidal cross section (D-shape). To achieve this, we implemented the results of a comprehensive study by Murgatroyd.[46] In addition, frequency dependent losses are minimized by using litz wires that suppress the skin effect and reduce proximity effect losses.[47] Due to the angular symmetry of the toroid, the winding core offers the possibility of parallel segmentation of the secondary side. Such parallel segments share the same enclosed field lines to compose a single composite toroid, as shown in Figs. 2(a) and 2(b), which can be used to shift the desired value for L_2 at a constant Q to change the desired turns ratio n. A trade-off must be made between wire diameter, feasible parallelization of toroidal segments, stacked wire layers near the symmetry axis, heat dissipation, and target inductance.

D. TxRx circuit symmetry

Symmetry refers to the HCR layout, where the capacitors are split into two separate banks for each inductor, as shown in Fig. 1(a). This offers the advantage of combining transmit and receive chains in a single circuit, as proposed by Sattel *et al.*[10] Here, the HCR acts simultaneously as a filter for the fundamental frequency, allowing it to tap the particle's response v_{TxRx} during transmission. However, a partial attenuation of the particle signal is inevitable using this configuration because the strength of the particle signal relies on the proportion of inductors L_2 and L_{Tx}, which we call the DFG matching condition.

E. Impedance matching modularization

For feasible impedance matching, a modularization into two matching stages is carried out, as shown in Fig. 1. The ICN can thus be designed without additional constraints regarding amplifier load matching, which is done separately by an amplifier matching stage. To this end, we use a ferrite-core transformer before the band-pass filter with a maximum amplitude below 10% of H_{sat}, as explained in Sec. II B, on the condition that the transformer's THD is similar to the amplifier's THD and a band-pass filter is implemented afterward.

III. THEORY

In this section, we present a systematic optimization of an inductive coupling network, delineating the theory and criteria employed to derive the configurations for both sides of the toroidal transformer. Our approach commences with an examination of the transformer's current gain G in Secs. III A and III B. The focus then shifts to optimizing the toroidal geometry with the goal of minimizing losses and maximizing inductance, as described in Sec. III C. This optimization process encompasses cross-sectional shape, multiple winding layers, segmentation, and primary winding characteristics. In order to select an appropriate inductance value, we proceed to the inductance matching condition specific to a symmetric setup of the HCR in Sec. III D, a consideration tailored for the MPI imaging modality.

Given the broader context of multichannel MPI systems, it is imperative to devise individualized ICNs for each channel and account for coupling, which is described in Sec. III E. Nevertheless, up to that point, the entire section focuses on a single channel with the resonance frequency f_1.

A. Maximum transformer current gain

The current amplification factor, denoted as G for the ICN transformer, will be investigated with the objective of maximizing it, according to design goal c. A first expression for G can be derived by considering the power P_2 on the secondary side, caused by the primary current i_1 that induces the voltage v_2, as in

$$P_2 = \frac{|v_2|^2}{R_s} = \frac{|j\omega M i_1|^2}{R_s} = \frac{\omega^2 M^2 |i_1|^2}{R_s}, \tag{1}$$

where $\omega = 2\pi f_1$ denotes the channel angular frequency, j denotes the imaginary unit, M denotes the mutual inductance of the transformer, and $R_s = R_2 + R_{\mathrm{Tx}}$ denotes the total series resistance of the secondary side at resonance (capacitor losses are neglected).[48] All components, currents, and voltages are shown in Fig. 3. Now, the power at resonance can be rewritten to obtain the current gain G by

$$|i_2|^2 R_s = \frac{\omega^2 M^2 |i_1|^2}{R_s} \quad \Rightarrow \quad G = \frac{i_2}{i_1} = \frac{\omega M}{R_s}. \tag{2}$$

In the following, this expression is rearranged for resonant transformers using characteristic transformer variables such as the turns ratio n, the coupling coefficient $k \in [0, 1]$, and the quality factor Q of the transformer's secondary side.[49,50] Note that voltages across the leakage inductance $L_{\sigma,1} = L_1(1 - k)$ and matching capacitor C_{m} of

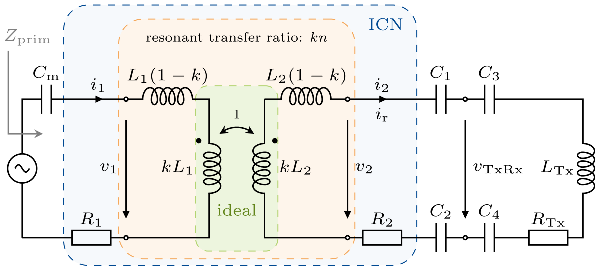

FIG. 3. Resonant transformer circuit diagram. A resonant transformer is shown, where an ideal transformer remains embedded in the center. The inductors are split into leakage and coupled inductances. The matching capacitor C_{m} resembles the filter output stage, which goes into resonance with the leakage inductance $L_{\sigma,1} = L_1(1 - k)$, and Z_{prim} becomes real at $\omega = 2\pi f_1$.

the band-pass filter cancel at resonance. Furthermore, L_2 is part of a resonant circuit on the secondary side; therefore, voltage and current are increased.

The turns ratio is defined by the number of primary turns N_1 to secondary turns N_2. For an ideal transformer that is perfectly coupled $(k = 1)$, there is no phase difference and, therefore, no losses between the two sides. In this case, n directly relates the magnitude of the voltages v_1 and v_2 and can be used to step up or step down the reflected impedance seen at the input,[50] as given in

$$n = \frac{N_1}{N_2} = \sqrt{\frac{L_1}{L_2}} = \frac{v_1}{v_2}. \tag{3}$$

L_1 and L_2 are the transformer's primary and secondary inductances. Next, to obtain the coupling coefficient, we first consider the coupling factors,

$$K_1 = \frac{\Phi_{21}}{\Phi_{11}} = \frac{M}{L_1}, \quad K_2 = \frac{\Phi_{12}}{\Phi_{22}} = \frac{M}{L_2} \tag{4}$$

for the general case of arbitrary transformer shapes. K_1 measures the proportion of the mutual magnetic flux Φ_{21} caused by a current i_1 in M and the magnetic flux Φ_{11} caused by a current i_1 in L_1. The same principle applies to K_2. Note that the value of K_i can be greater than 1. The mutual inductance M is reciprocal for all linear materials with symmetric tensors for electric conductivity, permittivity, and permeability.[51] Now, the definition of the coupling coefficient is given with

$$k = \frac{M}{\sqrt{L_1 L_2}} = \sqrt{K_1 K_2}. \tag{5}$$

Finally, a general expression for the quality factor Q is given by the ratio of stored energy to dissipated energy per cycle: For an inductor L, perfect capacitors, and assuming negligible radiation losses in the kHz region, the quality factor is

$$Q = 2\pi \frac{E_{\text{stored}}}{\frac{1}{f} P_{\text{diss}}} = 2\pi f \frac{\int_0^{\hat{i}} L\, i\, \mathrm{d}i}{\left(\frac{\hat{i}}{\sqrt{2}}\right)^2 R} = \frac{\omega L}{R}. \tag{6}$$

R is the total resistance of the considered resonance,[52] and $\hat{i}$ is the total current of the inductor.

Under the consideration of a dominant Q of the coils, the three constituents of the gain in (2) are replaced by the considered ICN, and the equation yields

$$G = \frac{\omega M}{R_s} = \frac{\omega L_2}{R_s} \frac{M}{\sqrt{L_1 L_2}} \sqrt{\frac{L_1}{L_2}} = Q\, k\, n. \tag{7}$$

Note that the inserted Q refers to the transformer with its energy stores L_2, C_1, and C_2, while the resonance on the right side acts as a real impedance, adding only the serial resistance R_{Tx} of the DFG.

There are three conclusions due to (7): The channel frequency should be chosen as high as reasonable, taking into account the drawback of increasing losses due to high-frequency effects in the transmit and receive chains. We consider fixed frequencies in the low kHz range (around 26 kHz) and discuss the frequency choice in Sec. VI. Second, a reduction of R_s is beneficial: The correct type of litz wire should be chosen,[47] connections within the HCR should be kept short, and the cross section shape of the inductor should be chosen to obtain a minimum R for a maximum L[46,53] to result in a high Q. Apart from minimizing R, the goal of maximizing M requires finding a toroid with both a high k and a large L. A high turns ratio n can be obtained by a dense primary winding and parallelizing the second transformer side. Third, as the total energy dissipated must equal the energy delivered in the resonant circuit, we obtain

$$|P_1|\Delta t = |P_2|\Delta t \quad \Rightarrow \quad \mathrm{Re}(Z_1) = G^2\, \mathrm{Re}(Z_2) \tag{8}$$

for a time interval Δt at steady-state, $Z_1 = v_1/i_1$ and $Z_2 = v_2/i_2$. The imaginary part is zero at resonance, and the real impedance seen by the primary side equals

$$\mathrm{Re}(Z_{\text{prim}}) = R_1 + G^2 R_s = R_1 + \frac{\omega^2 M^2}{R_s}. \tag{9}$$

B. Structural size limits Q

As argued above and evident from Eq. (7), we need a large secondary inductance to obtain a high transformer gain. A large structural size is beneficial because an increasing cross section A increases the inductance faster than its reduction by the growing center radius r_c, as approximated by the equation for a single-layer air-core toroid with a circular cross section,

$$L_{\text{toroid}} \approx \frac{\mu_0 N^2 A}{2\pi r_c}. \tag{10}$$

Here, μ_0 is the vacuum permeability, and the dimensions are shown in Fig. 2(b). However, a constant number of turns that are stretched around a growing cross section will reach a point where the changes in inductance and resistance compensate. This problem and its parameter dependencies are a well-known optimization problem, treated by Murgatroyd,[46,53] and an overview can be found in Ref. 54. A can be increased until an optimum is reached where the inductance is maximum for a given total wire length $l = N 2\pi r$ of all turns. This is a restraint on A, and there exists an optimum for the ratio of outer to inner radius for a finite l. The optimum number of turns for toroids with a circular cross section and wire diameter d lies at $N = 0.8165\sqrt{l/d}$, which in turn yields the ratio $r/r_i = (0.8165)^{-2} \approx 1.5$ and the optimal inductance,

$$L_{\text{toroid,opt,circ}} \approx \frac{\mu_0\, d}{2\pi} \left(0.2722 \left(\frac{l}{d} \right)^{\frac{3}{2}} + 0.25 \frac{l}{d} \right), \tag{11}$$

as derived by Murgatroyd.[54]

Optimal benefits are obtained from the correct area to radius ratio in combination with a large overall construction volume, coupled with a judicious selection of layers within the interior, as shown in Fig. 4(b) and explained in Sec. III C 2. The upper limit is reached if the interior space is fully occupied by wires, which also affects the cross section shape that deviates from a circle for the outer layers.[53,55] Overall, increasing the dimensions of the toroid leads to an increase in L_2, Q, and, thus, G. The maximum Q is defined by the available construction volume.

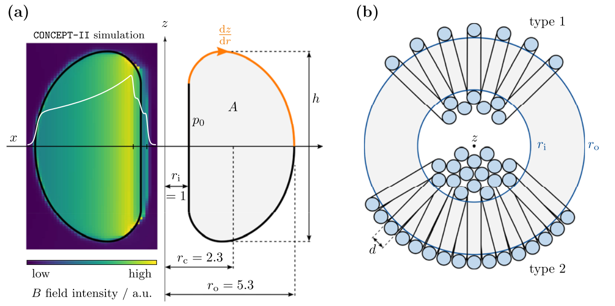

FIG. 4. Optimal D-shaped cross section and multi-layer toroids.[53] In (a), the optimal D-shape cross section is shown for the fixed optimum ratio of $r_\mathrm{o}/r_\mathrm{i} = 5.3$. The left toroid-half features a field intensity plot with the field profile along the x-axis in white (the toroid has three layers on the inside, simulated in CONCEPT-II[34]). Highlighted in orange in the right toroid-half is the curve obtained by a stepwise evaluation and integration of (13). In (b), two different types of winding arrangements of multi-layer toroidal inductors are shown.

C. Toroidal transformer

The ICN toroid is optimized for a finite available construction volume by optimizing the cross-sectional shape for a higher inductance, taking into account multiple layers of winding, and improving the coupling of the primary winding. Then, segmentation provides a tuning mechanism that allows us to change the nominal inductance with a constant inductance-to-resistance ratio[56] to a desired value.

1. Optimal cross section: D-shape

A circular cross section gives the largest area A for a fixed turn perimeter p_0, but it does not provide the highest inductance for this wire length. This discrepancy is caused by the non-uniform flux density within A, which is denser toward the inside for toroids,[54,57] as shown in Fig. 4(a). Due to the straight inner edge of the D-shape, it encompasses the higher magnetic flux density toward the z-axis of symmetry and yields ~15% more inductance than the circular window for the same p_0.[54]

For the single-layer DC loss optimized D-shape, the optimum was found to be

$$L_{\mathrm{toroid,opt,D}} \approx \frac{\mu_0\, d}{2\pi}\left(0.314\left(\frac{l}{d}\right)^{\frac{3}{2}} + 0.25\frac{l}{d}\right) \tag{12}$$

for $\frac{r_\mathrm{o}}{r_\mathrm{i}} = 5.3$ and $N = 0.565\sqrt{\frac{l}{d}}$,[53] as shown in Fig. 4(a). The slope (orange) is obtained by a stepwise evaluation along the radial direction, given by

$$\frac{\mathrm{d}z}{\mathrm{d}r} = \pm\frac{\ln\frac{\sqrt{r_\mathrm{i} r_\mathrm{o}}}{r}}{\sqrt{\ln\frac{r}{r_\mathrm{i}}\,\ln\frac{r_\mathrm{o}}{r}}}. \tag{13}$$

Integrating the slope $\mathrm{d}z/\mathrm{d}r$ yields coordinates for the optimized quarter section shapes.

AC losses are mainly eddy current losses due to proximity effects, since the skin effect plays only a minor role in litz wire windings. The impact of the proximity effect is twofold: internal magnetic fields due to neighboring currents cause eddy currents, but they are dominated by the second effect due to the main toroidal field through the rest of the coil, acting on the entire litz wire bundle.[47] Overall, this results in eddy currents causing local non-uniform current densities that require a more complex shape optimization for high frequencies, as can be found in Ref. 46. The optimum shape for high frequencies differs from a D-shape due to the stronger constraint of eddy current losses, which are highest near the center, causing the highest point of the slope to move outward. However, in the kHz range, the AC optimized shape converges to the DC optimized shape of (13) for litz wires with sufficiently small strands.

2. Multiple layers

Another way to effectively increase L_2, which optimizes Q, is by using multiple wire layers. However, insufficient heat dissipation from the inner layers becomes an issue that, in turn, increases copper resistance and might damage the litz wire insulation layer. To this end, we propose a single, nearly dense outer layer of turns, as shown in Fig. 4(b), which overlap on the inside near the axis of symmetry. This compromise gives satisfactory results and sufficient heat dissipation by air cooling. If the litz wire winding is not operated near its maximum current rating, e.g., for split-core toroids in filter stages,[11,23] multiple dense layers are an efficient option. A general study on optimal shapes for air cores and non-air core multilayered toroidal inductors can be found in Ref. 55.

3. Segmentation

The secondary side L_2 can be divided into N_s identical segments, which are wired in parallel but enclose a single common field, as shown in Figs. 2(a) and 2(b). If the winding remains otherwise unchanged, both the inductance and the resistance will be reduced with N_s^2 if N_s is increased. As an example, a segmentation into two halves is considered, where one half is limited to $N/N_\mathrm{s} = N/2$ turns. Intuitively, it seems that L is reduced quadratically and the resistance R is reduced linearly for a dense winding that remains unchanged, due to $L \propto N^2$ via (10) and $R \propto N$ via each turn perimeter. However, the effect for L is changed to $L \propto N$ due to the shorter magnetic core length l, exemplified by a long and straight solenoid with $L \propto N^2/l \propto N$ that has a constant turn density N/l. An additional slight decrease in L is caused by the now open magnetic circuit, which results in less coupling of the end turns with the rest of the toroid. Mutual coupling M compensates for this loss of self-inductance L for toroids since the halves now couple to the parallelized second half, i.e., to their neighbors at both ends if again arranged as a joint toroid after segmentation. However, parallelizing equal impedances results in a $1/N_\mathrm{s}$ division for both L and R. Overall, the linear contribution of the separation and the linear contribution of the parallelization result in a $1/N_\mathrm{s}^2$ scaling for both L and R.

A segmented toroid with $N_\mathrm{s} = 12$ segments is shown in Fig. 2(a), and the total current is distributed by a central node (copper plates) at the top and bottom. A lead wire from each segment is connected to the node as shown in Fig. 1(b) for $N_\mathrm{s} = 4$. Another aspect of the segmentation is that the current i_r of the HCR is divided equally among the parallel segments, thus relaxing the copper cross section requirements for the L_2 winding. In system design situations, the construction volume is usually constrained to a maximum bounding box. For an optimal shape, Q is thus fixed. Using this method, the design can start with an optimal single winding inductor and then use segmentation to tune for a desired L_2 and R_2.

4. Primary winding

A final design decision for the toroidal topology concerns the primary winding. For a reasonable volume and, therefore, limited Q, the primary winding should achieve a high coupling k, as shown in (7). Consequently, one choice is that L_1 is also toroidal and (sparsely) wound around the outside of L_2. This ensures that the majority of the field lines are shared by both transformer sides to maximize k. In Fig. 2(b), such a toroidal primary winding of L_1 (orange) is shown for a toroid with a circular cross section. Known from Rogowski coils[58] is the beneficial effect of a return wire in the xy-plane that counteracts the single turn of l along the center circumference of the toroid to diminish the field on the outside, which is in line with the z-axis. For ease of fabrication, we propose a return wire along the outside at r_o, which suppresses most of the stray field but deviates from the optimal enclosed position at r_c.

If a dense L_1 coil is used, i.e., a few turns at one point around the toroid, the result is a large K_1 and a very weak K_2. The overall k is small, which is only sufficient for a design with a very large Q. However, such a dense L_1 provides several advantages for peripheral measures, such as a pick-up coil to measure the current, i_r. Such a coil, L_3, could be mounted on the toroid opposite to L_1 to focus its sensitivity locally on L_2 and avoid coupling between L_1 and L_3.

D. DFG matching condition

We have previously shown that, in order to achieve high gain for design goal c, it is advantageous to obtain a high Q. Currently, the inductance of L_2 itself is not considered. In the following, a trade-off is identified that characterizes L_2 in its dependence on L_{Tx} to comply with design goal d. This consideration arises from the specific constraints imposed by the MPI imaging setup, in particular the circuit symmetry condition for simultaneous transmission and reception and the absolute power consumption, which has not been considered so far. Here, we assume a constant Q, which is justified for a fixed bounding box as reasoned in Sec. III B, resulting in a linear relationship between R_2 and L_2 at a fixed ω. The ohmic resistances of the capacitors and the DFG remain constant.

Our objectives are twofold, yet inherently contradictory: achieving both maximal particle signal strength at the v_{TxRx} port and minimal power consumption within the HCR. The particle response is characterized by the prevalence of high-order harmonics at the resonance frequency f_1. These harmonics experience a significant voltage drop across an inductive voltage divider formed by the inductances L_2 and L_{Tx} when compared to the relatively minor influences of their small series resistances within the mΩ range[11] and the associated HCR capacitors at harmonic frequencies. The winding configuration of L_{Tx} can be conceptualized as a distributed voltage source, thereby inducing the particle voltage at the virtual ground nodes of v_{TxRx}.[10] Ideally, in the scenario of an infinitely large L_2, the complete induced voltage would be dropped across L_2, leading to a maximal particle response at v_{TxRx}. In contrast, a diminished ratio of L_2/L_{Tx} would effectively short-circuit the receive voltage, advocating a maximum value for L_2. However, the cumulative series resistance $R_2 \propto N2\pi r$ of the toroid manifests the same increase as L_2 is augmented, as imposed by a constant Q via (6). The total power consumption increases with R_2, but it is limited to a feasible amount. This imposes a constraint on L_2 because the current amplitude at resonance i_r in the HCR must stay constant to maintain the same drive field strength. Consequently, a partial attenuation of the particle signal is inevitable due to the voltage division effect inherent in the inductance voltage divider of L_2 and L_{Tx}.

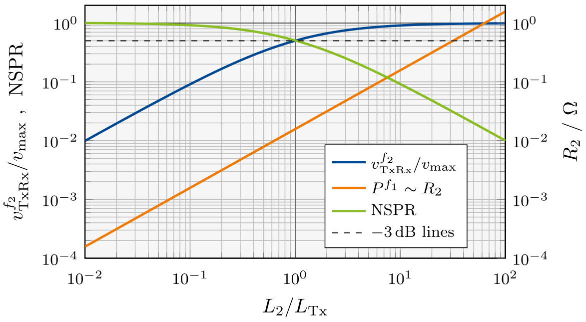

FIG. 5. Inductance matching condition of DFG and ICN. A trade-off is identified at $L_2 = L_{\mathrm{Tx}}$ when the received signal is halved (−3 dB), expressed by the intersection of the particle signal (blue) and the normalized signal-to-loss ratio (green). This graph demonstrates that additional power is required to avoid receiving signal attenuation.

The crucial point is that the power consumption at the fundamental f_1 scales linearly with R_2, and the particle voltage at frequencies $f > f_1$ drops depending on the inductive voltage divider when the impedance of capacitors becomes negligible. We consider a unit current $i_r = 1$ A and define the particle signal-to-power ratio (SPR) as

$$\mathrm{SPR} = \frac{v^{f_2}_{\mathrm{TxRx}}}{P^{f_1}} = \frac{v^{f_2}_{\mathrm{TxRx}}}{i_r^2\, R_2}. \tag{14}$$

The power consumption P^{f_1} is considered at the fundamental, but the particle signal $v^{f_2}_{\mathrm{TxRx}}$ is at the first harmonic. Note that for f_2 and all higher frequencies, the inductive voltage divider is the dominant part, and all harmonics are recorded. The maximum particle voltage v_{max} of $v^{f_2}_{\mathrm{TxRx}}$ is defined in the limit of a large L_2, where it is not attenuated. To remove the influence of the absolute value of R_2, we normalize (14) with its maximum in the parameter range and call it NSPR. The constituents of (14) and the NSPR are plotted in Fig. 5.

One possible trade-off position can be identified at −3 dB of NSPR and $v^{f_2}_{\mathrm{TxRx}}$, which results in halving the received signal (harmonics). This point coincides with $L_2 = L_{\mathrm{Tx}}$, where the inductances match, which we chose as the trade-off for the design of our ICNs. Consequently, a less attenuated particle signal requires more power. Note that (14) remains valid when L_{Tx} is varied instead of L_2, and the consideration of the inductance voltage divider remains identical.

E. Channel decoupling

The use of multiple channels in MPI has the advantage of simultaneous sampling of a 3D field-of-view (FOV). Due to the imperfect spatial orthogonality of these channels and the close proximity of resonance frequencies, typically within a range of less than $\Delta f = 0.03 f_1$,[59] strong coupling between the different drive-field channels is expected. Thus, even weak coupling coefficients present a particular challenge, especially in the case of resonant circuits with high Q, necessitating the development of effective decoupling mechanisms while introducing minimal additional resistance to the HCR.

Causes of channel coupling are misalignment of the drive-field coils, non-orthogonal field components, and undesired loops in the connecting wires. Small errors in positioning, e.g., for two planar coils with $k \propto \cos(\beta)$, can lead to coupling with significant currents. A $\beta = 3^\circ$ results in $k = 0.052$, which can generate a current $i_{\mathrm{r},2}$ in channel 2 of similar magnitude to the original current $i_{\mathrm{r},1}$ in channel 1. For this purpose, if we consider the complex impedance $Z_{\mathrm{HCR},2}$ of the second channel's HCR and let j be the imaginary unit, then the current $i_{\mathrm{r},2}$ in the second channel at the first angular frequency $\omega_{\mathrm{r},1}$ is caused by induction via $i_{\mathrm{r},1}$ and M, as in

$$\begin{aligned}\frac{i_{\mathrm{r},2}(\omega_{\mathrm{r},1})}{i_{\mathrm{r},1}(\omega_{\mathrm{r},1})} &= \frac{v_{\mathrm{ind},21}(\omega_{\mathrm{r},1})}{Z_{\mathrm{HCR},2}(\omega_{\mathrm{r},1})}\,\frac{1}{i_{\mathrm{r},1}(\omega_{\mathrm{r},1})}\\ &= \frac{j\omega_{\mathrm{r},1}M\, i_{\mathrm{r},1}(\omega_{\mathrm{r},1})}{Z_{\mathrm{HCR},2}(\Delta\omega + \omega_{\mathrm{r},2})\, i_{\mathrm{r},1}(\omega_{\mathrm{r},1})}\\ &\approx \frac{j\omega_{\mathrm{r},1}M}{j2\Delta\omega(L_{\mathrm{Tx},2} + L_{2,2})} \approx \frac{\omega_{\mathrm{r},1}M}{4\Delta\omega L_{2,2}} = \frac{1}{4}\,\frac{\omega_{\mathrm{r},1}}{\Delta\omega}\,k. \end{aligned} \tag{15}$$

Note that the matching criterion of Sec. III D is respected with $L_{\mathrm{Tx},2} = L_{2,2}$, and we approximate $Z_{\mathrm{HCR},2}$ near $\omega_{\mathrm{r},2}$ with $j2\Delta\omega L_{2,2}$, as shown in Appendix A 1. With $\frac{\Delta\omega}{\omega_{\mathrm{r},1}} = \frac{(\omega_{\mathrm{r},1} - \omega_{\mathrm{r},2})}{\omega_{\mathrm{r},1}} = \frac{1}{75}$ (see the beginning of Sec. V) and the aforementioned misalignment of $\beta = 3^\circ$, this example results in $\frac{i_{\mathrm{r},2}}{i_{\mathrm{r},1}} = 0.25 \cdot 75 \cdot 0.052 = 0.975 \approx 1$. The consequence is a severe distortion of the Lissajous trajectory, which is already significant for values $i_{\mathrm{r},2}/i_{\mathrm{r},1} \geq 10\%$.[60]

In order to avoid the negative effects of uncompensated couplings, such as trajectory distortion, additional power dissipation, detuning, and frequency beating that will act on the power amplifier, we consider three types of decoupling schemes: capacitive, inductive, and active compensation. Capacitive compensation is narrowband and requires additional connections between channels, but the equivalent series resistance (ESR) of capacitors is low. Inductive compensation is directed at counteracting M and is broad-band, but additional coils typically increase the series resistance, thus reducing Q. Finally, active decoupling uses the channel's amplifiers but demands reactive power in the band-pass filters [Fig. 1(a)] and for the mismatched HCR. Furthermore, it requires accurate feedback for current control. It should be considered a last resort, as the amplifier will see a reactive load at other frequencies, and maximum voltage ratings may be exceeded over the course of a full Lissajous trajectory cycle.

In general, capacitive decoupling may not offer an exact solution, and there are unsolvable combinations of coupling depending on the sign of the coupling coefficients. However, capacitive compensation is advantageous for the particle signal of a transmit–receive circuit because a large common series capacitor can be used, which becomes short at harmonic frequencies and has a very low series resistance compared to coil windings. This requires two common nodes between channels and similar inductive coupling coefficients of the same sign, due to the single narrowband decoupling point. We could use three capacitors, two within each channel, or, alternatively, one common capacitor for all channels. The mentioned low differences in drive-field frequencies in MPI are a premise, and a limitation is that the sum of all currents flows through this capacitor. A schematic is shown in Fig. 6(a), which represents only the right part of the symmetric HCR, with v_{TxRx} across each numbered a-b terminal pair, shown for three channels each.

Inductive compensation is a general alternative for all coupling coefficient signs. Either a coil is added in series to L_{Tx} for each unique off-diagonal entry of the system's impedance matrix, as shown in Fig. 6(b), or the same number of separate windings is used to introduce the desired compensation without a galvanic connection by careful positioning, as shown in Fig. 6(c). A disadvantage of the first technique is the additional high current lines, stray fields, their influence on the tuning of the resonators, and additional series resistance, as well as their mounting and cooling effort. The second technique uses separate windings that are sensitive to a partial amount of the drive-field, equal to the M introduced by coupling. A suitable

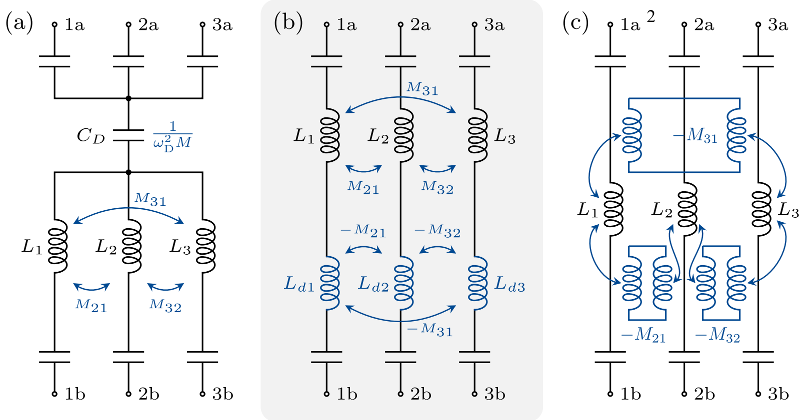

FIG. 6. Schematic of decoupling schemes with three TxRx channels. The schematics refer to one-half of the symmetric HCR, where v_{TxRx} can be tapped across each numbered a–b terminal pair (compare Fig. 1). Capacitive decoupling for a single frequency via a common capacitor C_D is shown in (a), with the condition that $M_{21} \approx M_{32} \approx M_{31}$. Inductive decoupling strategies (broadband) are shown in (b) and (c), for the case of series inductors and the case of separate windings, respectively.

inductive decoupling position is the ICN itself, as implied in the last paragraph of Sec. III C 4. Turns on the outer surface of the toroid are only capable of utilizing integer multiples to achieve a match with M. However, a slab outfitted with a wire loop can be introduced to encompass a partial quantity of the magnetic field inside: a loop on a slab that is inserted into a prepared gap within the toroid. Adjustment of the slabs can be used to fine-tune each channel if the ICN was prepared with such gaps. The sign can be adapted by inverting the orientation of the wire-loop. However, the principle remains the same if it is done with partial fields in the proximity of the DFG.

For our two-channel human-sized system,[11] we decided to use a single common capacitor that carries a peak current of $i_{\mathrm{r},1} + i_{\mathrm{r},2}$ (depending on the phase of the Lissajous cycle), introducing the same voltage as M into each circuit but with the opposite sign. The common decoupling capacitor C_{D} is calculated at a single frequency ω_{D} in-between both drive-field frequencies by

$$C_{\mathrm{D}} = \frac{1}{\omega_{\mathrm{D}}^2 M} = \frac{1}{(\pi(f_{\mathrm{r},2} + f_{\mathrm{r},1}))^2\, k\sqrt{L_{\mathrm{Tx},1}L_{\mathrm{Tx},2}}}. \tag{16}$$

This narrowband solution is acceptable for our implemented two-channel system, and the additional ESR introduced by the decoupling capacitor is small.

IV. METHODS AND IMPLEMENTATION

Guided by the theory to optimize the ICN for a given bounding box, we now describe the implementation and name the changes to our design that deviate from the stated optimum. We employ simulations to assess performance in Sec. IV A, which includes a D-shaped toroid. They are used to refine our decision on the number of segments and the type of primary winding. The construction of two ICNs is described in Sec. IV B, and the measurement methodology to analyze the prototypes is given in Sec. IV C.

A. Simulations

Linear circuit simulations are performed with LTspice 17.1 (Analog Devices, MA, USA).[61] Simulations of the magnetic field and the transformer's impedance matrix are performed using CONCEPT-II (Institut für Theoretische Elektrotechnik, Hamburg University of Technology, Germany).[34]

1. Toroid geometry

The CONCEPT-II software is based on the method of moments (MoMs) that solves electromagnetic boundary or volume integral equations in the frequency domain.[62] It is especially suited for the numerical computation of 3D radiation and scattering problems. CONCEPT-II is used in our work to calculate and test different toroidal transformer configurations. Input parameters include the general geometry (distances, shape and size of A, number of segments N_{s}, turns N_1 and N_2, primary winding shape, number of overlapping layers inside the toroid), while important output parameters include the impedance matrix $\mathbf{Z}$, 3D field plots, and conductor current densities. A two-port network is used to estimate k and G via the impedance matrix of the transformer,

$$\mathbf{Z} = \begin{bmatrix} Z_{11} & Z_{12} \\ Z_{21} & Z_{22} \end{bmatrix} \approx \begin{bmatrix} R_1 + j\omega L_1 & j\omega M \\ j\omega M & R_2 + j\omega L_2 \end{bmatrix}. \tag{17}$$

Different numbers of segments N_{s} are simulated, as well as the coupling between neighboring segments. Stray fields are minimized and coupling is maximized by looking at different winding options for L_1 (dense vs sparse/distributed), the suited number of turns N_1, and the current density in the copper-plates where parallel segments are joined. Litz wire windings are approximated by a single thin wire, assuming that the currents are restricted to the direction of the wire and the copper conductivity of surfaces and wires is set to $\sigma = 58 \times 10^6$ S m^{-1}. The results of the simulation are used to adapt the design and finally to compare the expectations with the manufactured prototypes in terms of L, k, n, and G. One simulated B-field plot is shown in Fig. 4(a) for a number of three overlapping wire layers on the inside. One complete model (four segments) is shown within the simulation framework in Fig. 1(b), including copper distribution plates.

2. Circuit analysis

With simulated values for L_1, L_2, k, and resistors as input parameters, the resonance behavior is analyzed in the schematic circuit analyzer tool LTspice. A model of the entire HCR is simulated, including the band-pass filter stage, the ICN, and two channels including crosstalk. Different decoupling strategies are tested to probe the schematic, based on Fig. 3, and to tune values for decoupling elements. The input impedance value, Z_{prim}, was also simulated with LTspice. A simplified LTspice model without the band-pass is provided in the supplements with two coupled channels, including the HCR, and approximate values for capacitors and inductors.

B. Construction of two toroidal ICNs

To weigh the different design decisions of the ICN, we followed the reasoning of Secs. III and IV A consecutively. The construction was performed after the simulation, with the probed values for parameters L, N, the number of segments $N_{\mathrm{s},1} = 4$ and $N_{\mathrm{s},2} = 6$, as given in Table I, and the chosen dimensions of $r_{\mathrm{i}} = 4$ cm, $r_{\mathrm{o}} = 9.2$ cm, and the height $h = 8.6$ cm for the D-shaped second side. Moreover, we use the channel frequencies $f_{1,1} = 25.699$ kHz and $f_{1,2} = 26.042$ kHz with a distance of $\Delta f = 343$ Hz.

The choice of $N_{\mathrm{s}} = 6$ segments for the second channel is owed to the fact that we implemented a saddle coil (DFG of channel 2), which requires a higher current than the first channel to meet field specifications;[11] thus, we chose to reduce R_2. Due to the fact that Q remains constant, the increase in gain is caused by the turns ratio n due to the shift in the ratio of L_1 to L_2. As reasoned in Sec. III C 3, the inductance decreases for a higher number of segments, which also better fits the lower DFG inductance of the saddle coil to comply with the matching condition of Sec. III D. To further increase the turns ratio n of the second channel, we chose $N_{1,2} = 13$ instead of $N_{1,1} = 12$. As a consequence, we were able to use the same support structure for winding, and both ICNs are of equal dimensions despite their different objectives. The 3D printed toroidal support structure of the ICN is made from the high temperature resin RS-F2-HTAM-02 (Formlabs, MA, USA). Air cooling along the symmetry axis is installed using shielded fans to prevent impedance changes caused by insufficient heat dissipation.

A difference between the derived optimal design and the constructed ICNs is the ratio of radii $r_{\mathrm{i}}/r_{\mathrm{o}} = 2.3$ for the D-shaped toroid.

TABLE I. Values from simulation (yellow) and measurement (blue) for both constructed ICNs. Bold fonts denote important values.

			$L\,/\,\mu$H	$R\,/\,$mΩ	N	$f_1\,/\,$Hz	$M\,/\,\mu$H	Q_{ICN}	Q_{HCR}	n	k	G	$Z_{\text{prim}}\,/\,\Omega$	$L_{\text{Tx}}\,/\,\mu$H	$R_{\text{Tx}}\,/\,$mΩ
ICN 1	sim.	pri.	6.21	200	12	25699	5.47	219	90.1	0.62	0.54	30.2	26.8		
		sec.	**16.3**	12.0	$4 \cdot 36$										
	meas.	pri.	6.65	233	12	25699	6.08	**215**	90.8	0.63	0.57	**33.0**	32.6	14.4	17.2
		sec.	**16.7**	12.5	$4 \cdot 36$										
ICN 2	sim.	pri.	6.88	200	13	26042	4.09	230	77.1	0.94	0.56	40.8	27.6		
		sec.	**7.73**	5.5	$6 \cdot 24$										
	meas.	pri.	6.85	210	13	26042	4.39	**220**	76.4	0.94	0.60	**43.0**	31.1	9.74	10.9
		sec.	**7.8**	5.8	$6 \cdot 24$										

This deviation from the optimum of $r_i/r_o = 5.3$ is a compromise to gain more space for a feasible winding through the center of the toroid, to reduce the number of inner layers, to increase the air cooling surface, and to comply with a limit on the available construction height. Basically, we calculated the optimal design to fully utilize the available construction space height h and then opted to increase r_i while keeping the other parameters constant.

Regarding the primary winding, a dense (localized) winding is unsuited due to a low k, as reasoned in Sec. III C 4. Sparse windings on a helical path yielded the best results, thereby forming a toroid on top of the outer surface around the L_2 toroid, as shown in Figs. 2(a), 2(b), and 7(a).

To minimize AC losses within the conducting material, a silk-wrapped litz wire of 2000 strands of 50 μm copper (effective copper cross section of 3.1 mm^2) is used for the secondary transformer winding. The primary winding consists of 400 strands of 50 µm copper (effective copper cross section of 0.78 mm^2) and is wrapped in a shrinking tube to increase durability and breakdown voltage. Parallel segments are connected on a 1 mm thick copper plate (top and bottom), which serves primarily as a distribution platform and connects parallel litz wires of the HCR and the ICN with a solder connection. In addition, balancing currents can be equalized on this low resistance copper plate.

C. Measurements

Measurements of inductors are performed with the LCR meter *Keysight* E4980AL (Keysight Technologies, CA, USA) at the channel's frequency. The coupling coefficient of a transformer is measured by using the short and open circuit inductances[63] in

$$k \approx \sqrt{1 - \frac{L_1|_{L_2\ \text{short}}}{L_1|_{L_2\ \text{open}}}}. \tag{18}$$

Note that L_2 needs to be sufficiently shorted (more difficult at high frequencies), and the quality factor of the secondary side should be $Q > 50$ for this model to be accurate. A comparison of different measurement techniques at higher leakage can be found in Ref. 64.

The LCR meter is used for Table I to determine L, the series resistance R, and k in the measured rows. All other values in these rows are calculated: M via (5), Q_{ICN} via (6) with L and R_2 of the same row, similarly Q_{HCR} with L and $R_s = R_2 + R_{\text{Tx}}$, n via (3) using the primary and secondary measured L, and G via (7) for each row. For the simulated rows of Table I, L and M were obtained from the simulation in CONCEPT-II, and k was calculated via (5) here.

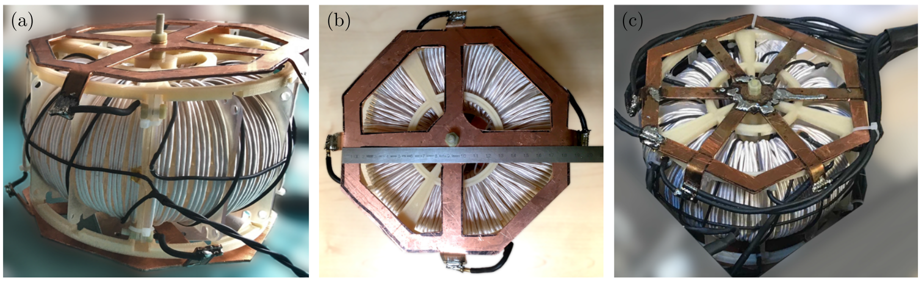

FIG. 7. Two ICNs for a two channel MPI system. In (a), the ICN 1 with N_s = 4 segments is shown (primary winding in black), and in (b), the top of the same ICN is shown with a reference scale in cm (without primary winding). ICN 2 with N_s = 6 segments is shown in (c) after installation. The connecting litz wire of the HCR and the primary winding are insulated with a black shrinking tube.

V. RESULTS

We have designed, simulated, and fabricated two ICNs with $f_{r_1} = 25.699$ kHz ($N_s = 4$) and $f_{r_2} = 26.042$ kHz ($N_s = 6$) for a two channel human-sized MPI system and integrated both into our MPI scanner.[11] The simulation and measurement results of the final design are summarized in Table I, and details of the construction are described in Sec. IV B. Pictures of both constructed ICNs are shown in Fig. 7.

The deviation between measured and simulated inductances L_2 is below 2.5% and below 1% for the first and second ICN, respectively. The measured value for k is about 5%–7% larger than the simulated value. Therefore, M is also larger in rows 2 and 4, because its calculation is based on k and L_2. This results in the measured G being 9.3% and 5.4% larger for ICN 1 and 2, respectively. Q_{ICN} refers only to the self-inductance L_2 and series R_2 of the secondary transformer side, while Q_{HCR} is the more important measure that includes the entire resonant load. Here, $R_s = R_2 + R_{\mathrm{Tx}}$ represents the losses of the HCR and resembles the gain actually achieved. Later current measurements showed a gain very similar to these values, although they are marginally lower due to losses of additional connections and wires (e.g., decoupling capacitors).

The inductors of DFG and ICN are nearly matched for both channels, as explained in Sec. III D, with $L_{\mathrm{Tx},1} = 14.4\ \mu\mathrm{H} \approx L_{2,1} = 16.7\ \mu\mathrm{H}$ for channel 1, and with $L_{\mathrm{Tx},2} = 9.74\ \mu\mathrm{H} \approx L_{2,2} = 7.8\ \mu\mathrm{H}$ for channel 2. Note that the target input impedance Z_{prim} of (9) remains for both ICNs at around 30 Ω, which is the load after the bandpass filter. In addition, the Q of both ICNs remains constant, with $215 \approx 220$ (measured values) for the different segmentations, as argued in Sec. III C. The increase in G is achieved by the augmentation of n due to the segmentation.

Due to the non-orthogonal DFG channels, there is a residual coupling of $k = 0.062$,[11] which has serious implications for both resonators, as described in Sec. III E. The channels were decoupled by −35 dB using a single common decoupling capacitor carrying both currents $i_{r,1}$ and $i_{r,2}$. This choice provided good results with minimal changes to the existing HCR without introducing a large series resistance and with high temperature stability.

VI. DISCUSSION

Applications that require highly linear transformers, such as MPI, rely on circuits that do not utilize magnetic materials that saturate. Any harmonic distortion may obscure the weak receiving signal and degrade the image quality. As a result, air-core structures are chosen at the expense of increasing component dimensions, which sets the maximum Q for an available construction volume. In this study, we present a blueprint for a high-gain linear transformer with a high quality factor. We formulate an expression for the gain as a function of mutual inductance, optimize the cross-sectional shape, employ segmentation to shift the nominal inductance, deduce a primary winding topology, and incorporate multiple layers to enhance performance. In the context of the emerging imaging modality MPI, we establish a matching condition that balances particle signal and power consumption. Furthermore, we elaborate on various decoupling techniques for multichannel systems and support our assessment of the ICN with simulations.

In terms of human safety, the entire HCR has floating potentials, and component voltages in patient proximity are reduced by the ICN due to its high current gain that drives the low-inductance DFG to generate the required MPI drive-field. The symmetric design of the HCR allows for fundamental filtering at the signal tap but results in partial received signal attenuation due to the inductive voltage divider of L_2 and L_{Tx}. The TxRx topology generally reduces power consumption by saving space through the elimination of dedicated receive coils, but consumption is approximately doubled by the ICN. In addition, common decoupling strategies, such as gradiometric receive coils, reduce the design requirements for linearity within the transmit chain. A direct comparison in signal quality between this TxRx topology and a gradiometric receive topology is currently pending, although other TxRx systems have been characterized.[24]

The presented toroidal transformer blueprint is limited by its restriction to the quasi-static regime of electromagnetics, where wave propagation effects are not dominant. In addition, if AC losses due to proximity effects dominate in the toroid, the D-shape optimization will result in a different shape.[46] Parameters given or assumed in this study, such as frequency or volume, require careful selection. Q increases linearly with frequency and should be chosen as high as possible, taking into account component voltages, high reactive power (in resonance),[9] signal induction, wave propagation effects at high harmonics, required receive bandwidth, PNS, and SAR limits.[3,6,65–67] Our decision regarding the deviation of r_o/r_i from the optimum was aimed at facilitating the winding process and reducing the number of stacked inner layers. This decision allowed the winding of a nearly dense outer layer with two to three stacked inner layers. Regarding (10) with a given constant area and a linearly increasing r_c, we assume that the deviation from the optimal inductance is small. The copper plates at the top and bottom (nodes of parallel segments) should be designed to facilitate air cooling of the inner layers.

A key insight is that the available construction space should be exhausted, and the quality factor of the ICN benefits from a large volume, yielding a high gain. Therefore, the construction volume should be as large as cost, weight, and size factors will allow. If a lower L_2 is desired compared to a single winding on the maximized toroid, segmentation provides the means to reduce both inductance and resistance at the same rate with a constant Q. Note that this also increases the turns ratio n, causing a higher gain G. Independent of geometric choices, the method of moment based simulation provided accurate results, and the simulated inductance value deviated less than 2.5% from the manufactured ICNs. Two linear ICNs were built based on our presented schematic optimization that fed a floating two-channel HCR, including crosstalk decoupling, for a human-sized MPI head scanner[11] to fulfill safety precautions on a path toward the clinical integration of MPI.

SUPPLEMENTARY MATERIAL

An LTspice simulation (.asc) and a brief guide (.pdf) are provided in the supplementary material. The simulation includes a two-channel ICN transmit chain with and without coupling to investigate HCR behavior and decoupling performance. Its use and configuration are briefly explained in the guide document.

ACKNOWLEDGMENTS

We are very grateful to Christian Findeklee for discussions, proofreading, and initial input on variations of resonant circuit decoupling. The authors would also like to thank Heinz-D. Brüns and Christian Schuster of the Institut für Theoretische Elektrotechnik from the Hamburg University of Technology for providing the CONCEPT-II software and assisting with questions regarding simulations.

This work was supported by the German Research Foundation (DFG, Grant Nos. GR 5287/2-1 and KN 1108/7-1) and the Forschungszentrum Medizintechnik Hamburg (Grant No. 01fmthh2018). The Fraunhofer IMTE is supported by the EU (EFRE) and the State of Schleswig-Holstein, Germany (Project: IMTE, Grant No. 124 20 002/LPW-E1.1.1/1536). Publishing fees are supported by the Funding Program Open Access Publishing of Hamburg University of Technology (TUHH).

AUTHOR DECLARATIONS

Conflict of Interest

The authors have no conflicts to disclose.

Author Contributions

F.M., F.F., F.T., T.K., and M.G. contributed to the conceptualization and theory. F.M. and F.F. performed the simulations and measurements. F.M., F.F., F.T., and M.G. constructed the MPI components. I.S. contributed to the multichannel circuit analysis and decoupling theory. T.K. and M.G. supervised the project. F.M. wrote the original draft with support of M.M., M.G., F.F., F.T., I.S., and T.K. All authors reviewed the manuscript.

Fabian Mohn: Conceptualization (equal); Data curation (equal); Formal analysis (equal); Investigation (equal); Methodology (equal); Software (equal); Validation (equal); Visualization (equal); Writing – original draft (equal); Writing – review & editing (equal). **Fynn Förger**: Conceptualization (equal); Data curation (equal); Formal analysis (equal); Investigation (equal); Methodology (equal); Software (equal); Writing – review & editing (equal). **Florian Thieben**: Conceptualization (equal); Data curation (equal); Formal analysis (equal); Investigation (equal); Methodology (equal); Validation (equal); Writing – review & editing (equal). **Martin Möddel**: Formal analysis (equal); Investigation (equal); Writing – original draft (equal); Writing – review & editing (equal). **Ingo Schmale**: Conceptualization (equal); Investigation (equal); Validation (equal); Writing – review & editing (equal). **Tobias Knopp**: Conceptualization (equal); Funding acquisition (equal); Methodology (equal); Project administration (equal); Resources (equal); Supervision (equal); Writing – review & editing (equal). **Matthias Graeser**: Conceptualization (equal); Data curation (equal); Formal analysis (equal); Funding acquisition (equal); Investigation (equal); Methodology (equal); Project administration (equal); Supervision (equal); Validation (equal); Writing – original draft (equal); Writing – review & editing (equal).

DATA AVAILABILITY

The data that support the findings of this study are available from the corresponding author upon reasonable request.

APPENDIX: SLIGHTLY DETUNED RESONATORS

Let ω_1 and ω_2 be the channel frequencies of channel 1 and 2, respectively, and $\Delta\omega = \omega_1 - \omega_2$. Only ω_1 in channel 1 is excited and we approximate the impedance of the coupled second resonator for small $\Delta\omega$. $R_{s,2}$ is the real part of the resistance of channel 2 at resonance. The first order Taylor series expansion of the impedance of channel 2 yields

$$\begin{aligned} Z_2(\omega_2 + \Delta\omega) &= Z(\omega_2) + \Delta\omega \cdot \left.\frac{\mathrm{d}Z(\omega)}{\mathrm{d}\omega}\right|_{\omega_2} \\ &= R_{s,2} + \Delta\omega\, j\left(L + \frac{1}{\omega_2^2 C}\right) \\ &= R_{s,2} + j2\Delta\omega\, L. \end{aligned} \tag{A1}$$

We insert $L = \frac{1}{\omega_2^2 C}$ which is an expression of the resonance condition $\mathrm{Im}(Z_2) = 0$ at ω_2 for a RLC resonant circuit. Here, L is the sum of all inductances within the circuit. Consequently, we can rewrite (A1) into

$$\begin{aligned} Z_2(\omega_2 + \Delta\omega) &= R_{s,2}\left(1 + j2\frac{\Delta\omega}{\omega_2}\frac{\omega_2 L}{R_{s,2}}\right) \\ &= R_{s,2}\left(1 + j2\frac{\Delta\omega}{\omega_2}Q\right). \end{aligned} \tag{A2}$$

With a $\frac{\Delta\omega}{\omega_2}$ of $\frac{1}{75}$ and a $Q > 200$, we obtain a dominating imaginary part and the equation simplifies to $Z_2(\omega_2 + \Delta\omega) \approx j2\Delta\omega L$.

REFERENCES

[1] B. Gleich and J. Weizenecker, "Tomographic imaging using the nonlinear response of magnetic particles," Nature **435**, 1214–1217 (2005).
[2] P. C. Lauterbur, "Image formation by induced local interactions: Examples employing nuclear magnetic resonance," Nature **242**, 190–191 (1973).
[3] I. Schmale, B. Gleich, J. Rahmer, C. Bontus, J. Schmidt, and J. Borgert, "MPI safety in the view of MRI safety standards," IEEE Trans. Magn. **51**, 6502604 (2015).
[4] O. Dössel and J. Bohnert, "Safety considerations for magnetic fields of 10 mT to 100 mT amplitude in the frequency range of 10 kHz to 100 kHz for magnetic particle imaging," Biomed. Tech./Biomed. Eng. **58**, 611–621 (2013).
[5] B. Gleich, J. Weizenecker, and J. Borgert, "Experimental results on fast 2D-encoded magnetic particle imaging," Phys. Med. Biol. **53**, N81–N84 (2008).
[6] I. Schmale, B. Gleich, J. Schmidt, J. Rahmer, C. Bontus, R. Eckart, B. David, M. Heinrich, O. Mende, O. Woywode, J. Jokram, and J. Borgert, "Human PNS and SAR study in the frequency range from 24 to 162 kHz," in *2013 International Workshop on Magnetic Particle Imaging, IWMPI 2013* (IEEE, 2013), p. 1.
[7] I. N. Weinberg, P. Y. Stepanov, S. T. Fricke, R. Probst, M. Urdaneta, D. Warnow, H. Sanders, S. C. Glidden, A. McMillan, P. M. Starewicz, and J. P. Reilly, "Increasing the oscillation frequency of strong magnetic fields above 101 kHz significantly raises peripheral nerve excitation thresholds," Med. Phys. **39**, 2578–2583 (2012).
[8] Z. W. Tay, D. W. Hensley, P. Chandrasekharan, B. Zheng, and S. M. Conolly, "Optimization of drive parameters for resolution, sensitivity and safety in magnetic particle imaging," IEEE Trans. Med. Imaging **39**, 1724–1734 (2020).

[9] I. Schmale, B. Gleich, O. Mende, and J. Borgert, "On the design of human-size MPI drive-field generators using RF litz wires," in *2015 5th International Workshop on Magnetic Particle Imaging (IWMPI)* (IEEE, Istanbul, Turkey, 2015), p. 1.

[10] T. F. Sattel, O. Woywode, J. Weizenecker, J. Rahmer, B. Gleich, and J. Borgert, "Setup and validation of an MPI signal chain for a drive field frequency of 150 kHz," IEEE Trans. Magn. **51**, 6501703 (2015).

[11] F. Thieben, F. Foerger, F. Mohn, N. Hackelberg, M. Boberg, J.-P. Scheel, M. Möddel, M. Graeser, and T. Knopp, "System characterization of a human-sized 3D real-time magnetic particle imaging scanner for cerebral applications," Commun Eng **3**, 47 (2024).

[12] Z. W. Tay, D. Hensley, J. Ma, P. Chandrasekharan, B. Zheng, P. Goodwill, and S. Conolly, "Pulsed excitation in magnetic particle imaging," IEEE Trans. Med. Imaging **38**, 2389–2399 (2019).

[13] F. Mohn, T. Knopp, M. Boberg, F. Thieben, P. Szwargulski, and M. Graeser, "System matrix based reconstruction for pulsed sequences in magnetic particle imaging," IEEE Trans. Med. Imaging **41**, 1862 (2022).

[14] S. Valtchev, E. Baikova, and L. Jorge, "Electromagnetic field as the wireless transporter of energy," Facta Univ., Ser.:Electron. Energ. **25**, 171–181 (2012).

[15] S. Morita, T. Hirata, E. Setiawan, and I. Hodaka, "Power efficiency improvement of wireless power transfer using magnetic material," in *2017 2nd International Conference on Frontiers of Sensors Technologies (ICFST)* (IEEE, Shenzhen, 2017), pp. 304–307.

[16] S. A. Mirbozorgi, H. Bahrami, M. Sawan, and B. Gosselin, "A smart multicoil inductively coupled array for wireless power transmission," IEEE Trans. Ind. Electron. **61**, 6061–6070 (2014).

[17] J. Yang, Y. Shi, W. Y. Wei, and H. Shen, "A wireless power transfer system based on impedance matching network," Int. J. RF Microwave Comput.-Aided Eng. **30**, e22437 (2020).

[18] Z. Tong, W. D. Braun, and J. M. Rivas-Davila, "3-D printed air-core toroidal transformer for high-frequency power conversion," in *2019 20th Workshop on Control and Modeling for Power Electronics (COMPEL)* (IEEE, Toronto, ON, Canada, 2019), pp. 1–7.

[19] P. Ziegler, J. Haarer, J. Ruthardt, M. Nitzsche, and J. Roth-Stielow, "Air-core toroidal transformer concept for high-frequency power converters," in *PCIM Europe Digital Days 2020; International Exhibition and Conference for Power Electronics, Intelligent Motion, Renewable Energy and Energy Management* (IEEE, 2020), pp. 1–5.

[20] J. Stelzner, G. Bringout, M. Graeser, and T. M. Buzug, "Toroidal variometer for a magnetic particle imaging device," in *International Workshop on Magnetic Particle Imaging (IWMPI)* (IEEE Xplore Digital Library, 2015), p. 1.

[21] K. Bernacki, D. Wybrańczyk, M. Zygmanowski, A. Latko, J. Michalak, and Z. Rymarski, "Disturbance and signal filter for power line communication," Electronics **8**, 378 (2019).

[22] B. Wang and Z. Cao, "Design of active power filter for narrow-band power line communications," MATEC Web Conf. **189**, 04012 (2018).

[23] E. Mattingly, E. Mason, M. Sliwiak, and L. L. Wald, "Drive and receive coil design for a human-scale MPI system," Int. J. Magn. Part. Imaging **8**(1), (published online, 2022).

[24] H. Paysen, O. Kosch, J. Wells, N. Loewa, and F. Wiekhorst, "Characterization of noise and background signals in a magnetic particle imaging system," Phys. Med. Biol. **65**, 235031 (2020).

[25] W. R. Johnson, "Filtering techniques for noise suppression in quasi-balanced circuits," Technical Report No. 32-945, Jet Propulsion Laboratory, 1966.

[26] P. Vogel, M. A. Rückert, C. Greiner, J. Günther, T. Reichl, T. Kampf, T. A. Bley, V. C. Behr, and S. Herz, "iMPI: Portable human-sized magnetic particle imaging scanner for real-time endovascular interventions," Sci. Rep. **13**, 10472 (2023).

[27] J. Borgert, J. D. Schmidt, I. Schmale, C. Bontus, B. Gleich, B. David, J. Weizenecker, J. Jockram, C. Lauruschkat, O. Mende, M. Heinrich, A. Halkola, J. Bergmann, O. Woywode, and J. Rahmer, "Perspectives on clinical magnetic particle imaging," Biomed. Tech./Biomed.Eng. **58**, 551–556 (2013).

[28] M. Graeser, T. Knopp, M. Grüttner, T. F. Sattel, and T. M. Buzug, "Analog receive signal processing for magnetic particle imaging," Med. Phys. **40**, 042303 (2013).

[29] M. Graeser, T. Knopp, P. Szwargulski, T. Friedrich, A. Von Gladiss, M. Kaul, K. M. Krishnan, H. Ittrich, G. Adam, and T. M. Buzug, "Towards picogram detection of superparamagnetic iron-oxide particles using a gradiometric receive coil," Sci. Rep. **7**, 6872 (2017).

[30] H. Radermacher, F. Schrank, D. Pantke, F. Mueller, M. Peters, and V. Schulz, "Highly flexible gradiometer coil arrangement offering improved passive compensation for multi-frequency MPI," Int. J. Magn. Part. Imaging **9**(1), (published online, 2023).

[31] C. McDonough, J. Pagan, and A. Tonyushkin, "Implementation of the surface gradiometer receive coils for the improved detection limit and sensitivity in the single-sided MPI scanner," Phys. Med. Biol. **67**, 245009 (2022).

[32] H. Paysen, J. Wells, O. Kosch, U. Steinhoff, J. Franke, L. Trahms, T. Schaeffter, and F. Wiekhorst, "Improved sensitivity and limit-of-detection using a receive-only coil in magnetic particle imaging," Phys. Med. Biol. **63**, 13NT02 (2018).

[33] J. Weizenecker, B. Gleich, J. Rahmer, H. Dahnke, and J. Borgert, "Three-dimensional real-time *in vivo* magnetic particle imaging," Phys. Med. Biol. **54**, L1–L10 (2009).

[34] Institut für Theoretische Elektrotechnik, *CONCEPT-II v12.0, TET*, 2023.

[35] A. A. Ozaslan, A. R. Cagil, M. Graeser, T. Knopp, and E. U. Saritas, "Design of a magnetostimulation head coil with Rutherford cable winding," Int. J. Magn. Part. Imaging **6**(2), (published online, 2020).

[36] Y. Zhaksylyk, E. Halvorsen, U. Hanke, and M. Azadmehr, "Analysis of fundamental differences between capacitive and inductive impedance matching for inductive wireless power transfer," Electronics **9**, 476 (2020).

[37] I. Daut, S. Hasan, S. Taib, R. Chan, and M. Irwanto, "Harmonic content as the indicator of transformer core saturation," in *2010 4th International Power Engineering and Optimization Conference (PEOCO)* (IEEE, Shah Alam, Selangor, Malaysia, 2010), pp. 382–385.

[38] J. Ramírez-Niño, C. Haro-Hernández, J. H. Rodriguez-Rodriguez, and R. Mijarez, "Core saturation effects of geomagnetic induced currents in power transformers," J. Appl. Res. Technol. **14**, 87–92 (2016).

[39] D. Shmilovitz, "On the definition of total harmonic distortion and its effect on measurement interpretation," IEEE Trans. Power Delivery **20**, 526–528 (2005).

[40] AETechron, "Datasheet: AE Techron 7136 high-speed AC/DC amplifier," AE Techron 7136, 2023.

[41] AETechron, "Datasheet: AE Techron 7224 gradient power amplifier," AE Techron 7224, 2023.

[42] Crown, "Datasheet: XLi series operation manual," Crown Audio by Harman, 2023.

[43] Dr. Hubert, "Datasheet: 4-quadrant precision amplifier A1110-40-QE," Dr. Hubert GmbH, 2023.

[44] I. Micrometals, "Datasheet: Power conversion and line filter applications," Micrometals Powder Core Solutions, 2007.

[45] D. Herceg, K. Chwastek, and D. Herceg, "The use of hypergeometric functions in hysteresis modeling," Energies **13**, 6500 (2020).

[46] P. N. Murgatroyd, "Some optimum shapes for toroidal inductors," IEE Proc. B **129**, 168–176 (1982).

[47] C. Sullivan, "Optimal choice for number of strands in a litz-wire transformer winding," IEEE Trans. Power Electron. **14**, 283–291 (1999).

[48] R. R. Mett, J. W. Sidabras, and J. S. Hyde, "MRI surface-coil pair with strong inductive coupling," Rev. Sci. Instrum. **87**, 124704 (2016).

[49] A. Ayachit and M. K. Kazimierczuk, "Transfer functions of a transformer at different values of coupling coefficient," IET Circuits Devices Syst. **10**, 337–348 (2016).

[50] A. Witulski, "Introduction to modeling of transformers and coupled inductors," IEEE Trans. Power Electron. **10**, 349–357 (1995).

[51] P. Zacharias, *Magnetic Components: Basics and Applications* (Springer Fachmedien Wiesbaden, Wiesbaden, 2022).

[52] A. Zolfaghari, A. Chan, and B. Razavi, "Stacked inductors and transformers in CMOS technology," IEEE J. Solid-State Circuits **36**, 620–628 (2001).

[53] P. Murgatroyd, "The optimal form for coreless inductors," IEEE Trans. Magn. **25**, 2670–2677 (1989).

[54] P. N. Murgatroyd and D. Belahrache, "Economic designs for single-layer toroidal inductors," IEEE Proc. B **132**, 315 (1985).

[55] P. N. Murgatroyd and D. P. Eastaugh, "Optimum shapes for multilayered toroidal inductors," IEEE Proc. **147**, 75 (2000).

[56] P. D. Evans and W. J. B. Heffernan, "Power transformers and coupled inductors with optimum interleaving of windings," Patent EP0547120B1, 1990.

[57] V. D. Shafranov, "Optimum shape of a toroidal solenoid," Sov. Phys.-Tech. Phys. **17**(9), 1433–1437 (1973) (Engl. Transl.).

[58] W. Rogowski and W. Steinhaus, "Die Messung der magnetischen Spannung: Messung des Linienintegrals der magnetischen Feldstärke," Arch. Elektrotech. **1**, 141–150 (1912).

[59] T. Knopp, N. Gdaniec, and M. Möddel, "Magnetic particle imaging: From proof of principle to preclinical applications," Phys. Med. Biol. **62**, R124–R178 (2017).

[60] A. von Gladiss, M. Graeser, and T. M. Buzug, "Influence of excitation signal coupling on reconstructed images in magnetic particle imaging," in *Informatik Aktuell*, edited by A. Maier, T. M. Deserno, H. Handels, K. H. Maier-Hein, C. Palm, and T. Tolxdorff (Springer, Berlin, Heidelberg, 2018), Vol. 211279, pp. 92–97.

[61] Analog Devices Inc., *LTspice v17.1.10*, ADI, 2023.

[62] W. C. Gibson, *The Method of Moments in Electromagnetics* (Chapman and Hall/CRC, Boca Raton, 2008).

[63] MIT Department of Electrical Engineering, *Magnetic Circuits and Transformers: A First Course for Power and Communication Engineers* (The MIT Press, 1977).

[64] J. Hayes, N. O'Donovan, M. Egan, and T. O'Donnell, "Inductance characterization of high-leakage transformers," in *Eighteenth Annual IEEE Applied Power Electronics Conference and Exposition, 2003. APEC'03* (IEEE, Miami Beach, FL, USA, 2003), Vol. 2, pp. 1150–1156.

[65] J. Bohnert and O. Dössel, "Effects of time varying currents and magnetic fields in the frequency range of 1 kHz to 1 MHz to the human body—A simulation study," in *2010 Annual International Conference of the IEEE Engineering in Medicine and Biology* (IEEE, Buenos Aires, 2010), pp. 6805–6808.

[66] E. U. Saritas, P. W. Goodwill, G. Z. Zhang, and S. M. Conolly, "Magnetostimulation limits in magnetic particle imaging," IEEE Trans. Med. Imaging **32**, 1600–1610 (2013).

[67] D. Grau-Ruiz, J. P. Rigla, E. Pallás, J. M. Algarín, J. Borreguero, R. Bosch, G. López-Comazzi, F. Galve, E. Díaz-Caballero, C. Gramage, J. M. González, R. Pellicer, A. Ríos, J. M. Benlloch, and J. Alonso, "Magneto-stimulation limits in medical imaging applications with rapid field dynamics," Phys. Med. Biol. **67**, 045016 (2022).

7

System Characterization of a Human-Sized 3D Real-Time Magnetic Particle Imaging Scanner for Cerebral Applications

To date, no MPI images incorporating a magnetic tracer material within the human body have been produced. A major contribution of this work is the conceptualization, implementation, and characterization of a real-time 3D head scanner and all its individual components required for safe operation in preparation for human in vivo trials in the near future.

Numerous publications contributed to the construction of the MPI scanner characterized in this chapter: The development of software is essential, such as the `Julia` measurement framework [89] and a flexible stack of RPs [90]. To avoid frequency drifts of the signal chain, the idea of active heating of the capacitor banks was presented in 2022 [O20] and the bachelor thesis "Development of an Active Heating Control for Resonance Trimming of Capacitors in Magnetic Particle Imaging" by Vincent Janetschek was completed at our institute at the TUHH on 20.12.2022, which optimized this approach. Parts of this chapter were also presented at the IWMPI 2023 conference in Aachen, Germany [O21]. First authors Thieben, Foerger, and Mohn contributed equally to the following work.

7.1 Nature - Communications Engineering

Manuscript received September 8, 2023.
Accepted March 1, 2024.
Published March 14, 2024.

Type: Open Access. CC-BY-4.0 license.
DOI: 10.1038/s44172-024-00192-6

communications engineering

Article

https://doi.org/10.1038/s44172-024-00192-6

System characterization of a human-sized 3D real-time magnetic particle imaging scanner for cerebral applications

Florian Thieben[1,2,5] ✉, **Fynn Foerger**[1,2,5], **Fabian Mohn**[1,2,5], **Niklas Hackelberg**[1,2], **Marija Boberg**[1,2], **Jan-Philipp Scheel**[3,4], **Martin Möddel**[1,2], **Matthias Graeser**[3,4] & **Tobias Knopp**[1,2,3]

Since the initial patent in 2001, the Magnetic Particle Imaging community has endeavored to develop a human-applicable Magnetic Particle Imaging scanner, incorporating contributions from various research fields. Here we present an improved head-sized Magnetic Particle Imaging scanner with low power consumption, operated by open-source software and characterize it with an emphasis on human safety. The focus is on the evaluation of the technical components and on phantom experiments for brain perfusion. We achieved 3D single- and multi-contrast imaging at 4 Hz frame rate. The system characterization includes sensitivity, resolution, perfusion and multi-contrast experiments as well as field measurements and sequence analysis. Images were acquired with a clinically approved tracer and within human peripheral nerve stimulation thresholds. This advanced scanner holds potential as a tomographic imager for diagnosing conditions such as ischemic stroke (different stages) or intracranial hemorrhage in environments lacking electromagnetic shielding, such as the intensive care unit.

Human-scale magnetic particle imaging (MPI) has the potential to provide background- and radiation-free tomographic images, at high temporal resolution. In comparison, computed tomography (CT) provides high-resolution images at the cost of radiation exposure and is ill-suited for reoccurring or long-term monitoring, whereas Magnetic Resonance Imaging (MRI) suffers from limited patient accessibility and lengthy scan durations. Both modalities come as large and fixed systems, which makes it challenging to use them in an intensive care unit (ICU). The main challenge is that patients usually need to be transported, which is not without risks and requires considerable preparation[1]. In addition, patients are highly encapsulated in MRI systems, making it difficult to monitor their condition[2]. These are also the reasons why portable devices such as chest radiographs and ultrasounds are mainstay imaging modalities in ICUs[3]. Recently, portable MRI systems with low B_0 fields proved the potential of bedside brain imaging devices in the ICU[4,5]. MPI also has great potential in this direction, due to its size and compatibility with the ICU environment. MPI brain images could be acquired inside the ICU, directly at the patient's bed, reducing the workload for medical staff, avoiding transport of the patient, and shortening the time of treatment decisions. As a quantitative and tracer-based imaging modality, MPI is able to visualize the structure of larger blood vessels or quantify tissue perfusion with high temporal resolution, among other diagnostic and therapeutic applications[6]. The potential application in ICUs targets neurovascular diseases like ischemic stroke, intracranial hemorrhage, and traumatic brain injury that require immediate attention and post-treatment monitoring to evaluate the procedure. More than 17 million cases occur each year worldwide and are a leading cause of death and disability[7,8], motivating further research and development.

Currently, MPI is in the process of upscaling[9] the preclinical (small rodent) bore size[10,11] to match human proportions like the head[8,12,13] or extremities[14]. Images are acquired with high spatiotemporal resolution, providing background-free contrast information, based on the nonlinear response of magnetic nanoparticles (MNPs)[15] with high sensitivity[16,17]. Various combined magnetic fields in the low kHz range allow the spatial selection and detection of a tracer, such as the established contrast agent Ferucarbotran from MRI, with up to 46 volumes per second[10]. MPI was shown to be capable of hyperthermia treatment[18,19], stem cell labeling[20], detection of lymph node metastatsis[21], gut bleeding[22] and lung perfusion imaging[23] in murine models, cancer detection[24], as well as being useful in

---

[1]Section for Biomedical Imaging, University Medical Center Hamburg-Eppendorf, Hamburg, Germany. [2]Institute for Biomedical Imaging, Hamburg University of Technology, Hamburg, Germany. [3]Fraunhofer IMTE, Fraunhofer Research Institution for Individualized and Cell-based Medical Engineering, Lübeck, Germany. [4]Institute of Medical Engineering, University of Lübeck, Lübeck, Germany. [5]These authors contributed equally: Florian Thieben, Fynn Foerger, Fabian Mohn. ✉e-mail: f.thieben@uke.de

interventional applications that involve guiding catheters[25,26] and stent positioning[27]. In addition, the MPI tracer can be used as a micro probe for several external and internal parameters that change the signal response, like the carrier medium viscosity[28] and temperature[29]. Furthermore, particle properties like binding state[30], the particle core-size[31,32], or the orientation[33], can be derived and visualized using multi-contrast imaging.

One objective of upscaling MPI scanners is to investigate clinical utility by evaluating the power required to generate the magnetic fields and by assessing the realistic resolution and sensitivity of real-time imaging at this scale. A major challenge is to minimize the scanners power consumption, especially of the selection field (SF)[34], as well as ensuring patient safety in proximity to high-power components. Our approach encompasses these conditions and attempts to combine standard-socket power supply, an unshielded environment and to meet local medical device safety regulations.

In this paper, we describe a human-sized MPI system for brain applications, and verify its functionality in several experiments using a clinically approved tracer[35]. The general scanner concept is based on Graeser et al.[8], although many hardware components were replaced, improved, or re-developed for this version to increase instrumental safety with a focus on future human trials. A major improvement is the realization of 3D imaging by using 2D excitation from two orthogonal drive-field coils (DFCs) and a slow shift of the dynamic selection field to achieve volumetric sampling at 4 Hz. In this work, we describe and analyze the full system design and implementation, including our excitation fields and the measured system matrix, as well as characterize the overall performance of the brain scanner with resolution-, sensitivity-, perfusion-, and multi-contrast experiments.

Our work represents a substantial step towards the clinical application of MPI and may pave the way for monitoring neurovascular diseases within the ICU. The scanner system described is suited for end users, with an adaptable and interactive graphical user interface (GUI), an open-source reconstruction framework, and redundant safety mechanisms, that facilitate performing MPI scans and the live inspection of results. We elaborate on all system components, explain how the magnetic fields are generated, provide insight into our custom signal receive chain, and characterize the imaging performance using the system matrix approach.

Results

System overview

The presented MPI brain scanner is captured in an image in Fig. 1a, and a schematic block diagram is depicted in Fig. 1b. The scanner can be classified into four main parts: operational control (subsubsection “Operational control”), field generation (subsubsections “Field generation and reception, Selection-field generation, and Imaging sequence”), signal reception (subsubsection “Signal reception”), and data processing (subsection “Data processing”), which are briefly introduced in this section for an overview.

The operational control is tasked with coordinating signal generation (digital-to-analog converter (DAC)) and reception (analog-to-digital converter (ADC)). The system devices are driven and coordinated by a collection of open-source software[36,37]. The combined software stack realizes a framework, which is adaptable and scalable to many different MPI applications. The framework accepts user inputs via a command line interface, and, more conveniently, via a GUI (https://github.com/MagneticParticleImaging/MPIUI.jl), that allows different types of measurements to be started, paused, aborted, or stopped. Also, it enables live displaying and analyzing measurement data and controlling and monitoring system devices such as temperature sensors or robots. The acquired MPI signals are stored in the open MPI data format (MDF)[38]. Another part of the operation control is a surveillance unit (SU) for monitoring, based on the micro-controller board *Arduino Mega 2560 Rev3*. It processes sensor data, controls the state of signal relays, and communicates via analog pins with amplifiers, temperature units, and control units, as well as serial communication with the operational software. Some functions, status information and relays are routed to a hardware user console, placed with the human operator, allowing interaction via buttons to activate or deactivate key parts of the system at will.

Field generation is initiated by four DACs, which generate two drive-field (DF) signals and two signals for the dynamic selection field. The DF signal of each channel is connected to a floating transmission chain with a 5th-order band-pass filter that powers the drive-field generator (DFG) via an inductive coupling network (ICN). The DFG is responsible for 2D field excitation in the *xz*-plane (5, 4 mT) and forms a high-quality-factor resonator that is designed to carry high currents at low voltage (referred to as high current resonator (HCR)). The ICN is a toroidal transformer that serves three purposes, high current gain, circuit symmetry, and floating potentials to increase human safety. The dynamic selection field is generated by the selection-field generator (SFG) with two coils mounted on an iron yoke inside a copper cabin, identical to this part of the setup in ref. 8. Identical 10 A coil currents generate a $0.24\,\mathrm{T\,m^{-1}}$ gradient field with a field-free-point (FFP) in the center of the field of view (FOV). By varying these currents, the FFP is moved along the *y*-direction to create a large nominal 3D FOV ($84 \times 85 \times 67\,\mathrm{mm}^3$). The dynamic selection-field current waveform can be chosen to be sinusoidal, or in our case, triangular, for a constant shifting motion with a 4 Hz imaging sequence. This principle is shown in Fig. 1c and explained along with all mentioned fields in more detail in the subsection “Field generation and reception”.

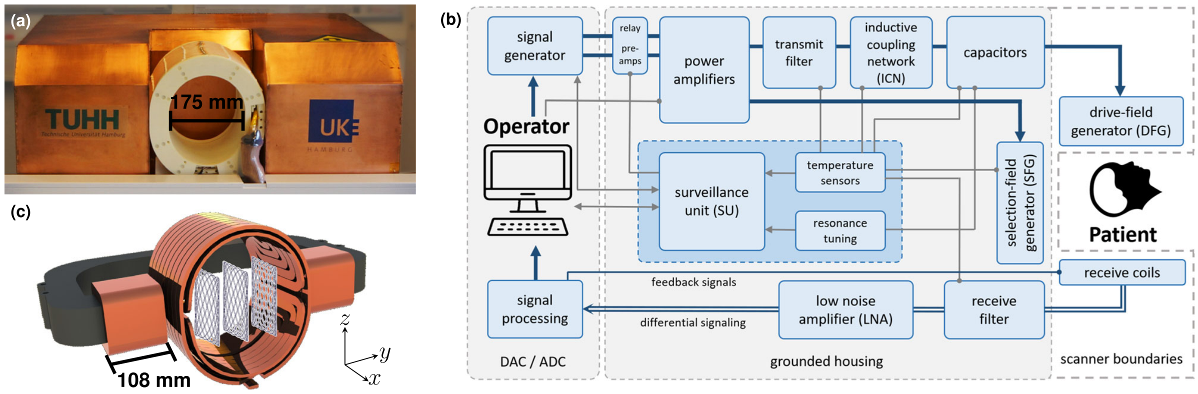

Fig. 1 | General setup of the Magnetic Particle Imaging (MPI) brain scanner. **a** Front view photo with the drive-field generator (DFG) in a white 3D-printed housing. **b** Schematic overview of the entire scanner using a flowchart that illustrates the key system components and their interactions. The digital-to-analog converter (DAC) and analog-to-digital converter (ADC) for signal generation and acquisition are realized by a stack of three RedPitaya STEMlab 125-14. **c** Rendering of the DFG, including the selection-field generator (SFG), which is an iron yoke that creates the dynamic selection field. Individual closed (ideal) 2D Lissajous trajectories are visualized in the *xz*-plane, that are shifted in *y*-direction.

Signal reception is realized with a gradiometric receive coil for feed-through suppression in the x-direction and a saddle coil in the y-direction. Given that both DFCs are orthogonal to the y-direction, this channel is not required to suppress high feedthrough signals by gradiometric turns. Both receive coils are connected to a symmetric fourth-order band-stop filter, transferred to single-ended signals via a balun transformer matching a single-ended custom low noise amplifier (LNA). Signals are then transferred differentially towards the ADCs, which are configured with a receive bandwidth of 976.56 kHz. Furthermore, two more signals are passed to the ADCs for feedback during the control step at the beginning of measurements, that automatically scales the transmit channel currents to match the desired DF strengths.

Data processing describes image reconstruction and further processing steps in the case of perfusion images. For image reconstruction, the system matrix approach is used, implemented by the open-source MPI reconstruction framework[39]. The measured data can be interpreted as multi-patch data corresponding to the selection-field shifts, or as a 3D single-patch dataset. We use a Kaczmarz-solver, system matrix over-gridding (interpolation), L^2-as well as L^1-regularization, background subtraction, and frequency selection to obtain images (see subsubsection "Image reconstruction" for details). These are presented for different experiments with individually tuned reconstruction parameters in the subsection "System characterization". Perfusion images are calculated based on reconstructed 3D volumes that are filtered and processed to obtain the time-to-peak (TTP), mean-transit-time (MTT), relative cerebral-blood flow (rCBF), and relative cerebral-blood volume (rCBV). The definition and details on the implementation can be found in the subsubsection "Perfusion image calculation".

System characterization

To evaluate the performance of the developed MPI brain scanner and its characteristics, several experiments were conducted. We start with a low-level evaluation of the scanner and first study the generated drive field and selection field by using appropriate field measurements. In the next step, we perform an analysis of the acquired system matrix $\boldsymbol{S}$, which allows to derive and predict the imaging performance, independent of specific phantoms. Then, the imaging performance is analyzed at the phantom level using simple sensitivity and resolution phantoms and later also using an application-relevant dynamic perfusion phantom. Finally, the suitability of the scanner for multi-contrast imaging is demonstrated.

Field analysis. The image quality of an MPI scanner is closely linked to the FFP trajectory, which in turn depends on the homogeneity of the drive and selection field. For the presented MPI scanner, the DFG is located in close proximity to the copper shielding of the selection-field generator (see Fig. 1). Hence, the drive field generates eddy currents inside the copper shielding, which in turn influences the field profile of the DFCs. For the selection-field coils, the cross-section area is relatively small compared to the distance between the coils, which leads to field inhomogeneities.

To obtain the actual imaging trajectory, the field profiles of the drive and selection fields can be represented as a spherical harmonic expansion by measuring a few points on a sphere rather than using a Cartesian grid interpolation, as reported by ref. 40. A 1D transmit sequence (0.248 s) at a defined DF amplitude of 5 and 4 mT was used to measure the x- and z-drive field. The dynamic magnetic fields were determined using a calibration robot with a mounted custom 3D coil sensor, with 86 measurement positions of a spherical 12-design[41,42]. Due to the x-receive coil turns at the front of the DFG, the FOV center and, thus the sphere center are shifted by 23 mm in x-direction from the geometric DFG center. In addition, these measurements were used to determine the fundamental total harmonic distortion (THD) of the drive fields[43]. The amplified and filtered DF signal induced into the coil sensor exhibits a THD of 0.0669% and 0.127% for the x- and z-channel, respectively. Regarding the selection field, the field of each coil was examined individually. Due to soft-iron-induced saturation behavior, a list of 2, 4, 6, 8, 10, 12, and 14 A DC currents was set to measure the magnetic field at 36 positions of a spherical eight-design[42] using a three-axis high-sensitivity Hall-effect sensor with a three-channel gaussmeter (Model 460, Lake Shore Cryotronics, Inc., USA). This measurement allowed the adjustment of the relationship between current, gradient strength, and FFP position[40]. In Fig. 2, the field profiles for the x- and z-drive fields are shown in the top rows. Field inhomogeneities become stronger towards the edges of the FOV.

The selection field for identical 10 A currents in both coils is shown in the third row of Fig. 2. The largest gradient is observed in the y-direction, reaching $0.24\,\mathrm{T\,m^{-1}}$. In comparison, the gradients in the x- and z-direction are half as strong, measuring $-0.12\,\mathrm{T\,m^{-1}}$. In the bottom row of Fig. 2, the 2D Lissajous trajectory is shown in the xz-plane for defined selection-field offsets of patches 3, 22, and 33. The trajectory is sampled by marking the FFP after the superposition of all three magnetic fields for certain time points. For visualization, the density of the trajectory is adapted by changing the frequency ratio to $\frac{16}{15}$. In the background, the selection field of each patch is shown in the xz-plane. From the measurements, the calculated 3D DF FOV spans a volume of $83 \times 80 \times 73\,\mathrm{mm}^3$.

System matrix analysis. In the next step, the imaging performance of the scanner is analyzed by studying a measured system matrix, which will later also be used for image reconstruction. The system matrix was acquired using a robot-based approach with a cubic 200 µL δ-sample filled with *Resotran* (b.e.imaging GmbH, Germany) in a concentration of $8.5\,\mathrm{mg_{Fe}mL^{-1}}$ ($152\,\mathrm{mol\,L^{-1}}$) to prevent magnetic dipole-dipole interactions[44]. The sample was shifted to $15 \times 15 \times 11$ positions covering a volume of $140 \times 110 \times 100\,\mathrm{mm}^3$, and at each position, one full 3D sequence (0.248 s) was applied. For later background subtraction and SNR analysis, 12 empty measurements after each xy-plane were performed by moving the sample with the calibration robot outside the scanner bore. During the acquisition, the DF feedback was tracked and the observed amplitudes and phases showed a standard deviation of below 0.4% over the 2491 measurements. All signals are considered in frequency space, which is common in MPI since it allows for direct filtering of interfering signals like the signal induced by the drive field.

The measured system matrix can be interpreted in two different ways. First, since the FFP movement induced by the selection-field generator is very slow, the data can be interpreted as a multi-patch dataset, where the 2D Lissajous trajectory (xz-plane) is slowly shifted to $M_y = 85$ positions along the y-axis. One can thus expect that the system-matrix patterns are just shifted in space, which was shown for idealized magnetic fields by refs. 45, 46. The measured system matrix considering this multi-patch processing is illustrated in Fig. 3. Shown are frequency patterns i.e., system matrix rows reshaped on the 3D grid at frequencies $f_k^{\mathrm{MP}} = k\Delta_f^{\mathrm{MP}}$ where $\Delta_f^{\mathrm{MP}} = \frac{1}{T_{\mathrm{cycle}}^{\mathrm{MP}}} \approx 342.654$ Hz is the frequency spacing derived from the 2D Lissajous sequence length $T_{\mathrm{cycle}}^{\mathrm{MP}} \approx 2.918$ ms and $k \in \mathbb{N}$ is the frequency index. The index k can be expressed using the mixing factors m_x and m_z as $k_{m_x,m_z} = m_x M_x + m_z M_z$ where $M_x = f_x^{\mathrm{DF}} T_{\mathrm{cycle}}^{\mathrm{MP}} = 76$ and $M_z = f_z^{\mathrm{DF}} T_{\mathrm{cycle}}^{\mathrm{MP}} = 75$, see ref. 47. The figure shows on the left selected frequency patterns $((f, m_x, m_z) \in \{(51.4\,\mathrm{kHz}, 2, 0), (102.8\,\mathrm{kHz}, 4, 0), (155.22\,\mathrm{kHz}, 3, 3)\}$ of the x-receive chain and on the right of the y-receive chain. Each pattern is visualized using an iso-surface rendering (lower left) and three orthogonal slices (upper left: xz, upper right: yz, lower right: xy) where the dotted line indicates the slice position. The complex-valued colormap encodes the amplitude in the saturation and the phase in the color[48]. In the middle part of the figure, the mean SNR over all patches is shown as a function of frequency. To illustrate both, the global and the local SNR progression is plotted for different frequency ranges. The lower part of the figure shows a 3D iso-surface rendering of frequency component 102.80 kHz combined with the actual FFP trajectory derived from the measured fields for the three considered patches. The measured system matrix shows the expected wave-like structure in which the number of extrema depends on the mixing factors[49]. For $m_x = 3$, $m_y = 3$ one can see oscillating

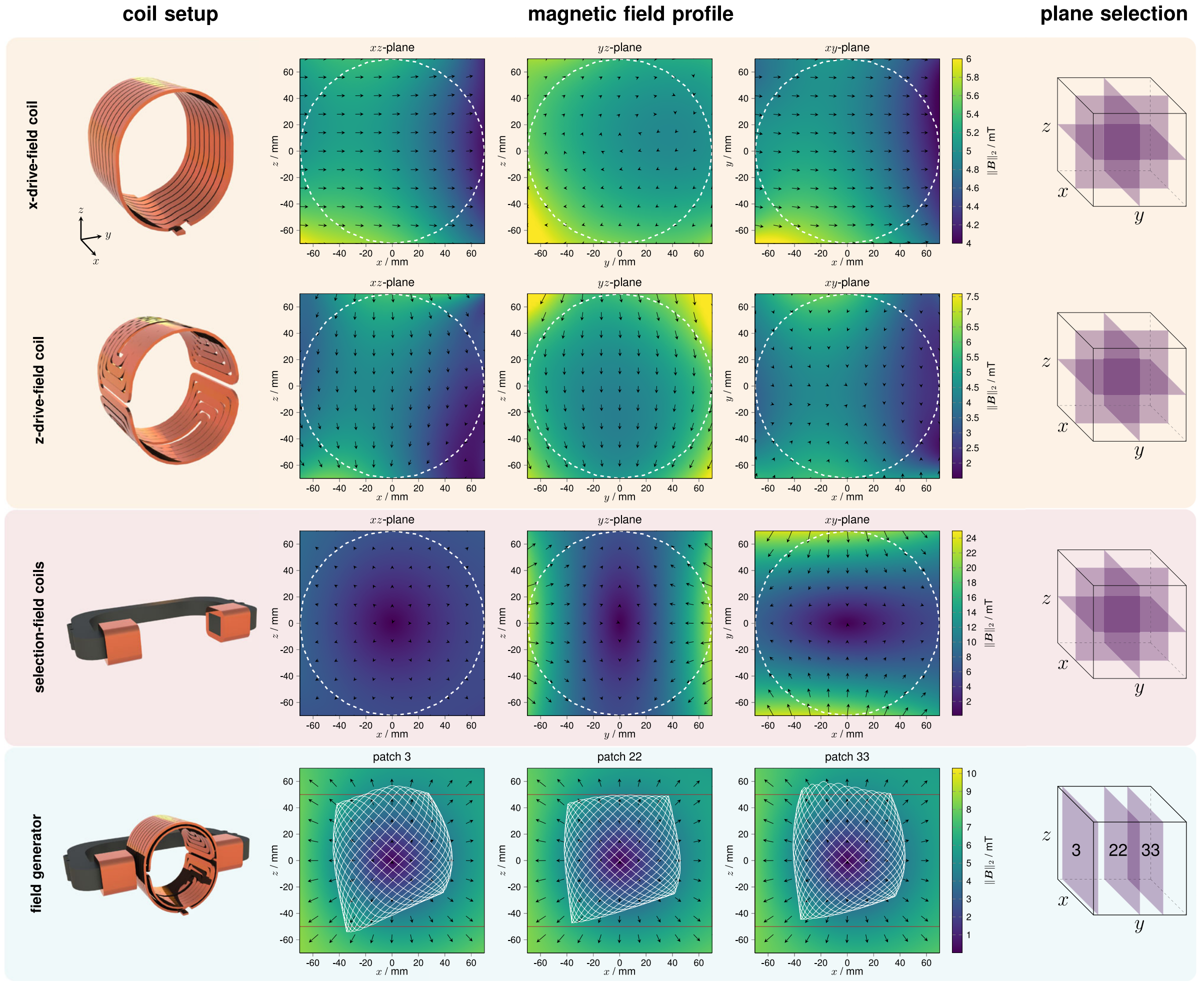

Fig. 2 | Field analysis of the magnetic field-generating coils. The field-generating coil setups are shown with the measured corresponding magnetic field profiles and an illustration of the respective planes. The drive field of the x- and z-channel and the selection field are plotted individually. All fields were measured on a sphere utilizing a three-axis field sensor within the actual setup. For better visualization, the copper shielding between selection-field coils and drive-field coils is not shown. With respect to the entire field generator, the drive-field trajectory of patches 3, 22, and 33 is displayed in the xz-plane, while the background features the corresponding selection field shifted in the y-direction. For visualization, the frequency ratio is adapted to $\frac{16}{15}$ and the system matrix field of view is outlined in red.

patterns in x- and z-direction, which shows that the sequence spatially encodes both directions. When considering the patch movement, it is clearly visible that the frequency patterns are shifted when the FFP sweeps slowly in the y-direction. However, slight distortions of the patterns are observable, which are caused by field imperfections and violate the true shift-invariance of the system.

Next, we consider the system matrix not as a multi-patch dataset but as a single-patch dataset. This is possible because there are no temporal gaps in the sequence, and thus the sequence can be considered to be 3D with fast FFP movement in the xz-plane and slow FFP movement in the y-direction. In turn, the sequence time increases to $T^{\mathrm{SP}}_{\mathrm{cycle}} = M_y T^{\mathrm{MP}}_{\mathrm{cycle}} \approx 248.06$ ms and the frequency spacing in turn decreases to 4.031 Hz. This means that the single-patch spectrum contains much more frequencies (factor M_y) but that the patch-encoding dimension is lost. This is illustrated in Fig. 4, which now shows in the SNR plot a signal with two levels of sub-bands. The SNR is slightly higher compared to the multi-patch case since an implicit averaging takes place when applying the Fourier transform to the longer time interval. In the single-patch case, the signal occurs at frequencies $f^{\mathrm{SP}}_k = k\Delta^{\mathrm{SP}}_f$ and the frequency index k can now be expressed as $k = m_y + M_y(m_xM_x + m_zM_z)$ where m_y is now a new mixing factor that encodes the finest level of frequency shifts. The upper part of Fig. 4 shows selected frequency components for various mixing factors sampling different sub-bands of the frequency space. Again, the expected wave-like patterns are visible, but this time the patterns do not only surround the trajectory plane, but cover the entire FOV and also show oscillating structures in the y-direction. The lower part of the figure shows the frequency component 102.7 kHz of the x-receive chain in combination with the full 3D FFP trajectory from three different angles. One can again see that both the system matrix pattern and the trajectory are rotated within the xz-plane due to field imperfections.

Sensitivity and spatial resolution experiments. To determine the sensitivity of the MPI scanner, we implemented the protocol using three different spatial positions developed in ref. 16. First, a dilution series of the tracer *Resotran* was prepared with 50 µL samples inside 200 µL Eppendorf tubes and ascending iron mass between 4 and 512 µg. Applying one full 3D sequence (0.248 s), eight samples were measured at three spatial locations each, positioned along the y-axis. This facilitates a distinction between the sample signal and reconstruction artifacts. The reconstruction results are shown in Fig. 5a for several iron masses. The spatial position can be resolved down to 8 µg iron. At 4 µg iron, a blurred dot can be seen, but its position does not change for different sample positions indicating that the seen dot is caused by the system background

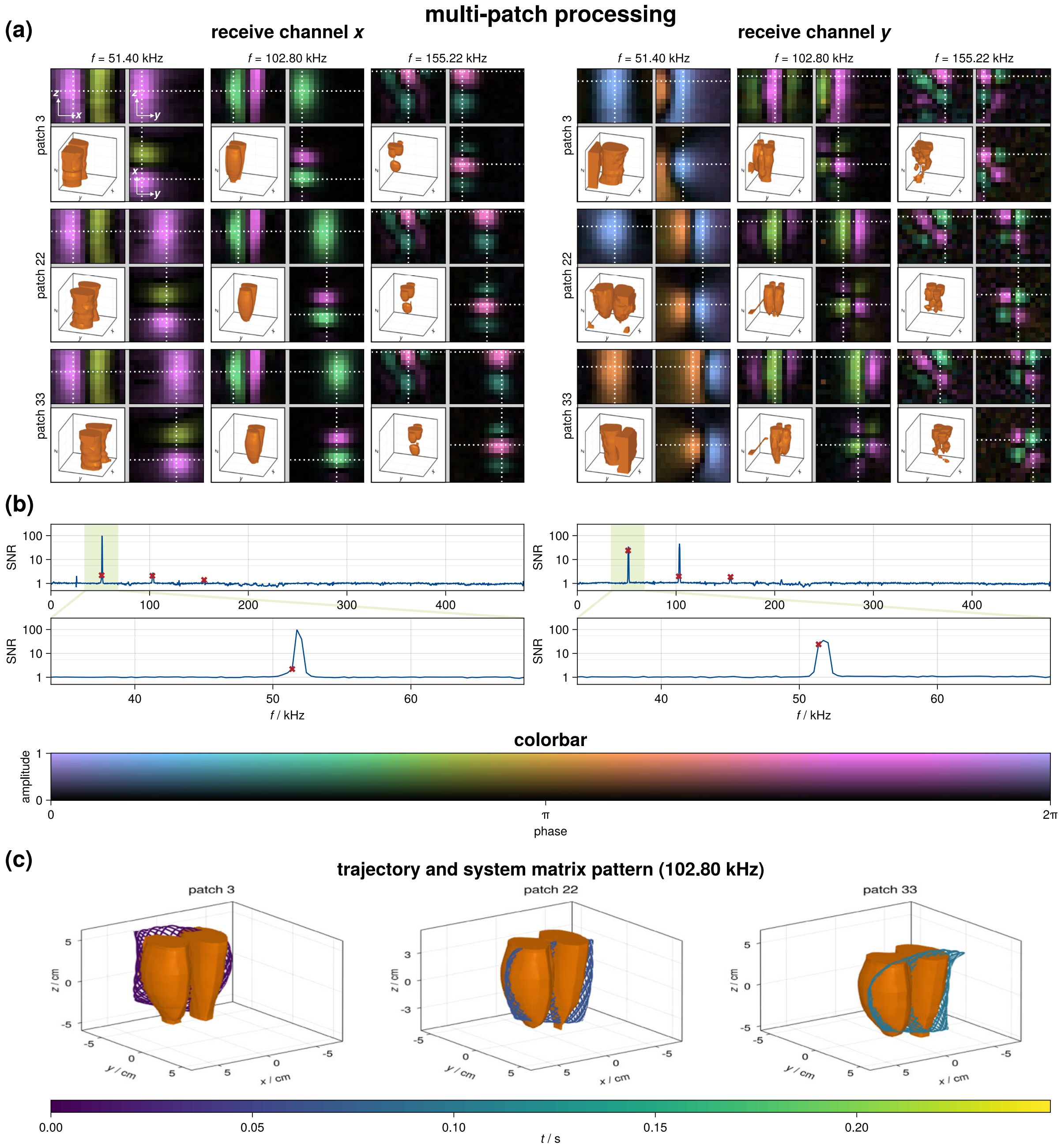

Fig. 3 | Measured system matrix considering a multi-patch processing. a Selected frequency components for the x-(left) and the y-(right) receive channel. Each 3D frequency component is visualized by plotting three orthogonal slices and an isosurface rendering of the magnitude. The slice position is indicated as a white dotted line, while the frequency component is shown for three different patch positions ($p \in \{3, 22, 33\}$). **b** Signal-to-noise ratio (SNR) of the system matrix rows as a function of frequency. The SNR is visualized in a hierarchical fashion using two different nested frequency ranges, which are indicated by light green boxes. **c** 3D isosurface rendering in combination with the actual field-free-point trajectory for the considered patch and one selected frequency component. Here, the color encodes the time within the full imaging sequence.

and not by the sample itself. Thus, the detection limit of the scanner is reached at 8 µg iron.

For quantitative analysis, a post-processing step sums the reconstructed particle concentration within the mask around the sample position and multiplies it by the iron mass of the system matrix δ-sample. The results are shown in Fig. 5b. At higher iron mass, the reconstructed iron content matches the applied iron content. For lower iron mass, below 32 µg, the reconstructed particle concentration becomes smaller than expected.

To assess the spatial resolution, a 200 µL δ-sample of *Resotran* with 8.5 $\mathrm{mg_{Fe}mL^{-1}}$ (152 mol $\mathrm{L^{-1}}$) iron was placed in the FOV center. A second, identical δ-sample was mounted on a rod, which could be positioned by a calibration robot. The latter was moved directly next to the centered sample. After imaging using the 3D sequence (0.248 s) without frame averaging, the edge-to-edge distance was increased by 0.5 mm until reconstruction could discriminate the two samples. This procedure was performed for all three main axes. For better reconstruction results, the system matrix grid was

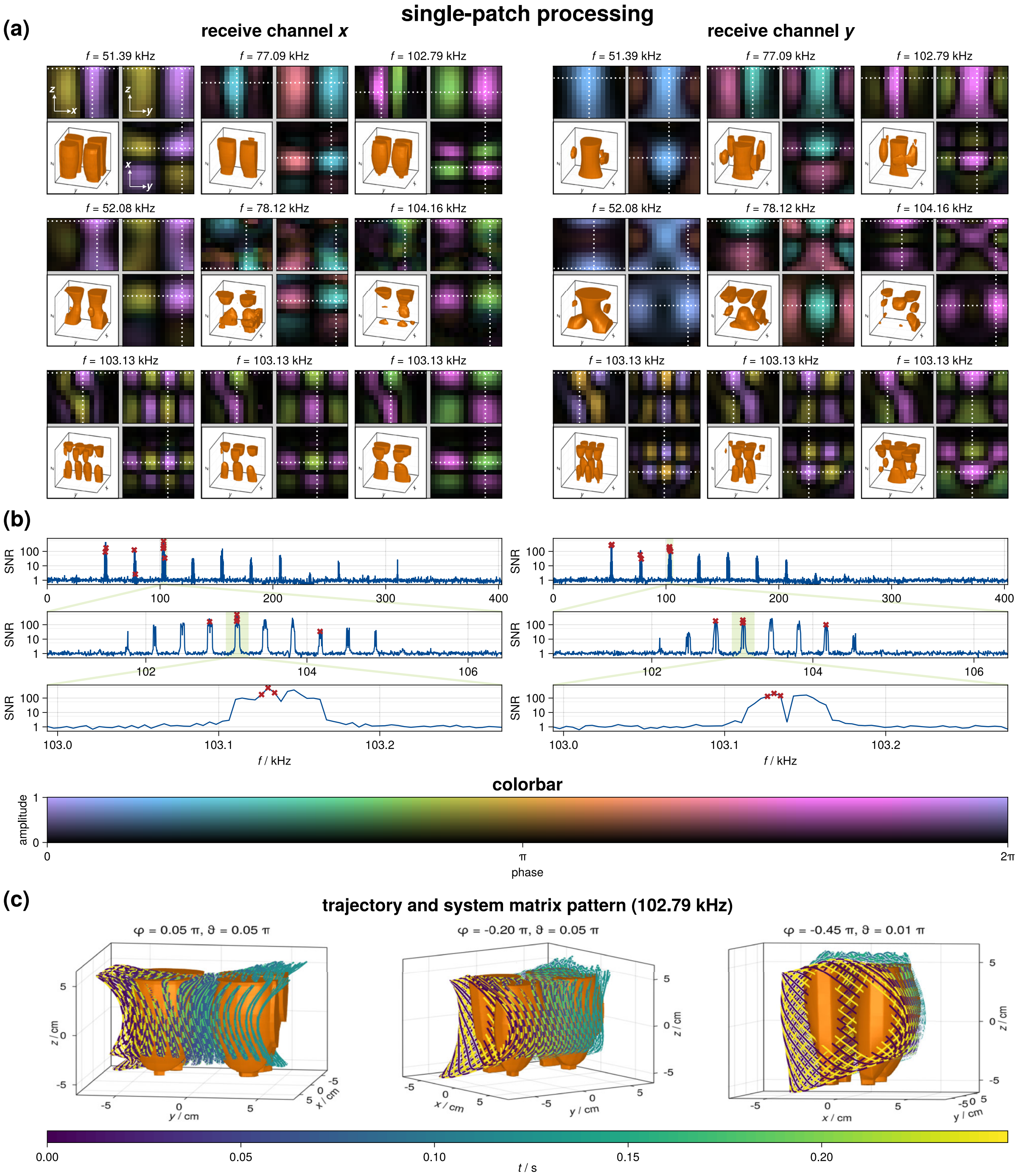

Fig. 4 | Measured system matrix considering a single-patch processing. **a** Selected frequency components for the x-(left) and the y-(right) receive channel. Each 3D frequency component is visualized by plotting three orthogonal slices and an iso-surface rendering of the magnitude. The slice position is indicated as a white dotted line. **b** Signal-to-noise ratio (SNR) of the system matrix rows as a function of frequency. The SNR is visualized in a hierarchical fashion using three different nested frequency ranges, which are indicated by a light green box. **c** For one selected frequency component, the 3D iso-surface rendering in combination with the actual field-free-point trajectory, viewed from three different angles, is shown. Here, the color encodes the time within the imaging sequence.

interpolated to $25 \times 25 \times 19$. The image signal was summed up over three voxels inside a mask around the direction of interest to generate profile lines. The reconstruction was defined to be resolved if the profile line dropped below half the maximum in the middle between the two samples. In Fig. 5c, the resolved reconstructions are shown for a half and quarter maximum criterion for all the directions. Additionally, the profile lines are shown in the reconstructed images. With the half maximum definition, the best spatial resolution is found in the y-direction with 6.7 mm, followed by 11.2 mm in x- and 31.2 mm in z-direction.

Dynamic perfusion experiments. For the analysis of volumetric imaging at high temporal resolution, we used a flow phantom filled with glass

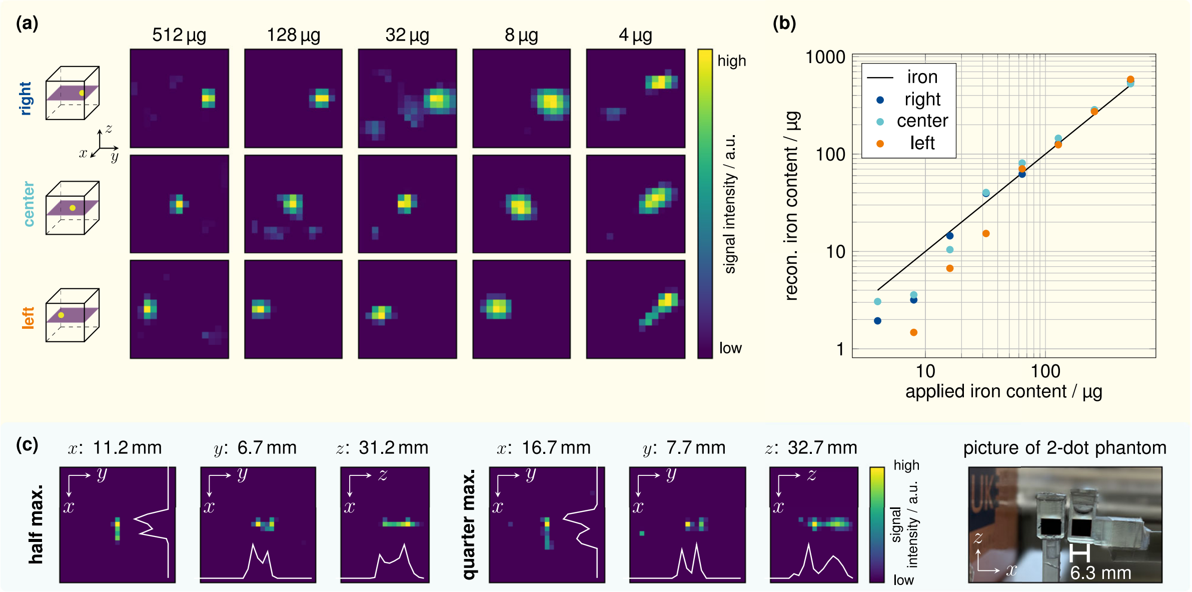

Fig. 5 | Sensitivity study and spatial resolution experiments. **a** Reconstruction results for the sensitivity of descending iron contents inside a 200 µL Eppendorf tube with 50 µL volume of tracer in the central *xy*-plane for multiple positions. **b** For each iron content and each position, the quantitative reconstructed iron content is mapped to the applied iron content. **c** For the spatial resolution experiment using *Resotran*, two δ-samples (200 µL each, 8.5 $\mathrm{mg_{Fe}mL^{-1}}$ (152 mol $\mathrm{L^{-1}}$)) were used. An edge-to-edge distance was achieved by placing one sample in the center of the field of view, while the other was moved by the calibration robot to defined positions with increasing distance (0.5-mm steps). Images were recorded using the 3D sequence with dedicated *x*- and *y*-receive channels, and reconstructions are based on a single frame (one average) with an interpolated grid 25 × 25 × 19. The spatial resolution was considered successful when the profile line in the middle between the two samples dropped below the half maximum (white line). Results for a quarter maximum criterion are shown as well.

spheres and bolus injections of *Resotran*. The phantom in this experiment is similar to the one developed by ref. 8. It consists of two tubes with a volume of 50 mL each, filled with 1 mm diameter glass spheres to simulate capillaries within the tissue. Two rods are placed inside the tubes with evenly distributed holes facing opposing directions, as shown in Fig. 6 on the top right. The tubes represent the two hemispheres of the brain and each tube is connected to a peristaltic pump, which uses suction to deliver an adjustable flow rate that is independent of the other hemisphere. Five experiments were conducted with different average flow rates: While the flow rate in the right hemispheres remained constant at 100 mL $\mathrm{min^{-1}}$, 0, 25, 50, 75, and 100% stenosis was obtained for the left hemisphere by reduced flow rates. Prior to experiments, the overall flow rates of outlets A and B were precisely matched by independent reference experiments to compensate for pressure differences. Applying the 3D sequence (0.248 s), each experiment was measured over 150 frames (37.2 s) and a 100 µL bolus of pure *Resotran* (28 $\mathrm{mg_{Fe}mL^{-1}}$) was administered. For imaging, the same 3D sequence was used for the sensitivity and resolution experiments, which is described in detail in the subsubsection “Imaging sequence”. During the perfusion measurements, the observed drive field showed a standard deviation below 0.3% over the 150 consecutive frames without additional control steps. The data processing is divided into a reconstruction step, described in the subsubsection “Image reconstruction”, and a post-processing step that is built upon the reconstruction results and yields different perfusion parameters, as described in detail in the subsubsection “Perfusion image calculation”. For the reconstruction, the system-matrix grid size was interpolated to $N = n_x \times n_y \times n_z = 25 \times 25 \times 18$ voxels. The reconstruction results revealed that the relevant data for the post-processing step ended after $t = 25$ s.

The results are illustrated in Fig. 6. They indicate that fast dynamic imaging is feasible and different levels of stenosis can be detected and distinguished through calculated perfusion maps. Throughout the referenced figure, a transversal 2D slice is shown, and its relative position is indicated in the picture of the phantom on the right side. This slice is exemplary for the entire 3D tomogram. The time response graphs in the leftmost column show reconstructed data for voxel A and B, prior to Hann-filtering. Post-processing produced the 3D TTP, MTT, rCBF, and rCBV maps, and the definitions of each perfusion parameter are sketched above each column. In the case of stenosis, the flow suppression is visualized by a delayed signal peak in the TTP map and an increasing transit time in the MTT map (dark colors). Relative blood flow and volume decrease with the severity of the stenosis, which is revealed by lighter colors and a smaller area of outlet A. The decreasing area can be attributed to the threshold mask, which eliminates values below 10% of peak intensity. Slight differences in MTT or rCBV in the case of equal flow rate (0% stenosis) are caused by variations of the phantoms, their filling, and air cavities, which all influence the internal flow. The entire set of four perfusion parameters reveal not only changes due to the stenosis, but also the increments of these changes become visible in each perfusion map.

Multi-contrast experiments. To demonstrate the ability of multi-contrast imaging within the MPI brain scanner, a simple two-dot phantom and two different tracers were chosen. The δ-samples of *Resotran* and *synomag* (micromod Partikeltechnologie, Germany) contained 200 µL each with an iron concentration of 8.5 $\mathrm{mg_{Fe}mL^{-1}}$ (152 mol $\mathrm{L^{-1}}$). For this proof-of-concept, applying the 3D sequence (0.248 s), two system matrices were recorded in the *xy*-plane on a 15 × 15 × 1 grid with a system matrix FOV of 140 × 110 $\mathrm{mm^2}$ in *x*- and *y*-directions. The δ-samples were used for the imaging experiments, mounted on a 3D-printed platform, and inserted by a calibration robot into the center of the scanner. The imaging sequence was the same as in all other experiments above. A single frame was recorded and reconstructed, using background subtraction. Reconstruction followed the protocol described in the subsubsection “Image reconstruction”, with the only difference that two measured system matrices are passed to the Kaczmarz-solver to separate the signal contributions of each tracer sample[31].

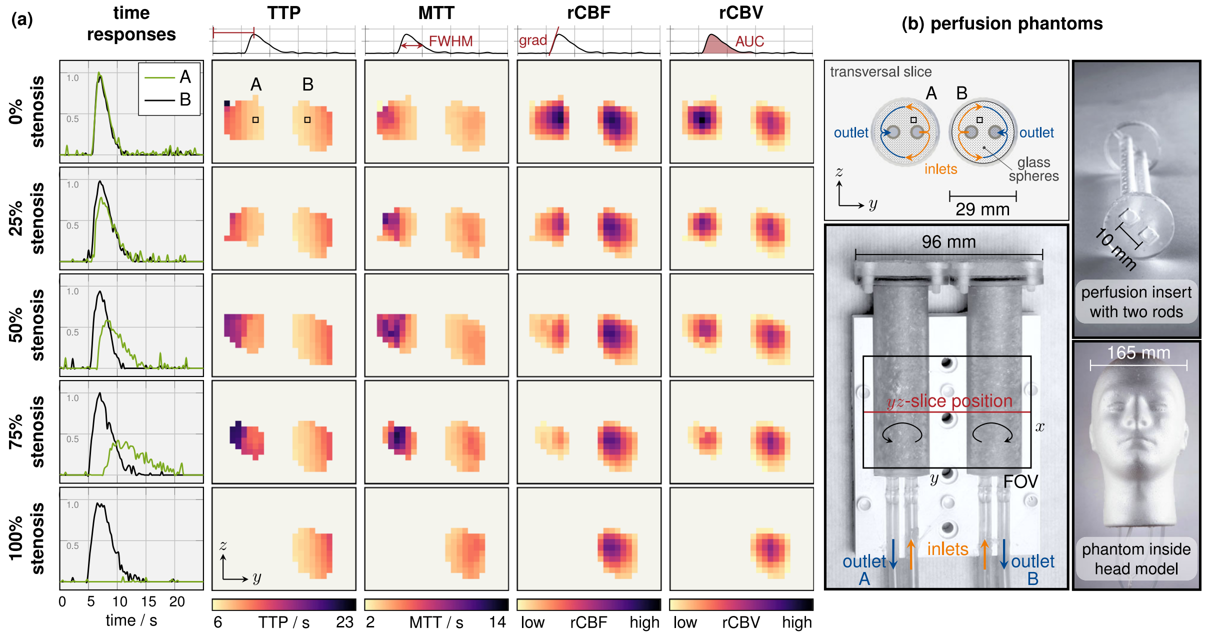

Fig. 6 | Perfusion experiment for fast dynamic imaging. b Two cylinders represent the left and right hemispheres of the brain. Each 50 mL cylinder is filled with 1 mm diameter glass spheres. Inside the cylinder is a perfusion insert with two perforated rods, one connected to the inlet (orange) and the other connected to the outlet (blue). They contain multiple holes on opposite sides to mimic tissue perfusion. **a** Perfusion parameters after bolus injection are visualized for the transversal *yz*-slice, that is depicted throughout the reconstructed images. The bolus contained 100 µL of pure *Resotran* (28 $\mathrm{mg_{Fe}mL^{-1}}$). The measurements were acquired with the 3D sequence. Different levels of stenosis in 25% of steps were simulated by using two independent peristaltic pumps, connected to one output each. The suction was regulated to match a flow rate of 100 $\mathrm{mL\,min^{-1}}$ for the healthy brain half (on the right in each case). For the highlighted voxels A and B, the time responses of the normalized concentration are shown. From the data of the time responses, TTP the time-to-peak, MTT mean-transit-time, rCBF relative cerebral-blood-flow, and rCBV relative cerebral-blood-volume perfusion maps were calculated. These calculations are based on the maximum peak identification, on the full width at half maximum (FWHM), on the gradient (grad), and on the area under the curve (AUC). The rCBF and rCBV were normalized to the maximum value in the imaging volume. All time data were shifted to the arrival time of the bolus.

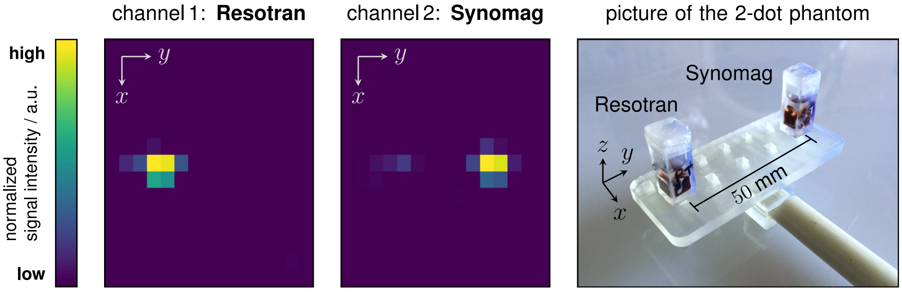

Fig. 7 | Multi-contrast experiment, using *Resotran* and *synomag*. The two δ-samples (200 µL each, 8.5 $\mathrm{mg_{Fe}mL^{-1}}$) were separated by a distance of 50 mm. The image was recorded using the 3D imaging sequence with *x*- and *y*-receive channels, and the reconstruction is based on a single frame (one average). In *x*-direction, the field of view size is 140 mm, while in *y*-direction, it is 110 mm. For each tracer channel (system matrix), the signal intensity is normalized individually. However, the MPI-tailored tracer *synomag* has a stronger particle response. Overall, the separation of the tracer samples was successful.

The resulting concentrations for both reconstruction channels are shown in Fig. 7, along with a picture of the phantom. Both δ-samples are correctly depicted in their respective channel and spatially separated. In the *synomag* channel, a residual signal from the *Resotran* sample can be observed. However, this channel leakage is small compared to the intrinsic signal of the *synomag* sample.

Discussion

In this study, we investigated a human-sized MPI brain scanner designed to provide 3D imaging with high spatial resolution, 4 Hz temporal resolution, and with a focus on enabling the detection of neurovascular diseases. We achieved a resolution of 12 mm in *x*-, 7 mm in *y*-, and 31 mm in *z*-direction using the clinically approved Ferucarbotran tracer *Resotran*. Moreover, our scanner was able to detect an iron dose down to 8 µg. Perfusion experiments were performed and images reveal that five levels of stenosis (25% increments) can be differentiated. Furthermore, we were able to discriminate *Resotran* and *synomag* within the same FOV in multi-contrast images. Instrumentation safety was a major focus in the design and implementation of the transmit- and receive chains, as well as obtaining a 3D imaging sequence that samples a 480 mL volume. The scanner can potentially be used in an ICU due to its manageable total power consumption of less than 4 kW and its robustness to electromagnetic interference in an unshielded environment.

Imaging capabilities

The spatial resolution of an MPI system is an elaborate interaction of gradient-field strength and drive field[50], imaging sequence[51], magnetization response of particles[50], and the receive chain[49]. All measurements were obtained at a DF amplitude of 5 mT in *x*- and 4 mT in *z*-direction, with a gradient strength of 0.24 Tm^{-1} in *y*-direction (measured in the FOV center). Despite being orthogonal to both DF directions, the best spatial resolution of 7 mm was found in the *y*-direction. It benefits from a stronger gradient strength, the dedicated receive coil, and the multi-patch excitation sequence. The *x*-direction benefits from being aligned with one of the DF directions and a dedicated receive coil, but we observe only about half the gradient strength. This culminates in a spatial resolution of 12 mm. Due to the lack of a dedicated receive coil and the same gradient strength as in *x*, the spatial resolution in the *z*-direction is inferior at 33 mm, although it aligns with a DF direction. In terms of sensitivity, a dilution series measured at different positions was required. In contrast to other imaging modalities, noise in MPI can lead to structured image artifacts. For low iron amounts, superimposed noise in combination with strong regularization parameters for the reconstruction algorithm, structured image artifacts structured image artifacts may occur[16].

Compared to the previous version of the head scanner[8], we reached a detection limit of 8 μg_{Fe}, whereas the old limit was 2 μg_{Fe}. However, this does not imply that the redesign has a lower sensitivity by a factor of 4, since a direct comparison does not prove to be feasible due to the differences in the experimental configuration and particle system. The reasons for an expected reduction of the sensitivity and spatial resolution are the topology of the imaging sequence that samples a 3D volume in the current version instead of a 2D slice. On the other hand, our new imaging sequence is only half as long, and the signal intensity of the tracer *Resotran* is lower than *perimag* (micromod Partikeltechnologie, Germany), which implies that the actual sensitivity difference is lower.

The dynamic perfusion experiment takes full advantage of the temporal resolution of 4 Hz and its 3D imaging capability. Setting realistic flow rates of 100 mL min^{-1}, we were able to visualize a bolus passing through our perfusion phantom[52]. In terms of temporal resolution, we calculated four different perfusion parameters in five different levels of stenosis. The spatial resolution of our scanner is sufficient to separate the left and right brain hemispheres in all experimental settings. However, the resolution required to image the cerebral vasculature (brain angiography) is not yet achieved. In a clinical scenario, the size of this bolus would need to be increased, due to the amount of blood delivered to the brain from an intravenous bolus (fraction of 15 to 20%[53]). Assuming a fraction of 20%, the amount of administered boli would be restricted to about 3 per prefilled vial (1.4 mL), although limitations depend on body mass and metabolism[54,55]. A plausible long-term monitoring scenario would require a larger number of administrable boli, to facilitate interventions and evaluate treatment success afterwards. To increase the number of boli, we could reduce the bolus concentration, as the ability of perfusion parameter calculation is likely possible for lower signal strengths of the time response curves. A specifically tailored MPI tracer, which could be clinically approved in the future, would increase the measurement signal leading to a lower iron dose per bolus. A complementary approach could make use of negative boli to increase the total number of administrable boli[56].

Multi-contrast imaging was performed utilizing the clinically approved tracer *Resotran* and the MPI-tailored tracer *synomag*. For this proof-of-concept, we used 200 μL samples at a concentration of 8.5 $\mathrm{mg_{Fe}mL^{-1}}$ (152 mol L^{-1}) and a single measurement without averaging. We observe minor channel leakage in the multi-contrast tomogram, which is typical for multi-contrast imaging[31]. In general, the underlying phenomena for the observed channel leakage in multi-contrast imaging needs to be further investigated. However, localization and discrimination of both samples was successful and has the potential to provide additional information like temperature in hyperthermia[29,57].

All experiments in this work have been performed at least twice to ensure reproducibility. Qualitatively, no significant difference could be found. The system-characterizing values obtained from the experiments are given without an accuracy estimate, but provide a good estimate of the corresponding order of magnitude. Future applications can use the high frame rate of the scanner to aggregate and statistically evaluate the acquired data.

Reconstructions of the presented results were performed retrospectively on the stored measurements. However, the operational control and data processing software makes it possible to reconstruct online. Although the software is not yet optimized for this use case, the GUI is able to perform online reconstruction with a latency of less than one second between signal acquisition and image visualization. Further latency reduction could be achieved by accessing the measurement data earlier in the processing pipeline and by adapting additional methods from ref. 58.

Common to the imaging sequence of the current and old scanner version, is the combination of a slow selection-field shift in *y*-direction with fast orthogonal DF excitation. The old scanner used a 1D drive field in the *x*-direction, which results in an imaging trajectory that samples a 2D FOV in the *xy*-plane at 2 Hz. In contrast, the current design uses a Lissajous-type DF excitation in *xz*-plane, sampling a 3D FOV (480 mL; the volume of an adult human brain is about 1200 mL[59]) at 4 Hz. We note that both sampling trajectories are redundant by a factor of two since they contain a sweep along the positive and negative *y*-direction. This yields the potential to increase the frame rate by a factor of two when reconstructing the two halves independently, as has been proposed by ref. 60. A major improvement of the redesign is the extension of the FOV to a 3D volume, sampled at twice the frame rate, which is a leap towards imaging the entire human brain. Prototypes of multi-coil iron core selection-field generators are in development, that further enlarge the FOV and extend the space of feasible imaging sequences[34,61].

Device safety

The presented scanner in this work uses the same selection-field yoke as the prior version by ref. 8, however, all other major hardware components (the DFG, ICN, HCR, transmit, and receive chain) were redesigned for this scanner upgrade to achieve 3D imaging and focus on human safety. To this end, the limitation of high voltages in the vicinity of the imaging volume and the implementation of an independent surveillance unit were key concerns.

On a path toward human trials, safety concerns and regulations regarding the specific absorption rate (SAR), peripheral nerve stimulation (PNS), and conductors in patient proximity influence the scanner design, and imaging sequence and limit maximum magnetic field strengths. The SAR limitations in the head are given with 3.2 W kg^{-1} for the chosen DF frequencies in the kHz range[57,62]. However, for sinusoidal electric fields below 100 kHz, PNS concerns prevail and are the limiting factor for alternating field strengths[63–65]. Heeding PNS limitations, the maximum DF amplitude was set to 5 mT, which is realistic for human trials[66,67]. Compared to MRI gradients, the maximum slew rate of the dynamic selection field ($\approx$24 $\mathrm{Tm}^{-1}\mathrm{s}^{-1}$) is very low and below the risk threshold for PNS[68,69]. In MRI, all ferromagnetic components must be excluded from entering the scanner, including pacemakers, mechanical ventilators and oxygen cylinders[1]. Potentially, this does not apply to our scanner, due to the confinement of high magnetic fields within the head region only. Further investigations on specific device compatibility are required.

Electrical safety regarding shock and discharge, are mainly addressed by reducing the inductance of the DFG. The necessary power to obtain the same field strength is thus provided by a high coil current, which creates a maximum voltage of 535 V (240 A at 5 mT, 14.4 μH) that is a reduction of a factor of about 4 compared to the previous version of the DFG[8]. To achieve the capability to conduct around 300 A with Litz wire, we used Rutherford wire parallelization in both DF coils, which also minimizes the proximity effect. Moreover, the polyamide housing of the DFG provides dielectric isolation and increases breakthrough voltage between DFG components and the patient. Due to the ICN, the entire HCR obtains a floating potential, which implies that touching a single exposed point of the circuit is not a hazard, because residual leakage currents towards the ground, e.g., caused by capacitive coupling, are below 20 mA[70]. Thus, the insulation would have to fail at two separate points simultaneously, and both would have to make contact with the patient to create a dangerous voltage drop across the body. The operational control of the scanner is implemented with multiple safety mechanisms, features an independent monitoring of relevant metrics, and has the ability to intervene in signal generation. For example, the SU is capable of disabling the transmission chain in the event of overheating. The same applies to the resonant tuning heating unit. An active imaging phase is only entered if no unexpected DF feedback is observed. Unintended high DF levels due to incorrect inputs or component failures are prevented by the chosen operating point at the upper power limit of the amplifier. In addition, the resonant transmit chain is frequency-specific and unexpected waveform changes or detuning of components in the transmit chain will reduce the power in the DFG. Finally, a human operator can use a hardware console to disable parts of the system at any point.

It should be noted that only phantoms were used in the studies presented. However, the corresponding measurement parameters were carefully chosen to be reasonable for future studies in humans. Ultimately, conclusive assertions concerning safety and tolerability in humans can only be made after animal or human studies[71].

Hardware implementation

The design concept for signal generation and reception, includes a symmetric approach to enable simultaneous signal generation and reception[72], called send-receive approach (TxRx). This utilizes a pick-up node within the HCR that is sensitive to the voltage signal induced by the particle magnetization response, while suppressing the excitation voltage. The implementation of this approach requires an ICN as one fundamental part. If built symmetrically with a similar serial resistance of the inductor to the DFG, twice the power is required to match the field generated by a single resonance circuit, limiting the maximum DF amplitude of the TxRx approach. In addition, the complexity of the send-receive chain increases, leading to a high susceptibility to disturbances generated within the HCR (e.g., from connections and eddy currents). In our case, the received signal acquired by this approach was inferior to the received signal of a dedicated receive coil, which is able to suppress signal distortions[73], justifying the utilization of the dedicated x-receive coil for this channel. A dedicated receive coil in the z-direction has not yet been developed due to the laborious design and intricate tuning process required for the cancellation coil. Due to the DF saddle coil, the magnetic field profiles in z have only a small homogeneous area, and coupling to other channels becomes an issue.

The sampling trajectory originates from a superposition of the slowly varying selection field and the fast-oscillating drive field. The arising FFP movement follows a trajectory, which samples the FOV and ideal MPI systems try to generate homogeneous and orthogonal drive fields with a linear selection field. However, to achieve low field imperfections, large coils are required that are less energy efficient. Restrictions of design space, power supply, and coil coupling[74] within the DFG of our scanner cause noticeable field imperfections, as shown in Fig. 2, that deviate from the ideal field. Especially towards the edges of the coils, field imperfections are severe and cause a deformation of the Lissajous-type trajectory in all spatial dimensions. Our magnetic field measurements contain systematic uncertainties due to errors in coil sensor size and orientation. Consequently, they can only shear and rotate the resulting trajectory, and the observed deformations can be attributed mainly to the imperfections of the magnetic fields.

Conclusion and outlook

We have performed a comprehensive system characterization of a 3D human-sized MPI scanner for real-time cerebral applications. The perfusion experiments conducted provide a proof-of concept that the discrimination of brain hemispheres and different severities of stenosis are possible. This will allow us to better assess which clinical application scenarios are feasible in the future. For example, MPI trials for the ischemic stroke scenario in human volunteers may soon be possible using the *Resotran* tracer. Tailored MPI tracers, such as *perimag* and *synomag*, with future clinical approvals, promise to increase system performance in sensitivity and spatial resolution and further expand the range of applications.

Methods

Field generation and reception

This section provides a detailed presentation of all scanner components and introduces the concept of how they interact to obtain MPI measurements. Beginning with the generation of magnetic fields, details are given on signal reception, imaging sequences, operation control, and data processing for image reconstruction and post-processing.

The scanners fundamental component for signal generation and acquisition is realized by a stack of three RedPitaya STEMlab 125-14 (RPs). These are a flexible low-cost hardware solution for integrating DACs and ADCs into a single device for precise real-time signal handling. The open-source software for the RPs by ref. 36, ensures a parallel and synchronous signal generation and reception by synchronizing the 125 MHz clock and logic of the three used RPs. This stack thus provides six radio-frequency input and output channels.

Drive-field generation. In Fig. 8, a simplified equivalent circuit diagram (ECD) of the transmit circuit is shown, with details of the transmit filter for one of the two channels. In the following, we describe the components of the transmit chain in detail from field to source: the drive-field generator (DFG), the high current resonator (HCR), the inductive coupling network (ICN), the transmit filter and the impedance matching transformer at the output of the amplifier.

Drive-field generator. The MPI brain scanner utilizes two DFCs in x- and z-direction, respectively. The solenoid x-DFC (with inductance L_x) and the saddle coil z-DFC (with inductance L_z) are nested, with the x-DFC placed on the inside. Both are manufactured using Rutherford wire parallelization with 12 individual strands of a high-frequency Litz wire (2000 isolated strands with 50 μm diameter, Elektrisola, Germany). It further serves the minimization of the self-inductance of the wire, keeps individual wires at identical lengths, and mitigates proximity- and skin-effect. By parallelizing 12 Litz wires, a minimized serial resistance is achieved while maintaining the ability to form and wind the wire into the desired coil topology[75]. In the FOV center, the manufactured DFCs exhibit coil sensitivities of 0.022 $\mathrm{mTA^{-1}}$ and 0.014 $\mathrm{mTA^{-1}}$ in x- and z-direction, respectively. Further details on the achieved component values can be found in Fig. 8. The support structure (PA2200) of the DFG forms an elliptic open bore with a width of 17.5 cm and a height of 21.5 cm. The resulting 2D drive field is set up in the xz-plane with DF frequencies set to $f_x = \frac{125}{4864}$ MHz ≈ 25.699 kHz and $f_z = \frac{125}{4800}$ MHz≈26.042 kHz. The frequency ratio between the two channels results in a closed 2D Lissajous trajectory after 76 and 75 periods for the x- and z-directions, respectively.

High-current resonator. In order to mitigate high voltages near the human brain, a design objective was to utilize parallelized low inductance DFCs that require high currents instead of high voltages for generating the desired drive field. To minimize reactive power and obtain symmetry, the DFCs are operated in resonance at the DF frequency by connecting two capacitors of equal size both upstream and downstream of the inductance. Instead of utilizing a capacitive voltage divider for impedance matching[76], a mirrored resonant setup with a toroidal transformer coil (L_{ICN2}) is connected to each DFC with the same resonance frequency. For resonance tuning, the capacities $C_{\mathrm{Hx}_i}, C_{\mathrm{Hz}_i}, i = 1, \ldots, 4$ are temperature controlled capacitors (CSM 150/200, Celem, Israel), which enables stable and precise resonance tuning[77].

Manufacturing orthogonal DFCs is challenging; hence residual coil coupling between DF channels must be addressed in order to avoid beat frequencies, undesired frequency shifts by mode splitting, and resulting losses. Due to the resonant behavior of the coupled coil circuit and the low difference of DF frequencies, the coupled signals also experience an amplification in the other circuit. Even the small coupling coefficient of $k_c = 0.06$ can lead to large currents in the orthogonal coil, resulting in a

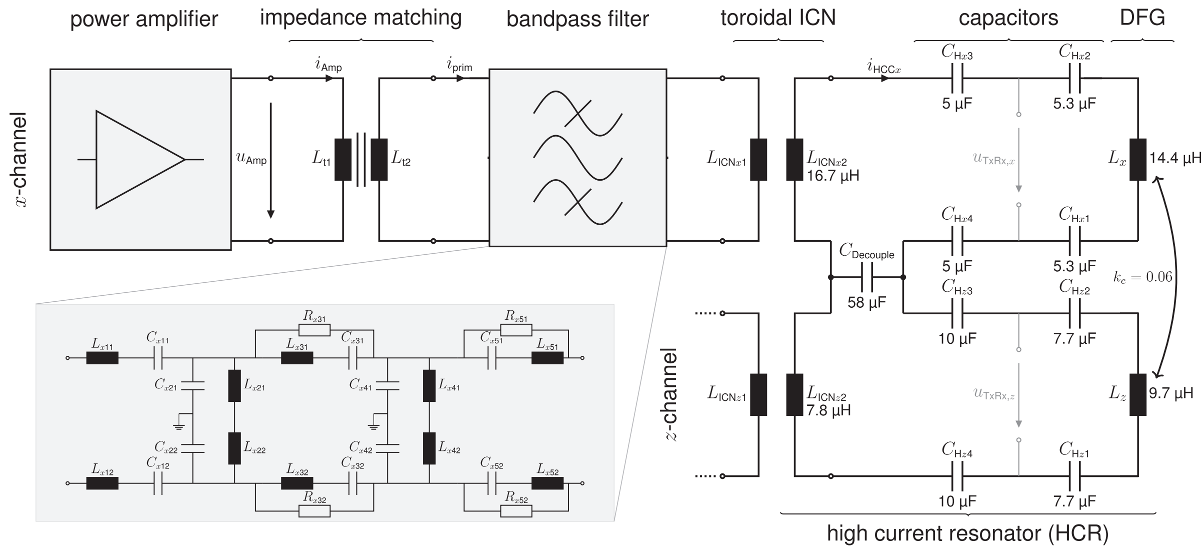

Fig. 8 | Simplified transmit circuit. The x- and z-drive-field (DF) excitation channels are designed to provide resonances at 25.699 and 26.042 kHz, respectively. Both channels consist of their own power amplifier, impedance matching transformer (with an iron core, ||) and band-pass filter. The band-pass filter is shown for x only, but is identical for the z-channel. The inductive coupling networks (ICNs) were individually developed with different litz-wire parallelizations (higher current in z) and roughly matched the inductance of the corresponding drive-field coils within the drive-field generator (DFG). Resonance is achieved by the high current resonator (HCR) circuit. Residual coupling of the DF channels and decoupling countermeasures are also shown. Values of major components are denoted in the equivalent circuit diagram. Since fine-tuning needs to be performed with a fully assembled HCR, the denoted HCR capacity values are guide values.

strong beating signal of the two frequencies. For the HCR, the field coupling far exceeds 10%, causing a distorted trajectory, which substantially degrades the image quality[74]. Coupling is reduced by a decoupling capacitor (C_{Decouple}) that is connected in series within both circuits. It carries both currents and matches the complex conjugate impedance of the mutual inductance $L_{\mathrm{M}} = k_c\sqrt{L_x L_z}$ between the two DFCs. As a result, the voltage drop across the capacitor cancels the induced voltage from the other channel within each channel loop. For our setup, we built a capacitor $C_{\mathrm{Decouple}} \approx 58$ μF by parallelization of $58 \cdot 1$ μF (MKP C4Q, Kemet, USA) and achieved a residual channel coupling of −35 dB.

Inductive coupling network. The aforementioned toroidal air-core transformer coil composes the inductive coupling network (ICN), one for each DF channel. The ICN serves the triple purpose of high current gain (impedance matching), circuit symmetry, and floating potentials. The last point is achieved by any transformer. It increases patient safety by requiring direct contact with two separate points of the circuit in order to cause a voltage drop across a grounded person. Also, a floating HCR avoids ground loops that may have a negative influence on signal reception.

The intention of circuit symmetry is to obtain two voltage nodes in each channel, between which the voltage of the fundamental frequency is zero. Both inductors of a channel (ICN and DFG) are in a series resonance with their corresponding capacitors, which have equal voltages but opposing sign at resonance. A pick-up point for the particle harmonics is thus created, which is nested in between the capacitors within the HCR, denoted by u_{TxRx} in Fig. 8, with a suppressed feedthrough[72]. For the higher harmonics induced by the particles, the inductors on both sides result in higher impedances, creating an inductive voltage divider for both noise and particle signals.

The ICN also plays a crucial role in providing current gain at the resonance of the HCR. This enables the transformation of filtered transmit signals into the desired low-voltage-high-current signal. Multiple Litz-wire parallelization on the secondary transformer side (L_{ICN2}) are used to achieve low losses and a high-quality factor; nevertheless, additional inductance and resistance is introduced by the ICN into the HCR. The HCR constitutes the load of the transformer, and the primary transformer coil (L_{ICN1}) shows a real load impedance ($Z_{\mathrm{ICN}} \approx 30$ Ω) at the resonance frequency and becomes part of the last stage of the transmit filter. The achieved current gain is 31 for the x-channel and 35 for the z-channel.

Transmit filter. A differential 5th-order band-pass filter is used to smoothen the excitation voltage before it is connected to the primary side of the ICN, shown in Fig. 8. The three odd stages of the filter consist of serial resonance circuits that act as a band-pass by having a minimum impedance at resonance. In-between these stages, two even stages act as parallel resonators that create a short for all other frequencies in order to dissipate the energy of undesired frequencies. The serial resonator (odd stages) is composed of a 3D-printed toroidal air coil ($L_{\mathrm{s,odd}} \approx 500$ μH, $R_{\mathrm{s,odd}} \approx 1$ Ω). For a symmetrical differential signal, the toroid is separated into two halves, with each half forming their own resonance together with a high voltage, polypropylene film capacitor (e.g., KEMET C4C series, 2 kV DC rated). Due to the mutual magnetic field within the toroidal coil, the field lines run through both sides of the toroid. Additional resistors across the second and third serial resonator stages are utilized to attenuate side lopes[76]. The two parallel resonators (even stages) are formed by smaller toroidal air coils ($L_{\mathrm{s,even}} \approx 250$ μH, $R_{\mathrm{s,even}} \approx 500$ mΩ) to pose a high impedance at the DF frequency between the two voltage rails. The assembled transmit-filter chains attenuate harmonic distortions of the DF signal by −65, −100, and −150 dB amplitude ratio for the second, third, and fourth harmonics, respectively. The overall differential filter setup provides common mode rejection.

Transformer. For maximum power transfer, we implemented an impedance matching transformer with an iron core (N87 material B65686A0000R087, TDK Electronics, Germany). To prevent distortion and harmonics due to core saturation effects, the core flux density is minimized to 16% of the saturation magnetization B_{sat}[76]. The secondary side of the transformer is connected to the transmit filter and ensures floating potentials and differential signaling. The turns ratio of the transformer changes the low impedance (≈2.5 Ω, amplifier side) to a high impedance (≈30 Ω, filter side) to minimize the current in the transmit filter.

Drive-field power amplifier. Two 1200 W power amplifier (A1110-40-QE-100, Dr. Hubert GmbH, Germany) are used in voltage mode for amplification of each DF signal. To generate the DF strength of 5 and 4 mT, a total power of 930 W for x and 1100 W for z has to be provided by the power amplifiers. For safety and control reasons, the initial signal from the DAC runs through a relay at the input of the amplifier that is only closed during measurements (by the SU). In addition, serial interlock commands are sent to the amplifier to ensure that the output is only enabled during a measurement. The advantage of this double safety configuration is that the SU is able to interrupt transmission in case of failure (e.g., temperature overshoot), even when the software activated the amplifier via the interlock mechanism. A pre-amplifier is used to amplify the voltage signal by a factor of 8 to scale it to the required input voltage of the power amplifier.

Feedback signal. To control the DF signal in amplitude and phase, one turn is wound around each ICN toroid. According to the law of induction, the induced voltage is proportional to the field, which is proportional to the HCR current and hence to the drive field. The induced signal is fed back to the RPs via a voltage divider, where it is processed during the DF control phase. To generate a stable DF trajectory, the control accuracy is set <1% and able to generate field strengths up to 5.5 mT for the x-channel and 4.5 mT for the z-channel.

Selection-field generation. The previously presented SFG in ref. 8 is used to generate the required gradient field, and further moves the FFP in y-direction with a maximum displacement amplitude of 70 mm from the center. The SFG consists of two coils (L_G = 200 mH) mounted on a soft-iron yoke at a distance of 31 cm from each other. The magnetic gradient field is generated by superimposing the two field contributions, in a Maxwell-like coil topology with opposing current directions. The setting of equal opposite coil currents creates an FFP in the FOV center. By changing the currents, the position of the FFP along the y-axis can be shifted and the maximum FFP offset is set to 43 mm to each side with respect to the FOV center. We chose the FFP velocity to be 68.8 cms^{-1}, which results in a similar trajectory density in the y-direction as in the xz-plane (see subsubsection "System matrix analysis"). The selection-field signals are generated by the aforementioned RedPitaya STEMlab 125-14 (RPs). A pre-amplifier is used to scale the input voltage according to the required voltage for the power amplifier for selection-field generation. For this purpose, two AE Techron 2105 (AE Techron, USA) in current mode feed the selection-field coils. For the generation of the gradient, a total power of 380 W is required.

Signal reception

Receive coils. Two dedicated receive coils are used for signal reception for all measured data in this work. The gradiometric x-coil has ten turns on a length of 10 cm and 18 counter turns at the rear end of the DFG. In the y-direction, a saddle coil with two times 20 turns is installed. Due to the orthogonal orientation of the two DFCs, a gradiometric setup is not required, and residual feedthrough voltages are suppressed by the receive filter. Both dedicated receive coils are located within the 3D-printed housing of the DFG, on the inside of the DFCs. A dedicated z-receive coil has not yet been implemented, due to its challenging design as a gradiometric saddle coil. The small homogeneous field region of the z-channel does not allow a clear spatial separation of the FOV and the sensitive region of the gradiometer.

However, as mentioned in the subsubsection "Drive-field generation" in the ICN paragraph, the symmetric circuit design included a second method for signal pick-up, referred to as the send-receive method (TxRx). Consequently, receive signals for x and z can be obtained in principle. The pick-up node is positioned in the LC circuits of the HCR between C_{H2}, C_{H3}, and C_{H1}, C_{H4}, for each DF channel (see Fig. 8). In theory, the voltage of the fundamental DF frequency is near zero at this node, and any induced particle signal will create a voltage drop across the DFC (and the parallel ICN, halving the received signal if $L_{\mathrm{ICN}x2} \approx L_x$, or $L_{\mathrm{ICN}z2} \approx L_z$). Between these nodes, the input of the receive chain can be connected, enabling signal reception during transmission[72].

Receive chain. The receive voltage u_{Rx} is composed of the particle signal, the background noise, distortions, and the direct signal feedthrough from the DFCs. Before the signal is connected to the LNA, a fourth-order resonance notch filter suppresses the fundamental frequencies around 26 kHz (20 to 33 kHz stopband). The filter is a differential circuit, shown in Fig. 9a. The odd stages feature a parallel resonance with high impedance at the DF frequency, and the even stages are serial resonances towards the ground with low impedance at the DF frequency. To avoid nonlinear effects due to high receive voltages, the first two stages utilize toroidal air coil resonators. The attenuated residual voltage in the last two stages allows the use of ferrite iron core coils (B64290, TDK Electronics, Germany). The filtered receive signal is connected to an improved version of the custom LNA by ref. 8 via a signal-matching transformer. The transformer and the input impedance of the LNA are used to shift the resonance frequency of LNA and receive coil to optimize signal amplification of higher harmonics in the 300 to 600 kHz range[78]. The LNA consists of three amplification stages, the first stage is built

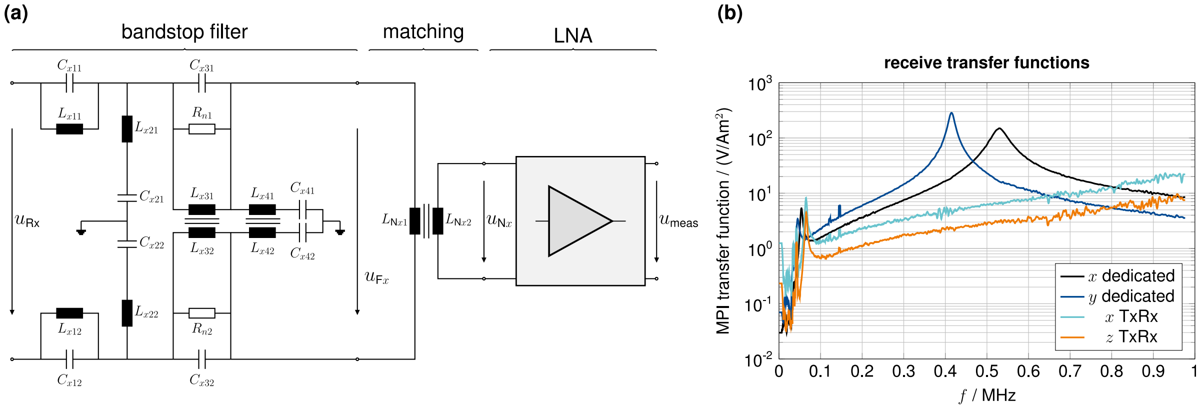

Fig. 9 | Receive path. a Equivalent circuit diagram of a receive filter circuit with signal matching for the low noise amplifier (LNA). In the receive circuit, a four-stage analog band-stop filter is installed for x-, y-, and z-feedthrough suppression, although only x and y are used for reconstruction in this work. The first two filter stages are utilized by air coil resonators and the last two stages by iron core coil resonators. A signal-matching transformer follows the filter to adjust the received signal prior to the LNA. For differential signaling, the LNA output is connected to a differential amplifier, and in front of the analog-to-digital converter, an instrumentation amplifier generates the single-ended measurement signal u_{meas}. **b** The receive path Magnetic Particle Imaging (MPI) transfer function for the transformation of u_{meas} into the magnetic moment m_{meas} is plotted for the two dedicated receive coils and the two signal paths using the send-receive approach (TxRx).

by parallelizing 20 JFETs (BF862, NXP Semiconductors, Netherlands), followed by two stages with non-inverting operational amplifier circuit using dual ICs (ADA4898, Analog Devices, USA)[79]. The output is converted into a differential signal by a fully differential amplifier (AD8138, Analog Devices, USA). Just before the input of the ADC of the RPs, an instrumentation amplifier (AD8253, Analog Devices, USA) generates the single-ended measurement signal u_{meas}.

For each of the four receive chains, the receive path calibration was performed utilizing a custom calibration coil[80]. In Fig. 9b, the individually measured MPI transfer functions are plotted. The two dedicated receive coils provide resonances at 531 and 414 kHz for x and y, respectively. It can be seen that the TxRx signal for x and z are less sensitive in the relevant 100 to 800 kHz range.

Imaging sequence. The MPI brain scanner superimposes two fast drive fields in the x- and z-direction and a dynamic selection field. The selection field is shifted along the y-axis, as explained in previous sections. Using and combining these constituents, it is possible to perform various imaging sequences. First of all, there are three different 2D sequences possible that drive the FFP either along a 2D Lissajous trajectory with a frequency ratio of $\frac{75}{76}$ (xz-plane) or along Cartesian trajectories (xy- and yz-plane) with flexible densities. For an overview of common MPI sampling trajectories, we refer the reader to ref. 51. In the case of the xz-sequence, both drive fields are activated, and a static FFP field is generated at an eligible y-position, using the SFG. For the other two cases, only one DF channel is activated, and the FFP is swept dynamically along the y-direction. The repetition time of the xz-sequence is fixed and given by $T^{xz}_{\text{cycle}} = 2.918\,\text{ms}$ and for the other two sequences, $T^{xy}_{\text{cycle}} = T^{yz}_{\text{cycle}} = 0.25\,\text{s}$ if we set the y-sequence to 4 Hz (the default value for the scanner). We note, that the first generation of the scanner published in ref. 8 was 2D only and limited to the xy-sequence with a frame rate of 2 Hz.

In addition to the 2D sequences, it is also possible to apply fully 3D sequences. This is done by using both DF channels and simultaneously generating a slowly varying selection field with an FFP moving along the y-axis[81]. The resulting sampling trajectory is a 2D Lissajous trajectory within the xz-plane that is slowly swept back and forth along the y-direction, as visualized in Fig. 1. In this way, the volume is sampled plane by plane, and the repetition time is derived from the y-sequence, resulting in $T^{xyz}_{\text{cycle}} = 0.25\,\text{s}$ for a 4 Hz sequence. The waveform of the currents applied to the selection field is chosen to be triangular, such that the sequence is always periodic, at constant velocity, and without sudden discontinuities, in order to avoid strong mechanical forces in the copper shield of the DFG due to eddy currents. Furthermore, a triangular sweep minimizes the likelihood of PNS and SAR by the selection field. The triangular waveform provides a constant slew rate, and results in an almost linear FFP movement as the iron cores are not yet saturated. The chosen sequence type depends on the spatial dimensions and the requirements for temporal resolution. Within this work, we only show experiments that were performed using the 3D imaging sequence and therefore focus on this particular sequence in the following. The nominal FOV captured by the 3D sequence assuming ideal magnetic fields is ($84 \times 85 \times 67\,\text{mm}^3$). The density of the FFP sampling trajectory within the xz-plane is inhomogeneous due to the sinusoidal excitation[51], and the largest gap can be derived from the Lissajous node points[82]. For the applied Lissajous sequence, the resulting distance is 1.819 mm. The distance between slices in the y-direction is equidistant with 1.982 mm. Both values are well below the expected spatial resolution between 5 and 20 mm, which ensures that the resolution is not limited by the sampling scheme.

Operational control. The task of the operation control is to implement the chosen imaging sequence by coordinating all scanner components used during measurement. Next to the synchronous signal handling, an imaging sequence also requires several asynchronous tasks, such as enabling the various amplifiers, moving a calibration robot, updating the RPs waveforms based on different imaging sequences, or informing the SU of an upcoming signal generation. These steps are handled by the open-source framework[37], which can implement a variety of different measurement scenarios, including system matrix calibrations and magnetic field measurements[40].

Depending on the type of measurement and sequence, the components and steps required may vary, but in general, each measurement can be divided into three phases. During the setup phase, the amplifiers are disabled, the RPs are neither transmitting nor receiving signals, and the resonance tuning heating is enabled. In this phase, various components are prepared for the next imaging sequence, e.g., the calibration robot is moved, or the RPs waveforms are updated. The next phase is the control phase. This is where the DF amplifiers are enabled, and the DF waveform is sent down the transmit chain. During these transmissions, the feedback signal is analyzed at the frequencies of the DF channels, and the transmitted amplitude and phase are adjusted to the desired values from the selected sequence. When the deviation between the selected and observed DF waveform is sufficiently small, the control phase ends. In measurement scenarios with frequent measurements, such as a system matrix calibration, the feedback signal from the previous measurement can be used instead to adjust the amplitude and phase. The third phase is the active imaging phase. Here the resonance tuning heating is switched off to prevent possible distortions, both the SF and DF waveforms are transmitted, and the signal is received via the RPs to be stored for further processing.

Data processing

Image reconstruction. The measured voltage signal of the j-th time frame $u_j(t, l)$ depends on the time $t \in \mathbb{R}_+$ and the receive channel $l \in \{1, \ldots, L\}$ where L is the number of receive channels, i.e., $L = 2$ in our case. The signal is sampled at time points $t_i = (i-1)/f_{\text{sample}}$, $i = 1, \ldots, K$ where $f_{\text{sample}} = \frac{125}{64}$ MHz and $K = 484{,}500$ for our 3D 4 Hz (0.248 s) sequence. Prior to reconstruction, we apply the standard signal processing[9], which involves Fourier transformation, a frequency selection based on a band-stop filter in the receive chain filter (see above for details), as well as a filtering based on the SNR using different thresholds ranging from 3 to 100, resulting in M frequency components. For better readability of the following paragraphs, we express the resulting discrete signal as the vector $\mathbf{u} \in \mathbb{C}^M$, omitting the frame index j.

The goal of image reconstruction is to recover an image $\mathbf{c} \in \mathbb{R}^N_+$ that is discretized on a (3D) grid with N voxels. The relationship between $\mathbf{u}$ and $\mathbf{c}$ is given by the linear system of equations $\mathbf{Sc} = \mathbf{u}$, where $\mathbf{S} \in \mathbb{C}^{M \times N}$ is the system matrix that encodes the physical process from the particle magnetization progression to the system-dependent measurement signal at the end of the receive chain. Since the linear system is ill-conditioned and the measured data is disturbed by noise, we consider a regularized least-squares approach

$$\underset{\mathbf{c} \in \mathbb{R}^N_+}{\operatorname{argmin}} \; \| \mathbf{Sc} - \mathbf{u} \|_2^2 + \lambda_{L^2} \; \| \mathbf{c} \|_2^2 + \lambda_{L^1} \; \| \mathbf{c} \|_1, \tag{1}$$

where the first term ensures data consistency, the second term penalizes large solutions and prevents that the particle concentration vector $\mathbf{c}$ is fitted to the noise in the measurement $\mathbf{u}$, and the last term allows to penalize non-sparse solutions, which helps in reducing noise. The optimization problem (1) is solved using the iterative Kaczmarz approach[83] using L^2-regularization as well as L^1-regularization[84,85]. The reconstruction has four parameters in total: $\lambda_{L^2}, \lambda_{L^1}$, the SNR threshold, and the number of iterations that are chosen based on visual inspection and experience.

The system matrix $\mathbf{S}$ encodes the applied imaging sequence and can be interpreted in two different ways. It can be interpreted either as a multi-patch dataset, where the entire 3D sequence is split into the individual 2D subsequences, or as a single-patch dataset. A patch refers to a subvolume that is moved by the dynamic selection field and consists of a single full DF cycle. The multi-patch approach is common when the applied selection field changes only in a step-wise fashion, but it can also be applied when the selection field changes only slowly compared to the rapid drive field-induced movement. This multi-patch reconstruction approach was used in the first generation of our perfusion imager[8] and studied in more detail by ref. 86. Alternatively, one can also interpret the entire imaging sequence as a single-patch dataset, which was considered by ref. 87 for Cartesian 2D trajectories. The multi-patch approach has the potential advantage that it may allow to exploit shift-invariant sub-blocks within the system matrix, which can accelerate operations involving the system matrix $\boldsymbol{S}$ within image reconstruction[45]. On the other hand, the single-patch approach can take field imperfections better into account and can also better prevent spectral leakage, which can be induced by non-periodic external signal contributions. Effectively, the key difference between both approaches is that the Fourier transform is applied to smaller signal snippets in the multi-patch case, while the single-patch case applies the Fourier transform to the entire time signal. Since the single-patch reconstruction is fast enough for our purposes, we use this approach in all experiments shown in this paper. For the system matrix analysis performed in the subsubsection “System matrix analysis” we, however, consider both the multi-patch and the single-patch data interpretation since this gives much deeper insight into the system matrix structure.

Perfusion image calculation. To evaluate perfusion experiments in the subsubsection “Dynamic perfusion experiments”, the reconstructed data is processed to obtain the time-to-peak (TTP), mean-transit-time (MTT), relative cerebral-blood-flow (rCBF), and relative cerebral-blood-volume (rCBV). Post-processing includes four consecutive steps: (i) time framing, (ii) filtering and offset correction, (iii) threshold masking, and (iv) parameter map calculation. After explaining these post-processing steps, we give the implemented definitions of the mentioned perfusion parameters. The definitions and the post-processing script that handles the data are based on the work by ref. 56, which provides more details.

Step (i) selects the relevant reconstructed data by taking the time frames that include the entire first passage of the administered bolus. It starts with the injection (5 s before bolus appearance), includes the administered bolus and stops after the passing levels to zero again. This step ensures that only relevant data is processed later, as shown in the leftmost column of Fig. 6. In step (ii), an appropriate filter type smooths the data for a more accurate peak detection and noise suppression. We avoided rectangular windows to reject ringing artifacts and selected a low-pass Hann-filter with a window size of ten samples. The Hann-filter is applied voxel-wise on the Fourier-transformed temporal data, which also shifts the concentration offset to zero by excluding the DC component. Afterwards, in step (iii), a threshold mask reduces image noise by excluding any voxels with an intensity lower than 10% of the maximum value. This increases the readability of perfusion maps, by excluding irrelevant regions, e.g., outside (phantom) vessels. A last post-processing step (iv), calculates the mentioned perfusion parameters based on the following definitions, which are also sketched in the top row of Fig. 6. The reconstructed time-dependent solution of the entire volume in the FOV is $\tilde{\mathbf{c}} : [0, T] \to \mathbb{R}_+^N$ with $N = n_x \times n_y \times n_z$ voxels. $\tilde{\mathbf{c}}(t)$ describes the reconstructed volume of all measured time frames, that record the entire bolus administration.

TTP. We define the time-to-peak (TTP) as the time elapsed between a chosen reference point (the bolus injection t_0) and the measured signal maximum of the bolus passing. The $\mathbf{TTP} \in \mathbb{R}^N$ is calculated element-wise for all voxel $n \in \{1, \ldots, N\}$ via $\mathrm{TTP}_n = \arg\max_t(\tilde{c}_n(t))$, where $\tilde{c}_n(t)$ is the concentration over time of the nth voxel[88].

MTT. With mean-transit-time (MTT), we refer to the measure of the average time interval that a particle or blood cell spends inside an organ or vessel and it strongly correlates with the full width at half maximum (FWHM) of the bolus concentration on passing (for low tissue perfusion)[89,90]. The time interval of the FWHM was therefore selected as the $\mathrm{MTT} \in \mathbb{R}^N$ in this work.

rCBF. The relative cerebral-blood-flow (rCBF) equals the highest positive gradient of the concentration over time $\tilde{c}_n(t)$, as in $\mathrm{rCBF}_n = \arg\max_t(\frac{\mathrm{d}}{\mathrm{d}t}\tilde{c}_n(t))$, which is evaluated element-wise for all voxels n to obtain $\mathbf{rCBF} \in \mathbb{R}^N$.

rCBV. We derive the relative cerebral-blood-volume (rCBV) data $\mathbf{rCBV} \in \mathbb{R}^N$ from an element-wise evaluation of the integral (area under the curve (AUC)) of the concentration $\tilde{c}_n(t)$ in the nth voxel, over the time interval of the passing bolus ($\tilde{c}_n(t) > 0$) as in $\mathrm{rCBV}_n = \int \tilde{c}_n(t)\,\mathrm{d}t$.

Blood flow and volume are both calculated in a relative manner, due to a missing correct arterial input function (e.g., feeding phantom hose), which poses as a reference by providing the undisturbed flow (without perfusion).

Data availability

Data sets generated during the current study are available from the corresponding author on reasonable request.

Code availability

The code supporting the findings of this study is publicly available on GitHub. You can access the code repositories through the following links: GUI: https://github.com/MagneticParticleImaging/MPIUI.jl Signal generation and reception: https://github.com/tknopp/RedPitayaDAQServer Hardware and measurement control: https://github.com/MagneticParticleImaging/MPIMeasurements.jl Image reconstruction: https://github.com/MagneticParticleImaging/MPIReco.jl

Received: 8 September 2023; Accepted: 1 March 2024;

References

1. Porté, F., Basit, R. & Howlett, D. Imaging in the intensive care unit. *Surgery* **27**, 496–499 (2009).
2. Rotello, L., Radin, E., Jastremski, M., Craner, D. & Milewski, A. MRI protocol for critically ill patients. *Am. J. Crit. Care* **3**, 187–190 (1994).
3. Lohan, R. Imaging of ICU Patients. in *Thoracic Imaging* (ed. Chawla, A.) 173–194 (Springer, 2019).
4. Kimberly, W. T. et al. Brain imaging with portable low-field MRI. *Nat. Rev. Bioeng.* **1**, 617–630 (2023).
5. Mazurek, M. H. et al. Detection of intracerebral hemorrhage using low-field, portable magnetic resonance imaging in patients with stroke. *Stroke* **54**, 2832–2841 (2023).
6. Ludewig, P. et al. Magnetic particle imaging for assessment of cerebral perfusion and ischemia. *Wiley Interdiscip. Rev. Nanomed. Nanobiotechnol.* **14**, e1757 (2022).
7. Feigin, V. L. et al. Global and regional burden of stroke during 1990-2010: findings from the Global Burden of Disease Study 2010. *Lancet* **383**, 245–255 (2014).
8. Graeser, M. et al. Human-sized magnetic particle imaging for brain applications. *Nat. Commun.* **10**, 1936 (2019).
9. Knopp, T., Gdaniec, N. & Möddel, M. Magnetic particle imaging: from proof of principle to preclinical applications. *Phys. Med. Biol.* **62**, R124–R178 (2017).
10. Weizenecker, J., Gleich, B., Rahmer, J., Dahnke, H. & Borgert, J. Three-dimensional real-time in vivo magnetic particle imaging. *Phys. Med. Biol.* **54**, L1–L10 (2009).
11. Vogel, P. et al. First in vivo traveling wave magnetic particle imaging of a beating mouse heart. *Phys. Med. Biol.* **61**, 6620–6634 (2016).
12. Borgert, J. et al. Perspectives on clinical magnetic particle imaging. *Biomed. Tech.* **58**, 551–556 (2013).
13. Mason, E. E. et al. Design analysis of an MPI human functional brain scanner. *Int. J. Magn. Part Imaging* **3**, 1703008 (2017).
14. Vogel, P. et al. iMPI: portable human-sized magnetic particle imaging scanner for real-time endovascular interventions. *Sci. Rep.* **13**, 10472 (2023).

15. Gleich, B. & Weizenecker, J. Tomographic imaging using the nonlinear response of magnetic particles. *Nature* **435**, 1214–1217 (2005).
16. Graeser, M. et al. Towards picogram detection of superparamagnetic iron-oxide particles using a gradiometric receive coil. *Sci. Rep.* **7**, 6872 (2017).
17. Graeser, M. et al. Design of a head coil for high resolution mouse brain perfusion imaging using magnetic particle imaging. *Phys. Med. Biol.* **65**, 235007 (2020).
18. Murase, K., Takata, H., Takeuchi, Y. & Saito, S. Control of the temperature rise in magnetic hyperthermia with use of an external static magnetic field. *Phys. Med.* **29**, 624–630 (2013).
19. Tay, Z. W. et al. Magnetic particle imaging-guided heating in vivo using gradient fields for arbitrary localization of magnetic hyperthermia therapy. *ACS Nano* **12**, 3699–3713 (2018).
20. Bulte, J. W. M. et al. Quantitative "hot-spot" imaging of transplanted stem cells using superparamagnetic tracers and magnetic particle imaging. *Tomography* **1**, 91–97 (2015).
21. Harisinghani, M. G. et al. Noninvasive detection of clinically occult lymph-node metastases in prostate cancer. *N. Engl. J. Med.* **348**, 2491–2499 (2003).
22. Yu, E. Y. et al. Magnetic particle imaging for highly sensitive, quantitative, and safe in vivo gut bleed detection in a murine model. *ACS Nano* **11**, 12067–12076 (2017).
23. Ludewig, P. et al. Magnetic particle imaging for real-time perfusion imaging in acute stroke. *ACS Nano* **11**, 10480–10488 (2017).
24. Yu, E. Y. et al. Magnetic particle imaging: a novel in vivo imaging platform for cancer detection. *Nano Lett.* **17**, 1648–1654 (2017).
25. Rahmer, J., Wirtz, D., Bontus, C., Borgert, J. & Gleich, B. Interactive magnetic catheter steering with 3-D real-time feedback using multi-color magnetic particle imaging. *IEEE Trans. Med. Imaging* **36**, 1449–1456 (2017).
26. Herz, S. et al. Magnetic particle imaging guided real-time percutaneous transluminal angioplasty in a Phantom model. *Cardiovasc. Intervent. Radiol.* **41**, 1100–1105 (2018).
27. Ahlborg, M. et al. First dedicated balloon catheter for magnetic particle imaging. *IEEE Transi Medi Imaging* **41**, 3301–3308 (2022).
28. Möddel, M., Meins, C., Dieckhoff, J. & Knopp, T. Viscosity quantification using multi-contrast magnetic particle imaging. *N. J. Phys.* **20**, 83001 (2018).
29. Stehning, C., Gleich, B. & Rahmer, J. Simultaneous magnetic particle imaging (MPI) and temperature mapping using multi-color MPI. *Int. J. Magn. Part. Imaging* **2**, 1–6 (2016).
30. Viereck, T., Kuhlmann, C., Draack, S., Schilling, M. & Ludwig, F. Dual-frequency magnetic particle imaging of the Brownian particle contribution. *J. Magnet. Magnet. Mater.* **427**, 156–161 (2017).
31. Rahmer, J., Halkola, A., Gleich, B., Schmale, I. & Borgert, J. First experimental evidence of the feasibility of multi-color magnetic particle imaging. *Phys. Med. Biol.* **60**, 1775 (2015).
32. Shasha, C. et al. Discriminating nanoparticle core size using multi-contrast MPI. *Phys. Med. Biol.* **64**, 74001 (2019).
33. Möddel, M., Griese, F., Kluth, T. & Knopp, T. Estimating orientation using multi-contrast MPI. *Int. J. Magn. Part. Imaging* **6**, 1–3 (2020).
34. Foerger, F. et al. Flexible selection field generation using iron core coil arrays. *Int. J. Magn. Part. Imaging*. https://journal.iwmpi.org/index.php/iwmpi/article/view/624 (2023).
35. Hartung, V. et al. Resotran® meets MPI – clinically approved ferucarbotran reintroduced: a major leap towards MPI in humans. *Int. J. Magn. Part. Imaging*. https://www.journal.iwmpi.org/index.php/iwmpi/article/view/635 (2023).
36. Hackelberg, N., Schumacher, J., Graeser, M. & Knopp, T. A Flexible high-performance signal generation and digitization plattform based on low-cost hardware. *Int. J. Magn. Part. Imaging*. https://journal.iwmpi.org/index.php/iwmpi/article/view/375 (2022).
37. Hackelberg, N. et al. MPIMeasurements.jl: an extensible Julia framework for composable magnetic particle imaging devices. *Int. J. Magn. Part. Imaging* https://journal.iwmpi.org/index.php/iwmpi/article/view/605 (2023).
38. Knopp, T. et al. MDF: magnetic particle imaging data format. Preprint at arXiv https://arxiv.org/abs/1602.06072 (2016).
39. Knopp, T. et al. MPIReco.jl: Julia package for image reconstruction in MPI. *Int. J. Magn. Part. Imaging* **5**, 1–2 (2019).
40. Boberg, M., Knopp, T. & Möddel, M. Unique compact representation of magnetic fields using truncated solid harmonic expansions. Preprint at arXiv:2302.07591 (2023).
41. Thieben, F., Boberg, M., Graeser, M. & Knopp, T. Efficient 3D drive-field characterization for magnetic particle imaging systems. *Int. J. Magn. Part. Imaging*. https://www.journal.iwmpi.org/index.php/iwmpi/article/view/376 (2022).
42. Hardin, R. H. & Sloane, N. J. A. Library of 3-d designs. http://neilsloane.com/sphdesigns/dim3/ (2023).
43. Shmilovitz, D. On the definition of total harmonic distortion and its effect on measurement interpretation. *IEEE Trans. Power Deliv.* **20**, 526–528 (2005).
44. Löwa, N., Radon, P., Kosch, O. & Wiekhorst, F. Concentration dependent MPI tracer performance. *Int. J. Magn. Part. Imaging* **2**, 1–5 (2016).
45. Szwargulski, P., Moddel, M., Gdaniec, N. & Knopp, T. Efficient joint image reconstruction of multi-patch data reusing a single system matrix in magnetic particle imaging. *IEEE Trans. Med. Imaging* **38**, 932–944 (2019).
46. Boberg, M., Knopp, T., Szwargulski, P. & Moddel, M. Generalized MPI multi-patch reconstruction using clusters of similar system matrices. *IEEE Trans. Med. Imaging* **39**, 1347–1358 (2020).
47. Rahmer, J., Weizenecker, J., Gleich, B. & Borgert, J. Analysis of a 3-D system function measured for magnetic particle imaging. *IEEE Trans. Med. Imaging* **31**, 1289–1299 (2012).
48. Albers, H., Knopp, T., Möddel, M., Boberg, M. & Kluth, T. Modeling the magnetization dynamics for large ensembles of immobilized magnetic nanoparticles in multi-dimensional magnetic particle imaging. *J. Magn. Magn. Mater.***543**, 168534 (2022).
49. Szwargulski, P. & Knopp, T. Influence of the receive channel number on the spatial resolution in magnetic particle imaging. *Int. J. Magn. Part. Imaging*. https://www.journal.iwmpi.org/index.php/iwmpi/article/view/102 (2017).
50. Rahmer, J., Weizenecker, J., Gleich, B. & Borgert, J. Signal encoding in magnetic particle imaging: properties of the system function. *BMC Med. Imaging*. https://doi.org/10.1186/1471-2342-9-4 (2009).
51. Knopp, T. et al. Trajectory analysis for magnetic particle imaging. *Phys. Med. Biol.* **54**, 385–397 (2008).
52. Chu, B. C. et al. Flow volume in the common carotid artery detected by color duplex sonography: an approach to the normal value and predictability of cerebral blood flow. *Radiat. Med.* **18**, 239–244 (2000).
53. Xing, C.-Y. et al. Distribution of cardiac output to the brain across the adult lifespan. *J. Cereb. Blood Flow Metab.* **37**, 2848–2856 (2017).
54. Reimer, P. & Balzer, T. Ferucarbotran (Resovist): a new clinically approved RES-specific contrast agent for contrast-enhanced MRI of the liver: properties, clinical development, and applications. *Eur. Radiol.* **13**, 1266–1276 (2003).
55. Southern, P. & Pankhurst, Q. A. Commentary on the clinical and preclinical dosage limits of interstitially administered magnetic fluids for therapeutic hyperthermia based on current practice and efficacy models. *Int. J. Hyperthermia* **34**, 671–686 (2018).
56. Mohn, F. et al. Saline bolus for negative contrast perfusion imaging in magnetic particle imaging. *Phys. Med. Biol.* **68**, 175026 (2023).
57. Chandrasekharan, P. et al. Using magnetic particle imaging systems to localize and guide magnetic hyperthermia treatment: tracers,

hardware, and future medical applications. *Theranostics* **10**, 2965–2981 (2020).
58. Knopp, T. & Hofmann, M. Online reconstruction of 3D magnetic particle imaging data. *Phys. Med. Biol.* **61**, N257–N267 (2016).
59. Parent, A. & Carpenter, M. B.*Carpenter's Human Neuroanatomy* (Williams & Wilkins, 1996),
60. Brenner, M. & Gladiss, A. v. Recovering higher harmonics when increasing the frame rate in MPI. *Int. J. Magn. Part. Imaging*. https://www.journal.iwmpi.org/index.php/iwmpi/article/view/644 (2023).
61. Gdaniec, N., Szwargulski, P. & Knopp, T. Fast multiresolution data acquisition for magnetic particle imaging using adaptive feature detection:. *Med. Phys.* **44**, 6456–6460 (2017).
62. Bohnert, J. & Dössel, O. Effects of time varying currents and magnetic fields in the frequency range of 1 kHz to 1 MHz to the human body - a simulation study. *Annual International Conference of the IEEE Engineering in Medicine and Biology Society. IEEE Engineering in Medicine and Biology Society. Annual International Conference* **2010**, 6805–6808 (2010).
63. Dalziel, C. F. & Mansfield, T. H. Effect of frequency on perception currents. *Trans. Am. Inst. Electric. Eng.* **69**, 1162–1168 (1950).
64. Chatterjee, I., Wu, D. & Gandhi, O. P. Human body impedance and threshold currents for perception and pain for contact hazard analysis in the VLF-MF band. *IEEE Trans. Biomed. Eng.* **BME-33**, 486–494 (1986).
65. Reilly, J. Maximum pulsed electromagnetic field limits based on peripheral nerve stimulation: application to IEEE/ANSI C95.1 electromagnetic field standards. *IEEE Trans. Biomed. Eng.* **45**, 137–141 (1998).
66. Saritas, E. U., Goodwill, P. W., Zhang, G. Z. & Conolly, S. M. Magnetostimulation limits in magnetic particle imaging. *IEEE Trans. Med. Imaging* **32**, 1600–1610 (2013).
67. Ozaslan, A. A. et al. PNS limits for human head-size MPI systems: preliminary results. *Int. J. Magn. Part. Imaging*. https://journal.iwmpi.org/index.php/iwmpi/article/view/453 (2022).
68. Davids, M. et al. Peripheral nerve stimulation informed design of a high-performance asymmetric head gradient coil. *Magn. Reson. Med.* **90**, 784–801 (2023).
69. Zhang, B. et al. Peripheral nerve stimulation properties of head and body gradient coils of various sizes. *Magn. Reson. Med.* **50**, 50–58 (2003).
70. Burgess, R. C. Electrical safety. *Handb. Clin. Neurol*. **160**, 67–81 (2019).
71. Billings, C., Langley, M., Warrington, G., Mashali, F. & Johnson, J. A. Magnetic particle imaging: current and future applications, magnetic nanoparticle synthesis methods and safety measures. *Int. J. Mol. Sci.* **22**, 7651 (2021).
72. Sattel, T. F. et al. Setup and validation of an MPI signal chain for a drive field frequency of 150 kHz. *IEEE Trans. Magn.* **51**, 1–3 (2015).
73. Paysen, H. et al. Improved sensitivity and limit-of-detection using a receive-only coil in magnetic particle imaging. *Phys. Med. Biol.* **63**, 13NT02 (2018).
74. von Gladiss, A., Graeser, M. & Buzug, T. M. in *Informatik aktuell* (eds Maier, A. et al.) (Springer, 2018).
75. Ozaslan, A. A., Cagil, A. R., Graeser, M., Knopp, T. & Saritas, E. U. Design of a magnetostimulation head coil with Rutherford cable winding. *Int. J. Magn. Part. Imaging*. https://journal.iwmpi.org/index.php/iwmpi/article/view/259 (2020).
76. Mattingly, E. et al. A drive filter design for MPI with harmonic notching and selective damping. *Int. J. Magn. Part. Imaging*. https://journal.iwmpi.org/index.php/iwmpi/article/view/452 (2020).
77. Thieben, F. et al. Heat it up: thermal stabilization by active heating to reduce impedance drifts in capacitive matched networks. *Int. J. Magn. Part. Imaging*. https://journal.iwmpi.org/index.php/iwmpi/article/view/434 (2022).
78. Zheng, B. et al. Optimal broadband noise matching to inductive sensors: application to magnetic particle imaging. *IEEE Trans. Biomed. Circuit. Syst.* **11**, 1041–1052 (2017).
79. Mattingly, E. et al. A sensitive, stable, continuously rotating FFL MPI system for functional imaging of the rat brain. *Int. J. Magn. Part. Imaging*. https://journal.iwmpi.org/index.php/iwmpi/article/view/483 (2022).
80. Thieben, F. et al. On the receive path calibration of magnetic particle imaging systems. *IEEE Trans. Instrum. Meas.* **72**, 1–15 (2023).
81. Kaethner, C., Ahlborg, M., Bringout, G., Weber, M. & Buzug, T. M. Axially elongated field-free point data acquisition in magnetic particle imaging. *IEEE Trans. Med. Imaging* **34**, 381–387 (2015).
82. Kaethner, C. et al. Non-equispaced system matrix acquisition for magnetic particle imaging based on Lissajous node points. *IEEE Trans. Med. Imaging* **35**, 2476–2485 (2016).
83. Knopp, T. et al. Weighted iterative reconstruction for magnetic particle imaging. *Phys. Med. Biol.* **55**, 1577–1589 (2010).
84. Lieb, F. & Knopp, T. A wavelet-based sparse row-action method for image reconstruction in magnetic particle imaging. *Med. Phys.* **48**, 3893–3903 (2021).
85. Dittmer, S., Kluth, T., Henriksen, M. T. R. & Maass, P. Deep image prior for 3D magnetic particle imaging: a quantitative comparison of regularization techniques on Open MPI dataset. Preprint at arXiv:2007.01593 [cs, eess, math] (2020).
86. Szwargulski, P. et al. Moving table magnetic particle imaging: a stepwise approach preserving high spatio-temporal resolution. *J. Med. Imaging* **5**, 5–11 (2018).
87. Werner, F., Gdaniec, N. & Knopp, T. First experimental comparison between the Cartesian and the Lissajous trajectory for magnetic particle imaging. *Phys. Med. Biol.* **62**, 3407–3421 (2017).
88. Fieselmann, A., Kowarschik, M., Ganguly, A., Hornegger, J. & Fahrig, R. Deconvolution-based CT and MR brain perfusion measurement: theoretical model revisited and practical implementation details. *Int. J. Biomed. Imaging* **2011**, 1–20 (2011).
89. Kealey, S. M., Loving, V. A., Delong, D. M. & Eastwood, J. D. User-defined vascular input function curves: influence on mean perfusion parameter values and signal-to-noise ratio. *Radiology* **231**, 587–593 (2004).
90. Østergaard, L. Principles of cerebral perfusion imaging by bolus tracking. *J. Magn. Reson. Imaging* **22**, 710–717 (2005).

Acknowledgements

We thank Florian Sevecke for technical support during the realization of numerous scanner components. We further thankfully acknowledge the financial support by the German Research Foundation (DFG, grant numbers KN 1108/7-1 and GR 5287/2-1). We also thank the developers of Makie.jl supporting us by answering technical questions when creating Figs. 3 and 4. Finally, we are grateful to Christian Findeklee for their discussions and insights into resonant circuit decoupling.

Author contributions

F.T., F.F., F.M., T.K. and M.G. contributed to the system's conceptualization. F.T., F.F. and F.M. constructed the MPI components. N.H. and T.K. developed the software. F.T., F.F., F.M., N.H., M.B., M.M. and T.K. contributed to experiment planning and execution. J.S. provided assistance with the reception system. T.K. and M.G. supervised the project. F.T., F.F., F.M. and T.K. contributed to writing the paper with the support of N.H., M.B. and M.M. All authors reviewed the manuscript.

Funding

Open Access funding enabled and organized by Projekt DEAL.

Competing interests

The authors declare no competing interests.

Additional information

Supplementary information The online version contains supplementary material available at https://doi.org/10.1038/s44172-024-00192-6.

Correspondence and requests for materials should be addressed to Florian Thieben.

Peer review information *Communications Engineering* thanks Ashley Makela and the other, anonymous, reviewer(s) for their contribution to the peer review of this work. Primary Handling Editors: Or Perlman, Anastasiia Vasylchenkova, Rosamund Daw. A peer review file is available.

8

Characterization of the Clinically Approved MRI Tracer Resotran for Magnetic Particle Imaging in a Comparison Study

Commencing with applications of MPI, we validate and classify the MPI performance of the medically approved MRI tracer Resotran (b.e.imaging GmbH, Baden-Baden, Germany), which is based on Ferucarbotran. The hypothesis of this chapter is that the MNPs are very similar to the well known and established MNPs Resovist, both Ferucarbotran-based, that are used in human MRI applications since 2003 [220] with a low rate of reported incidents [299]. We compare Resotran and Resovist with two more MNPs by using a variety of 5 different methods to determine the size, magnetic properties and MPI imaging performance [O4]. This work is a comprehensive study on the eligibility of Resotran for future human trials, as well as to indicate room of improvement by using superior MPI tailored tracers.

Parts of this chapter were presented at the IWMPI 2023 conference in Aachen, Germany [O19].

8.1 IOPscience - Physics in Medicine & Biology

Manuscript received February 9, 2024.
Revised May 21, 2024.
Accepted June 13, 2024.

DOI: 10.1088/1361-6560/ad5828

Editor's Choice of the month July 2024.

IOP Publishing Phys. Med. Biol. 69 (2024) 135014 https://doi.org/10.1088/1361-6560/ad5828

Physics in Medicine & Biology

IPEM
Institute of Physics and Engineering in Medicine

RECEIVED
9 February 2024

REVISED
21 May 2024

ACCEPTED FOR PUBLICATION
13 June 2024

PUBLISHED
1 July 2024

PAPER

Characterization of the clinically approved MRI tracer resotran for magnetic particle imaging in a comparison study

Fabian Mohn[1,2,*], **Konrad Scheffler**[1,2], **Justin Ackers**[3], **Agnes Weimer**[3,4], **Franz Wegner**[5], **Florian Thieben**[1,2], **Mandy Ahlborg**[3], **Patrick Vogel**[6], **Matthias Graeser**[3,7] **and Tobias Knopp**[1,2,3]

[1] Institute for Biomedical Imaging, Hamburg University of Technology, Hamburg, Germany
[2] Section for Biomedical Imaging, University Medical Center Hamburg-Eppendorf, Hamburg, Germany
[3] Fraunhofer IMTE, Fraunhofer Research Institution for Individualized and Cell-based Medical Engineering, Lübeck, Germany
[4] Institute of Physical Chemistry, University of Hamburg, Hamburg, Germany
[5] Institute for Interventional Radiology, University of Lübeck, Lübeck, Germany
[6] Department of Experimental Physics 5 (Biophysics), University of Würzburg, Würzburg, Germany
[7] Institute of Medical Engineering, University of Lübeck, Lübeck, Germany
[*] Author to whom any correspondence should be addressed.

E-mail: fabian.mohn@tuhh.de

Keywords: MPI, Resovist, ferucarbotran, DLS, VSM, TEM, MPS

Abstract

Objective. The availability of magnetic nanoparticles (MNPs) with medical approval for human intervention is fundamental to the clinical translation of magnetic particle imaging (MPI). In this work, we thoroughly evaluate and compare the magnetic properties of an magnetic resonance imaging (MRI) approved tracer to validate its performance for MPI in future human trials. *Approach.* We analyze whether the recently approved MRI tracer Resotran is suitable for MPI. In addition, we compare Resotran with the previously approved and extensively studied tracer Resovist, with Ferrotran, which is currently in a clinical phase III study, and with the tailored MPI tracer Perimag. *Main results.* Initial magnetic particle spectroscopy (MPS) measurements indicate that Resotran exhibits performance characteristics akin to Resovist, but below Perimag. We provide data on four different tracers using dynamic light scattering, transmission electron microscopy, vibrating sample magnetometry measurements, MPS to derive hysteresis, point spread functions, and a serial dilution, as well as system matrix based MPI measurements on a preclinical scanner (Bruker 25/20 FF), including reconstructed images. *Significance.* Numerous approved MNPs used as tracers in MRI lack the necessary magnetic properties essential for robust signal generation in MPI. The process of obtaining medical approval for dedicated MPI tracers optimized for signal performance is an arduous and costly endeavor, often only justifiable for companies with a well-defined clinical business case. Resotran is an approved tracer that has become available in Europe for MRI. In this work, we study the eligibility of Resotran for MPI in an effort to pave the way for human MPI trials.

1. Introduction

Magnetic particle imaging (MPI) is an emerging tomographic technique that combines high magnetic nanoparticle (MNP) sensitivity with high temporal and spatial resolution (Gleich and Weizenecker 2005). The main principle is the exploitation of the nonlinear magnetization behavior of MNPs in a periodic magnetic excitation field (drive field). A spatial resolution is achieved by using a magnetic gradient field (selection field) keeping the MNPs in saturation everywhere except in a small field-free-region. As a promising tomographic technique without ionizing radiation, MPI has high potential in numerous medical applications. Due to its very high temporal resolution, a main focus is cardiovascular and periinterventional imaging (Weizenecker *et al* 2009, Haegele *et al* 2012, 2016a, 2016b, Bakenecker *et al* 2018, Herz *et al* 2019, Wegner 2021) as well as perfusion imaging (Ludewig 2017, Kaul *et al* 2018, Mohn *et al* 2023). Due to the multifaceted properties of MNPs that can be exploited by MPI, further applications are part of extensive research: development of dedicated MPI instruments for treatment of vascular stenosis (Ahlborg 2022), cellular tracking (Zheng *et al* 2015, Sehl *et al* 2020, Remmo *et al* 2022), local magnetic hyperthermia (e.g. tumor imaging and therapy without surgery) (Chandrasekharan 2020, He *et al* 2023) and navigation of magnetic micro-robots for targeted drug delivery and treatment of cerebral aneurysms (Bakenecker *et al* 2021, Bui *et al* 2021, 2023). The authors refer to reviews for detailed insight on the full functionality of MPI as well as the progress made from the first prototype in 2005 to the first commercial preclinical systems, given by Knopp *et al* (2017). Further outlines over current research and applications can be found in Billings *et al* (2021), Neumann (2022), Yang *et al* (2022).

Besides upscaling MPI hardware to human-sized scanners (Sattel *et al* 2015, Mason *et al* 2017, Rahmer *et al* 2018, Graeser 2019, Vogel *et al* 2023) and addressing safety concerns (Saritas *et al* 2013, Schmale 2013, Thieben *et al* 2024), the availability of suitable MNPs with medical approval is crucial for a clinical translation of MPI. The development of medical MNPs is primarily driven for the application in magnetic resonance imaging (MRI). Unfortunately, most MNPs developed for MRI do not have the specific magnetic properties that are needed to generate a strong signal in MPI. If nanoparticles are too small, the thermal energy dominates the magnetic energy, inducing a rather linear magnetization behavior. Thus, they are not suited for MPI, where signal generation and spatial encoding is based upon a nonlinear magnetization. On the other hand, if particles are too large, they block the Néel relaxation process due to strong magnetic anisotropies. This reduces their ability to follow the magnetic field at excitation frequencies between 10 kHz to 150 kHz (Deissler *et al* 2014, Tay *et al* 2017). An important MRI MNP that has magnetic properties suitable for MPI is ferucarbotran, namely Resovist, formerly with medical approval in Germany (Bayer Schering Pharma, Berlin, Germany) and still approved in Japan (I'rom Pharmaceuticals, Tokyo, Japan). However, due to a wide particle size distribution with the majority of particles being smaller than 15 nm, only a small fraction of the total iron mass contributes to a useful MPI signal (Yoshida *et al* 2013). First dedicated MNPs, tailored to enhance the MPI specific performance, were published by Ferguson *et al* (2009). Later, a monodisperse iron core MNP coated with polyethylene glycol (Ferguson 2015), evolving into the formerly commercially available MNPs LS-008 (LodeSpin Labs, Seattle, USA) was developed. In 2013, dextran coated multicore magnetic iron oxide nanoparticles were presented by Eberbeck *et al* (2013), commercially available as the preclinical MNPs Perimag and Synomag (micromod Partikeltechnologie, Rostock, Germany). The mean magnetic core size of Perimag is about 19 nm, in the range where a coupled Brownian and Néel relaxation occurs (Eberbeck *et al* 2013, Ludwig *et al* 2013). Moreover, MNPs can also undergo a system-specific optimization, i.e. to match a particular type of excitation: the formation of particle chains has improved the nonlinear response in 1D excitation (Tay 2021). A comparison of commercial MNPs with respect to their MPI performance is given by Lüdtke-Buzug *et al* (2013) and Ludwig *et al* (2013) and more recently by Irfan *et al* (2021a). A recent overview of the development of MPI tailored MNPs is given by Harvell-Smith *et al* (2022).

The research on MPI tailored tracers increased in the last years (Antonelli *et al* 2020, Liu *et al* 2021, Moor *et al* 2022, Thieben *et al* 2023a), however, none of these tracers has reached a level of development that would warrant the costs of a medical approval and consequently their use in clinical MPI remains distant. Such an approval requires a well-defined business case and a long-term market to justify the multi-annual process and investment in a new approval. Fortunately, Resotran (b.e.imaging GmbH, Baden–Baden, Germany; medical approval granted in Oct. 2022 under reg. no. 7002 837.00.00 in Germany), containing ferucarbotran MNPs, has recently received approval in certain countries, including Germany and Sweden. Additionally, there is a phase III clinical trial underway for ferumoxtran MNPs called Ferrotran, consisting of ultrasmall superparamagnetic iron-oxide nanoparticles (USPIONs). Both MNPs are officially authorized for MRI liver imaging and initial measurements showed similar MPI performance (Hartung *et al* 2023, Scheffler *et al* 2023). General concerns regarding toxicity of MNPs in long-term metabolism remain (Sun *et al* 2008, Billings *et al* 2021, Rubia-Rodríguez 2021), although the incidence of adverse events for ferucarbotran (Resovist) is low with 7.1% (Wang 2011). The performance of known ferucarbotran-based tracers such as Resovist and VivoTrax (Magnetic Insight Inc. Alameda, USA) is similar (Song *et al* 2018, Gevaert *et al* 2022, Yeo *et al* 2022). A comparison of VivoTrax and Perimag is found in Irfan *et al* (2021b), Synomag is also included by Yeo *et al* (2022), and Synomag, Perimag, and Resovist are compared in Ludewig (2022).

The purpose of this paper is to provide a comprehensive characterization of the MNPs Resotran and Ferrotran with a focus on their applicability to MPI. Comparisons will be made with the extensively studied MRI MNPs Resovist as well as with the MPI tailored MNPs Perimag. We chose Perimag because of its established position and its appearance in a wide range of publications and open datasets (Knopp *et al* 2020). In this work, we address the characterization of the four MNPs Perimag, Resotran, Resovist and Ferrotran by transmission electron microscopy (TEM), dynamic light scattering (DLS), vibrating sample magnetometry (VSM) and magnetic particle spectroscopy (MPS) measurements. In addition, 2D MPI reconstructions for two different phantoms are compared at the system matrix level and in the image domain for future applications in MPI. We present and discuss the results of applying these methods to all four MNPs.

2. Materials and methods

For a comprehensive characterization of the four MNPs Perimag, Resotran, Resovist and Ferrotran regarding their suitability in MPI, we analyze shape parameters, magnetic properties, system matrix performance and image reconstructions.

First, the hydrodynamic diameter can be determined using DLS and the core diameter of the magnetite can be determined using TEM. The latter provides a detailed visualization of the inner iron core in a sub-nanometer resolution and thus of the relationship between the iron structure and performance in MPI. Second, regarding the magnetic properties, we determine the static magnetization characteristic by VSM and the dynamic particle response to a drive field by MPS. The VSM data are used to observe the MNPs in the saturation region as well as their nonlinear slope through the origin according to the Langevin model. MPS measurements show the particle spectrum and can reveal relaxation induced hysteresis as a function of excitation amplitude. We also measure a dilution series and different offset-field combinations to plot two types of point spread functions (PSFs) that can be used to estimate image resolution. Third, prior to reconstruction, the signal-to-noise ratio (SNR) and system matrix patterns are analyzed to estimate the performance and compare Resotran to Resovist in the frequency domain. The fineness of the frequency pattern indicates the expected resolution of the reconstructed image. Finally, the MNPs are evaluated in a typical MPI imaging scenario to demonstrate suitability and resolution for medical imaging, using a commercial imaging system (Bruker MPI 25/20 FF). Two different phantoms are measured and we also perform cross reconstructions using the Resotran system matrix to reconstruct all other tracers to assess compatibility. In the following we introduce each of these methods in detail and describe the performed experiments and their implications.

2.1. MNP material

The MNPs are measured at a concentration of $8.5\,\mathrm{mg_{Fe}\,ml^{-1}} \approx 152\,\mathrm{mmol\,l^{-1}}$, a threshold that is chosen to avoid concentration dependent behavior (Löwa *et al* 2016). For Perimag, we use stock dispersion with this concentration (LOT 045 211). Both Resotran (LOT F1901) and Resovist (LOT 20F01) are supplied with $28\,\mathrm{mg_{Fe}\,ml^{-1}}$ and are therefore diluted with distilled water. Ferrotran (LOT PRX19L02) is shipped as freeze-dried powder and has a concentration of $20\,\mathrm{mg_{Fe}\,ml^{-1}}$ once dispersed in water, which we dilute to the same level of $8.5\,\mathrm{mg_{Fe}\,ml^{-1}}$. All MNPs are made from iron oxide and coated with a dextran shell. More specifically, Resovist and Resotran are made from ferucarbotran and Ferrotran is made from ferumoxtran-10 lyophilisate and additionally coated with sodium citrate.

2.2. DLS

The hydrodynamic diameter of the aqueous iron oxide nanoparticle dispersion is measured using DLS on a Zetasizer Pro-Blue (Malvern Panalytical Ltd, Malvern, United Kingdom) device at a laser wavelength of 633 nm. The sample is diluted 1:100 with Milli-Q (Merck Group, Darmstadt, Germany) water and measured in a plastic cuvette at an optical path length of 1 cm. Each measurement is recorded over three cycles (3 averages) of 30 s each and an intensity weighted mean hydrodynamic diameter of the particle ensemble (z-average) is calculated with the respective polydispersity index (PDI). The z-average is based on the method of cumulants (Koppel 1972), where the monochromatic light source is scattered by the MNPs in suspensions and the light intensity of the interference pattern is evaluated for a logarithmic normal size distribution (Thomas 1987). The light scattering is caused by the particle ensemble surface and the results include the dextran shell, therefore a size distribution of the hydrodynamic diameter is shown, not the magnetite core. The data is analyzed using the ZS XPLORER software version 3.2.0.84 (Malvern Panalytical Ltd, Malvern, United Kingdom).

2.3. TEM

TEM measurements are performed with a JEOL JEM-1011 (JEOL Ltd, Tokyo, Japan) at 100 kV equipped with two spherical aberration correction devices (CETCOR and CESCOR by CEOS GmbH, Heidelberg, Germany) and a Gatan 4K UltraScan 1000 (Gatan Inc., Pleasanton, USA) camera. For the preparation, $10\,\mu\mathrm{l}$ of the diluted nanoparticle dispersion are placed on a carbon-coated TEM copper slide with a 400 mm mesh. The excess solvent is removed with a filter paper and the TEM grid is air-dried. The recorded images achieve a $2 \cdot 10^5$-fold magnification at 100 kV. For a quantitative analysis, the size of 250 individual particles is measured using the software ImageJ (NIH, Bethesda, USA) and plotted in a histogram to visualize the size-distribution, following the guidelines of (2014) for counting (Pyrz and Buttrey 2008). Our evaluation only accounts for the short-axis diameter (Pyrz and Buttrey 2008, Verleysen *et al* 2019) of individual particles and we do not count any particle clusters or chains (Bender 2018, Bresch *et al* 2022).

2.4. VSM

The magnetization of the liquid samples in response to static magnetic fields are characterized using a VSM (Lakeshore 8607 VSM, Westerville, USA). A quantity of 20 μl is filled into the sample holder and covered with oil, resulting in an almost spherical sample shape. A sweep of the external magnetic field in the range of ± 2 T (step size 20 mT) and in the range of ± 30 mT (step size 0.5 mT) is performed. The signal is averaged for 1 s at each step. The results are given in the domain of the magnetic moment, calibrated by the VSM (Foner 1959) and divided by 2 to match the iron mass of the MPS samples of 85 μg_{Fe} (10 μl). Direct measurement of 10 μl would have been possible, but accurately pipetting amounts below 20 μl into the VSM sample holder proved more error prone than measuring the larger sample and relying on the linear signal response (Knopp *et al* 2017) (refer to the dilution series of section 3.4).

2.5. MPS

We use an arbitrary waveform MPS to measure different 10 μl samples of MNPs exposed to a combination of a static and a dynamic magnetic field (Mohn *et al* 2022). These fields are homogeneous inside the measurement chamber and consist of two quantities, a sinusoidal drive-field B_{drive} at 26.042 kHz and a static offset field B_{offset} for saturation. In this case, both fields are oriented in the same direction. A set of static offsets in the range of ± 30 mT (step size 0.5 mT) is measured for different drive-field amplitudes in the range of 4 to 20 mT (step size 2 mT). All measurements are averaged over 45 drive-field periods (1.73 ms) to reduce noise at low drive-field values. The receive bandwidth of the MPS device is 7.8125 MHz, using a stack of two RedPitaya STEMlab 125-14 and the open source software stack composed of RedPitayaDAQServer (Hackelberg *et al* 2022) and MPIMeasurements.jl (Hackelberg *et al* 2023). The system is calibrated using a transfer function measured with a small calibration coil (Thieben *et al* 2023b). By calibrating the entire receive chain, we can express the particle response in terms of the net magnetic moment m and thus obtain device-independent measurements that are particle specific. The hysteresis curve is obtained by plotting m against the actual drive-field B_{drive}, using the calibrated reference channel in mT of the device.

2.5.1. PSF

Two types of PSFs are calculated to visualize tracer differences using the MPS data. A narrow and steep PSF is generally indicative for high resolution MPI (Croft *et al* 2012), while relaxation effects cause asymmetries and broadening of the PSF. The dynamic PSF is based on a straight forward approach by plotting one half-cycle of $\frac{\mathrm{d}m}{\mathrm{d}t}$ against the excitation B_{drive} (positive half-cycle only). Consequently, the PSF approaches a zero-crossing at the maximum amplitude of B_{drive}. The calculation of the x-space PSF is typically based on partial field-of-views (FOVs) and a DC-recovery step (Goodwill *et al* 2012, Lu *et al* 2013), which becomes obsolete when the fundamental is not filtered, i.e. when using a gradiometric arbitrary waveform MPS, as validated by Tay *et al* (2016). To this end, we plot the value of $\frac{\mathrm{d}m}{\mathrm{d}t}$ at the maximum field gradient of B_{drive} against each offset step value. The data is then normalized to facilitate the comparison of the full width at half maximum (FWHM) of the x-space PSF.

2.5.2. Serial dilution

To investigate the linearity between the particle magnetization and the total amount of iron in a sample, we perform a dilution series with an MPS with 1D sinusoidal excitation with 20 mT at 26.042 kHz. Each measurement is performed using 10 background frames and 10 foreground frames, using a transfer function correction and a sample of 10 μl of each MNP. Starting with 8.5 $\text{mg}_{\text{Fe}}\,\text{ml}^{-1}$ the concentration is halved seven times, dispersed with the same amount of distilled water, leading to a set of 8 measurements per tracer with $8.5 \cdot \left(1/2\right)^i \text{mg}_{\text{Fe}}\,\text{ml}^{-1}$ for $i = 0, \ldots, 7$. Despite working with highest precision, potential inaccuracies while pipetting increase with a diminishing total iron amount. We evaluate the absolute values of the third harmonic of the measured magnetization response in the frequency domain (Löwa *et al* 2020) to compare the results of the 4 different MNPs.

2.6. MPI

MPI is performed using the preclinical Bruker MPI system 25/20 FF. We use a 2D Lissajous excitation in xy-direction with an amplitude of 12 mT at a frequency of 24.509 kHz/26.041 kHz in x-/y-direction and a selection field gradient of $(-1, -1, 2)$ T m^{-1} generating a FOV of 24×24 mm^2. All measurements are taken with a dedicated 3D receive coil with an open bore of 72 mm, based on the gradiometric approach, a custom built low noise amplifier, and corrected with a measured transfer function (Graeser *et al* 2017). The 2D system matrices are measured using a delta-sample of $1 \times 1 \times 5$ mm^3 filled with 4 μl of each tracer diluted to a common iron concentration of 8.5 $\mathrm{mg_{Fe}\,ml^{-1}}$ on $29 \times 29 \times 1$ equidistant grid positions covering $29 \times 29 \times 5\,\mathrm{mm}^3$. A quantitative comparison of the different MNPs on system matrix level is done by considering the SNR profiles and characteristics (Franke *et al* 2016) as well as the structural similarity index measure (SSIM) (Wang *et al* 2004) over all frequency components. Furthermore, a qualitative comparison is given on three selected frequency components with high (99.57 kHz), medium (104.17 kHz), and low (108.76 kHz) SNR.

The MPI reconstructions are performed on two different phantoms, each measured with 500 averages (10 s measurement time). The first phantom consists of three $1 \times 1 \times 1\,\mathrm{mm}^3$ square samples, filled with 0.8 μl of the tracer at 8.5 $\mathrm{mg_{Fe}\,ml^{-1}}$, placed in the corners of an equilateral triangle with an edge length of 9.24 mm. If the MNPs are MPI suitable, the individual dots should be easily separable. The second phantom is more complex and consists of a spiral with two full windings. The round vessel phantom consists of windings with an inner diameter of 2.5 mm, separated by an edge-to-edge distance of 2.8 mm. It is filled with a concentration of 8.5 $\mathrm{mg_{Fe}\,ml^{-1}}$. Although the total iron amount is much higher than in the three-dot phantom, a complete resolution of the spiral is expected to be more challenging than for the three-dot phantom. Image reconstruction is performed using the iterative Kaczmarz method and a careful selection of frequency components and regularization strength for each individual image. Complete fairness in the comparison is a hard problem due to its complexity and is currently part of research (Weizenecker *et al* 2007, Dittmer *et al* 2021, Hackelberg *et al* 2024, Scheffler *et al* 2024).

3. Results

All measurements of section 2 were performed identically for the four considered MNPs. With the exception of the dilution series and the DLS experiments, all MNPs were prepared at identical concentrations of 8.5 $\mathrm{mg_{Fe}\,ml^{-1}}$ (152 $\mathrm{mmol\,l^{-1}}$).

3.1. DLS

Results of the DLS measurements are shown in figure 1. Light intensity is given in percent for each size bin (round marks) with respect to all measured bins of the log normal size distribution. Perimag exhibits the largest hydrodynamic sizes with a peak value at 114 nm (z-average 102.5 nm, PDI 0.1853), followed by Resotran with a narrower distribution and a peak at 74 nm (z-average 66.32 nm, PDI 0.1806). Resovist is roughly comparable to Resotran, with a peak value at 65 nm (z-average 55.97 nm, PDI 0.2007). Ferrotran is a ultra-small superparamagnetic iron oxide (USPIO) and has a hydrodynamic diameter of around 28 nm (z-average 27.82 nm, PDI 0.09) and the narrowest distribution of all tracers.

3.2. Transmission emission microscopy

In figure 2, TEM images and a histogram of individual particles for a count of $n = 250$ short-axis core diameter measurements are shown for each tracer. The mean μ and the standard deviation σ are given in the top right corners. TEM images provide indications of shape, structure, size and uniformity of the nanoparticles. Note that the counting rule applied significantly influences the classification (Bresch *et al* 2022), but we mostly observe spherical individual particles without strong elongation and do not classify particle clusters.

Perimag and Ferrotran exhibit the smallest mean core diameter, followed by Resotran and Resovist in increasing order. As TEM images show the magnetite cores, clusters and particle-chains are visible as well as overlapping particles. Especially for Perimag, such clusters and chains are visible in the pictures and the cores tend to form large clusters in the range of 20 to 50 nm. Visual inspection of Resotran and Resovist indicates a similar structure and size of both tracers. Ferrotran shows isolated cores, separated by their ligand hull, which reduces magnetic interaction in between particles. Seemingly, no clusters are formed and particles do not overlap, which agrees with DLS results for this USPIO.

3.3. VSM

The results of the VSM measurements are shown in figure 3. All particle samples show the expected superparamagnetic behavior with sigmoidal magnetization curves and no detectable hysteresis. In the ±2 T range plot, the magnetization curves of Resovist and Resotran are very similar, reaching almost the same saturation magnetization at about 83.6 $\mathrm{Am^2\,kg_{Fe}{}^{-1}}$. The saturation magnetization of Perimag is around 89.3 $\mathrm{Am^2\,kg_{Fe}{}^{-1}}$. Ferrotran has the highest saturation magnetization of the investigated particles (93.88 $\mathrm{Am^2\,kg_{Fe}{}^{-1}}$), but has a much lower initial slope with an almost linear curve in the MPI relevant range ±30 mT, when the origin of the left plot in figure 3 is considered. In contrast, Perimag shows the strongest nonlinearity with an initial slope around 1.23 $\mu\mathrm{Am^2\,mT^{-1}}$, whereas Resotran exhibits 0.67 $\mu\mathrm{Am^2\,mT^{-1}}$ and Resovist is lower with 0.45 $\mu\mathrm{Am^2\,mT^{-1}}$ (evaluated at ±1 mT).

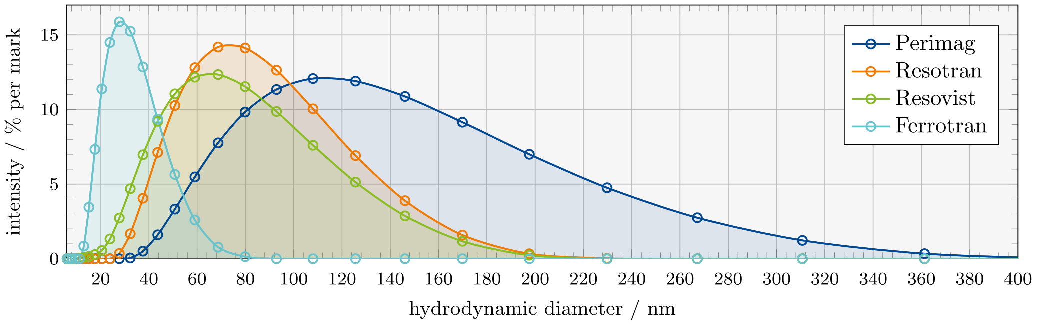

Figure 1. Intensity weighted log normal size distribution by DLS. A sample with a 1:100 dilution of each tracer was measured using DLS to determine the hydrodynamic particle diameter, that includes the dextran shell coating (laser wavelength of 633 nm, 30 s measurement time, 3 averages).

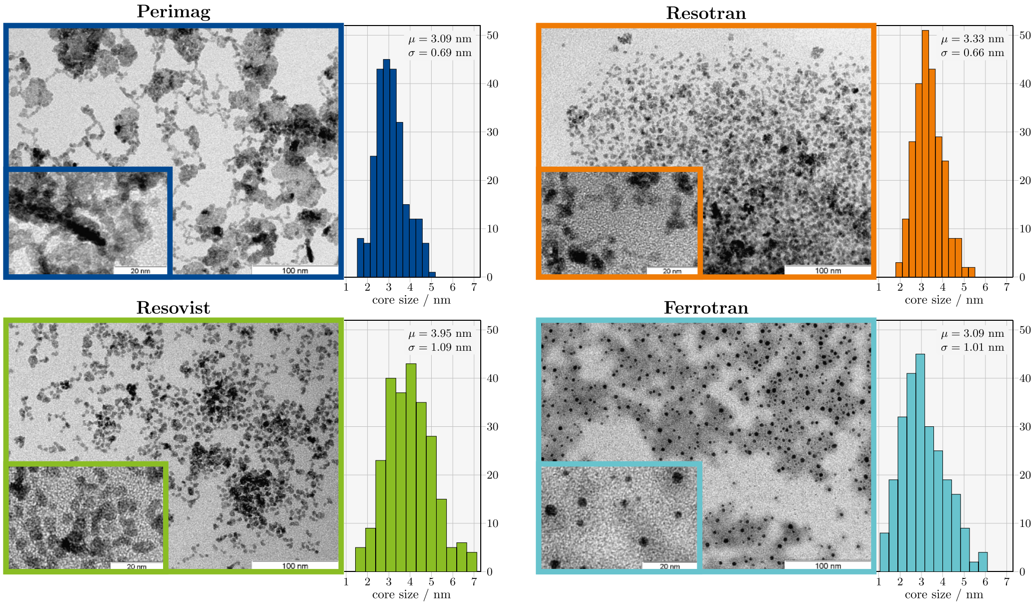

Figure 2. TEM images. Samples of each tracer as visualized by TEM for two different zoom levels at 20 nm and 100 nm reference scale, showing the iron-oxide core. Each histogram lists the mean μ and the standard deviation σ of the core short-axis diameter for a count of $n = 250$ particles categorized into 12 individual size bins. Note, that Perimag, Resotran and Resovist form clusters and chains, which were not counted, whereas Ferrotran accounts for the smallest and individual particles (USPIOs).

3.4. MPS

Four types of plots are generated in figure 4, each containing measurements of the four MNPs under investigation. On the top, the spectrum for 6 mT and 20 mT excitation amplitude is shown, because these amplitudes refer to a realistic range for human-sized MPI (Ozaslan *et al* 2022, Thieben *et al* 2024). We only plotted the odd harmonics, because they contain the majority of the information on the nonlinear magnetization of MNPs in a homogeneous sinusoidal excitation field (without offset fields). The spectrum of Resotran and Resovist are very similar for both 6 mT and 20 mT, the amplitude of Resotran being slightly higher in the range of 5%–15%. Compared to Resotran, Perimag has a 1.5–2.0 fold higher signal amplitude at low harmonic indices, increasing to 2.5 at higher indices above 400 kHz. Ferrotran has an overall low signal amplitude, as already indicated by the linear slope in figure 3. Even at 20 mT excitation, useful signal is only detectable below 300 kHz, indicating insufficient MPI signal.

In the middle row, the hysteresis curve is plotted, which shows a residual magnetization for all tracers, except for Ferrotran, which does not seem to undergo a measurable, relaxation-induced hysteresis. On the bottom the different normalized PSFs are plotted. We state the FWHM for the *x*-space PSF to facilitate comparison. At 6 mT, all tracers except Ferrotran indicate very similar magnetic properties, however, the difference in terms of FWHM between both PSF types are large. This effect reduces at 20 mT with a trend for the *x*-space PSF to broaden and the dynamic PSF to narrow. The PSFs show that the relaxation behavior of

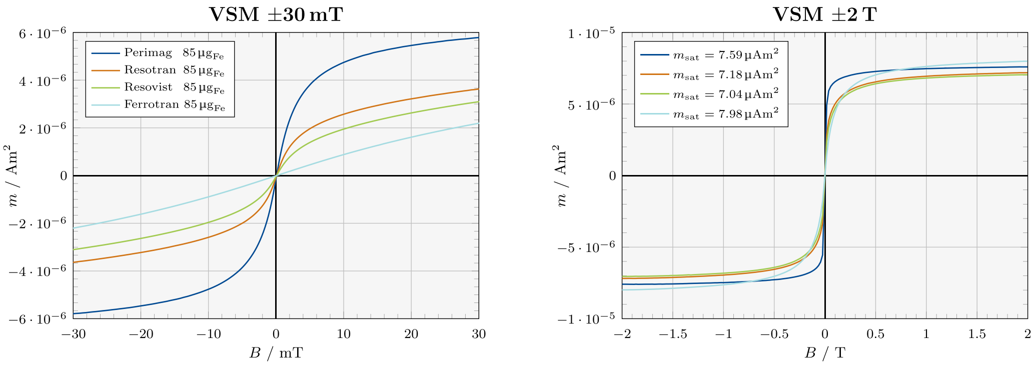

Figure 3. VSM results. The magnetic moment is plotted against the external field for two different ranges with identical samples. The steeper the slope of the net magnetic moment m at the origin, the stronger is the nonlinear response which is the useful signal in MPI.

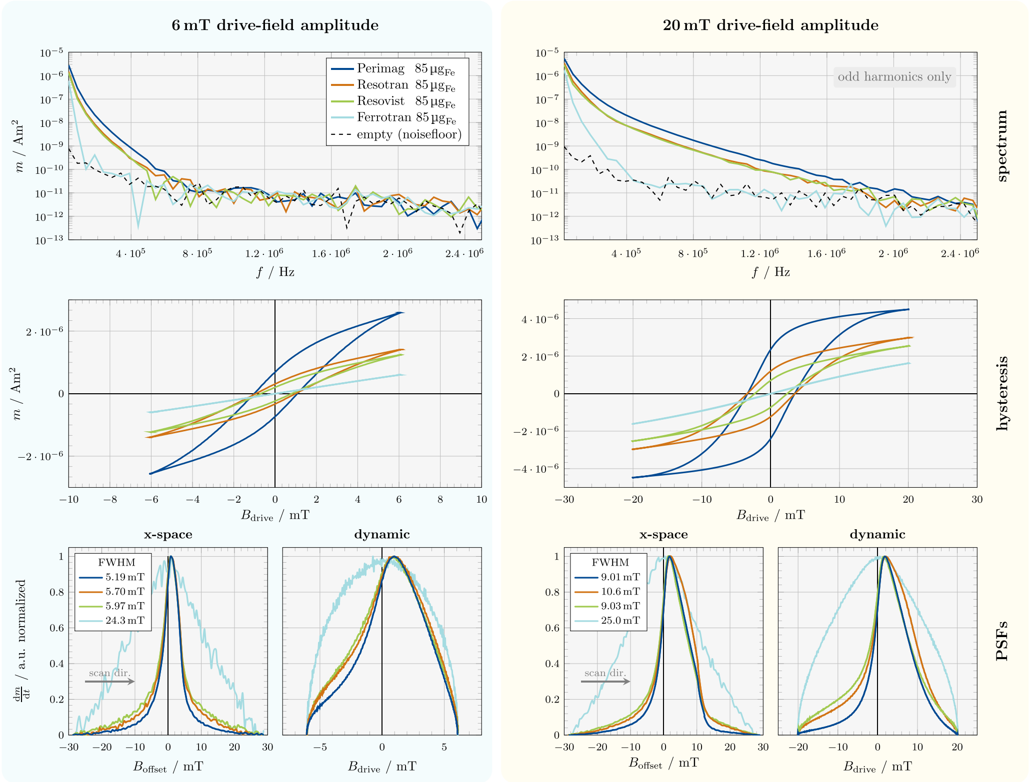

Figure 4. Arbitrary waveform MPS results. Spectrum, hysteresis and PSFs from top to bottom for 6 mT and 20 mT sinusoidal drive-field excitation. The frequency spectrum only contains odd harmonics of the fundamental $f_1 = 26.042$ kHz. The FWHM of the x-space PSF is given in the legend and the gray arrow indicates the scan direction (positive half-wave).

the first three tracers is very similar, especially at low excitation amplitudes. At 20 mT the measured Resotran sample seems to broaden slightly, possibly due to a stronger Brownian component. Both PSFs indicate an inferior MPI image quality for Ferrotran. The noisy shape is caused by the normalization, which maps all peak amplitudes to one. Their original relation of maximum signal can be deduced from the saturation region of the hysteresis curve above.

In a deeper MPS analysis, we refer to three different types of plots in figure 5. On the left side, the results of the MPS dilution series are shown. We observe a linear behavior in the absolute magnitude of the third harmonic over all concentrations down to $8.5 \cdot \left(1/2\right)^7 \approx 0.066\,\mathrm{mg\,ml^{-1}}$ for Perimag, Resotran and Resovist. While Perimag produces the highest signal, the results indicate that Resotran and Resovist are relatively comparable in signal strength, with Resotran's signal being slightly higher. Ferrotran gives a much weaker

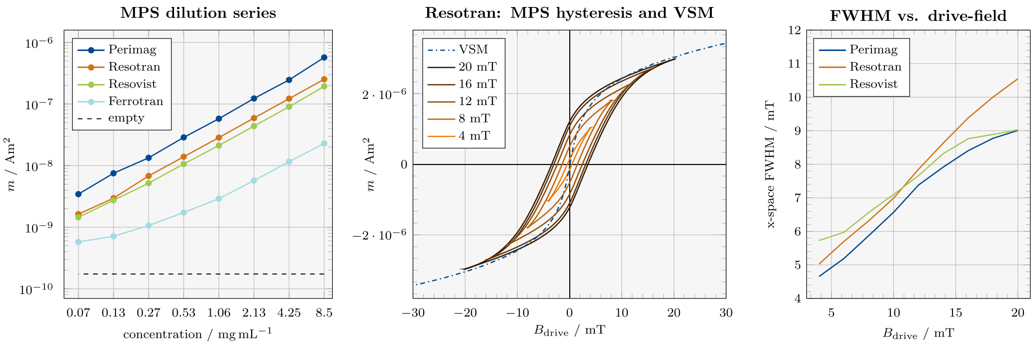

Figure 5. MPS data analysis. On the left, a dilution series of all tracers is shown. The absolute value of the third harmonic of exponentially decreasing concentrations between $8.5 \cdot \left({}^{1}\!/_{2}\right)^{0}$ mg ml^{-1} and $8.5 \cdot \left({}^{1}\!/_{2}\right)^{7}$ mg ml^{-1} is plotted (20 mT, 26.042 kHz). The center plot focuses on Resotran: the hysteresis for 5 different excitation amplitudes is plotted (bright to dark for increasing amplitude) with an overlay of the VSM curve (dash-dot). On the right, the FWHM is plotted against the drive-field amplitude. Ferrotran was omitted to retain a detailed scale.

MPS signal, starting with a linear result for higher concentrations, but loosing linearity by the 4th dilution step towards lower concentrations. At the lowest two concentrations, the response is barely higher than the background signal.

In the center of figure 5, the hysteresis curve for Resotran is plotted in a range of 4 to 20 mT with 4 mT steps for the excitation fields. In addition, the VSM curve of Resotran is overlaid, as obtained from figure 3. The hysteresis broadens with increasing amplitude and the turning point in saturation (maximum/minimum of B_{drive}) seems to approach the VSM line at high amplitudes.

The x-space PSF was evaluated at varying excitation amplitudes between 4–20 mT in 2 mT intervals, as shown on the right-hand side of figure 5. The resulting plot displays the FWHM of the PSFs against the drive-field amplitude and provides detailed insights into its tendency to increase with amplitude, which was previously observed in figure 4. Specifically, the FWHM seems to increase linearly with amplitude. However, the linear increase is only applicable to a small region, and both Perimag and Resovist demonstrate a decline above 16 mT. On the other hand, Resotran maintains a consistent linear pattern throughout our measurement range.

3.5. MPI

For a quantitative comparison of the system matrices, we consider the SNR profile of the x-channel as well as an SSIM comparison with Resotran over all frequencies of the x-channel, shown in the upper part of figure 6. As expected, Perimag achieves the highest SNR over the entire frequency band. Especially for higher harmonics above 350 kHz the measured signal outperforms the other tracers. Ferrotran clearly shows the lowest SNR profile. Only the first 4 harmonics reach SNR levels suitable for MPI. In contrast, Resotran and Resovist achieve SNR profiles suitable for good MPI measurements with useful frequency components up to 500 kHz. Higher harmonics show good SNR levels above 10 up to 350 kHz. Overall, Resotran and Resovist show very similar SNR profiles. This is supported by the SSIM comparison in the 3rd row of figure 6. Moreover, the SSIM indicates, that the Resotran and Resovist system matrix patterns are similar in structure. Especially around the harmonics with a SNR above 10, the SSIM is high and the system matrix patterns of Resotran and Resovist are very similar. We also considered mean absolute error and mean squared error between the different spectra and the Resotran spectrum, but the results are very similar to the SSIM course and we decided to focus on the SSIM to reduce redundant information.

A qualitative comparison of the system matrices on three selected frequency components with high SNR (99.57 kHz), medium SNR (104.76 kHz) and low SNR (108.76 kHz) is displayed in the bottom part of figure 6, which are sidebands of the fourth harmonic. The fourth harmonic was selected for analysis, because it has a higher SNR than the third on the Bruker MPI 20/25 FF, in part due to our custom receive chain without harmonic notching (Mattingly *et al* 2022). The close resemblance of the system matrix components of Resotran and Resovist can be seen in phase and amplitude. Moreover, the wave patterns show the same structure when compared to Perimag. Visible differences compared to Perimag can be seen in the component with medium SNR, especially in the outer corners and in the component with low SNR, where Resotran and especially Resovist have significantly more noise. At the highest frequency we also see Resotran and Resovist differing in quality. The system matrix components of Ferrotran are clearly different and the wave patterns

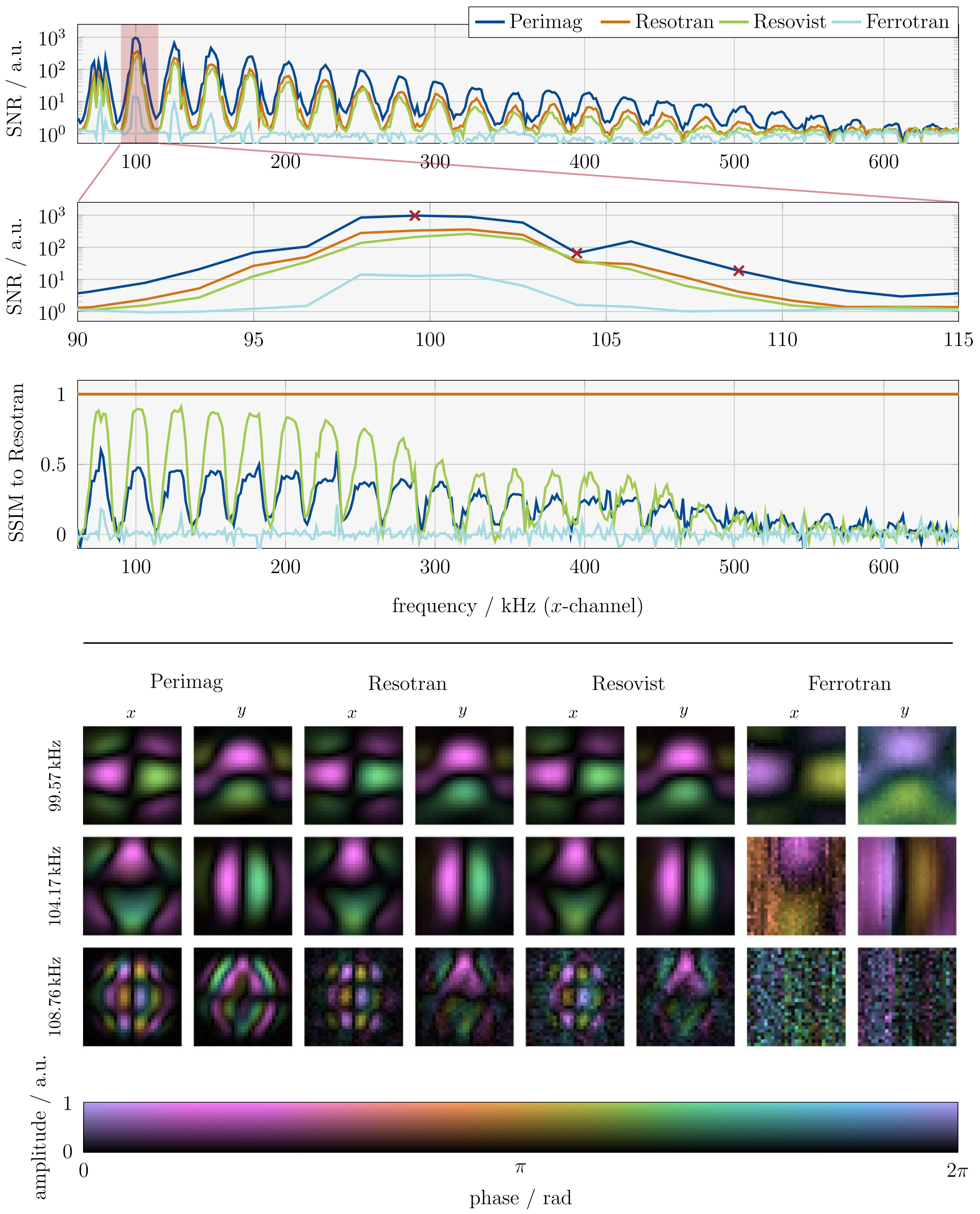

Figure 6. MPI system matrices. On the top, the SNR of the x-channel of all MNPs is shown, as measured with the preclinical system Bruker MPI 20/25 FF with xy-excitation. The relation of signal amplitudes and visible harmonics is similar to the MPS measurements. The second row shows a zoom on the fourth harmonic including its sidebands, from 90 to 115 kHz. The third row displays the SSIM of Perimag, Resovist and Ferrotran with respect to Resotran for the full spectrum. Below, the complex color-coded system matrix pattern are shown for three frequencies (marked by red crosses above) across all tracers.

are not represented correctly even for the component with the high SNR value. Phase and amplitude are also different and noise is clearly dominant.

Lastly, we consider the reconstruction results of two phantoms, a 3-dot phantom and a spiral phantom, given in figure 7. In the upper part, reconstructions with the dedicated system matrices are shown. In the lower part, cross-reconstructions with the Resotran system matrix are shown for all other tracers. The SSIM to the reconstruction result of Resotran is superposed in the lower right corner for all reconstructions.

The images indicate, that both phantoms can be reconstructed successfully by using Perimag, Resotran and Resovist. Here, Perimag visibly achieves the best image quality, followed by Resotran. Ferrotran is not able to resolve the phantoms at all. Cross-reconstructions using the Resotran system matrix are possible for Perimag and Resovist on both phantoms. While the result for Perimag gets worse, the reconstruction result

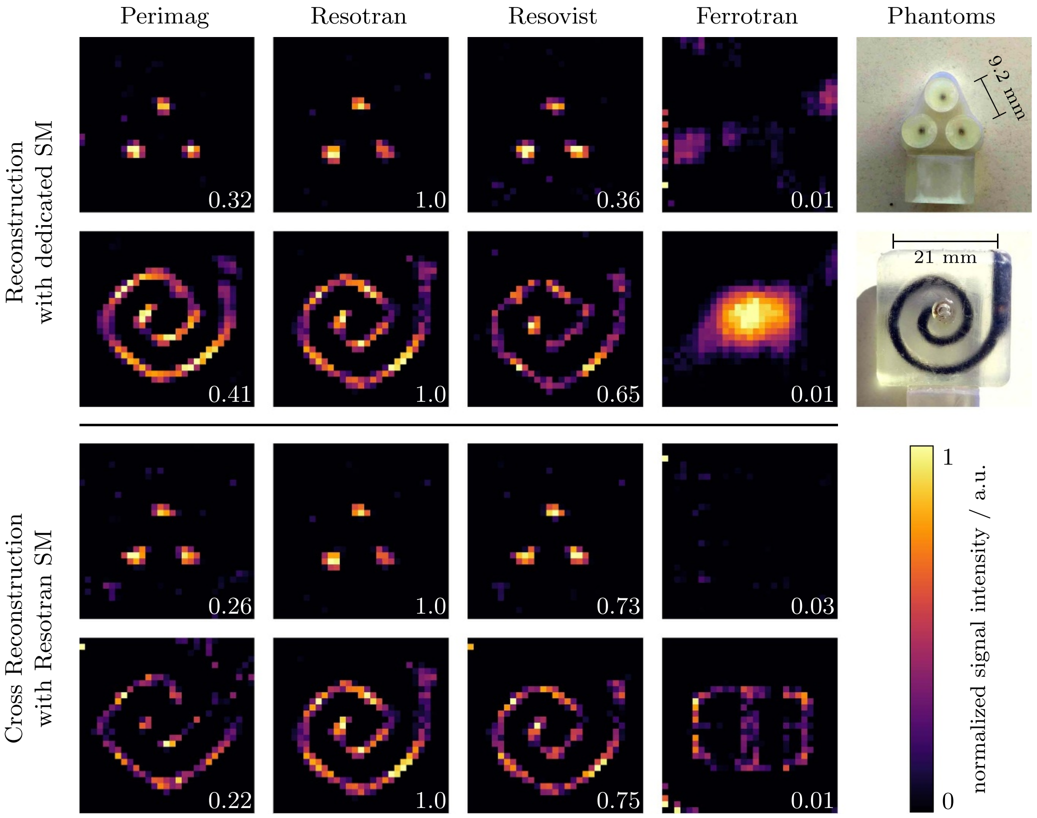

Figure 7. Comparison of MPI reconstructions. Results of the four different MNPs in two different phantoms are shown, each with an iron concentration of 8.5 $\mathrm{mg_{Fe}\,ml^{-1}}$. The signal intensity is normalized for each image individually and the reconstructed image has a size of $29 \times 29\,\mathrm{mm}^2$. The MPI tailored tracer Perimag provides the best image quality. Resotran and Resovist are similar, but Ferrotran has a very weak particle response. The SSIM to the reconstruction unsing Resotran (row-wise) is superposed in the lower right corner.

for Resovist improves when using the Resotran system matrix. This is supported by the increasing SSIM to the reconstruction of the Resotran spiral (0.75) in comparison to the reconstruction of the spiral using the Resovist system matrix (0.65). One reason may be that there are more disruptions and noise in the Resovist system matrix, as it can be seen in the lowest system matrix component in figure 6. The MNP concentration in the spiral phantom should be consistent, but due to the different representation of the windings by 1 to 3 voxels, the reduced physical resolution towards the edges of the FOV, and the influence of regularization and solver on the reconstruction (Hackelberg *et al* 2024), the intensity seems to vary in the image.

4. Discussion

This work evaluates the four particles Perimag, Resotran, Resovist, and Ferrotran by classifying their sizes, magnetic properties, and imaging performance. We have shown that Resotran and Resovist are similar in composition and performance, with acceptable imaging results, and that Ferrotran is unsuitable for MPI. The reintroduction of ferucarbotran-based MNPs in Germany offers the potential for future human trials in MPI, which motivates a comparison of Resotran with the established but discontinued Resovist.

The purpose of this study is threefold: first, to establish a relationship of the well-known and thoroughly studied MNPs Resovist to the newly MRI approved MNP Resotran, both ferucarbotran, to indicate similar properties and MPI performance. Secondly, this work makes a contribution on the way to an official approval of Resotran for human applications in MPI for vascular imaging based on its similarity to Resovist. Toxicological risks of MNPs on the metabolism remain (Chen *et al* 2010, Singh *et al* 2010, Winer *et al* 2012), however, the long-term application of ferucarbotran in human MRI (Reimer *et al* 1995, Amemiya *et al* 2009) since its introduction in 2003 (Reimer and Balzer 2003) has so far not raised any major concerns (Wang 2011). Third, we complement our study with two more MNPs, one MPI tailored tracer called Perimag to indicate possible future increases in performance and dosage and another called Ferrotran, USPIOs currently in a Phase III study, but not suitable for MPI due to their linear magnetization behavior caused by their low magnetic energy and their small size. We chose Perimag because it is well studied in the literature (Eberbeck *et al* 2013, Lüdtke-Buzug *et al* 2013, Szwargulski 2020, Ludewig 2022, Vogel *et al* 2023) over a period of 10 years, it appears in various open datasets (Knopp *et al* 2020), its synthesis process is analogous to ferucarbotran and it is expected to perform well in viscous (partially immobilized) media such as blood (Wöckel *et al* 2019, Antonelli *et al* 2020). However, other tracers such as Synomag (Gavilán 2017, Vogel *et al* 2021), VivoTrax (Irfan *et al* 2021b, Gevaert *et al* 2022, Yeo *et al* 2022), PrecisionMRX (Imagion Biosystems Ltd Melbourne, Australia) (Tay *et al* 2017), LS-008 (Vogel 2019), or magnetosomes (Makela *et al* 2022, Thieben *et al* 2023a) have also shown significant potential and even superior magnetic properties for MPI compared to Perimag (Irfan *et al* 2021a, Yeo *et al* 2022).

The size discrepancy of DLS and TEM measurements shows how the hydrodynamic diameter reveals clusters and chains: although Perimag and Ferrotran have similar individual mean core diameters around 3.1 nm (TEM, figure 2), they have very different hydrodynamic diameters (DLS, figure 1), e.g. due to embedded cluster within a single dextran shell for Perimag. Clusters are known to be the MPI active component for signal generation (Eberbeck *et al* 2011) of small MNPs like Perimag and our images show a similar core size of around 5 nm as reported by Eberbeck *et al* (2013). While the short-axis has been considered in our analysis (section 2.3), the long-axis is more relevant to the magnetic properties under investigation. In alignment with the easy axis, particle clusters, chains, and particle-particle interactions play a dominant role in the observed magnetic response in the kHz range (Eberbeck *et al* 2011). However, manual quantification of agglomerates and aggregates (2014) is difficult and prone to user bias and errors in detecting edges and boundaries of overlapping particles (Pyrz and Buttrey 2008, Bresch *et al* 2022). The effective MNP size of Perimag is thus in a range of 20 to 50 nm (visual inspection of figure 2) and these particle ensembles are then surrounded by the dextran shell which yields a hydrodynamic size at around 100 nm as reported in figure 1 by DLS.

Regarding Resovist and Resotran, Gleich and Weizenecker (2005) reported that only 3% of the total iron mass are expected to be MPI active, which agrees with our findings to the extent that the performance of Resotran/Resovist is better than Ferrotran, but worse than Perimag, suggesting that most particle ensembles are too small (Yoshida *et al* 2013). Also, visual inspection of the TEM images reveal small clusters in the 10 to 20 nm range and Resotran/Resovist MNPs overlap much less than Perimag, with a hydrodynamic diameter of about 65 nm. Accordingly, in the case of Ferrotran, the separation by the hull prevents any overlapping particles and particle-particle interactions are suppressed, resulting in MNPs that are too small for MPI with an almost linear magnetization curve in the relevant excitation range. The magnetic properties of Ferrotran indicate that it is not eligible for MPI, which was confirmed with images of poor quality, that do not resemble the measured phantoms in figure 7.

In this study, we did not perform an in-depth analysis regarding the relaxation behavior by blocking Brownian rotation using immobilization methods (Riahi 2020). Regarding Perimag, its third harmonic of a liquid and an immobilized sample have a ratio of $18.31/13.1 \approx 1.4$ (Wöckel *et al* 2019). This ratio indicates a coupled relaxation with a predominant Néel relaxation. From our PSF results, the similarity between Perimag, Resotran and Resovist indicates a similar coupled relaxation behavior. For Ferrotran, almost no relaxation behavior is visible, indicating a fast Néel relaxation, as expected for USPIONs (Krishnan 2010). All four MNPs have similar core sizes around 3 to 4 nm, but very different hydrodynamic diameters with the relationship that the larger the hydrodynamic diameter, the better the MPI performance. A clear distinction in Brownian and Néel relaxation cannot be made on the basis of our results without immobilization. However, our results are analogous to the performance improvement seen due to a larger effective core size as reported by Yoshida *et al* (2013).

The differences in saturation magnetization observed by VSM most likely result from the different material composition ratios for the iron oxides magnetite and maghemite with a saturation magnetization of $98\,\mathrm{Am^2\,kg_{Fe}}^{-1}$ and $82\,\mathrm{Am^2\,kg_{Fe}}^{-1}$, respectively (Colombo *et al* 2012). Additionally, the presence of clusters with particle-particle interaction contribute to a difference in the initial slope of the magnetization curve as indicated by the VSM data in figure 3. Further, VSM successfully predicted the magnetization curve that was measured using MPS, without the hysteresis that is induced by the dynamic excitation field. The center plot of figure 5 confirms this behavior, as the hysteresis curve widens with increasing excitation amplitude and the maximum saturation approaches the values measured with VSM for high amplitudes, without surpassing them. The 1D MPS results are supported by the achieved SNR levels of the measured MPI system matrices and indicate that the imaging quality of the tailored tracer Perimag outperforms all other tracers, which was eventually shown by the reconstruction of the spiral phantom. The analysis of MPS data on tracer performance correlates well with the image reconstructions for all 4 tracers using the system matrix approach. We did not perform x-space reconstructions in the time-domain but expect our findings to generalize to other imaging sequences and reconstruction techniques. The FWHM of the x-space PSF also implies a good performance of Perimag and a bad performance of Ferrotran, indicated by a narrow and broad PSF (Croft *et al* 2012), respectively.

Throughout all conducted measurements, the properties and performance of Resovist and Resotran proofed to be akin and the remaining differences could be due to variations between LOT numbers or due to different distributions of the iron oxides magnetite and maghemite. The reconstructed images of figure 7 confirm suitability of Resotran for intricate MPI applications and our work indicates its suitability for 2D sequences, where particle clustering is relevant. On this basis, suitability for more elaborate 3D sequences can be assumed, because the excitation direction is changing for a 2D sequence as well, which is the main difference of 2D/3D excitation to colinear 1D sequences. This is crucial for the medical translation of MPI, although the performance of ferucarbotran-based MNPs does not reach the level of tailored MPI tracers. Cross-reconstructions of Resotran and Resovist are possible, emphasizing their resemblance, and surprisingly even improving the reconstruction result for Resovist using the Resotran system matrix. This might be due to a slightly higher SNR of the Resotran system matrix, as indicated by the analysis in figure 6, similar to the boost in SNR in hybrid system calibration approaches (Von Gladiss *et al* 2017). More investigations on this matter using different particle batches are necessary.

5. Conclusion

Resotran qualifies as a tracer for MPI and its deployment in preclinical trials and system characterizations (Thieben *et al* 2024) could positively impact an official medical approval for MPI. Furthermore, it will facilitate the process of clinical translation of MPI, even if the signal performance is surpassed by tailored MNPs. Due to its similarity to the established MNPs Resovist in both, performance and composition, insights gained on Resovist are in principle transferable to Resotran. With Resovist no longer licensed in most countries, the main benefit of Resotran is the reintroduction of a ferucarbotran-based tracer for medical imaging.

Data availability statement

The data cannot be made publicly available upon publication because they are not available in a format that is sufficiently accessible or reusable by other researchers. The data that support the findings of this study are available upon reasonable request from the authors.

Acknowledgments

This work was supported by the Cluster of Excellence 'CUI: Advanced Imaging of Matter' of the Deutsche Forschungsgemeinschaft (DFG)-EXC 2056-Project ID 390715994. Publishing fees supported by Funding Programme Open Access Publishing of Hamburg University of Technology (TUHH).

Author contributions

A W performed the DLS measurements and carried out the sample preparation for TEM. The TEM measurements were performed by Stefan Werner at the Division of Electron Microscopy of the Chemistry Department at University of Hamburg under the direction of Dr Charlotte Ruhmlieb. J A performed the VSM measurements. F M performed the MPS measurements and analysis. K S measured the dilution series. K S and F M performed the MPI measurements. K S and T K reconstructed the MPI images and did the SNR analysis. T K supervised the project. F M, K S, F W, F T, M A, P V, M G and T K contributed to the conceptualization and theory. F M, K S, J A, A W and F W wrote the original draft. All authors reviewed the final manuscript.

ORCID iDs

Fabian Mohn https://orcid.org/0000-0002-9151-9929
Konrad Scheffler https://orcid.org/0000-0002-6842-9204
Justin Ackers https://orcid.org/0000-0003-1049-0528
Agnes Weimer https://orcid.org/0000-0002-7180-3009
Franz Wegner https://orcid.org/0000-0001-5969-3428
Florian Thieben https://orcid.org/0000-0002-2890-5288
Mandy Ahlborg https://orcid.org/0000-0002-0192-8033
Patrick Vogel https://orcid.org/0000-0003-0801-5146

Matthias Graeser https://orcid.org/0000-0003-1472-5988
Tobias Knopp https://orcid.org/0000-0002-1589-8517

References

Ahlborg M *et al* 2022 First dedicated balloon catheter for magnetic particle imaging *IEEE Trans. Med. Imaging* **41** 3301–8

Amemiya S, Akahane M, Aoki S, Abe O, Kamada K, Saito N and Ohtomo K 2009 Dynamic contrast-enhanced perfusion MR imaging with SPIO: a pilot study *Investigative Radiol.* **44** 503–8

Antonelli A, Szwargulski P, Scarpa E S, Thieben F, Cordula G, Ambrosi G, Guidi L, Ludewig P, Knopp T and Magnani M 2020 Development of long circulating magnetic particle imaging tracers: use of novel magnetic nanoparticles and entrapment into human erythrocytes *Nanomedicine* **15** 739–53

Bakenecker A C, Ahlborg M, Debbeler C, Kaethner C, Buzug T M and Lüdtke-Buzug K 2018 Magnetic particle imaging in vascular medicine *Innov. Surg. Sci.* **3** 179–92

Bakenecker A C, Von Gladiss A, Schwenke H, Behrends A, Friedrich T, Lüdtke-Buzug K, Neumann A, Barkhausen J, Wegner F and Buzug T M 2021 Navigation of a magnetic micro-robot through a cerebral aneurysm phantom with magnetic particle imaging *Sci. Rep.* **11** 14082

Bender P *et al* 2018 Relating magnetic properties and high hyperthermia performance of iron oxide nanoflowers *J. Phys. Chem.* C **122** 3068–77

Billings C, Langley M, Warrington G, Mashali F and Johnson J A 2021 Magnetic particle imaging: current and future applications, magnetic nanoparticle synthesis methods and safety measures *Int. J. Mol. Sci.* **22** 7651

Bresch H, Hodoroaba V-D, Schmidt A, Rasmussen K and Rauscher H 2022 Counting small particles in electron microscopy images—proposal for rules and their application in practice *Nanomaterials* **12** 2238

Bui M P, Le T-A and Yoon J 2021 A magnetic particle imaging-based navigation platform for magnetic nanoparticles using interactive manipulation of a virtual field free point to ensure targeted drug delivery *IEEE Trans. Ind. Electron.* **68** 12493–503

Bui M P, Park M, Le T-A and Yoon J 2023 A development of 3D navigation system for micro-nano robot based on a magnetic particle imaging system *Int. J. Magn. Part. Imaging* **9**

Chandrasekharan P *et al* 2020 Using magnetic particle imaging systems to localize and guide magnetic hyperthermia treatment: tracers, hardware and future medical applications *Theranostics* **10** 2965–81

Chen Y-C, Hsiao J-K, Liu H-M, Lai I-Y, Yao M, Hsu S-C, Ko B-S, Chen Y-C, Yang C-S and Huang D-M 2010 The inhibitory effect of superparamagnetic iron oxide nanoparticle (ferucarbotran) on osteogenic differentiation and its signaling mechanism in human mesenchymal stem cells *Toxicol. Appl. Pharmacol.* **245** 272–9

Colombo M, Carregal-Romero S, Casula M F, Gutiérrez L, Morales M P, Böhm I B, Heverhagen J T, Prosperi D and Parak W J 2012 Biological applications of magnetic nanoparticles *Chem. Soc. Rev.* **41** 4306

Croft L R, Goodwill P, Ferguson M, Krishnan K and Conolly S 2012 Relaxation in x-space magnetic particle imaging *Springer Proc. Phys.* **140** 149–53

Deissler R J, Wu Y and Martens M A 2014 Dependence of Brownian and Néel relaxation times on magnetic field strength *Med. Phys.* **41** 012301

Dittmer S, Kluth T, Henriksen M T R and Maass P 2021 Deep image prior for 3D magnetic particle imaging: a quantitative comparison of regularization techniques on open MPI dataset *Int. J. Magn. Part. Imaging* **7**

Eberbeck D, Dennis C L, Huls N F, Krycka K L, Gruttner C and Westphal F 2013 Multicore magnetic nanoparticles for magnetic particle imaging *IEEE Trans. Magn.* **49** 269–74

Eberbeck D, Wiekhorst F, Wagner S and Trahms L 2011 How the size distribution of magnetic nanoparticles determines their magnetic particle imaging performance *Appl. Phys. Lett.* **98** 182502

Ferguson R M *et al* 2015 Magnetic particle imaging with tailored iron oxide nanoparticle tracers *IEEE Trans. Med. Imaging* **34** 1077–84

Ferguson R M, Minard K R and Krishnan K M 2009 Optimization of nanoparticle core size for magnetic particle imaging *J. Magn. Magn. Mater.* **321** 1548–51

Foner S 1959 Versatile and sensitive vibrating-sample magnetometer *Rev. Sci. Instrum.* **30** 548–57

Franke J, Heinen U, Lehr H, Weber A, Jaspard F, Ruhm W, Heidenreich M and Schulz V 2016 System characterization of a highly integrated preclinical hybrid MPI-MRI scanner *IEEE Trans. Med. Imaging* **35** 1993–2004

Gavilán H *et al* 2017 Colloidal flower-shaped iron oxide nanoparticles: synthesis strategies and coatings *Part. Part. Syst. Charact.* **34** 1700094

Gevaert J, Van Beek K, Sehl O C and Foster P J 2022 VivoTrax+ improves the detection of cancer cells with magnetic particle imaging *Int. J. Magn. Part. Imaging* **8**

Gleich B and Weizenecker J 2005 Tomographic imaging using the nonlinear response of magnetic particles *Nature* **435** 1214–7

Goodwill P W, Lu K, Zheng B and Conolly S M 2012 An X-space magnetic particle imaging scanner *Rev. Sci. Instrum.* **83** 33708–9

Graeser M *et al* 2019 Human-sized magnetic particle imaging for brain applications *Nat. Commun.* **10** 1936

Graeser M, Knopp T, Szwargulski P, Friedrich T, Von Gladiss A, Kaul M, Krishnan K M, Ittrich H, Adam G and Buzug T M 2017 Towards picogram detection of superparamagnetic iron-oxide particles using a gradiometric receive coil *Sci. Rep.* **7** 6872

Hackelberg N, Grosser M, Tsanda A, Mohn F, Scheffler K, Möddel M and Knopp T 2024 RegularizedLeastSquares.jl: modality agnostic Julia package for solving regularized least squares problems *Int. J. Magn. Part. Imaging* **10**

Hackelberg N, Schumacher J, Ackers J, Möddel M, Förger F, Graeser M and Knopp T 2023 MPIMeasurements.Jl: an extensible julia framework for composable magnetic particle imaging devices *Int. J. Magn. Part. Imaging* **9**

Hackelberg N, Schumacher J, Graeser M and Knopp T 2022 A flexible high-performance signal generation and digitization plattform based on low-cost hardware *Int. J. Magn. Part. Imaging* **8**

Haegele J *et al* 2016a Magnetic particle imaging: a resovist based marking technology for guide wires and catheters for vascular interventions *IEEE Trans. Med. Imaging* **35** 2312–8

Haegele J, Rahmer J, Gleich B, Borgert J, Wojtczyk H, Panagiotopoulos N, Buzug T M, Barkhausen J and Vogt F M 2012 Magnetic particle imaging: visualization of instruments for cardiovascular intervention *Radiology* **265** 933–8

Haegele J, Vaalma S, Panagiotopoulos N, Barkhausen J, Vogt F M, Borgert J and Rahmer J 2016b Multi-color magnetic particle imaging for cardiovascular interventions *Phys. Med. Biol.* **61** N415–26

Hartung V, Günther J, Augustin A M, Reichl T, Gruschwitz P, Rückert M, Bley T A, Behr V, Herz S and Vogel P 2023 Resotran® meets MPI—clinically approved ferucarbotran reintroduced: a major leap towards MPI in humans *Int. J. Magn. Part. Imaging* **9**

Harvell-Smith S, Tung L D and Thanh N T K 2022 Magnetic particle imaging: tracer development and the biomedical applications of a radiation-free, sensitive and quantitative imaging modality *Nanoscale* **14** 3658–97

He J, Li Y, Zhu T, Zhong J, Hui H and Tian J 2023 Simulation study of a magnetic particle imaging device capable of hyperthermia *Int. J. Magn. Part. Imaging* **9**

Herz S, Vogel P, Kampf T, Dietrich P, Veldhoen S, Rückert M A, Kickuth R, Behr V C and Bley T A 2019 Magnetic particle imaging–guided stenting *J. Endovasc. Ther.* **26** 512–9

Irfan M, Dogan N, Bingolbali A and Aliew F 2021b Synthesis and characterization of $NiFe_2O_4$ magnetic nanoparticles with different coating materials for magnetic particle imaging (MPI) *J. Magn. Magn. Mater.* **537** 168150

Irfan M, Dogan N, Sapmaz T and Bingolbali A 2021a Development of MPI relaxometer for characterization of superparamagnetic nanoparticles *J. Magn. Magn. Mater.* **536** 168082

ISO 13322-1 2014 *Static Image Analysis Methods* (International Organisation for Standardization)

Kaul M G, Salamon J, Knopp T, Ittrich H, Adam G, Weller H and Jung C 2018 Magnetic particle imaging for *in vivo* blood flow velocity measurements in mice *Phys. Med. Biol.* **63** 64001

Knopp T, Gdaniec N and Möddel M 2017 Magnetic particle imaging: from proof of principle to preclinical applications *Phys. Med. Biol.* **62** R124–78

Knopp T, Szwargulski P, Griese F and Gräser M 2020 OpenMPIData: an initiative for freely accessible magnetic particle imaging data *Data Brief* **28** 104971

Koppel D E 1972 Analysis of macromolecular polydispersity in intensity correlation spectroscopy: the method of cumulants *J. Chem. Phys.* **57** 4814–20

Krishnan K M 2010 Biomedical nanomagnetics: a spin through possibilities in imaging, diagnostics and therapy *IEEE Trans. Magn.* **46** 2523–58

Löwa N, Gutkelch D, Welge E-A, Welz R, Meier F, Baki A, Bleul R, Klein T and Wiekhorst F 2020 Novel benchtop magnetic particle spectrometer for process monitoring of magnetic nanoparticle synthesis *Nanomaterials* **10** 2277

Löwa N, Radon P, Kosch O and Wiekhorst F 2016 Concentration dependent MPI tracer performance *Int. J. Magn. Part. Imaging* **2** 1–5

Lüdtke-Buzug K, Haegele J, Biederer S, Sattel T F, Erbe M, Duschka R L, Barkhausen J and Vogt F M 2013 Comparison of commercial iron oxide-based MRI contrast agents with synthesized high-performance MPI tracers *Biomed. Tech.* **58** 527–33

Liu S, Chiu-Lam A, Rivera-Rodriguez A, DeGroff R, Savliwala S, Sarna N and Rinaldi-Ramos C M 2021 Long circulating tracer tailored for magnetic particle imaging *Nanotheranostics* **5** 348–61

Lu K, Goodwill P W, Saritas E U, Zheng B and Conolly S M 2013 Linearity and shift invariance for quantitative magnetic particle imaging *IEEE Trans. Med. Imaging* **32** 1565–75

Ludewig P *et al* 2017 Magnetic particle imaging for real-time perfusion imaging in acute stroke *ACS Nano* **11** 10480–8

Ludewig P *et al* 2022 Magnetic particle imaging for assessment of cerebral perfusion and ischemia *Wiley Interdiscip. Rev.-Nanomed. Nanobiotechnol.* **14** e1757

Ludwig F, Eberbeck D, Löwa N, Steinhoff U, Wawrzik T, Schilling M and Trahms L 2013 Characterization of magnetic nanoparticle systems with respect to their magnetic particle imaging performance *Biomed. Tech./Biomed. Eng.* **58**

Makela A V, Schott M A, Madsen C S, Greeson E M and Contag C H 2022 Magnetic particle imaging of magnetotactic bacteria as living contrast agents is improved by altering magnetosome arrangement *Nano Lett.* **22** 4630–9

Mason E E, Cooley C Z, Cauley S F, Griswold M A, Conolly S M and Wald L L 2017 Design analysis of an MPI human functional brain scanner *Int. J. Magn. Part. Imaging* **3**

Mattingly E, Śliwiak M, Drago J, Mason E, Graeser M and Wald L 2022 A drive filter design for MPI with harmonic notching and selective damping *Int. J. Magn. Part. Imaging* **8**

Mohn F, Exner M, Szwargulski P, Möddel M, Knopp T and Graeser M 2023 Saline bolus for negative contrast perfusion imaging in magnetic particle imaging *Phys. Med. Biol.* **68** 175026

Mohn F, Knopp T, Boberg M, Thieben F, Szwargulski P and Graeser M 2022 System matrix based reconstruction for pulsed sequences in magnetic particle imaging *IEEE Trans. Med. Imaging* **41** 1862–73

Moor L, Scheibler S, Gerken L, Scheffler K, Thieben F, Knopp T, Herrmann I K and Starsich F H L 2022 Particle interactions and their effect on magnetic particle spectroscopy and imaging *Nanoscale* **14** 7163–73

Neumann A *et al* 2022 Recent developments in magnetic particle imaging *J. Magn. Magn. Mater.* **550** 169037

Ozaslan A A, Utkur M, Canpolat U, Tuncer M A, Karli Oguz K and Saritas E U 2022 PNS limits for human head-size MPI systems: preliminary results *Int. J. Magn. Part. Imaging* **8**

Pyrz W D and Buttrey D J 2008 Particle size determination using TEM: a discussion of image acquisition and analysis for the novice microscopist *Langmuir* **24** 11350–60

Rahmer J, Stehning C and Gleich B 2018 Remote magnetic actuation using a clinical scale system *PLoS One* **13** e0193546

Reimer P and Balzer T 2003 Ferucarbotran (Resovist): a new clinically approved res-specific contrast agent for contrast-enhanced MRI of the liver: properties, clinical development and applications *Eur. Radiol.* **13** 1266–76

Reimer P, Schuierer G, Balzer T and Peters P E 1995 Application of a superparamagnetic iron oxide (Resovis®) for MR imaging of human cerebral blood volume *Magn. Reson. Med.* **34** 694–7

Remmo A, Löwa N, Kosch O, Eberbeck D, Ludwig A, Kampen L, Grüttner C and Wiekhorst F 2022 Cell tracking by magnetic particle imaging: methodology for labeling THP-1 monocytes with magnetic nanoparticles for cellular imaging *Cells* **11** 2892

Riahi K *et al* 2020 Magnetic performance of Synomag® nanoparticles in various environments *Int. J. Magn. Part. Imaging* **6**

Rubia-Rodriguez I *et al* 2021 Whither magnetic hyperthermia? A tentative roadmap *Materials* **14** 706

Saritas E U, Goodwill P W, Zhang G Z and Conolly S M 2013 Magnetostimulation limits in magnetic particle imaging *IEEE Trans. Med. Imaging* **32** 1600–10

Sattel T F, Woywode O, Weizenecker J, Rahmer J, Gleich B and Borgert J 2015 Setup and validation of an MPI signal chain for a drive field frequency of 150 kHz *IEEE Trans. Magn.* **51** 1–3

Scheffler K, Boberg M and Knopp T 2024 Solving the MPI reconstruction problem with automatically tuned regularization parameters *Phys. Med. Biol.* **69** 045024

Scheffler K, Thieben F, Mohn F, Graeser M and Knopp T 2023 MPI signal performance of Resotran *12th Int. Workshop on Magnetic Particle Imaging (IWMPI 2023)* vol 9 p 1

Schmale I *et al* 2013 Human PNS and SAR study in the frequency range from 24 to 162 kHz *2013 Int. Workshop on Magnetic Particle Imaging, IWMPI 2013* p 1

Sehl O C, Gevaert J J, Melo K P, Knier N N and Foster P J 2020 A perspective on cell tracking with magnetic particle imaging *Tomography* **6** 315–24

Singh N, Jenkins G J S, Asadi R and Doak S H 2010 Potential toxicity of superparamagnetic iron oxide nanoparticles (SPION) *Nano Rev.* **1** 5358

Song G, Chen M, Zhang Y, Cui L, Qu H, Zheng X, Wintermark M, Liu Z and Rao J 2018 Janus iron oxides @ semiconducting polymer nanoparticle tracer for cell tracking by magnetic particle imaging *Nano Lett.* **18** 182–9

Sun C, Lee J S H and Zhang M 2008 Magnetic nanoparticles in MR imaging and drug delivery *Adv. Drug. Deliv. Rev.* **60** 1252–65

Szwargulski P *et al* 2020 Monitoring intracranial cerebral hemorrhage using multicontrast real-time magnetic particle imaging *ACS Nano* **14** 13913–23

Tay Z W *et al* 2021 Superferromagnetic nanoparticles enable order-of-magnitude resolution & sensitivity gain in magnetic particle imaging *Small Methods* **5** 2100796

Tay Z W, Goodwill P W, Hensley D W, Taylor L A, Zheng B and Conolly S M 2016 A high-throughput, arbitrary-waveform, MPI spectrometer and relaxometer for comprehensive magnetic particle optimization and characterization *Sci. Rep.* **6** 34180

Tay Z W, Hensley D W, Vreeland E C, Zheng B and Conolly S M 2017 The relaxation wall: experimental limits to improving MPI spatial resolution by increasing nanoparticle core size *Biomed. Phys. Eng. Express* **3** 035003

Thieben F, Foerger F, Mohn F, Hackelberg N, Boberg M, Scheel J-P, Möddel M, Graeser M and Knopp T 2024 System characterization of a human-sized 3D real-time magnetic particle imaging scanner for cerebral applications *Commun. Eng.* **3** 47

Thieben F, Knopp T, Boberg M, Foerger F, Graeser M and Moddel M 2023b On the receive path calibration of magnetic particle imaging systems *IEEE Trans. Instrum. Meas.* **72** 1–15

Thieben F, Mickoleit F, Tessaro S, Ludewig P, Schüler D, Garbayo J R, Uebe R and Knopp T 2023a Development of optimized magnetic particle imaging tracers utilizing genetically engineered magnetosomes *Int. J. Magn. Part. Imaging* **9**

Thomas J C 1987 The determination of log normal particle size distributions by dynamic light scattering *J. Colloid Interface Sci.* **117** 187–92

Verleysen E, Wagner T, Lipinski H-G, Kägi R, Koeber R, Boix-Sanfeliu A, De Temmerman P-J and Mast J 2019 Evaluation of a TEM based approach for size measurement of particulate (nano)materials *Materials* **12** 2274

Vogel P *et al* 2019 Micro-traveling wave magnetic particle imaging—sub-millimeter resolution with optimized tracer LS-008 *IEEE Trans. Magn.* **55** 1–7

Vogel P, Kampf T, Rückert M, Grüttner C, Kowalski A, Teller H and Behr V 2021 Synomag®: the new high-performance tracer for magnetic particle imaging *Int. J. Magn. Part. Imaging* **7**

Vogel P, Rückert M A, Greiner C, Günther J, Reichl T, Kampf T, Bley T A, Behr V C and Herz S 2023 iMPI: portable human-sized magnetic particle imaging scanner for real-time endovascular interventions *Sci. Rep.* **13** 10472

Von Gladiss A, Graeser M, Szwargulski P, Knopp T and Buzug T M 2017 Hybrid system calibration for multidimensional magnetic particle imaging *Phys. Med. Biol.* **62** 3392–406

Wöckel L, Wells J, Kosch O, Lyer S, Alexiou C, Grüttner C, Wiekhorst F and Dutz S 2019 Long-term stable measurement phantoms for magnetic particle imaging *J. Magn. Magn. Mater.* **471** 1–7

Wang Y-X J 2011 Superparamagnetic iron oxide based MRI contrast agents: current status of clinical application *Quant. Imaging Med. Surg.* **1** 35–40

Wang Z, Bovik A C, Sheikh H R and Simoncelli E P 2004 Image quality assessment: from error visibility to structural similarity *IEEE Trans. Image Process.* **13** 600–12

Wegner F *et al* 2021 Magnetic particle imaging: in vitro signal analysis and lumen quantification of 21 endovascular stents *Int. J. Nanomed.* **ume 16** 213–21

Weizenecker J, Borgert J and Gleich B 2007 A simulation study on the resolution and sensitivity of magnetic particle imaging *Phys. Med. Biol.* **52** 6363–74

Weizenecker J, Gleich B, Rahmer J, Dahnke H and Borgert J 2009 Three-dimensional real-time *in vivo* magnetic particle imaging *Phys. Med. Biol.* **54** L1–L10

Winer J L, Liu C Y and Apuzzo M L J 2012 The use of nanoparticles as contrast media in neuroimaging: a statement on toxicity *World Neurosurg.* **78** 709–11

Yang X, Shao G, Zhang Y, Wang W, Qi Y, Han S and Li H 2022 Applications of magnetic particle imaging in biomedicine: advancements and prospects *Front. Physiol.* **13** 898426

Yeo K H, Rodrigo I, Kuo R, Chandrasekharan P, Fellows B and Conolly S 2022 Characterizing the performance of commercial magnetic particles for magnetic particle imaging *Int. J. Magn. Part. Imaging* **8**

Yoshida T, Othman N B and Enpuku K 2013 Characterization of magnetically fractionated magnetic nanoparticles for magnetic particle imaging *J. Appl. Phys.* **114** 173908

Zheng B, Vazin T, Goodwill P W, Conway A, Verma A, Ulku Saritas E, Schaffer D and Conolly S M 2015 Magnetic particle imaging tracks the long-term fate of *in vivo* neural cell implants with high image contrast *Sci. Rep.* **5** 14055

9

Saline Bolus for Negative Contrast Perfusion Imaging in Magnetic Particle Imaging

In this chapter we investigate the feasibility of using negative contrast perfusion imaging to generate perfusion maps and compare them to the ground truth of positive boli for a rat-sized heart phantom [O5].

The experiments, the measured data and its evaluation in this chapter originated during the master thesis of Miriam Exner, which was completed at the Institute of Biomedical Imaging of the Hamburg University of Technology between 2021 and 2022 [56]. Parts of this chapter have also been presented at the IWMPI 2023 conference in Aachen, Germany, with a published proceedings [O9] prior to publication of the full paper.

9.1 IOPscience - Physics in Medicine & Biology

Manuscript received March 9, 2023.
Revised June 9, 2023.
Accepted June 29, 2023.

Type: Open Access. CC-BY-4.0 license.
DOI: 10.1088/1361-6560/ace309

IOP Publishing Phys. Med. Biol. 68 (2023) 175026 https://doi.org/10.1088/1361-6560/ace309

Physics in Medicine & Biology

IPEM
Institute of Physics and Engineering in Medicine

OPEN ACCESS

RECEIVED
9 March 2023

REVISED
9 June 2023

ACCEPTED FOR PUBLICATION
29 June 2023

PUBLISHED
22 August 2023

PAPER

Saline bolus for negative contrast perfusion imaging in magnetic particle imaging

Fabian Mohn[1,2], **Miriam Exner**[1], **Patryk Szwargulski**[1], **Martin Möddel**[1,2], **Tobias Knopp**[1,2,3] and **Matthias Graeser**[1,2,3,4]

[1] Institute for Biomedical Imaging, Hamburg University of Technology, Hamburg, Germany
[2] Section for Biomedical Imaging, University Medical Center Hamburg-Eppendorf, Hamburg, Germany
[3] Fraunhofer Research Institution for Individualized and Cell-based Medicine, IMTE, Lübeck, Germany
[4] Institute for Medical Engineering, University of Lübeck, Lübeck, Germany

E-mail: fabian.mohn@tuhh.de

Keywords: magnetic particle imaging, perfusion imaging, magnetic tracer, negative contrast, long term monitoring

Abstract

Objective. Magnetic particle imaging (MPI) is capable of high temporal resolution measurements of the spatial distribution of magnetic nanoparticles and therefore well suited for perfusion imaging, which is an important tool in medical diagnosis. Perfusion imaging in MPI usually requires a fresh bolus of tracer material to capture the key signal dynamics. Here, we propose a method to decouple the imaging sequence from the injection of additional tracer material, without further increasing the administered iron dose in the body with each image. *Approach.* A bolus of physiological saline solution without any particles (negative contrast) diminishes the steady-state concentration of a long-circulating tracer during passage. This depression in the measured concentration contributes to the required contrast dynamics. The presence of a long-circulating tracer is therefore a prerequisite to obtain the negative contrast. As a quantitative tracer based imaging method, the signal is linear in the tracer concentration for any location that contains nanoparticles and zero in the surrounding tissue which does not provide any intrinsic signal. After tracer injection, the concentration over time (positive contrast) can be utilized to calculate dynamic diagnostic parameters like perfusion parameters in vessels and organs. Every acquired perfusion image thus requires a new bolus of tracer with a sufficiently large iron dose to be visible above the background. *Main results.* Perfusion parameters are calculated based on the time response of the proposed negative bolus and compared to a positive bolus. Results from phantom experiments show that normalized signals from positive and negative boli are concurrent and deviations of calculated perfusion maps are low. *Significance.* Our method opens up the possibility to increase the total monitoring time of a future patient by utilizing a positive-negative contrast sequence, while minimizing the iron dose per acquired image.

1. Introduction

Magnetic particle imaging (MPI) is a tracer based imaging modality which measures the spatial concentration of magnetic nanoparticles (Gleich and Weizenecker 2005). After rapid development, the method has already proven its potential in several clinical applications like control of the temperature rise in magnetic hyperthermia (Murase *et al* 2013), monitoring of cellular grafts (Zheng *et al* 2016), cancer detection (Yu *et al* 2017), quantification of vascular stenosis (Vaalma *et al* 2017), lung perfusion imaging (Zhou *et al* 2017), traumatic brain injury imaging (Orendorff *et al* 2017) and stroke detection (Ludewig *et al* 2017, Szwargulski *et al* 2020). Recent developments show that MPI is feasible on a human scale (Rahmer *et al* 2018, Graeser *et al* 2019, Mason *et al* 2021, Vogel *et al* 2022, Thieben *et al* 2023).

MPI uses the nonlinear magnetization behavior, which is controlled by the superposition of a static spatial encoding field (selection field) and an oscillating homogeneous field (drive field). The first creates a field-free-region (FFR), the second deflects the FFR and causes the particles to realign to the current field vector, which can be measured using Faraday's law of induction (Gleich and Weizenecker 2005). Due to the non-linearity of the particles, the receive signal contains higher harmonics, encoding a location depend spectral fingerprint. Using Fourier transform, a solution to the underlying system of linear equations reveals the location and concentration of the tracer (Gleich and Weizenecker 2005).

As MPI depends on a magnetic tracer injected into the human body, several questions regarding the safety of these tracers arise. The iron oxide particles are usually coated either by dextran or PEG shells making the tracer compatible to the body (Reimer and Balzer 2003, Arbab *et al* 2005, Oh and Park 2011). If coated with dextran, the particles are taken up by Kupffer-cells in short time intervals (≈10 min half-life) (Reimer and Balzer 2003, Haegele *et al* 2014) and are integrated in the human iron pool by the liver. Certain PEG shells remain longer within the blood pool with a circulation half-life of approximately 7 h in mice (Liu *et al* 2021). After that, these particles are also taken up by the liver and spleen (Liu *et al* 2021). A long half-life is as well achieved by labeling red blood cells with magnetic particles, where 30% of signal remains after 24 h (Antonelli *et al* 2013). Once in the liver, the particles take up to several weeks to be dismantled (Reimer and Balzer 2003). Therefore, in the case of MPI, the maximum iron dose is typically a threshold for a safe use of magnetic tracer in humans. The range of iron doses for human use varies from 2.24 $\mathrm{mg_{Fe}/kg}$ (Resovist) to 8.5 $\mathrm{mg_{Fe}/kg}$ (Feraheme) (Southern and Pankhurst 2018). As both are designed and medically approved for very different purposes, a specific MPI tracer has yet to be approved for imaging in humans. Nevertheless, the doses of these tracers can be used as an indication for safety in humans. Concerns remain if particles can be fully incorporated naturally or if toxicity remains in long-term metabolism (Sun *et al* 2008, Billings *et al* 2021, Rubia-Rodríguez *et al* 2021), which motivates to reduce the added iron amount as much as possible.

In Graeser *et al* (2019), a surveillance scenario for a stroke patient was presented by investigating brain perfusion imaging. Perfusion imaging is an important technique to provide hemodynamics which are used to characterize pathological conditions (Cha and Perfusion 2003, Wintermark *et al* 2005). For perfusion imaging, usually short circulating tracers are used, because long circulating tracers would only lead to a higher background signal after distribution within the body. In such a scenario, a bolus injection is given in every imaging sequence, e.g. when monitoring a stroke patient. To comply with the above-mentioned limits, each single bolus may only contain a fraction of the total iron dose, with a minimum dose based on the system's sensitivity. Also, each bolus needs to be visible above the background of prior boli (baseline concentration). Thus, each additional bolus reduces the number of future images that can be acquired safely.

In order to calculate perfusion parameters, the shape, peak, timing and area under the curve (AUC) of an increase in concentration is assessed (Østergaard *et al* 1996, Cha and Perfusion 2003, Østergaard 2005, Wintermark *et al* 2005, Ludewig *et al* 2017, Graeser *et al* 2019, 2020, Kaul *et al* 2021, Ludewig *et al* 2022). Other work focused on blood flow velocity (Kaul *et al* 2018), kidney perfusion (Molwitz *et al* 2019) or blood flow with stenosis (Siepmann *et al* 2021), using similar methods. Apart from an increase in concentration, perfusion parameters may also be obtained from a concentration decrease, known from magnetic resonance imaging (MRI) as negative contrast (Detre *et al* 1992, Barbier *et al* 2001). Other works in MPI also took advantage of a decrease in concentration to identify and track changes e.g. for the inflation condition of a balloon catheter (Salamon *et al* 2016).

In this work, we present an approach that will enable long-term monitoring of a future patient, without increasing the administered iron dose in the body with every image. Using long circulating tracers, we decouple the imaging sequence from the injection of additional tracer material. To acquire the necessary dynamics in the signal, from which perfusion parameters are calculated, we use physiological neutral saline solution to shortly reduce the concentration of the tracer circulating within the perfused tissue (negative contrast). After image processing, this depression in concentration can be used in the same way as the positive change in concentration of a bolus to derive perfusion parameters. The underlying principle requires a minimum baseline or steady-state concentration of tracer to be present in the volume of interest (VOI).

A circulatory experimental setup is employed in our study, with a rat-scaled heart phantom on a pre-clinical MPI system. We show that signals from negative and positive boli are concurrent, that the deviations in shape and AUC are low after normalization and that perfusion maps can be obtained from negative boli. This method has great potential to increase the number of diagnostic perfusion examinations of a future patient within the safety limits of the total iron dose.

This paper is the full and extended version of our conference abstract (Mohn *et al* 2023).

2. Methods

We consider a scenario that requires a baseline tracer concentration, which could be reached with either a single large initial bolus, by labeled and administered red blood cells or accumulated over time by several smaller

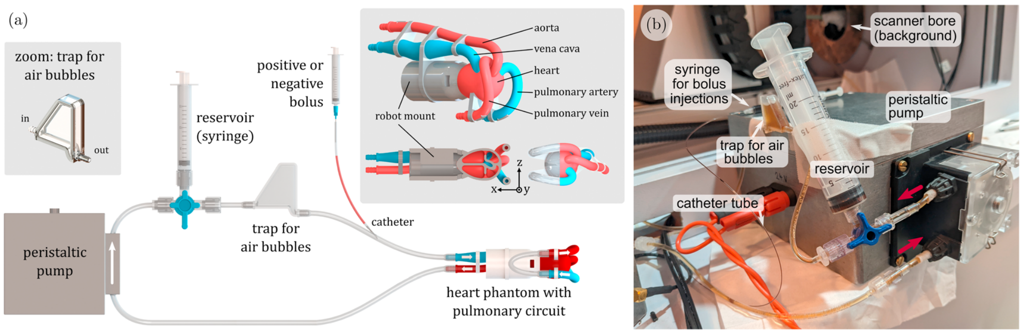

Figure 1. Experimental Setup. A visualization of the experimental setup in (a), stated in flow direction: peristaltic pump, reservoir (syringe), air bubble trap, bolus injection point, 3D printed heart phantom, return tube. Only the heart phantom is located inside the scanner bore. The bubble trap and the phantom are shown as a blow-up in the upper corners. To the right (b), a labeled photo of the setup at the scanner is shown. The tubes reach inside the scanner bore in the background where the phantom is placed. All other parts from (a) are visible.

positive boli. Once the tracer concentration has reached a homogeneous steady-state in the circulating blood pool, a bolus of saline solution can be imaged due to the negative contrast (a reduced signal over time) that is created by tracer dilution. To prove this hypothesis, perfusion parameters are derived from the time response of negative and positive boli. Positive boli serve as the ground truth in this work and verification is done by comparing dynamic subtraction images, normalized time curves and perfusion maps between negative and positive bolus types, namely the time-to-peak (TTP), relative blood-flow (rBF), relative blood-volume (rBV) and mean-transit-time (MTT). In this work, we administer an initial large positive bolus for a baseline concentration and continue with alternating small positive and negative boli, and measure the time depended concentration variations using MPI.

2.1. Experimental setup

To validate the feasibility of negative boli, we constructed a rat-sized heart phantom for circulatory flow experiments, shown in figure 1. The hollow phantom is connected to a peristaltic pump using an average flow rate of 31 ml min^{-1}, a realistic cardiac output for a rat (Treuting 2018), to circulate the imitated blood pool (desalinated water). The heart phantom has a volume of 1763 mm^3, with a portion of 60% for the actual heart consisting out of 4 chambers (left/right atrium/ventricle). All partial volumes are realistically scaled and designed on the basis of a 200 g rat (Exner *et al* 2019). Different details of the phantom are displayed in figure 1(a). The total volume of the imitated blood pool is 14 ml including all tube lengths and reservoirs, similar to the blood volume of a 200 g rat (Belcher and Harriss 1957). The phantom was placed in the center of the MPI system via a robotic mount. Following the experimental setup shown in figure 1, the fluid passes a reservoir of 1 ml first, to compensate pressure and changes in volume when a bolus is injected. Next is a 3D printed trap for air bubbles, which filters arising air from pressure variation or by injection to keep the phantom free of trapped air. The injection point is located at a realistic distance (vena caudalis) from the heart phantom, where a small catheter tube (0.28 mm diameter) is connected to the bolus syringe. The pulmonary circuit consists of a loop with a tube length of 9 cm and 1.6 mm diameter to achieve a delay of 1 s, which is the pulmonary transit time (PTT) of a healthy rat (Su *et al* 2022). It should be noted that for simplicity in these flow experiments, tissue mimicry to simulate real organ perfusion was neglected at this small organ scale. Before measurements, the peristaltic pump was fitted in a shielded housing and measurements were performed to exclude any influence of the motor on the MPI measurement signal.

2.2. Phantom measurements

The measurements were performed using a Bruker preclinical MPI system (MPI FF 20/25, Bruker BioSpin MRI GmbH, Ettlingen Germany) with a gradient field set to 1.2 Tm^{-1} in z-direction and a drive-field amplitude of 12 mT in all spatial directions. Consequently, the image field of view (FOV) spans 40 × 40 × 20 mm^3. For detection, a 3D gradiometric receive coil with an open bore of 72 mm was used, which enables high signal-to-noise ratio (SNR) and sensitivity (Paysen *et al* 2018), similar to the one constructed in Graeser *et al* (2017). Measurements of 12 000 frames were recorded without averaging at 21.54 ms repetition time to observe changes in the concentration over 4.3 min per bolus. A baseline concentration of 237 μg_{Fe} ml^{-1} (4.24 mmol l^{-1}) Perimag (micromod GmbH, Rostock, Germany) was chosen for the 14 ml imitated blood pool volume and administered via a single initial bolus which circulated until homogeneously dispersed (in total 3.3 mg iron). During

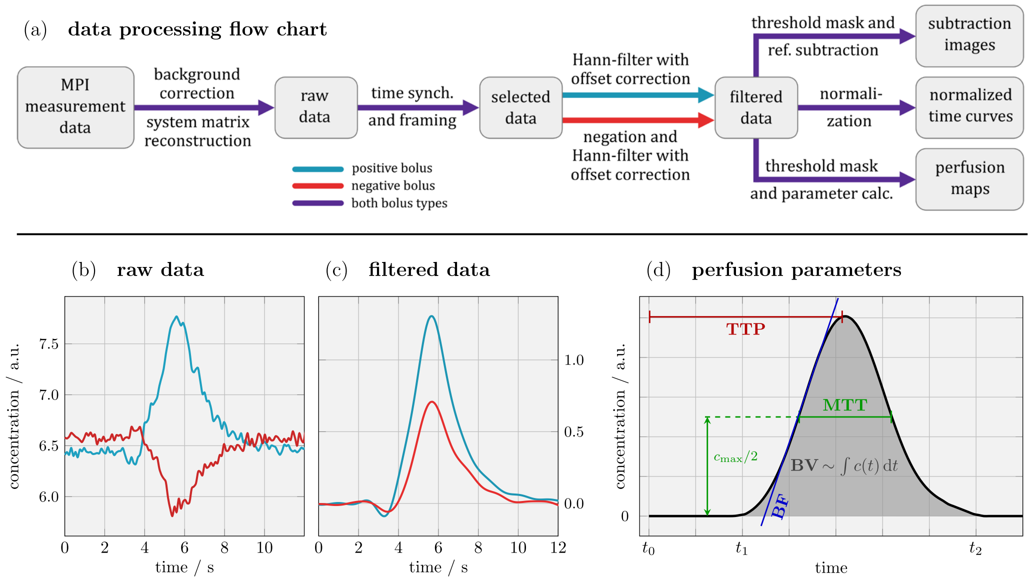

Figure 2. Processing flow chart and signal analysis. The data processing flow chart is shown in (a). The measurement data is reconstructed, the relevant time frame containing the first passing of the bolus (12 s) is selected, then negated (negative bolus only), and filtered before post processing. A threshold mask selects only relevant voxels. Raw data and filtered data are shown exemplarily for one voxel in (b) and (c), respectively. In (d), the applied definitions of perfusion parameters are visualized.

measurements, positive and negative boli were applied alternatingly to minimize concentration changes between boli. A total of 8 boli was given, 4 boli of each type. The time between boli was set to approximately 5 min while the pump continuously circulated the pool to reach a homogeneous distribution before the next injection. A volume of 150 μl was chosen for all boli, either as a tracer dispersion of 1 $\mu g_{Fe}\ \mu l^{-1}$ (positive) or consisting of physiological neutral saline solution (negative). Before injection of another bolus, 150 μl were drawn out of the pool to guarantee identical starting conditions. The injection was queued in the catheter tube, with a leading tiny air pocket to avoid dispersion of the bolus during preparation and to obtain identical constant injection rates. By means of the long catheter tube, the bolus can be conveniently applied from outside the scanner. A syringe-pump was not used due to the high pressure necessary to operate the small bolus syringe. Ongoing experiments were supervised with an online reconstruction software (Knopp and Hofmann 2016) to evaluate success (bolus passages) and confirm a homogeneous steady-state distribution.

2.3. Image reconstruction and post processing

All images were reconstructed using the system matrix approach described in Gleich and Weizenecker (2005). The system matrix was recorded on a 22 × 22 × 22 grid, spanning a system matrix FOV of 44 × 44 × 22 mm^3. This includes an overscan of 1 voxel compared to the image FOV and yields a voxelsize of 2 × 2 × 1 mm^3. Each single point response was averaged 150 times. Solutions were obtained by solving a Tikhonov regularized least squares problem using the MPI reconstruction framework MPIReco.jl (Knopp *et al* 2019). For reconstruction, a relative regularization parameter of $\lambda = 0.01$ and 5 iterations were chosen. Frequency selection includes frequencies from 80 kHz to 1.25 MHz with an SNR of at least 2. A background measurement (without the phantom in the scanner) was subtracted from the phantom measurements before reconstruction. The reconstructed solution $\boldsymbol{c} \in \mathbb{R}^{N \times n_t}$ with $N = n_x \times n_y \times n_z = 22^3$ voxels has $n_t = 12\,000$ time frames. The term $c_{i,t}$ refers to the i-th voxel and t-th time frame of the discrete solution. Furthermore, $\boldsymbol{c}_t^{\text{bolus}\,j}$ refers to all voxels of the j-th bolus.

The entire data processing chain is displayed as a flow-chart in figure 2, along with data examples and parameter definitions. After reconstruction, the post processing includes time synchronization, data negation, Hann-filtering, voxel masking and lastly the perfusion parameter calculation. In the order of mention: the time is synchronized over all boli by selecting a time frame that starts with the injection (t_0), includes the first bolus (t_1 to t_2) and stops after the first passing ($t = 12$ s). This step ensures that only relevant data is processed later. For negative boli the concentration is inverted, so they can be processed identically to positive boli by the same code that works e.g. by using the maximum intensity. Afterwards, an appropriate filter type was chosen to smoothen the data for a more accurate peak detection and data interpolation, which also shifts the concentration offset to zero. To reject ringing artifacts, we avoided rectangular windows and selected a low-pass Hann-filter with a window-size of 10 samples. The Hann-filter is applied voxel-wise on the Fourier transformed temporal data. The last step before perfusion parameters are calculated is the determination of a threshold mask, which reduces image noise by excluding any voxel with an intensity lower than 6% of the maximum value for the selected time frame. The term ‘raw data’ refers to data reconstructed from the measurement signal before any processing, and ‘filtered data’ is a term for the final Hann-filtered data prior to post processing. This last step includes subtraction images, normalization and perfusion maps.

Subtraction images. To visualize small changes in concentration, a pre-bolus reference is subtracted (pre contrast) from all following images (post contrast) to remove the native concentration, and consequently only changes in the concentration become visible (Hecht *et al* 2004). Dynamic subtraction images are based on the filtered data and calculated by subtracting with the identical spatial slice at t_0, that is before the administered bolus reaches the FOV.

Normalized images. By using a normalization, the time response of positive and negative boli can be overlaid e.g. to compare rise times or the shape of the bolus. To this end, the filtered data was used and normalization was applied to match maxima (in this graph only). The normalization is done via linear regression to match the maxima of the first peak without distorting the underlying time axis. Based on the linear model $\boldsymbol{c}_t^{\text{bolus }1} = a_j \boldsymbol{c}_t^{\text{bolus }j} + b_j$ for all $j \in \{2,\ldots,8\}$ boli, a slope a_j and an offset correction b_j is determined for all time samples t, so each bolus can be mapped individually to one selected positive bolus (Zou *et al* 2003).

Perfusion images. In order to assess the feasibility of negative boli in perfusion imaging, calculations were performed on the filtered data for positive and negative boli using a threshold mask as described above and in figure 2(d). The data is not normalized for this calculation and the identical functions were used for positive and negative boli. The only difference is that negative boli are inverted before filtering. Perfusion maps are generated for TTP, rBF, rBV and MTT. The definition of individual perfusion parameters follows in section 2.4 below.

2.4. Perfusion parameters

The following definitions are formulated continuously by using $c_i(t)$, to provide a more general consideration. However, our data were processed using the discrete solution $c_{i,t}$.

TTP: the TTP is defined as the time elapsed between a chosen reference point (the bolus injection, here t_0) and the measured signal maximum of the first bolus passing (see figure 2(d)). The $\mathbf{TTP} \in \mathbb{R}^N$ is calculated element-wise for all voxel $i \in \{1,\ldots,N\}$ via

$$\mathrm{TTP}_i = \arg\max_t(\, c_i(t)), \tag{1}$$

where $c_i(t)$ is the concentration over time of the ith voxel (Fieselmann *et al* 2011).

PTT: the PTT is the time that a particle or blood cell needs to pass from the right to the left ventricle, therefore the average time that the blood circulates through the lung. It can be calculated by the difference of the TTPs of the ventricles (Deán-Ben *et al* 2015). In this work it is defined by a length of tube and the flow rate that was chosen to introduce a delay of about 1 s (see section 2.2).

rBF: the rBF equals the highest positive gradient in $c_i(t)$

$$\mathrm{rBF}_i = \arg\max_t\left(\frac{d}{dt}c_i(t)\right), \tag{2}$$

as shown in figure 2(d). A calculation for all voxels yields $\mathbf{rBF} \in \mathbb{R}^N$. The BF and BV are calculated in a relative manner, due to a missing correct arterial input function.

rBV: the rBV can be derived from an element-wise evaluation of the AUC in the ith voxel, divided by the AUC in the artery to yield $\mathbf{rBV} \in \mathbb{R}^N$. Therefore, the blood volume is proportional to the integral of $c_i(t)$, divided by the integral of $c_{\mathrm{art}}(t)$ in the artery, over their respective time intervals $[t_1, t_2]$ (see figure 2(d)), that mark the time the bolus needs for the first passing, as in

$$\mathrm{rBV}_i = \frac{\int_{t_1}^{t_2} c_i(t)\,dt}{\int_{t_1}^{t_2} c_{\mathrm{art}}(t)\,dt}. \tag{3}$$

MTT: the MTT is a measure of the average time that a particle or blood cell spends inside a vessel or organ. It is usually defined by the ratio of rBV to rBF or via the first moment of the AUC (Weisskoff *et al* 1993, Østergaard *et al* 1996), however, it strongly correlates with the full width at half maximum (FWHM) of the concentration peak (Kealey *et al* 2004, Østergaard 2005), especially for measurements with low tissue perfusion. To avoid error propagation due to inaccuracies in rBV and rBF (Weisskoff *et al* 1993, Østergaard *et al* 1996), we took the time interval FWHM as the MTT (Østergaard 2005), shown in figure 2(d).

2.5. Comparison of positive and negative boli performance

Negative and positive boli are qualitatively compared by visual inspection of subtraction images, normalized data and perfusion maps. All these calculations are based on the filtered data set, but with an increasing computational effort in the mentioned order. The subtraction images reveal small changes in the concentration over time and require just the filtered time data and a threshold mask. Normalized images require a normalization step via linear regression and perfusion maps need to be processed according to section 2.4. All of these calculations were done for all boli, however, in the results only some boli and some perfusion maps are shown exemplarily. Positive boli are taken as the ground truth during comparison to negative boli in this work.

3. Results

3.1. Comparison of signal time histories, difference images, and normalization of the positive and negative boli

In figure 3(a), raw data of positive and negative boli in the left ventricle are shown, displaying several bolus passages over 100 s. The steady-state level increases slightly after each additional positive bolus (boli are administered alternately). Due to the relation of the chosen bolus concentration and initial baseline, peaks of negative boli are about 43% lower in the raw data.

Below in figure 3(b), normalized curves based on filtered data of all 8 boli are shown for the right atrium and left ventricle. The normalized overlay of all 8 boli at the same location shows that curvature, shape and AUC coincide and are almost identical. On average, the FWHM is 12% smaller for negative boli in the right atrium and 5% smaller in the left ventricle, which predicts shorter rise times for negative boli. Boli were applied with identical procedure and alternatingly, hence a systematical fault in the setup is unlikely. An excessive low-pass filter setting would result in underestimating the bolus peak and equalize the FWHM difference between bolus types.

Dynamic time responses at different positions in the heart phantom are displayed in figure 4(a). The delay, in other words the transition times between different areas, and the shape of the bolus peak can be distinguished. We expected the width of the peak to increase with time, the AUC to remain constant, and the peak to be highest in the vena cava at the beginning. Limited resolution and unfortunate voxel spacing resulted in partial volume effects that led to locally lower concentrations compared with these expectations. The voxelsize of $2 \times 2 \times 1\ \mathrm{mm}^3$ is the lower limit for the represented resolution, but the smallest features of the 3D printed phantom were tubes with diameters below 2 mm, e.g. for the vena cava, aorta and pulmonary vessels. As a result, these concentrations are underestimated for both bolus types, which is visible here in the maxima and AUCs of the vena cava and aorta in figure 4(a).

Below in figure 4(b), subtraction images are shown, suggesting that negative boli do not show significant deviation from the positive ground truth and dynamic imaging is possible. Each bolus can be seen to enter the right ventricle first, then passing through the pulmonary circuit and on to the left side of the heart. A small air bubble accumulated over the course of the experiments in the right ventricle in spite of all efforts to prevent air from entering the phantom. This caused a void in the images as no concentration changes occur except by movement of the bubble. Therefore, the bubble appears with zero intensity in subtraction images.

3.2. Comparison of perfusion parameter maps of positive and negative boli

In figure 5, the TTP map is shown for a positive and a negative bolus, on the left and right, respectively. The top row shows the vena cava (blue) and the aorta (red), which are at the extremes of the colorbar, as they mark inlet and outlet of the heart phantom (compare to reference on bottom left). The bottom row shows the tubes of the pulmonary circuit (the return bend is outside the FOV), which are very similar in color shape due to the small time difference ($\mathrm{PTT} = 1$ s). The center of the heart phantom (layer 13) is enhanced to show that the 4 chambers of the heart are identifiable by slight differences in shading. The TTP was successfully obtained from a negative bolus and deviations between the two bolus types are low and in the same range of variations between administered boli of identical type. Note that the filtered data used in these results is not normalized, as this would impact the rBF, rBV, MTT, and the shape of the curve is therefore preserved.

Further perfusion parameters, namely the rBF, rBV and MTT, are shown in figure 6. Differences between the results of positive and negative bolus are small. The slightly darker tint of the negative rBF corresponds to the above mentioned difference in the FWHM, also visible in the data in figure 3(b). The same tendency can be seen in the MTT, which is a little shorter for negative boli. However, the MTT is generally around 2.5 s for both boli types and due to minor dispersion of the boli, the shading is darker in the left ventricle compared to the right ventricle, indicating that the bolus passed first through the right heart chamber and then through the left chamber. In the area of the pulmonary artery and the pulmonary vein, the actual blood flow is expected to be higher due to the smaller cross-section. The calculated blood flow shows the opposite due to the lower measured concentration. As already mentioned above with regard to figure 4(a), the local underestimation can be

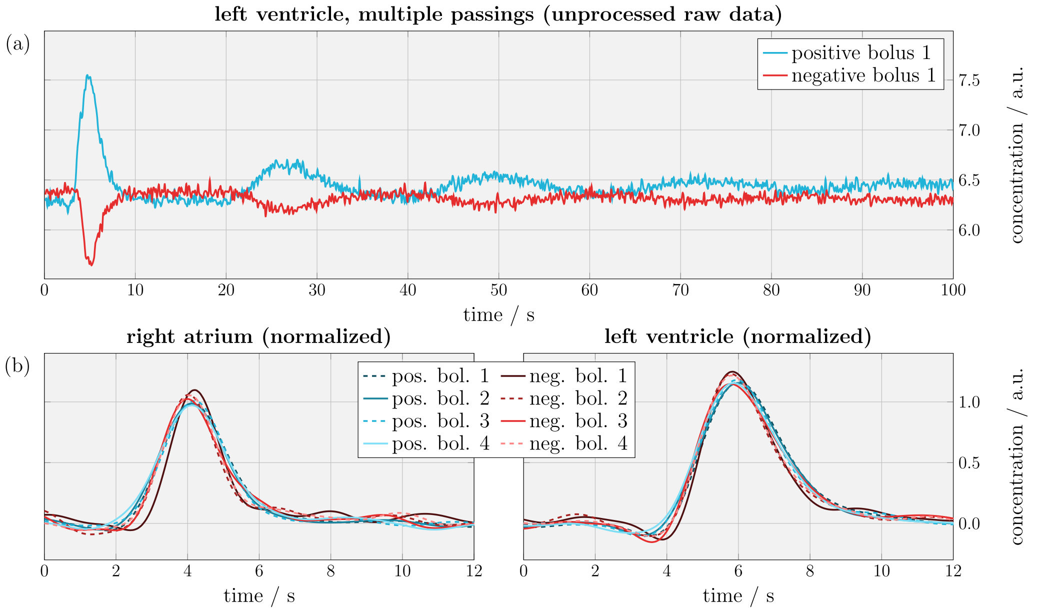

Figure 3. Raw data and normalized data. In (a), the exemplary raw data of a consecutive positive and negative bolus for 100 s are shown. Several bolus passages are visible, indicated by numerous peaks. The baseline steady-state concentration of the negative bolus (prior to first pass) is increased due to the preceding positive bolus. Below in (b), the right atrium and the left ventricle of the filtered data including the normalization step are shown for all 8 boli.

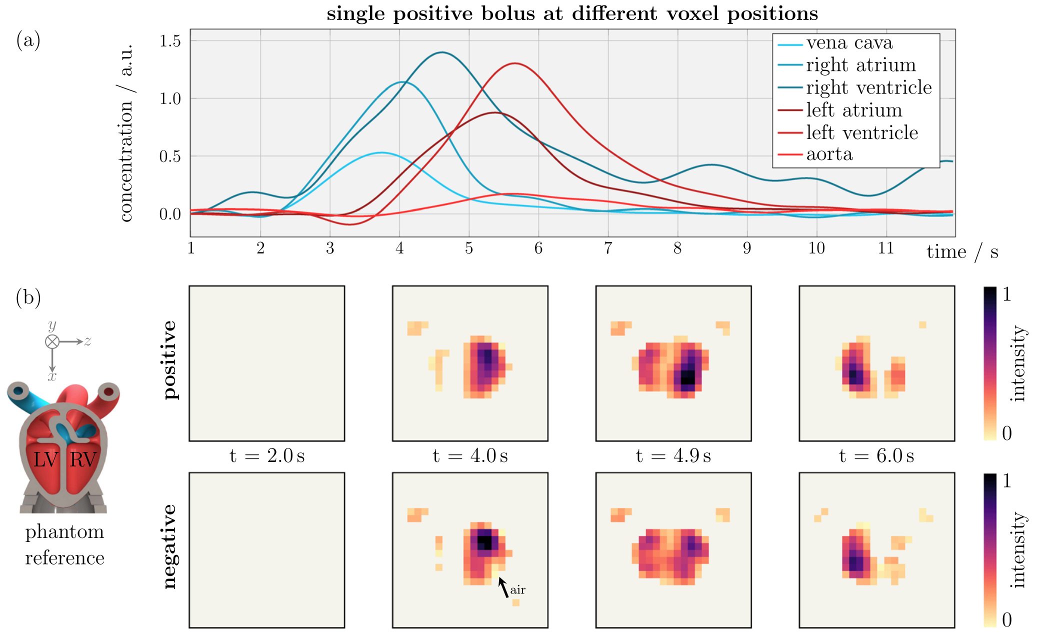

Figure 4. Local time responses and subtraction images. In (a), the time response of a single bolus is tracked at different voxel locations in the heart phantom (filtered data). This is mapped in (b) below, where subtraction images are displayed for a positive and a negative bolus. A phantom reference slice on the left shows the orientation and layout of the 4 phantom heart chambers.

explained by partial volume effects and that the system matrix resolution is lower than the smallest vessels cross-section. This is consequently not a problem for the comparison between positive and negative boli, but a resolution-related limitation by the imaging system. Low resolution and partial volume effects prevented a correct definition of the arterial input function, consequently the BF and BV were calculated in a relative manner. Note that rBF and rBV are relative, however, they are scaled identically for positive and negative bolus types. These two images for one perfusion parameter are not normalized individually, therefore they refer to a common colormap for direct comparability.

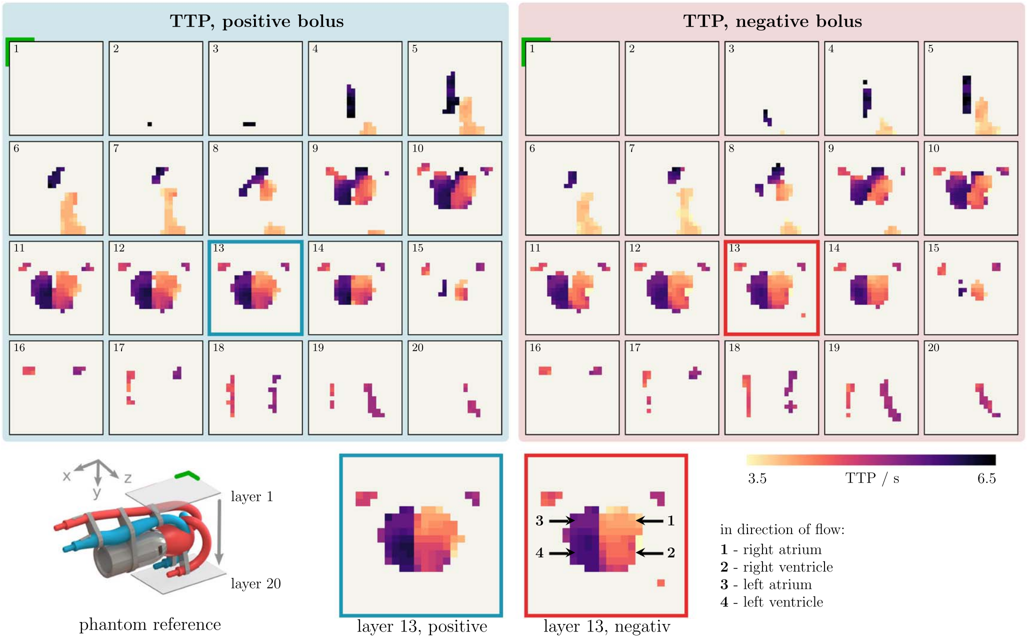

Figure 5. Spatial progression of the TTP. On the left, a positive bolus was administered and on the right a negative bolus. The data were processed according to figure 2. The time is mapped from bright colors (3.5 s) to dark colors (6.5 s) and 0 s corresponds to the time of injection, identical to all time graphs above. The equidistant progression (1–20) along the *y*-axis shows different *xz*-slices of the FOV. Layer 13 is magnified on the bottom and the 4 heart chambers can be identified for each bolus type. The phantom reference slice is marked with a green corner for image orientation.

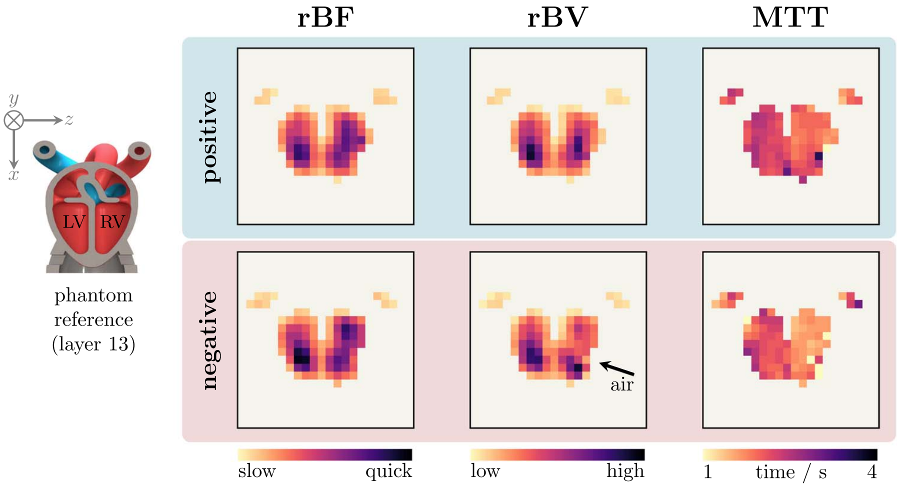

Figure 6. The rBF, rBV and MTT for both bolus types. Shown is a single slice (layer 13) for a positive and a negative bolus on the top and bottom respectively. Note that the images of each perfusion parameter are scaled to a single common colormap vertically and not normalized individually.

As mentioned in section 2.2, the tiny air pockets used to avoid dispersion during bolus preparation accumulated in the phantom, due to the position of the catheter just in front on the phantom. However, a bubble trap behind the catheter would have caused high dispersion of the bolus. Air also arose from cavitation in proximity to the pump, which prevented long experiments with more than 10 boli (around 5 min each).

4. Discussion

We presented a novel method without the need of additional tracer dosage for calculating perfusion maps in MPI. The method was evaluated based on phantom measurements, including the visibility of negative boli in the raw data (figure 3(a)), in normalized data (figure 3(b)), in dynamic subtraction images (figure 4(b)), and in perfusion maps (figures 5 and 6). Overall deviations between the reconstructed images of a negative bolus and a positive bolus are low and in a similar range to the variations seen with multiple administrations of a positive bolus.

Regarding signal quality, negative boli do not need to be identical in volume to positive boli for perfusion imaging, they could be chosen larger for a better SNR, since the human body is compatible with large amounts of neutral saline solution as opposed to magnetic particles. The maximum achievable SNR of a negative bolus depends on the baseline concentration in advance to the injection and on the injection volume of the bolus itself. If chosen in such a way that the negative bolus completely displaces all tracer from a VOI during passing, maximum contrast is created. However, this is not desirable due to the intensity plateau that it creates, just as input-clipping of a large positive bolus should be avoided for the correct calculation of all perfusion parameters. A mindful selection of bolus volume and baseline concentration is necessary, similar to the selection of a sufficient dose for positive boli that is just visible for the planned imaging scenario. Further tracer-specific investigations regarding the baseline concentration for sufficient *in vivo* SNR should be conducted.

Limitations to the efficiency and impact of the presented method are rooted in the availability and performance of a long circulating tracer for humans that upholds the mandatory baseline concentration. In addition, the *in vivo* performance of saline solution as a bolus has not been investigated. Some modifications to reduce dispersion in real blood may be required before the bolus reaches the desired organ (e.g. the brain).

Although our study chose an exemplary scenario of a rat-heart phantom, and therefore a focus on cardiovascular imaging, the proof of concept to use negative boli for perfusion maps is transferable to other areas e.g. cerebrovascular imaging. In a scenario that encompasses a long-term observation e.g. the monitoring of a future stroke patient, positive boli should be dosed as before, with a minimum of iron added for each acquisition of the perfusion parameters. Following several administered positive boli of a long circulating tracer, when a baseline concentration is reached, the observation can be continued using negative boli without adding to the particle iron mass in the body. A combination of positive-negative boli allows for a much longer observation with shorter intermediate boli time compared to positive boli only. Positive boli should be used if the blood pool concentration falls short of the baseline concentration for a negative bolus, caused by tracer which is taken up by the liver. Another potential application is in endovascular interventions, e.g. stenosis assessment and stent implantation. The morphology of the vessel would be visible from the long circulating tracer and the catheter via a marker (Herz *et al* 2019). A small negative bolus could be administered directly in the FOV, without dispersion, to evaluate the procedure e.g. by calculating the blood flow. This can be repeated without adding more iron compared to positive bolus evaluation.

Generally valid quantitative statements about the amount of tracer reduction cannot be made on the basis of our experiments. The specific iron reduction by using negative boli depends on the surveillance scenario, the number of boli administered, the half-life of the tracer in blood, and other monitoring specific parameters.

In conclusion, our study proposes a method for obtaining perfusion images in MPI with a positive-negative contrast sequence. The results from phantom experiments demonstrate that the negative bolus approach effectively contributes an image contrast resulting in concurrent signals with positive boli. Furthermore, our proposed method enables an increased monitoring time of a future patient while keeping the total iron dose constant. We believe that our results can significantly contribute to making MPI perfusion imaging techniques applicable in a clinical scenario with long monitoring times.

Acknowledgments

The authors would like to thank Marija Boberg for proof reading and fruitful additions to the figures. The authors thankfully acknowledge the financial support by the German Research Foundation (DFG, grant number KN 1108/7-1 and GR 5287/2-1). Publishing fees supported by Funding Programme Open Access Publishing of Hamburg University of Technology (TUHH).

Data availability statement

The data cannot be made publicly available upon publication because no suitable repository exists for hosting data in this field of study. The data that support the findings of this study are available upon reasonable request from the authors.

ORCID iDs

Fabian Mohn https://orcid.org/0000-0002-9151-9929
Miriam Exner https://orcid.org/0000-0002-3756-3822
Patryk Szwargulski https://orcid.org/0000-0003-2563-9006
Martin Möddel https://orcid.org/0000-0002-4737-7863
Tobias Knopp https://orcid.org/0000-0002-1589-8517
Matthias Graeser https://orcid.org/0000-0003-1472-5988

References

Antonelli A, Sfara C, Rahmer J, Gleich B, Borgert J and Magnani M 2013 Red blood cells as carriers in magnetic particle imaging *Biomed. Tech./Biomed. Eng.* **58** 517–25

Arbab A S, Wilson L B, Ashari P, Jordan E K, Lewis B K and Frank J A 2005 A model of lysosomal metabolism of dextran coated superparamagnetic iron oxide (SPIO) nanoparticles: implications for cellular magnetic resonance imaging *NMR Biomed.* **18** 383–9

Barbier E L, Lamalle L and Décorps M 2001 Methodology of brain perfusion imaging: methodology of brain perfusion imaging *J. Magn. Reson. Imaging* **13** 496–520

Belcher E H and Harriss E B 1957 Studies of plasma volume, red cell volume and total blood volume in young growing rats *J. Physiol.* **139** 64–78

Billings C, Langley M, Warrington G, Mashali F and Johnson J A 2021 Magnetic particle imaging: current and future applications, magnetic nanoparticle synthesis methods and safety measures *Int. J. Mol. Sci.* **22** 7651

Cha S 2003 Perfusion MR imaging: basic principles and clinical applications *Magn. Reson. Imaging Clinics North Am.* **11** 403–13

Deán-Ben X L, Ford S J and Razansky D 2015 High-frame rate four dimensional optoacoustic tomography enables visualization of cardiovascular dynamics and mouse heart perfusion *Sci. Rep.* **5** 10133

Detre J A, Leigh J S, Williams D S and Koretsky A P 1992 Perfusion imaging *Magn. Reson. Med.* **23** 37–45

Exner M, Szwargulski P, Knopp T, Graeser M and Ludewig P 2019 3D printed anatomical model of a rat for medical imaging *Curr. Directions Biomed. Eng.* **5** 187–90

Fieselmann A, Kowarschik M, Ganguly A, Hornegger J and Fahrig R 2011 Deconvolution-based CT and MR brain perfusion measurement: theoretical model revisited and practical implementation details *Int. J. Biomed. Imaging* **2011** 1–20

Gleich B and Weizenecker J 2005 Tomographic imaging using the nonlinear response of magnetic particles *Nature* **435** 1214–7

Graeser M, Thieben F, Szwargulski P, Werner F, Gdaniec N, Boberg M, Griese F, Möddel M, Ludewig P, Van de Ven D, Weber O.M., Woywode O, Gleich B, Knopp T *et al* 2019 Human-sized magnetic particle imaging for brain applications *Nat. Commun.* **10** 1936

Graeser M, Knopp T, Szwargulski P, Friedrich T, Von Gladiss A, Kaul M, Krishnan K M, Ittrich H, Adam G and Buzug T M 2017 Towards picogram detection of superparamagnetic iron-oxide particles using a gradiometric receive coil *Sci. Rep.* **7** 6872

Graeser M, Ludewig P, Szwargulski P, Foerger F, Liebing T, Forkert N D, Thieben F, Magnus T and Knopp T 2020 Design of a head coil for high resolution mouse brain perfusion imaging using magnetic particle imaging *Phys. Med. Biol.* **65** 235007

Haegele J, Duschka R L, Graeser M, Schaecke C, Panagiotopoulos N, Lüdtke-Buzug K, Buzug T M, Barkhausen J and Vogt F M 2014 Magnetic particle imaging: kinetics of the intravascular signal in vivo *Int. J. Nanomed.* **9** 4203–9

Hecht E M, Israel G M, Krinsky G A, Hahn W Y, Kim D C, Belitskaya-Levy I and Lee V S 2004 Renal masses: quantitative analysis of enhancement with signal intensity measurements versus qualitative analysis of enhancement with image subtraction for diagnosing malignancy at MR imaging *Radiology* **232** 373–8

Herz S, Vogel P, Kampf T, Dietrich P, Veldhoen S, Rückert M A, Kickuth R, Behr V C and Bley T A 2019 Magnetic particle imaging-guided stenting *J. Endovascular Ther.* **26** 512–9

Kaul M G, Mummert T, Graeser M, Salamon J, Jung C, Tahir E, Ittrich H, Adam G and Peldschus K 2021 Pulmonary blood volume estimation in mice by magnetic particle imaging and magnetic resonance imaging *Sci. Rep.* **11** 4848

Kaul M G, Salamon J, Knopp T, Ittrich H, Adam G, Weller H and Jung C 2018 Magnetic particle imaging for *in vivo* blood flow velocity measurements in mice *Phys. Med. Biol.* **63** 64001

Kealey S M, Loving V A, Delong D M and Eastwood J D 2004 User-defined vascular input function curves: influence on mean perfusion parameter values and signal-to-noise ratio *Radiology* **231** 587–93

Knopp T and Hofmann M 2016 Online reconstruction of 3D magnetic particle imaging data *Phys. Med. Biol.* **61** N257–67

Knopp T, Szwargulski P, Griese F, Grosser M, Boberg M and Möddel M 2019 MPIReco.jl: Julia package for image reconstruction in MPI *Int. J. Magn. Part. Imaging* **5** 1–2

Liu S, Chiu-Lam A, Rivera-Rodriguez A, DeGroff R, Savliwala S, Sarna N and Rinaldi-Ramos C M 2021 Long circulating tracer tailored for magnetic particle imaging *Nanotheranostics* **5** 348–61

Ludewig P *et al* 2017 Magnetic particle imaging for real-time perfusion imaging in acute stroke *ACS Nano* **11** 10480–8

Ludewig P, Gaeser M, Forkert N D, Thieben F, Rández-Garbayo J, Rieckhoff J, Lessmann K, Förger F, Szwargulski P, Magnus T and Knopp T 2022 Magnetic particle imaging for assessment of cerebral perfusion and ischemia *WIREs Nanomed. Nanobiotechnology* **14** e1757

Mason E E, Mattingly E, Herb K, Śliwiak M, Franconi S, Cooley C Z, Slanetz P J and Wald L L 2021 Concept for using magnetic particle imaging for intraoperative margin analysis in breast-conserving surgery *Sci. Rep.* **11** 13456

Mohn F, Exner M, Szwargulski P, Möddel M, Knopp T and Graeser M 2023 Using negative bolus in dynamic MPI *Int. J. Magn. Part. Imaging IJMPI* **9** 1

Molwitz I, Ittrich H, Knopp T, Mummert T, Salamon J, Jung C, Adam G and Kaul M G 2019 First magnetic particle imaging angiography in human-sized organs by employing a multimodal ex vivo pig kidney perfusion system *Physiol. Meas.* **40** 105002

Murase K, Takata H, Takeuchi Y and Saito S 2013 Control of the temperature rise in magnetic hyperthermia with use of an external static magnetic field *Phys. Med.* **29** 624–30

Oh J K and Park J M 2011 Iron oxide-based superparamagnetic polymeric nanomaterials: design, preparation, and biomedical application *Prog. Polym. Sci.* **36** 168–89

Orendorff R *et al* 2017 First *in vivo* traumatic brain injury imaging via magnetic particle imaging *Phys. Med. Biol.* **62** 3501–9

Østergaard L 2005 Principles of cerebral perfusion imaging by bolus tracking *J. Magn. Reson. Imaging* **22** 710–7

Østergaard L, Weisskoff R M, Chesler D A, Gyldensted C and Rosen B R 1996 High resolution measurement of cerebral blood flow using intravascular tracer bolus passages. Part i: Mathematical approach and statistical analysis *Magn. Reson. Med.* **36** 715–25

Paysen H, Wells J, Kosch O, Steinhoff U, Franke J, Trahms L, Schaeffter T and Wiekhorst F 2018 Improved sensitivity and limit-of-detection using a receive-only coil in magnetic particle imaging *Phys. Med. Biol.* **63** 13NT02

Rahmer J, Stehning C and Gleich B 2018 Remote magnetic actuation using a clinical scale system *PLoS One* **13** e0193546

Reimer P and Balzer T 2003 Ferucarbotran (resovist): a new clinically approved RES-specific contrast agent for contrast-enhanced MRI of the liver: properties, clinical development, and applications *Eur. Radiol.* **13** 1266–76

Rubia-Rodríguez I *et al* 2021 Whither magnetic hyperthermia? A tentative roadmap *Materials* **14** 706

Salamon J *et al* 2016 Magnetic particle/magnetic resonance imaging: *in vitro* MPI-guided real time catheter tracking and 4D angioplasty using a road map and blood pool tracer approach *PLoS One* **11** e0156899

Siepmann R, Nilius H, Mueller F, Mueller K, Luisi C, Dadfar S M, Straub M, Schulz V and Reinartz S D 2021 Image-derived mean velocity measurement for prediction of coronary flow reserve in a canonical stenosis phantom using magnetic particle imaging *PLoS One* **16** e0249697

Southern P and Pankhurst Q A 2018 Commentary on the clinical and preclinical dosage limits of interstitially administered magnetic fluids for therapeutic hyperthermia based on current practice and efficacy models *Int. J. Hyperth.* **34** 671–86

Su F, Shi Y-Y, Wang B and Zheng X-Z 2022 Comparison of the effects of adenosine, isoproterenol and their combinations on pulmonary transit time in rats using contrast echocardiography *Med. Ultrasonography* **24** 58

Sun C, Lee J S H and Zhang M 2008 Magnetic nanoparticles in MR imaging and drug delivery *Adv. Drug Deliv. Rev.* **60** 1252–65

Szwargulski P *et al* 2020 Monitoring intracranial cerebral hemorrhage using multicontrast real-time magnetic particle imaging *ACS Nano* **14** 13913–23

Thieben F, Mohn F, Foerger F, Hackelberg N, Scheel J-P, Graeser M and Knopp T 2023 Safe and rapid 3D imaging: upgrade of a human-sized brain MPI system *Int. J. Magn. Part. Imaging IJMPI* **9** 1

2018 *Comparative Anatomy and Histology: A Mouse, Rat and Human Atlas* Treuting P M *et al* (ed) (London: Academic Press, An Imprint of Elsevier) 2nd edn 978-0-12-802919-0

Vaalma S, Rahmer J, Panagiotopoulos N, Duschka R L, Borgert J, Barkhausen J, Vogt F M and Haegele J 2017 Magnetic particle imaging (MPI): experimental quantification of vascular stenosis using stationary stenosis phantoms *PLoS One* **12** e0168902

Vogel P *et al* 2022 iMPI—interventional magnetic particle imaging *Int. J. Magn. Part. Imaging* **8** 2022

Weisskoff R M, Chesler D, Boxerman J L and Rosen B R 1993 Pitfalls in MR measurement of tissue blood flow with intravascular tracers: which mean transit time? *Magn. Reson. Med.* **29** 553–8

Wintermark M *et al* 2005 Comparative overview of brain perfusion imaging techniques *Stroke* **36** 9

Yu E Y, Bishop M, Zheng B, Ferguson R M, Khandhar A P, Kemp S J, Krishnan K M, Goodwill P W and Conolly S M 2017 Magnetic particle imaging: a novel *in vivo* imaging platform for cancer detection *Nano Lett.* **17** 1648–54

Zheng B, Von See M P, Yu E, Gunel B, Lu K, Vazin T, Schaffer D V, Goodwill P W and Conolly S M 2016 Quantitative magnetic particle imaging monitors the transplantation, biodistribution, and clearance of stem cells *in vivo Theranostics* **6** 291–301

Zhou X Y, Jeffris K E, Yu E Y, Zheng B, Goodwill P W, Nahid P and Conolly S M 2017 First *in vivo* magnetic particle imaging of lung perfusion in rats *Phys. Med. Biol.* **62** 3510–22

Zou K H, Tuncali K and Silverman S G 2003 Correlation and simple linear regression *Radiology* **227** 617–28

10

Real-time multi-contrast MPI for the detection of gastrointestinal bleeding

We investigate in this chapter the detection of GI bleeding using MPI experiments with human-sized bowel phantoms and ex vivo porcine small bowel specimen. Single- and multi-contrast experiments as well as subtraction and threshold images are used to evaluate the robustness and feasibility of the technique for future interventions. The main advantage is the use of two tracers, one administered orally and one injected, to detect GI bleeding by multi-contrast MPI when both tracers mix at the same location [O6].

The following work originated in a collaboration of the Department of Diagnostic and Interventional Radiology and Nuclear Medicine, together with the Section for Biomedical Imaging, both affiliated with the University Medical Center Hamburg-Eppendorf (UKE). The collaboration aims to involve physicians who are part of the daily routine of a hospital in conceptualizing possible MPI applications that could facilitate their job in the future.

Parts of this work were presented at the European Congress of Radiology 2022, Vienna, Austria [O18] and at the IWMPI 2024, Switzerland [O10].

10.1 Nature - Scientific Reports

Manuscript received April 30, 2023.
Accepted December 14, 2023.
Published December 27, 2023.

DOI: 10.1038/s41598-023-50041-3

www.nature.com/scientificreports

scientific reports

OPEN

Real-time multi-contrast magnetic particle imaging for the detection of gastrointestinal bleeding

Fabian Mohn[1,2], **Patryk Szwargulski**[1,2], **Michael G. Kaul**[3], **Matthias Graeser**[1,2,4,5], **Tobias Mummert**[3], **Kannan M. Krishnan**[6], **Tobias Knopp**[1,2], **Gerhard Adam**[3], **Johannes Salamon**[3] & **Christoph Riedel**[3]✉

Gastrointestinal bleeding, as a potentially life-threatening condition, is typically diagnosed by radiation-based imaging modalities like computed tomography or more invasively catheter-based angiography. Endoscopy enables examination of the upper gastrointestinal tract and the colon but not of the entire small bowel. Magnetic Particle Imaging (MPI) enables non-invasive, volumetric imaging without ionizing radiation. The aim of this study was to evaluate the feasibility of detecting gastrointestinal bleeding by single- and multi-contrast MPI using human-sized organs. A 3D-printed small bowel phantom and porcine small bowel specimens were prepared with a defect within the bowel wall as the source of a bleeding. For multi-contrast MPI, the bowel lumen was filled with an intestinal tracer representing an orally administered tracer. MPI was performed to evaluate the fluid exchange between the vascular compartment of the bowel wall and the lumen while a blood pool tracer was applied. Leakage of the blood pool tracer was observed to the bowel lumen. Multi-contrast MPI enabled co-registration of both tracers at the same location within the bowel lumen indicating gastrointestinal bleeding. Single- and multi-contrast MPI are feasible to visualize gastrointestinal bleeding. Therefore, MPI might emerge as a useful tool for radiation-free detection of bleeding within the entire gastrointestinal tract.

Gastrointestinal (GI) bleeding represents as a clinical manifestation of a variety of diseases[1]. GI bleeding occurs within the entire GI tract and can be classified based on its anatomic location into upper, middle, and lower GI bleeding. Upper GI bleeding is located between mouth to duodenum above the ampulla of Vater[2]. Peptic ulcer disease followed by gastritis and esophagitis are the most common causes, while bleeding from esophageal varices and neoplasms are associated with the highest mortality[3]. A bleeding in the middle GI tract, between the ampulla of Vater to the terminal ileum[2], might arise from vascular pathologies (e.g. angiodysplasia, Dieulafoy's lesions), inflammatory bowel disease, Meckel's diverticulum, ulcers or neoplasms[4–6]. A lower GI bleeding occurs in the colon or rectum[7]. The most common causes include colonic diverticulosis followed by internal hemorrhoids and ischemic colitis[8].

A GI bleeding might present as an overt or as an occult bleeding. An overt bleeding is characterized by visible signs of a bleeding like hematemesis, hematochezia, or melena. Acute overt GI bleeding, as a potentially life-threatening condition, requires prompt clinical evaluation and treatment[1]. Typically, in both the upper and the lower GI tract endoscopy serves as initial modality (i.e. esophagogastroduodenoscopy and ano-/sigmoido-/colonoscopy) to locate the bleeding source with the advantage to enable therapeutic intervention[8,9]. However, if endoscopic evaluation is not feasible or inconclusive, further imaging techniques like computed tomography (CT) might be necessary[1,10]. The diagnostic evaluation of a bleeding in the middle GI tract depends on the clinical presentation of the patient. If an acute overt bleeding in the small bowel is suspected, ^{99m}Tc-labeled red blood cell scintigraphy, CT angiography or, in case of a hemodynamically unstable patient, conventional catheter angiography might reveal the bleeding source by extravasation of a tracer or contrast agent[4]. An occult bleeding might present with iron deficiency anemia or a positive fecal occult blood test, but without visible signs of

[1]Section for Biomedical Imaging, University Medical Center Hamburg-Eppendorf, Hamburg, Germany. [2]Institute for Biomedical Imaging, Hamburg University of Technology, Hamburg, Germany. [3]Department of Diagnostic and Interventional Radiology and Nuclear Medicine, University Medical Center Hamburg-Eppendorf, Martinistrasse 52, 20246 Hamburg, Germany. [4]Fraunhofer Research Institution for Individualized and Cell-based Medical Engineering, IMTE, Lübeck, Germany. [5]Institute of Medical Engineering, University of Lübeck, Lübeck, Germany. [6]Department of Materials Science and Engineering, University of Washington, Seattle, USA. ✉email: ch.riedel@uke.de

a bleeding[1,5,11]. Initially, colonoscopy and esophagogastroduodenoscopy might be performed to find a bleeding source in the lower or upper GI tract, respectively. If no bleeding source is detected, CT enterography, video capsule endoscopy (VCE) and double balloon endoscopy (DBE) can be used to evaluate the small bowel[1]. VCE enables the noninvasive evaluation of the entire small bowel. However, limitations of this technique include the inability to influence the GI passage and the possibility to miss clinically important lesions[4]. DBE is performed in sedation and enables deep intubation of the small bowel with the possibility for therapeutic intervention. Nonetheless, lesions might be missed if a total enteroscopy is not achieved[4].

Here, a non-invasive, radiation-free imaging technique with coverage of the entire GI tract is desirable for bleeding detection. Magnetic Particle Imaging (MPI) is a technique for volumetric imaging at a high spatiotemporal resolution without ionizing radiation based on superparamagnetic iron oxide nanoparticles (SPIONs)[12,13]. Potential applications encompass e.g. the in vivo evaluation of blood flows[14,15], the assessment of brain perfusion[16], MPI-derived angiography[17], and MPI-guided vascular interventions[18,19]. Furthermore, MPI enabled the detection of an induced acute GI bleeding in a murine model[20]. In comparison to other imaging modalities like CT, MPI offers the advantage of multi-contrast imaging[21] with the possibility to visualize more than one tracer simultaneously or to exploit the physical link of the magnetization behavior to measure viscosity or temperature[22–24]. Multi-contrast MPI has been used to detect intracranial bleeding and to monitor the expansion of the hematoma in a murine model[22].

In this study we demonstrate the feasibility of non-invasive MPI to visualize real-time tracer enhancement of a bowel wall and to detect gastrointestinal bleeding in human-sized organs. Therefore, single- and multi-contrast experiments were performed on 3D-printed phantoms in the scale of human small bowel and on ex vivo porcine small bowel specimens to visualize extravasation of a blood pool tracer to the bowel lumen. In multi-contrast experiments, an additional intraluminal tracer represented an orally administered tracer providing an anatomic reference of the affected bowel segment.

Methods

To prove and validate the registration of GI bleeding with MPI, fundamentals on data acquisition and image reconstruction are explained first. Then, a verification of the used tracers is laid out to verify their separability for multi-contrast MPI with a dilution series. Afterwards, the phantom construction process and phantom experiments are described. Finally, ex vivo porcine small bowel specimen measurements are specified, and experiments are performed in analogy to the phantom experiments.

The following four experiments were conducted on both phantoms and ex vivo porcine small bowel specimen.

- Single-contrast (blood pool tracer only), bowel intact (control)
- Single-contrast (blood pool tracer only), bowel perforated
- Multi-contrast, bowel intact (control)
- Multi-contrast, bowel perforated.

The purpose of control measurements was to demonstrate the absence of a bleeding, so any registered bleeding in a perforated bowel experiment could be attributed to the actual perforation of the phantom or bowel specimen.

Magnetic particle imaging

Visualization of the spatial distribution of SPIONs was performed on a pre-clinical MPI system (Bruker Biospin GmbH, Ettlingen, Germany) using a gradiometric x-receive coil with a bore diameter of 72 mm. The receive coil was connected to a custom developed receive chain that filters, amplifies, and samples the signal. The measurements were recorded with a gradient strength of $G = \mathrm{diag}(-0.75, -0.75, 1.5)$ T/m and drive field amplitudes $A_x = A_y = A_z = 12$ mT resulting in a field of view (FOV) of $32 \times 32 \times 16$ mm^3. The repetition time was 21.54 ms, resulting in the acquisition of 46 volumes per second. With the use of a custom online reconstruction software, the experiments were displayed in real-time to monitor the process and outcome of the measurements at the scanner[25]. The final image reconstructions were performed afterwards, where parameters were visually optimized to obtain the best results[26].

MPI image reconstruction

Multi-contrast reconstructions were performed using the iterative Kaczmarz method[27,28], yielding the particle concentrations $\boldsymbol{c}_1$ and $\boldsymbol{c}_2$ by solving the linear system of equations

$$\widehat{\boldsymbol{S}}\boldsymbol{c} = \begin{bmatrix} \widehat{\boldsymbol{S}}_1 & \widehat{\boldsymbol{S}}_2 \end{bmatrix} \begin{bmatrix} \boldsymbol{c}_1 \\ \boldsymbol{c}_2 \end{bmatrix} = \widehat{\boldsymbol{u}}_{\text{receive}},$$

where $\widehat{\boldsymbol{u}}_{\text{receive}} \in \mathbb{C}^K$ is the Fourier transform of the received voltage with K frequency components and $\widehat{\boldsymbol{S}}_i \in \mathbb{C}^{K \times N}$ for $i = 1, 2$ are the tracer specific system matrices in the frequency domain. The system matrices were acquired on a grid of $20 \times 20 \times 20$ voxels (voxel size $2 \times 2 \times 1$ mm^3) in phantom experiments and on a grid of $26 \times 26 \times 26$ voxels (voxel size $1.5 \times 1.5 \times 0.75$ mm^3) for the porcine small bowel specimens. This included an overscan of at least 2 voxels in all directions to reduce boundary artifacts[29]. In case of single-contrast reconstruction, only a single tracer is regarded and $\widehat{\boldsymbol{S}}_2, \boldsymbol{c}_2$ are neglected. For all reconstructions, the following least squares problem is solved

$$\boldsymbol{c}^{\lambda}_{\text{reco}} = \underset{\boldsymbol{c} \in \mathbb{R}^N_+}{\operatorname{argmin}} \|\widehat{\boldsymbol{S}}\boldsymbol{c} - \widehat{\boldsymbol{u}}_{\text{receive}}\|_2^2 + \lambda \|\boldsymbol{c}\|_2^2,$$

where $\|\widehat{\boldsymbol{S}}\boldsymbol{c}-\widehat{\boldsymbol{u}}_{\text{receive}}\|_2^2$ is the data discrepancy term and $\|\boldsymbol{c}\|_2^2$ is the penalization term that is utilized to dampen large oscillations in the solution. The solution of the concentration distribution $\boldsymbol{c}_{\text{reco}}^{\lambda}$ contains both concentration vectors $\boldsymbol{c}_1$ and $\boldsymbol{c}_2$ and is used to display the distributions in different colors. Therefore, voxels that contain signal from both tracers appear as a blend of these two colors. $\lambda\epsilon\mathbb{R}_+$ controls the relative regularization parameter that reduces the image noise at the cost of spatial resolution. The frequency selection, the parameter λ, and the number of iterations were adapted individually for each reconstruction to obtain best image results. However, parameters were identical for both tracers as the two system matrices constituted to a single minimization problem. For visualization purposes, images were averaged to a temporal resolution of 1.72 s (80 averages) to reduce noise.

Post-processing of MPI reconstructions

Post-processing techniques might be used to improve the visualization of tracer extravasation and consequently increase the sensitivity for bleeding detection. For single-contrast MPI, digital subtraction images were calculated by voxel-wise subtraction of signal intensities at two different timepoints (t_2-t_1). Consequently, only the temporal changes in signal intensities between both timepoints were visible. For multi-contrast MPI, overlay images highlighting a mixture of both tracers were reconstructed. Therefore, only voxels with signal intensities of both tracers above a defined threshold were displayed. The thresholds were visually determined to obtain the best delineation of the tracer mixture. Here, MPI at a single timepoint is sufficient to calculate this image.

Tracer separability for multi-contrast MPI

In this study, the tracer Perimag® (Micromod Partikeltechnologie GmbH, Rostock, Germany) was used as blood pool tracer and LS-008 (Lodespin Labs, Seattle, United States) was used as intestinal tracer. LS-008 is a single-core tracer with polyethylene glycol coating[30,31], whereas Perimag is a multi-core tracer with dextran coating[32]. To separate their signal contributions to the receive signal $\widehat{\boldsymbol{u}}_{\text{receive}}$, an image of a specimen was reconstructed using both system matrices to plot each tracer's intensity. Before actual experiments were performed, a dilution series was used to compare the signal contribution in known samples of different tracer compositions. Specimens of 100 µl were prepared at different volume ratios of both tracers, Perimag (at $c_{\text{Fe}}=266$ µg/ml (4.75 mmol/l)) and LS-008 (at $c_{\text{Fe}}=321$ µg/ml (5.75 mmol/l)). Concentrations were chosen to obtain similar peak signal intensities and to match the signal-to-noise ratio of both tracers which prevents signal dominance of one tracer over the other. Volume ratios of Perimag/LS-008 were set in 10% steps (100/0, 90/10, 80/20, …, 10/90, 0/100) to evaluate the channel leakage and tracer separability by their signal contributions after image reconstruction. Due to the underlying linear signal model of MPI[13], the signal intensity of each channel is expected to scale linearly from 0 to 100%.

3D-printed small bowel phantom experiments

Phantoms resembling a small bowel segment were 3D-printed using clear resin in a stereolithography printer (Form 3, Formlabs Inc., Somerville, USA). Coated with NanoSeal (NanoSeal LLC, Conroe, USA), the printed structures were hydrophobic and impermeable for liquids. The core structure of the phantom had the shape of an oval cylinder (Fig. 1a–d). The interior oval lumen measured 7.0 mm × 13.5 mm which is in the range of human small bowel[33]. The surrounding bowel wall was constructed with a hollow layer of 2.0 mm representing the vascular compartment in a perfused bowel wall. One phantom was created with a separation of the vascular and the luminal compartment and served as control (Phantom I, Fig. 1b). Another phantom was created with a perforation of 2.0 mm between both compartments representing the source of a bleeding (Phantom II, Fig. 1c). The luminal compartment was filled with water for single-contrast MPI and with a tracer suspension of LS-008 ($c_{\text{Fe}}=321$ µg/ml (5.75 mmol/l)) as intestinal tracer for multi-contrast MPI. During the experiments, the inlet and outlet of the lumen were sealed. The vascular compartment was accessible via an inlet and an outlet. Both inlet and outlet were connected to a water-filled circulatory system (total volume 15 ml) with a flow pump and a three-way valve enabling the injection of a blood pool tracer (Fig. 1e). The peristaltic flow pump was set to a flow rate of 93 ml/min. The phantoms were placed at the center of the MPI scanner by guidance of a small delta sample mounted on the phantoms. Phantoms were imaged dynamically in the MPI scanner to evaluate the exchange process between the vascular compartment and the lumen while a bolus of 1 ml Perimag ($c_{\text{Fe}}=850$ µg/ml (15.2 mmol/l)) was injected as the blood pool tracer.

The following experiments were conducted:

- Single-contrast (blood pool tracer only), bowel intact (phantom I)
- Single-contrast (blood pool tracer only), perforated bowel (phantom II)
- Multi-contrast, bowel intact (phantom I)
- Multi-contrast, perforated bowel (phantom II)

Porcine small bowel specimens and ex vivo experiments

In analogy to the four phantom experiments, similar ex vivo experiments for single- and multi-contrast MPI were performed using porcine small bowel specimens (Fig. 2a) of a female pig (German landrace, approx. 85 kg). The pig was euthanized at the University Medical Center Hamburg-Eppendorf within the scope of a different study approved by the national authority for animal protection (Behörde für Gesundheit und Verbraucherschutz, Hamburg, Germany). It conforms to the Guide for the Care and Use of Laboratory Animals, eighth edition, updated by the US National Research Council Committee in 2011 and was performed in accordance with the European Directive 2010/63 EU. The original approval does not address our experiments. Subsequent experiments on residual cadaver tissue are allowed without additional approval in Germany. To avoid further animal

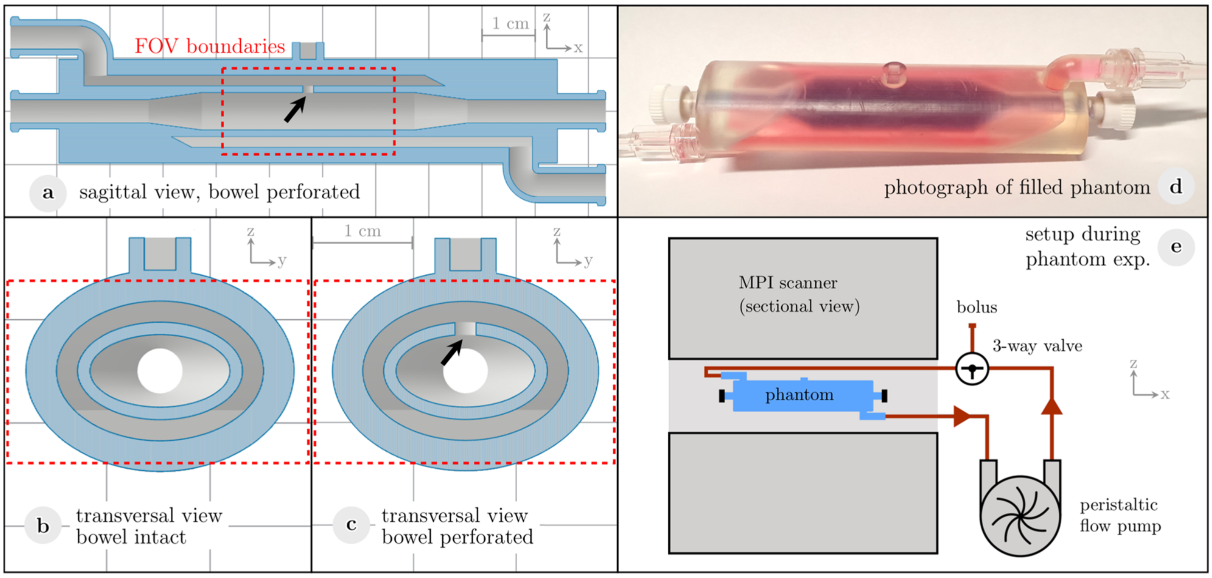

Figure 1. Phantoms of a small bowel segment. (**a**) Sectional view of the phantom illustrates the design of the small bowel phantom in a sagittal cross section consisting of an inner bowel lumen and an outer vascular compartment. The vascular compartment was accessible via an inlet and an outlet to enable the connection to a circulatory system. (**b**) The transversal cross section of the control phantom shows a separation of the vascular and the luminal compartment. (**c**) Another phantom was created with a perforation (arrow) between both compartments representing the source of a bleeding. (**d**) Photograph of a phantom with separated compartments, dyed for illustration (blue = bowel lumen, red = vascular compartment). (**e**) The phantoms were placed within the MPI scanner and the vascular compartment was connected to a circulatory system.

experiments, the residual cadaver tissue of the pig was used to prepare small bowel specimens. No animal was euthanized within the scope of this study. Small bowel specimens were prepared of a length of 3–4 cm including the adjacent mesenteric tissue. An incision in the mucous membrane of a length of 0.5 cm represented the source of a bleeding. Specimens with an intact mucous membrane served as control. Small bowel specimens were ligated at both ends and a mesenteric vessel was cannulated using a 24G catheter to enable the injection of a blood pool tracer (Fig. 2b). The bowel lumen was filled with water for single-contrast MPI and with a tracer suspension of LS-008 as intestinal tracer for multi-contrast MPI. The specimens were placed at the center of the MPI scanner and imaged dynamically in the MPI scanner to evaluate the exchange process between the vascular compartment and the lumen while a bolus of 1 ml Perimag was injected manually through the cannulated mesenteric vessel followed by slow injection of 1 ml water.

Results

Tracer separability

Image reconstructions using the MPI multi-contrast approach of 100 µl samples provided the signal intensities of different volume ratios of Perimag/LS-008 in equidistant 10% steps shown in Fig. 3. The multi-contrast reconstruction of 100% Perimag resulted only in a signal in the Perimag channel without relevant signal leakage to the LS-008 channel. A decreasing volume fraction of Perimag led to a strictly monotonically decreasing signal intensity of Perimag. At a volume ratio of 90% Perimag/10% LS-008, the LS-008 signal was not detectable. At higher concentrations of LS-008, an increasing volume fraction of LS-008 led to a strictly monotonically increasing signal intensity of LS-008. The multi-contrast reconstruction of 100% LS-008 resulted only in a signal in the LS-008 channel without signal leakage to the Perimag channel. A mixture of both tracers could be clearly determined at volume ratios between 80% Perimag/20% LS-008 and 10% Perimag/90% LS-008.

Phantom experiments

MPI enabled real-time 3D tracer visualization in all phantom experiments. The measured signal intensities of phantom experiments for the four different scenarios, intact bowel vs. perforated bowel using both single- and multi-contrast MPI, are shown in Fig. 4. A side-by-side comparison of single- and multi-contrast MPI of small bowel phantoms with an intact and a perforated bowel wall is shown in Supplementary Video S1. After injection at 10 s, the signal of the blood pool tracer increased within the bowel wall and reached a plateau phase in all experiments.

Single-contrast measurements with an intact bowel wall did not detect any tracer within the bowel lumen. Single-contrast measurements with a perforated bowel wall revealed a signal increase of the blood pool tracer within the bowel lumen after injection caused by extravasation of the tracer from the vascular to the luminal

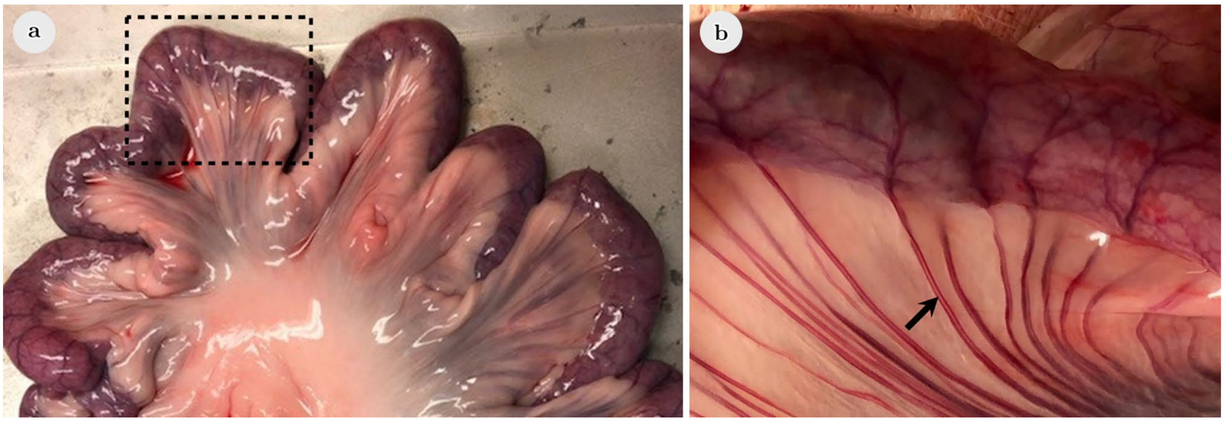

Figure 2. Photograph of porcine ex vivo small bowel specimen. (**a**) Porcine small bowel was used for preparation of small bowel specimen of 3–4 cm (rectangle). (**b**) An adjacent mesenteric vessel was cannulated to enable injection of the blood pool tracer (arrow).

compartment. The extravasation was observed immediately after bowel wall enhancement. Within the lumen, the signal intensity was higher at the bottom of the lumen due to sedimentation of the tracer.

Multi-contrast MPI enabled the visualization of the bowel lumen before injection of the blood pool tracer. After tracer injection to the intact bowel phantom, the signal of the intestinal tracer remained nearly constant without any detectable blood pool tracer within the bowel lumen. Multi-contrast MPI of the perforated bowel phantom revealed a co-registration of the signal of both vascular and intestinal tracer at the same location within the lumen. This leakage of the blood pool tracer with consecutive mixture of both tracers indicated GI bleeding. The mixture was observed immediately after bowel wall enhancement. The signal intensity of the intestinal tracer decreased overtime, being partially diluted by the inflowing blood pool tracer through the perforation.

Digital post-processing enabled a clear identification of GI bleeding in single- and multi-contrast MPI of small bowel phantoms (Fig. 5). Digital subtraction of reconstructed single-contrast images at $t_2 = 60$ s and immediately after bowel wall enhancement at $t_1 = 15$ s does not show a GI bleeding for the intact bowel wall. The perforated bowel wall led to a residual signal after digital subtraction indicating GI bleeding. For multi-contrast MPI, overlay of multi-contrast MPI-derived signal intensities above a defined threshold of both the intestinal tracer and the blood pool tracer clearly indicated GI bleeding only in case of a perforated bowel wall.

Small bowel ex vivo experiments

Single- and multi-contrast MPI enabled real-time 3D tracer visualization in ex vivo porcine small bowel specimens during tracer injection. The signal intensities of ex vivo small bowel measurements for the four different scenarios, intact bowel vs. perforated bowel using both single- and multi-contrast MPI, are shown in Fig. 6. After injection of the blood pool tracer, the signal increased partially within the bowel wall, but without enhancement of the entire circumference.

Single-contrast measurements with an intact mucous membrane did not detect any tracer within the bowel lumen. Single-contrast measurements after incision of the mucous membrane revealed a signal increase of the blood pool tracer within the bowel lumen after injection caused by extravasation of the tracer from the vascular to the luminal compartment. The extravasation was observed immediately after bowel wall enhancement. Similar

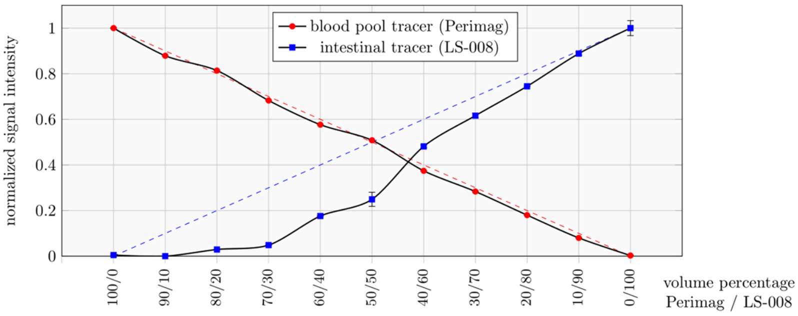

Figure 3. Multi-contrast MPI-derived signal intensities of different volume ratios of Perimag/LS-008 in equidistant 10% steps-contrast. MPI-derived signal intensity mean and variance of different volume ratios of Perimag/LS-008 in equidistant 10% steps obtained from 20 measurements (frames). Both curves are normalized with their maximum signal intensity and dashed lines indicate the expectation based on the linear MPI model.

to the corresponding phantom experiment, the signal intensity was higher at the bottom of the lumen due to sedimentation of the tracer.

Using a blood pool tracer and an intestinal tracer, multi-contrast MPI enabled the visualization of the bowel wall and the lumen. After injection of the blood pool tracer to the intact bowel segment, the signal increased partially within the bowel wall, but without enhancement of the entire circumference. The signal of the intestinal tracer remained nearly constant without a detectable signal increase of the blood pool tracer within the bowel lumen. Multi-contrast MPI after incision of the mucous membrane showed an extravasation of the blood pool tracer to the lumen with partial displacement of the intestinal tracer and mixture of both tracers. The mixture led to a co-registration of the signal of both blood pool tracer and intestinal tracer at the same location within the lumen. This leakage of the blood pool tracer with consecutive mixture of both tracers indicated GI bleeding. The mixture was observed immediately after bowel wall enhancement.

The subsequent injection of water led to a signal decrease of the bowel wall in two experiments (i.e., single-contrast MPI with incision of the mucous membrane and multi-contrast MPI with an intact bowel wall), indicating a washout of the blood pool tracer. For single-contrast MPI with an intact bowel wall and multi-contrast MPI with incision of the mucous membrane, parts of the blood pool tracer remained within the bowel wall.

Discussion

We successfully demonstrated the feasibility of MPI to detect gastrointestinal bleeding in a human-sized bowel in real-time. MPI enabled visualization of the tracer enhancing bowel wall in both 3D-printed bowel phantoms and ex vivo porcine bowel specimen. Accumulation of the blood pool tracer within the bowel lumen as an

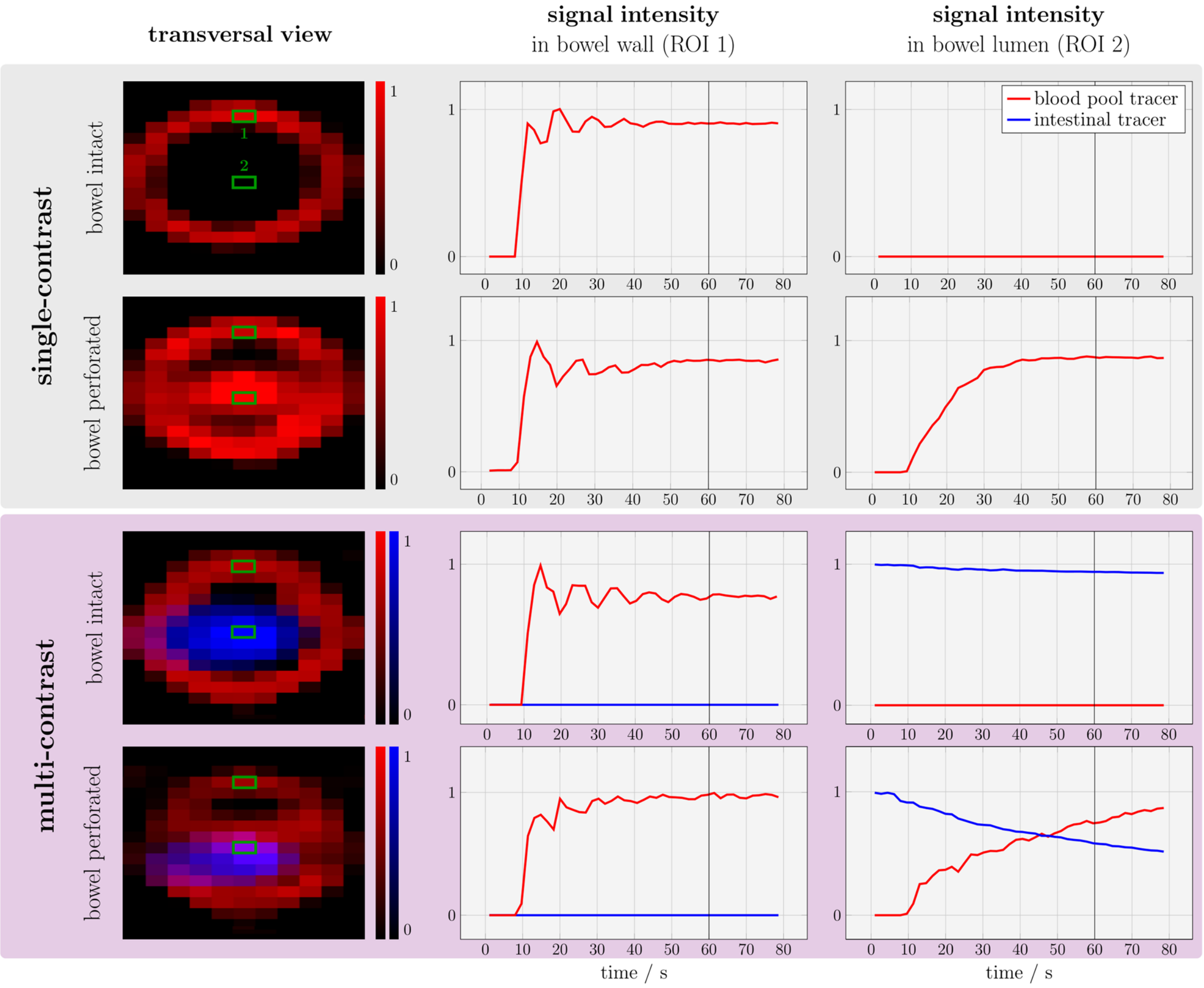

Figure 4. MPI of small bowel phantoms. Images on the left show MPI reconstructions at 60 s. MPI enabled visualization of the enhancing bowel wall after injection of the blood pool tracer (red). In case of multi-contrast MPI, the luminal compartment is visualized by the intestinal tracer (blue). A representative region of interest (ROI) in the bowel wall (ROI 1) and the lumen (ROI 2) was identified manually. A signal increase of the blood pool tracer within the bowel lumen was only observed in case of a perforation between the vascular and the luminal compartment and indicated GI bleeding. For multi-contrast MPI, leakage of the blood pool tracer led to co-registration of both tracers at the same location within the lumen and indicated GI bleeding.

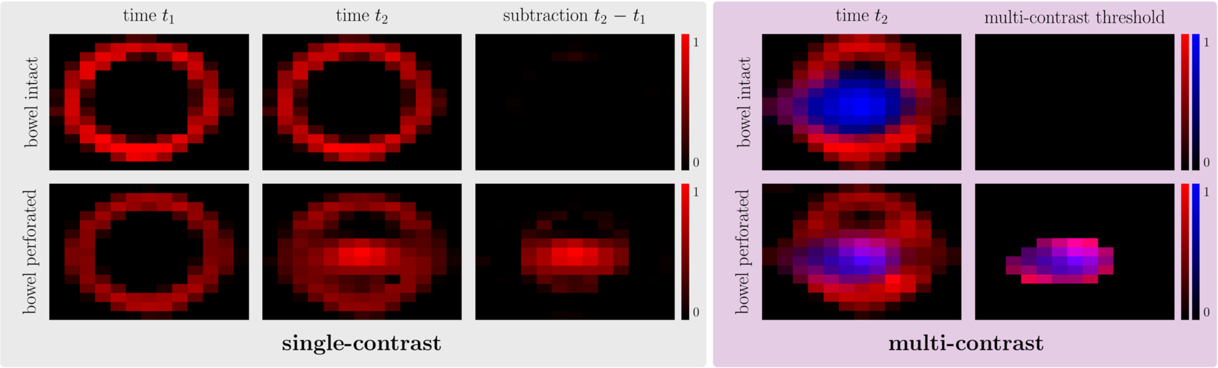

Figure 5. Post-processed single- and multi-contrast MPI of small bowel phantoms. Left: Digital subtraction of the reconstructed images at $t_2 = 60$ s and immediately after bowel wall enhancement at $t_1 = 15$ s. A GI bleeding was not detected for the intact bowel wall. The perforated bowel wall led to a residual signal after digital subtraction indicating GI bleeding. Right: Overlay of multi-contrast MPI-derived signal intensities above a defined threshold. The thresholds were visually determined to obtain the best delineation of the tracer mixture with the used setup and reconstruction parameters (threshold blood pool tracer: 28% of the maximum signal intensity; threshold intestinal tracer: 38% of the maximum signal intensity). Co-registration of both tracers at the same location was only observed in case of a perforated bowel wall and indicated GI bleeding.

indicator for GI bleeding was observed using single-contrast imaging. Multi-contrast MPI enabled detection of GI bleeding by co-registration of both tracers at the same location within the bowel lumen.

GI bleeding, as a potentially life-threatening condition, requires prompt clinical evaluation[1]. Therefore, a noninvasive technique for comprehensive real-time imaging of the entire GI tract is desirable. Esophagogastroduodenoscopy or colonoscopy might serve as initial modality to locate the bleeding source[8,9], but do not enable assessment of the entire GI tract. Further, endoscopic techniques might require bowel preparation and patient sedation[1]. Other techniques like CT and catheter angiography enable bleeding detection in the entire GI tract but require the use of ionizing radiation. MPI does not apply ionizing radiation and is therefore potentially safe for patients if applied magnetic fields stay within safety limits[12].

Similar to CT, tracer extravasation to the bowel lumen indicates GI bleeding. In our study, the detection of tracer extravasation was already possible after image reconstruction. In more complex cases, such as small GI bleedings, the additional use of post-processing techniques might enable a superior visualization of GI bleedings and consequently increase the sensitivity for bleeding detection. However, future studies need to prove a beneficial detection rate before implementation of these post-processing techniques.

Unfortunately, if an intravascular MPI tracer is cleared from the blood pool, single-contrast MPI does not provide an anatomical reference and allocation of tracer extravasation to a specific bowel segment is not possible. Here, the use of a long-circulating blood pool tracer might help to overcome this issue[34–37]. After reaching a steady state blood pool concentration of the tracer, a first MPI scan could provide the anatomical reference. A repeated MPI scan with subsequent image subtraction might enable visualization of tracer accumulation within the bowel lumen. Multi-contrast MPI with the use of a second, intestinal tracer is an alternative method to obtain an anatomical reference. After oral administration, MPI enables the detection of tracer-filled bowel. The mixture of both intestinal and blood pool tracer within the bowel lumen indicates GI bleeding. Here, GI bleeding detection might also be improved with a long-circulating blood pool tracer. In case of slow bleeding, MPI might be performed or repeated after a defined period of time when the amount of tracer extravasation is considered to be detectable. In case of an intermittent bleeding, MPI could be performed or repeated when bleeding is suspected to be active. Measurements can be repeated multiple times without the need of ionizing radiation. Thus, the sensitivity of GI bleeding detection might be improved with the multi-contrast approach.

All experiments were performed on a pre-clinical MPI system. This system enabled the investigation of a FOV encompassing small bowel phantoms in a human-sized scale or porcine small bowel segments. However, the basic principle of bleeding detection by extravasation of a blood pool tracer to the lumen applies to the entire GI tract. Therefore, MPI would enable bleeding detection within the entire GI tract including esophagus, stomach, colon and rectum if adequate MPI systems with a FOV encompassing the entire abdomen are developed for clinical applications[38].

With regard to limitations, motion-related artifacts (e.g. caused by bowel or patient movements) were not considered, since all experiments were performed on phantoms or ex vivo bowel specimen. These artifacts cause blurring in averaged images and consecutive reduction of image quality but might not have a major influence due to the high temporal resolution of MPI. However, bleeding detection by post-processing techniques using images of more than one timepoint (i.e. digital subtraction) will be impaired due to bowel or patient movement. Here, multi-contrast MPI has the advantage to enable co-registration of a blood pool tracer and an intraluminal tracer within the bowel lumen at a single timepoint and has a higher robustness against such motion-related artifacts.

Tracer separability was confirmed by a dilution series to demonstrate that multi-contrast MPI enabled co-registration of two tracers in the same voxel. This feature was used to detect extravasation of the blood pool tracer to the lumen with consecutive mixture with the intestinal tracer. Depending on the voxel size, partial

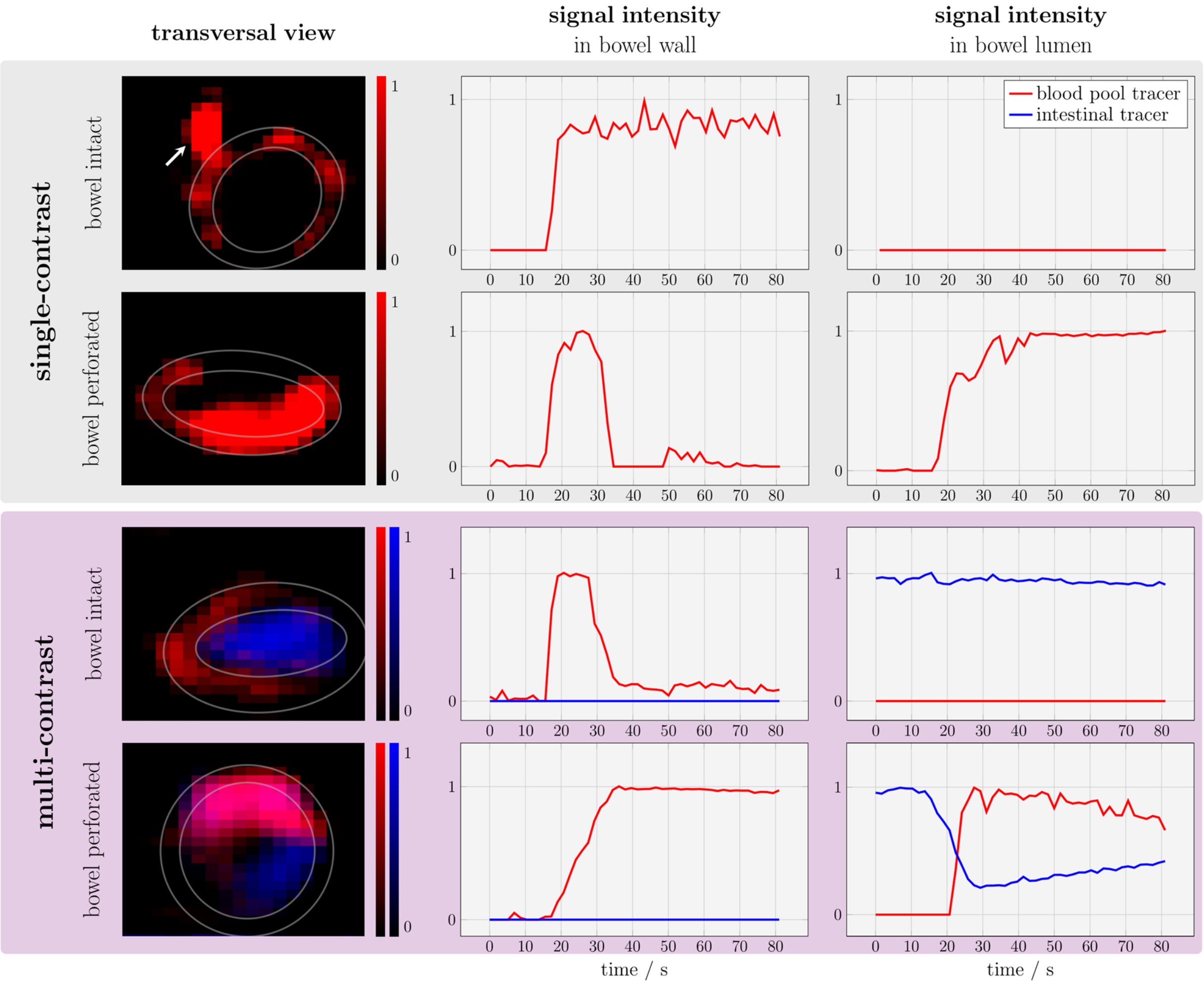

Figure 6. MPI of ex vivo porcine small bowel specimen. These experiments were conducted in analogy to phantom experiments. Single contrast MPI enabled visualization of the enhancing bowel wall after bolus injection. Note the enhancement of the feeding vessel for this bowel segment (arrow). A signal increase of the blood pool tracer within the bowel lumen was only detected after incision in the mucous membrane. In multi-contrast MPI, co-registration of both tracers at the same location in the lumen represented the mixture of tracers and indicated GI bleeding.

volume effects at the border of the lumen to the bowel wall might occur and imitate a mixture of both tracers. Such partial volume effects have not been investigated in this feasibility study.

Experiments were performed on porcine ex vivo small bowel specimen. After injection of the blood pool tracer, only parts of the bowel wall enhanced. A possible explanation for this phenomenon might be an occlusion of capillaries during specimen preparation. Here, future in vivo studies will potentially observe a more uniform bowel wall enhancement.

In conclusion, MPI enables the visualization of tracer enhancement of the bowel wall in bowel phantoms and ex vivo porcine bowel specimen. Further, both single- and multi-contrast MPI enable the detection of a GI bleeding. Therefore, MPI might emerge as a useful tool for noninvasive, radiation-free detection of acute and chronic GI bleeding if adequate MPI systems for clinical use are developed and suitable MPI tracers are approved.

Data availability

The datasets generated during and/or analyzed during the current study are available from the corresponding author on reasonable request.

Received: 30 April 2023; Accepted: 14 December 2023

References

1. Kim, G., Soto, J. A. & Morrison, T. Radiologic assessment of gastrointestinal bleeding. *Gastroenterol. Clin. N. Am.* **47**, 501–514 (2018).

2. Raju, G. S., Gerson, L., Das, A. & Lewis, B. American Gastroenterological Association (AGA) Institute medical position statement on obscure gastrointestinal bleeding. *Gastroenterology* **133**, 1694–1696 (2007).
3. Wuerth, B. A. & Rockey, D. C. Changing epidemiology of upper gastrointestinal hemorrhage in the last decade: A nationwide analysis. *Digest. Diseases Sci.* **63**, 1286–1293 (2018).
4. Gerson, L. B., Fidler, J. L., Cave, D. R. & Leighton, J. A. ACG clinical guideline: diagnosis and management of small bowel bleeding. *Am. J. Gastroenterol.* **110**, 1265–1287 (2015) (**quiz 1288**).
5. Van de Bruaene, C., Hindryckx, P., Van de Bruaene, L. & De Looze, D. Bleeding lesion of the small bowel: An extensive update leaving no stone unturned. *Curr. Gastroenterol. Rep.* **20**, 5 (2018).
6. Gunjan, D., Sharma, V., Rana, S. S. & Bhasin, D. K. Small bowel bleeding: A comprehensive review. *Gastroenterol. Rep.* **2**, 262–275 (2014).
7. Gralnek, I. M., Neeman, Z. & Strate, L. L. Acute lower gastrointestinal bleeding. *N. Engl. J. Med.* **376**, 1054–1063 (2017).
8. Ghassemi, K. A. & Jensen, D. M. Lower GI bleeding: Epidemiology and management. *Curr. Gastroenterol. Rep.* **15**, 333 (2013).
9. Lau, L. H. S. & Sung, J. J. Y. Treatment of upper gastrointestinal bleeding in 2020: New techniques and outcomes. *Digest. Endosc.* **33**, 83–94 (2021).
10. Wells, M. L. *et al.* CT for evaluation of acute gastrointestinal bleeding. *Radiogr. Rev. Publ. Radiol. Soc. N. Am. Inc.* **38**, 1089–1107 (2018).
11. Naut, E. R. The approach to occult gastrointestinal bleed. *Med. Clin. N. Am.* **100**, 1047–1056 (2016).
12. Knopp, T., Gdaniec, N. & Moddel, M. Magnetic particle imaging: from proof of principle to preclinical applications. *Phys. Med. Biol.* **62**, R124–R178 (2017).
13. Gleich, B. & Weizenecker, J. Tomographic imaging using the nonlinear response of magnetic particles. *Nature* **435**, 1214–1217 (2005).
14. Kaul, M. G. *et al.* Magnetic particle imaging for in vivo blood flow velocity measurements in mice. *Phys. Med. Biol.* **63**, 064001 (2018).
15. Kaul, M. G. *et al.* Pulmonary blood volume estimation in mice by magnetic particle imaging and magnetic resonance imaging. *Sci. Rep.* **11**, 4848 (2021).
16. Graeser, M. *et al.* Human-sized magnetic particle imaging for brain applications. *Nat. Commun.* **10**, 1936 (2019).
17. Molwitz, I. *et al.* First magnetic particle imaging angiography in human-sized organs by employing a multimodal ex vivo pig kidney perfusion system. *Physiol. Meas.* **40**, 105002 (2019).
18. Weller, D. *et al.* Combining direct 3D volume rendering and magnetic particle imaging to advance radiation-free real-time 3D guidance of vascular interventions. *Cardiovasc. Intervent. Radiol.* **43**, 322–330 (2020).
19. Salamon, J. *et al.* Magnetic particle/magnetic resonance imaging: In-vitro MPI-guided real time catheter tracking and 4D angioplasty using a road map and blood pool tracer approach. *PloS One* **11**, e0156899 (2016).
20. Yu, E. Y. *et al.* Magnetic particle imaging for highly sensitive, quantitative, and safe in vivo gut bleed detection in a murine model. *ACS Nano* **11**, 12067–12076 (2017).
21. Rahmer, J., Halkola, A., Gleich, B., Schmale, I. & Borgert, J. First experimental evidence of the feasibility of multi-color magnetic particle imaging. *Phys. Med. Biol.* **60**, 1775–1791 (2015).
22. Szwargulski, P. *et al.* monitoring intracranial cerebral hemorrhage using multicontrast real-time magnetic particle imaging. *ACS Nano* **14**, 13913–13923 (2020).
23. Salamon, J. *et al.* Visualization of spatial and temporal temperature distributions with magnetic particle imaging for liver tumor ablation therapy. *Sci. Rep.* **10**, 7480 (2020).
24. Möddel, M., Meins, C., Dieckhoff, J. & Knopp, T. Viscosity quantification using multi-contrast magnetic particle imaging. *N. J. Phys.* **20**, 083001 (2018).
25. Knopp, T. & Hofmann, M. Online reconstruction of 3D magnetic particle imaging data. *Phys. Med. Biol.* **61**, N257-267 (2016).
26. Knopp, T. *et al.* MPIReco.jl: Julia package for image reconstruction in MPI. *Int. J. Mag. Part. Imag.* **5**, 1907001 (2019).
27. Kaczmarz, S. Angenäherte Auflösung von Systemen linearer Gleichungen. *Bull. Int. Acad. Polonica Sci. Lett.* **A 35**, 355–357 (1937).
28. Knopp, T. *et al.* Weighted iterative reconstruction for magnetic particle imaging. *Phys. Med. Biol.* **55**, 1577–1589 (2010).
29. Weber, A., Werner, F., Weizenecker, J., Buzug, T. M. & Knopp, T. Artifact free reconstruction with the system matrix approach by overscanning the field-free-point trajectory in magnetic particle imaging. *Phys. Med. Biol.* **61**, 475–487 (2016).
30. Khandhar, A. P., Ferguson, R. M., Arami, H., Kemp, S. J. & Krishnan, K. M. Tuning surface coatings of optimized magnetite nanoparticle tracers for in vivo Magnetic Particle Imaging. *IEEE Trans. Magn.* **51**, 1–4 (2015).
31. Ferguson, R. M. *et al.* Magnetic particle imaging with tailored iron oxide nanoparticle tracers. *IEEE Trans. Med. Imag.* **34**, 1077–1084 (2015).
32. Eberbeck, D. *et al.* Multicore magnetic nanoparticles for magnetic particle imaging. *IEEE Trans. Magnet.* **49**, 269–274 (2013).
33. Cronin, C. G., Delappe, E., Lohan, D. G., Roche, C. & Murphy, J. M. Normal small bowel wall characteristics on MR enterography. *Eur. J. Radiol.* **75**, 207–211 (2010).
34. Rahmer, J. *et al.* Nanoparticle encapsulation in red blood cells enables blood-pool magnetic particle imaging hours after injection. *Phys. Med. Biol.* **58**, 3965–3977 (2013).
35. Kaul, M. G. *et al.* In vitro and in vivo comparison of a tailored magnetic particle imaging blood pool tracer with Resovist. *Phys. Med. Biol.* **62**, 3454–3469 (2017).
36. Kratz, H. *et al.* Tailored magnetic multicore nanoparticles for use as blood pool MPI tracers. *Nanomaterials (Basel)* **11**, 1532 (2021).
37. Liu, S. *et al.* Long circulating tracer tailored for magnetic particle imaging. *Nanotheranostics* **5**, 348–361 (2021).
38. Rahmer, J., Stehning, C. & Gleich, B. Remote magnetic actuation using a clinical scale system. *PloS One* **13**, e0193546 (2018).

Acknowledgements

The authors would like to thank Florian Sevecke for his assistance during the 3D-printing procedure. The authors thank Dr. Aline Reitmeier for providing the porcine bowel specimen.

Author contributions

M.G., T.K., G.A., J.S., and C.R. designed the study. F.M., P.S., M.G., K.M.K., T.K., and C.R. established the methodology. F.M., P.S., T.M., and C.R. performed sample preparation and data acquisition. F.M., P.S., M.G.K., J.S., and C.R. analyzed and interpreted the data. F.M. and C.R. drafted the manuscript. All authors revised the manuscript and approved the final version.

Funding

Open Access funding enabled and organized by Projekt DEAL. This work was supported by the German Research Foundation (DFG), Collaborative Research Center 841, Project SP1. We acknowledge financial support from the Open Access Publication Fund of UKE - Universitätsklinikum Hamburg-Eppendorf and DFG – German Research Foundation.

Competing interests

The authors declare no competing interests.

Additional information

Supplementary Information The online version contains supplementary material available at https://doi.org/10.1038/s41598-023-50041-3.

Correspondence and requests for materials should be addressed to C.R.

11

Discussion and Outlook

11.1 Conclusion

Medical imaging is a vital component of contemporary healthcare, providing invaluable guidance for interventions and establishing diagnoses. Its advancement is contingent upon the concurrent evolution of both applications and instrumentation, which must be integrated with the existing workflow of medical personnel. This thesis considered key aspects of both, application and instrumentation utilized in Magnetic Particle Spectroscopy and Magnetic Particle Imaging. The objective was to address challenges related to hardware, sequence emulation, image quality improvement, fast 3D imaging, patient safety, and also to find application-specific optimizations.

In order to facilitate future human MPI trials, a safe, human-sized 3D head scanner was refined and developed for diagnostic purposes, including fast cerebral imaging to calculate perfusion maps [O2, O3]. Continuing in the field of neurology, our research efforts have focused on two key areas: the investigation of suitable MPI tracers that are approved for human injection [O4] an on the development of negative contrast perfusion imaging to reduce the total tracer uptake [O5]. By leveraging the advantage of long-circulating MNPs, we demonstrated that excellent negative imaging contrast can be achieved by administering a saline bolus. This approach enables the long-term monitoring of patients with conditions such as ischemic stroke or intracerebral hemorrhage, which are major causes of mortality and morbidity. With the aim of gaining insight into arbitrary waveform sequences, including their instrumentation, calibration, and performance, we developed an arbitrary waveform MPS, which can be used for an MPI scanner emulation. Our approach, as outlined in [O1], builds upon the concept of pulsed excitation, which was introduced in 2019 [269] and differs from the hitherto vision of most MPI scanner designs. A versatile, custom software framework was developed and used to emulate multiple sequences for different types of scanners [O17] and we measured particle dynamics in various pulsed excitation fields to compare their system matrix reconstruction results [O1].

11.2 Discussion

The major part of this work contributes to the research fields of instrumentation and signal encoding in MPI, as indicated in Figure 4.1, which is also the focus of this discussion.

System Matrix Reconstruction for Pulsed Sequences. The approach in chapter 5 used real particle measurements with different offsets to generate a 2D sequence based on concatenating different subsets of the data, adding realistic system noise, and avoiding inverse crime during reconstruction by using different measurement grids for offsets. This is a versatile approach that allows a moving sequence to be emulated based on measured arbitrary waveform data that can be adapted to different topologies. The device was also used for MNP spectroscopy with arbitrary waveforms and offsets in two orthogonal directions, to analyze relaxation behavior, different PSFs and harmonic content. However, the step of analyzing different particle core sizes as described by Tay et al. [269], which we hypothesized would no longer provide sufficient phase information at high slew rates, was not investigated further. Instead of losing information due to concurrent relaxation, the particle system we measured (Perimag) provided sufficient phase information due to its rapid relaxation and ability to follow the excitation. In preparation for this analysis, we have tried to apply the idea of a Radon-based reconstruction approach, similar to an FFL [129], which recovers lost phase information by rotating the excitation direction, hence the development and focus on a shift-radial sequence in [O1]. Although the conceptual validation of the approach using Perimag was successful, we did not proceed with measurements of larger single-core MNPs as planned. Thus, the hypothesis of loss of phase information for large particles could not yet be confirmed, only the opposite for Perimag, as shown in Figure 4.3, which provides sufficient phase information for reconstruction using µs slew-rates [O8]. Due to its small core size [52], this ability to follow high slew rates was expected, because of its Néel-dominated relaxation [317]. For the arbitrary waveform MPS, it was not possible to increase the slew rate any further due to amplifier performance limitations in combination with the load inductance and power dissipation of the drive-field coil. Especially for long sequences with fine offset grids and large amplitude, detuning due to thermal drift was a problem. A follow-up of this original idea was discontinued after the publication of the conceptual validation with Perimag in [O1], although measurements of different single-core particles were partially performed but not fully evaluated.

Although we restricted our research in chapter 5 to a 2D plane and 1D excitation, the approach of using arbitrary excitation and offset signals can be translated to a 3D volume. 3D MPS devices with sinusoidal excitation exist [42, 294, 296], but not yet for arbitrary excitation, which is currently under construction at the Fraunhofer IMTE, Lübeck, Germany [234]. A device with such measuring capabilities can be used to measure the dynamic and saturation regions of MNPs with a large overscan and an arbitrary excitation vector. This dataset can then be cropped and concatenated in an analog fashion to our approach in [O1], to fully mimic the movement of a 3D time sequence without building the required selection and drive field coils. Continued development of the software framework by other groups lead to its adaptation for FFL trajectory simulations [O17]. The calibration and optimization of the slew-rate inspired an optimized amplifier voltage mode model [O12].

Other aspects that could be investigated with an arbitrary waveform or pulsed MPS include multi-contrast separability and channel leakage reduction for two or more MNPs [191, 192]. Multi-contrast system matrix reconstructions may be improved when MNPs are excited with both a sinusoidal and a pulsed waveform, each of which captures different relaxation processes that produce different spectral fingerprints. However, the improvement of such reconstructions is difficult to determine: First, a metric for channel leakage, separability, and resolution must be defined, which strongly depends on the implemented solver [O16, 191]. The use of masks for channel leakage classification requires the definition of parameters for weighting or edge sharpness. Second, once a set of meaningful metrics, a suitable noise floor, reconstruction parameters (grid search), and a solver is chosen, the question of computational time or number of iterations required does not allow clear statements about performance. For example, if a pulsed excitation with a very broad spectrum requires fewer iterations than a narrower sinusoidal spectrum, each iteration may contain a very large number of frequency components due to the high SNR, resulting in a longer overall computation time. For sinusoidal excitations, more iterations performed in the same time may yield reconstruction results of identical quality. In turn, the computational time depends, among other things, on the processor power, the number of kernels, the code implementation, and the way the inverse problem is posed. Third, the choice of emulated acquisition sequence for a 2D reconstruction, such as meandering or radial, also has a significant impact on the resolution and shape of edges, artifacts, and the object being resolved. As a result, statements about multi-contrast using pulsed vs. sinusoidal waveforms are narrowly focused on specific system parameters and metrics, making a general prediction of improvement very difficult. However, its general feasibility can be postulated by the difference in spectral fingerprints that are visible in the spectra of pulsed and sinusoidal MPS measurements [O1].

The deployment of the pulsed MPS also included arbitrary waveform spectroscopy with and without DC offsets. Using a TF calibration [276], the hysteresis curve in the domain of the net magnet moment of the particles was determined [O4]. Using offsets along the excitation direction, a static PSF was calculated [163, 268], as for example required for Cartesian reconstructions based on a time-domain convolution with a suitable kernel, like x-space MPI (see Figure 2.5). The versatility of the pulsed MPS as a spectrometer was used in chapter 8, where four different MNPs were measured and compared [O4]. The device was cross-validated by measuring the same MNP sample at identical sinusoidal excitation with a standard resonant MPS without offsets [O19] that was developed, calibrated, and described in [276].

Human-sized 3D Head Scanner with Inductive Coupling Network. Beyond the scope of the detailed discussion of imaging capabilities, device safety and hardware implementation in chapter 7 [O3], this section addresses the remaining steps toward clinical trials and unmentioned issues that affect both the ICN and the head scanner in hindsight.

Verification of the MPI system before conducting human trials should include PNS testing, tracer approval for the desired deployment, electrical verification by a third party, and agreement of the local ethics committee regarding human volunteers. Part of the documentation laid before the ethics committee should contain a thorough risk assessment table, device description, study description, clear assignment of roles and responsibilities, as well as a checklist to show conformity with the general safety and performance requirements (GSPR) set out in Annex I of regulation (EU) 2017/745 on medical devices. The electrical verification concerns discharge-, contact-, and earth-currents, dielectric strength, insulation, and mechanical impact resistance of the DFG. Next to the approval of an MNP injection, a reasonable expected resolution should be shown for the selected application, to emphasize suitability [O2, O3]. PNS tests can be carried out based on thresholds determined in [200, 230], however, these results do not included a 2D excitation in the 26 kHz region. It stands to reason that a combination of both fields will reduce the applicable threshold further [243], and the fields should be ramped up carefully. Also, the PNS threshold for extremities such as the arm or leg depends on the orientation of the nerves with respect to the $\boldsymbol{B}$ field and is not transferable to the human head, which has very different values for ϵ and σ, making it more sensitive to stimulation [1].

Initial design goals of the ICN included the reduction of complexity of the receive chain, reducing power consumption by saving space and providing a receive channel in z-direction. Although the ICN was successfully designed and implemented, it failed to reduce the complexity of the receive chain, which still required an f_1 filter. The ICN rather increased the complexity and design process of the transmit chain, as well as the power consumption. It should be noted, that the increased power consumption was mainly due to the low inductance design with a high-current DFG as listed in Table 4.1, which was intentional to increase safety, and a complete duplicate compensation system would require even more power [177]. Therefore, a comparison of power consumption between the two versions is misleading. The additional increase in power consumption for this DFG and the signal trade-off from the ICN became apparent after the ICN was completed and commissioned [O11]. For best signal quality, a dedicated receive coil was nested inside the DFG, as the TxRx signal quality was inferior and had a high harmonic content. A dedicated z-receive coil was difficult to design, as argued in subsection 4.1.2, but the expected improvement in spatial resolution in the range of 12 to 22 % [260] would be worth investigating further. As a gradiometer coil can adapt to changes during image acquisition, they provide dynamic background compensation and are known to suppress interference [77, 119].

Nevertheless, the implementation of the ICN in chapter 6 and the redesign of the head scanner in chapter 7 were successful, the overall device safety strongly increased, 3D imaging capabilities at high spatiotemporal resolution achieved, and a roadmap to clinical trials presented.

Applications in MPI and Conclusion. In the context of the above statement, several common objectives link the application part of this thesis to the instrumentation part via perfusion imaging. These include the focus of the characterization study on the Ferucarbotran-based tracer Resotran of chapter 8, which was central to all experiments in chapter 7, and the optimization of cerebral perfusion imaging for specific scenarios in chapter 9. Here, the monitoring of a stroke patient could potentially include the presented head scanner as a future rapid diagnostic tool in the ICU. This allows for the following illustration of contributions within this thesis: The ultimate goal of perfusion imaging in the ICU is enabled by the head scanner [O2, O3] and optimized by iron dose reduction and a long-circulating tracer [O5]. The intermediate and necessary step of clinical evaluation and trials on humans is based on the well-studied Ferucarbotran [O4] that is next to Gadolinium-based agents [107] one of the best understood MNPs in human metabolism with a low reported number of incidence of adverse events [299].

11.3 Challenges for MPI

MPI has numerous advantages if introduced into clinical practice as a medical imaging modality, demonstrated in the introduction in Table 1.1. Its predicted spatial resolution, high temporal resolution, linear quantification, and background-free acquisition without tissue attenuation are unique features. However, the underlying physics of its successful implementation are complex, and some issues have persisted since its invention 20 years ago. One of these issues include the correlation of spatial resolution, gradient, sensitivity and FOV size. A high gradient is desired for a high spatial selectivity, to minimize the responsive FFR, which increases resolution. However, this also reduces the strength of the signal response, because a smaller volume of MNPs is excited and flipped. Furthermore, the FOV size is decreased by a high gradient for a constant drive field strength, which is determined by the ratio of drive field to gradient as explained in section 2.3. When an FFL is employed instead of an FFP, the number of concurrently responding particles is augmented [310], relaxing restraints on one constituent of the above correlation at the cost of more complex sequence encoding and reconstruction. Although the origin of the dilemma is well documented, it cannot be entirely resolved [70, 130]. One approach is the use of multi-patch sequences to increase the overall FOV size [33, 70, 210, 261] at constant high resolution. The entire FFR is thus shifted by slow offset-fields and concatenated to increase the overall FOV within the scanner bore. Again, large focus field shifts and more complex sequences tend to require more power, which can also become a bottleneck for instrumentation because space and infrastructure are limited or require more money. Power consumption can be reduced by utilizing permanent magnets, as seen in Halbach configuration [16, 303] for the selection field that can also used to shift the FFR [3, 184].

One large issue for MPI is PNS, as elaborated above in section 11.2, which limits the usable drive-field strength significantly [230]. Approaches to increase the drive frequency promise higher PNS thresholds [109, 242], but other instrumentation-related problems are encountered concerning increased losses in hardware components, required bandwidth and background signals [35, 242]. Although sensation of PNS is unpleasant and should be avoided, the range between barely perceptible and clearly noticeable could be exploited, before the sensation becomes unpleasant [243], especially due to large ranges of individual perception. Homogeneous regions, at further distance to the DFG are expected to have higher thresholds [243]. Small scale pre-clinical devices and regional application tend to have a higher PNS threshold compared to full torso systems [229, 243]. It should be noted, that the applied field direction is correlated to the sensation and depends on nerve and tissue alignment and composition [1, 263].

Other challenges include the mitigation of noise and background signals [272, 308]. Noise may appear in different categories, such as coil noise (thermal), patient noise [240], random noise, background noise (short-, mid-, and long-term regime), distortions [203, 240] and image noise [50, 257, 308]. LNA noise matching is required [328] and improves the detection threshold significantly [78]. Remedies against random noise are limited and a careful analysis of sources is required, however systematic occurrences in the background are often mitigated using empty measurements, either before and/or after the particle measurement [131, 143]. Although background subtraction is effective, it is not a substitute for feedthrough compensation due to the limited dynamic range of the LNA and the superior signal quality if passive and/or active compensation is applied [77, 202]. In particular, the gradiometer coil has demonstrated its utility by pushing limits for sensitivity [78] and due to its adaptability to changes during ongoing measurements [77, 204, 207]. The concept of TxRx systems has difficulties due to the increased amount of noise sources by (partly) sharing transmit and receive chains [203, 231, O3] and loss in signal strength [O11]. Concerning image noise, the regularization technique and implemented solver have a large influence on the trade-off between spatial resolution, edge drop-off, and graininess of the image [50, O16, 190, 279].

In order to address the issue of lengthy calibration times associated with measurement-based approaches [135] for system matrix reconstructions, a number of methods have been developed to facilitate and speed up the system matrix acquisition. These include sparse reconstructions like compressed sensing [83–85, 150, 295, 301], using hybrid reconstructions [265, 294, 297] by utilizing a 3D MPS [296], or model-based and learning-based approaches [8, 126]. Especially the combination of model-based and learning-based approaches show high potential [139].

A final major challenge is the approval of an MPI-tailored clinical tracer [O4] and more insight on the long-term toxicity and metabolisation of MNPs [27, 250, 307, 316]. To reach the full potential of MPI, several tracers suited for different purposes such as 1D excitations [271], long- and short-circulation [10], multi-contrast imaging (high separability), or hyperthermia actuation are desirable. With suited and available instrumentation, the costly process of tracer approval might soon become remunerating for large institutions or companies. This would in turn increase the usability of clinical MPI due to the improvement in resolution, sensitivity, and variety of approved tailored MNPs.

11.4 Outlook

As the number of obstacles to the use of MPI in medical imaging is gradually overcome by recent research, the applicability and versatility of MNP-based diagnostic and therapeutic tools is becoming increasingly evident [95]. The persistence of many research institutions and companies to develop and enhance new and existing fields, as evidenced by the overview of Figure 4.1, is a constant driver despite the fact that clinical integration has not yet commenced [95, 201]. One possible step towards this goal is the combination of existing devices, such as low-field MRI systems [124, 181], which are already in clinical practice with our proposed head-sized scanner [O3]. As a combined tool for cerebral applications directly at the bedside, the benefit would be great for staff and patients, minimizing the transport and increasing monitoring time with a low-cost transportable system. MRI reference scans provide the anatomical information, while MPI perfusion imaging yields dynamic data with high temporal and spatial resolution, which are both feasible at the bedside [20]. Such devices can be designed efficiently to share most pieces of system hardware [63, 290] and thus bridge the gap for a clinical transition of MPI. In a similar manner, the introduction of devices capable of targeted hyperthermia have a high potential to successfully bridge the gap into clinical practice [37].

The implementation of neural networks is on a trajectory where these will quickly gain a larger role in MPI by reducing calibration times [139], denoising [88], improving regularization [O16, 279], reconstructing images with deep image priors [50], augmenting data and reducing artifacts [21, 298].

Concerning future instrumentation, active cancellation is a research field with a lot of potential to increase signal quality and reduce interference, before signal conversion at the ADC stage [106, 264, 330]. Recent developments show that a combination of active and passive feedthrough compensation [202, 321] is a promising approach, which could pose a new strategy to implement the missing z-receive channel in our system presented in [O3]. Immediate steps of the roadmap towards human MPI trials include the full documentation, risk assessment, PNS tests, a study design and ethics approval.

Acknowledgments

Language tools were used in the preparation of this dissertation. In particular, DeepL Write (DeepL SE, Cologne, Germany) was of great help for enhancing linguistic accuracy and dict.cc (dict.cc GmbH, Vienna, Austria) as a German-English dictionary. These tools were employed solely for the refinement of language and did not influence the content or the original research presented in this thesis.

Major thanks goes to all my colleagues, present and former, at the Institute of Biomedical Imaging at TUHH/UKE and and their support over the last 4 years. Without our team, not a single paper would have been published and I could not have grown professionally in this way. I can only admire their unwavering support and tenacity to investigate open questions and the huge investment of time and patience within the team. I would like to extend these thanks to all my other co-authors, who helped me with prompt and accurate answers to all my inquires and gladly shared their experience and knowledge in their fields. In addition, I would like to thank the invisible people in the background who helped in many non-academic ways, such as our technician Florian Sevecke or those who provided infallible IT support at all hours to get 3D printers, machines and measurements up and running.

My gratitude is also directed towards several long-term mentors, who have supported me since my bachelor and master thesis at Philips Research Hamburg, always ready to answer basic and though questions. To name just one, Christian Findeklee has given me many insights and refreshed my memory countless times on all topics of electrical engineering. Thank you Tobias Knopp for the close supervision, your readiness to jump at every request in coding, and the opportunity to work in your team. I am very thankful to a whole bunch of other people in my life who, for various reasons, will never read this work, and likewise writing down their names cannot even remotely express my full gratitude and appreciation towards them and their support.

Bibliography

Original works

[O1] F. Mohn, T. Knopp, M. Boberg, F. Thieben, P. Szwargulski, and M. Graeser. "System Matrix Based Reconstruction for Pulsed Sequences in Magnetic Particle Imaging". *IEEE Transactions on Medical Imaging* 41.7 (July 2022), pp. 1862–1873. DOI: 10.1109/TMI.2022.3149583.

[O2] F. Mohn, F. Förger, F. Thieben, M. Möddel, I. Schmale, T. Knopp, and M. Graeser. "Resonant Inductive Coupling Network for Human-Sized Magnetic Particle Imaging". *Review of Scientific Instruments* 95.4 (Apr. 2024), p. 044701. DOI: 10.1063/5.0192784.

[O3] F. Thieben, F. Foerger, F. Mohn, N. Hackelberg, M. Boberg, J.-P. Scheel, M. Möddel, M. Graeser, and T. Knopp. "System Characterization of a Human-Sized 3D Real-Time Magnetic Particle Imaging Scanner for Cerebral Applications". *Communications Engineering* 3.1 (Mar. 2024), p. 47. DOI: 10.1038/s44172-024-00192-6.

[O4] F. Mohn, K. Scheffler, J. Ackers, A. Weimer, F. Wegner, F. Thieben, M. Ahlborg, P. Vogel, M. Graeser, and T. Knopp. "Characterization of the Clinically Approved MRI Tracer Resotran for Magnetic Particle Imaging in a Comparison Study". *Physics in Medicine & Biology* 69.13 (July 2024), p. 135014. DOI: 10.1088/1361-6560/ad5828.

[O5] F. Mohn, M. Exner, P. Szwargulski, M. Möddel, T. Knopp, and M. Graeser. "Saline Bolus for Negative Contrast Perfusion Imaging in Magnetic Particle Imaging". *Physics in Medicine & Biology* 68.17 (Sept. 2023), p. 175026. DOI: 10.1088/1361-6560/ace309.

[O6] F. Mohn, P. Szwargulski, M. G. Kaul, M. Graeser, T. Mummert, K. M. Krishnan, T. Knopp, G. Adam, J. Salamon, and C. Riedel. "Real-Time Multi-Contrast Magnetic Particle Imaging for the Detection of Gastrointestinal Bleeding". *Scientific Reports* 13.1 (Dec. 2023), p. 22976. DOI: 10.1038/s41598-023-50041-3.

[O7] F. Mohn, T. Knopp, F. Thieben, M. Boberg, P. Szwargulski, and M. Graeser. "Image Reconstruction in Magnetic Particle Imaging for Pulsed Sequences". *Book of Abstracts - BMT 2021 - Annual Conference, Hannover* 66.s1 (Oct. 2021), p. 385. DOI: 10.1515/bmt-2021-6061.

[O8] F. Mohn, T. Knopp, and M. Graeser. "Role of Phase Encoding in Pulsed Magnetic Particle Imaging". *International Journal on Magnetic Particle Imaging* (Mar. 2022), Vol 8 No 1 Suppl 1 (2022). DOI: 10.18416/IJMPI.2022.2203021.

[O9] F. Mohn, M. Exner, P. Szwargulski, M. Möddel, T. Knopp, and M. Graeser. "Using Negative Bolus in Dynamic MPI". *International Journal on Magnetic Particle Imaging IJMPI* (Mar. 2023), Vol 9 No 1 Suppl 1 (2023). DOI: 10.18416/IJMPI.2023.2303022.

[O10] F. Mohn, P. Szwargulski, M. G. Kaul, M. Graeser, T. Mummert, K. M. Krishnan, T. Knopp, G. Adam, J. Salamon, and C. Riedel. "In Vitro Detection of Gastrointestinal Bleeding Using Single- and Multi-Contrast MPI". 10.1 Suppl 1 (Mar. 2024). DOI: 10.18416/IJMPI.2024.2403031.

[O11] F. Mohn, F. Foerger, F. Thieben, M. Möddel, T. Knopp, and M. Graeser. "Trade-off between Power Consumption and Receive Signal Strength for Inductively Coupled Transmit-Receive Circuits in MPI". 10.1 Suppl 1 (Mar. 2024). DOI: 10.18416/IJMPI.2024.2403021.

[O12] J. Ackers, F. Mohn, N. Hackelberg, T. Knopp, T. M. Buzug, and M. Graeser. "Model-Based Voltage Predictions for Arbitrary Waveform Excitation in Magnetic Particle Imaging". *International Journal on Magnetic Particle Imaging IJMPI* (Mar. 2023), Vol 9 No 1 Suppl 1 (2023). DOI: 10.18416/IJMPI.2023.2303088.

[O13] F. Foerger, J.-P. Scheel, F. Thieben, F. Mohn, T. Knopp, and M. Graeser. "Multi-Channel Current Control System for Coupled Multi-Coil Arrays". *International Journal on Magnetic Particle Imaging* (Mar. 2022), Vol 8 No 1 Suppl 1 (2022). DOI: 10.18416/IJMPI.2022.2203076.

[O14] F. Foerger, N. Hackelberg, M. Boberg, J.-P. Scheel, F. Thieben, L. Mirzojan, F. Mohn, M. Möddel, M. Graeser, and T. Knopp. "Flexible Selection Field Generation Using Iron Core Coil Arrays". *International Journal on Magnetic Particle Imaging IJMPI* (Mar. 2023), Vol 9 No 1 Suppl 1 (2023). DOI: 10.18416/IJMPI.2023.2303023.

[O15] F. Foerger, N. Hackelberg, M. Boberg, M. Möddel, F. Thieben, F. Mohn, and T. Knopp. "Single-Shot Magnetic Field Measurements for MPI". *International Journal on Magnetic Particle Imaging IJMPI* 10.1 Suppl 1 (2024).

[O16] N. Hackelberg, M. Grosser, A. Tsanda, F. Mohn, K. Scheffler, M. Möddel, and T. Knopp. "RegularizedLeastSquares.Jl: Modality Agnostic Julia Package for Solving Regularized Least Squares Problems". 10.1 Suppl 1 (Mar. 2024). DOI: 10.18416/IJMPI.2024.2403028.

[O17] F. Niebel, J. Schumacher, F. Mohn, M. Ahlborg, T. M. Buzug, and M. Graeser. "A Novel Approach to FFL Trajectory Analysis". *International Journal on Magnetic Particle Imaging IJMPI* (Mar. 2023), Vol 9 No 1 Suppl 1 (2023). DOI: 10.18416/IJMPI.2023.2303074.

[O18] C. Riedel, F. Mohn, P. Szwargulski, T. Knopp, M. G. Kaul, G. Adam, M. Graeser, and J. Salamon. "Multi-Colour Magnetic Particle Imaging for Real-Time Detection of Gastrointestinal Hemorrhage (PP 23-11)". *ECR 2022 Book of Abstracts* 13.S4 (Dec. 2022), p. 394. DOI: 10.1186/s13244-022-01337-x.

[O19] K. Scheffler, F. Thieben, F. Mohn, M. Graeser, and T. Knopp. "MPI Signal Performance of Resotran". *12th International Workshop on Magnetic Particle Imaging (IWMPI 2023).* 9.1 Suppl 1 (2023), pp. 1–1.

[O20] F. Thieben, F. Foerger, F. Mohn, F. Sevecke, T. Knopp, and M. Graeser. "Heat It up: Thermal Stabilization by Active Heating to Reduce Impedance Drifts in Capacitive Matched Networks". *International Journal on Magnetic Particle Imaging* (Mar. 2022), Vol 8 No 1 Suppl 1 (2022). DOI: 10.18416/IJMPI.2022.2203014.

[O21] F. Thieben, F. Mohn, F. Foerger, N. Hackelberg, J.-P. Scheel, M. Graeser, and T. Knopp. "Safe and Rapid 3D Imaging: Upgrade of a Human-Sized Brain MPI System". *International Journal on Magnetic Particle Imaging IJMPI* (Mar. 2023), Vol 9 No 1 Suppl 1 (2023). DOI: 10.18416/IJMPI.2023.2303045.

[O22] F. Thieben, H. Albers, F. Mohn, F. Foerger, M. Boberg, K. Scheffler, M. Möddel, T. Kluth, and T. Knopp. "Experimental Parameter Calibration of the Scanner Model for Model-Based MPI". 10.1 Suppl 1 (Mar. 2024). DOI: 10.18416/IJMPI.2024.2403025.

References

[1] J. Abart, K. Eberhardt, H. Fischer, W. Huk, E. Richter, F. Schmitt, T. Storch, and E. Zeitler. "Peripheral Nerve Stimulation by Time-Varying Magnetic Fields:" *Journal of Computer Assisted Tomography* 21.4 (July 1997), pp. 532–538. DOI: 10.1097/00004728-199707000-00005.

[2] J. J. Abbott, O. Ergeneman, M. P. Kummer, A. M. Hirt, and B. J. Nelson. "Modeling Magnetic Torque and Force for Controlled Manipulation of Soft-Magnetic Bodies". *IEEE Transactions on Robotics* 23.6 (Dec. 2007), pp. 1247–1252. DOI: 10.1109/TRO.2007.910775.

[3] E. Aderhold, T. Liebing, A. C. Bakenecker, T. M. Buzug, T. Knopp, and M. Graeser. "Rotation Unit for Permanent Magnet Based MPI Devices". *International Journal on Magnetic Particle Imaging* (Mar. 2022), Vol 8 No 1 Suppl 1 (2022). DOI: 10.18416/IJMPI.2022.2203066.

[4] M. Ahlborg, C. Kaethner, T. Knopp, P. Szwargulski, and T. M. Buzug. "Using Data Redundancy Gained by Patch Overlaps to Reduce Truncation Artifacts in Magnetic Particle Imaging". *Physics in Medicine & Biology* 61.12 (2016), pp. 4583–4598. DOI: 10.1088/0031-9155/61/12/4583.

[5] M. Ahlborg, T. Friedrich, T. Gottsche, V. Scheitenberger, R. Linemann, M. Wattenberg, A. T. Buessen, T. Knopp, P. Szwargulski, M. G. Kaul, J. Salamon, T. M. Buzug, J. Barkhausen, and F. Wegner. "First Dedicated Balloon Catheter for Magnetic Particle Imaging". *IEEE Transactions on Medical Imaging* 41.11 (Nov. 2022), pp. 3301–3308. DOI: 10.1109/TMI.2022.3183948.

[6] Akiko Ohki, Tomomi Kuboyabu, Marina Aoki, Mikiko Yamawaki, and Kenya Murase. "Quantitative Evaluation of Tumor Response to Combination of Magnetic Hyperthermia Treatment and Radiation Therapy Using Magnetic Particle Imaging". *International Journal of Nanomedicine and Nanosurgery* 2.3 (2016). DOI: 10.16966/2470-3206.117.

[7] H. Albers and T. Kluth. "Immobilized Nanoparticles with Uniaxial Anisotropy in Multi-Dimensional Lissajous-type Excitation: An Equilibrium Model Approach". *International Journal on Magnetic Particle Imaging* (Mar. 2022), Vol 8 No 1 Suppl 1 (2022). DOI: 10.18416/IJMPI.2022.2203048.

[8] H. Albers, F. Thieben, M. Boberg, K. Scheffler, T. Knopp, and T. Kluth. "Model-Based Calibration and Image Reconstruction with Immobilized Nanoparticles". *International Journal on Magnetic Particle Imaging IJMPI* (Mar. 2023), Vol 9 No 1 Suppl 1 (2023). DOI: 10.18416/IJMPI.2023.2303002.

[9] Analog Devices. "Datasheet: ADA 4898-2. High Voltage, Low Noise, Low Distortion, Unity-Gain Stable, High Speed Op Amp." *https://www.analog.com/media/en/technical-documentation/data-sheets/ADA4898-1_4898-2.pdf* (2024).

[10] A. Antonelli, P. Szwargulski, E. S. Scarpa, C. Grüttner, L. Guidi, G. Ambrosi, T. Knopp, and M. Magnani. "Encapsulation of New MPI Tracer Nanoparticles in the Human Red Blood Cells". *International Journal on Magnetic Particle Imaging* 6.2 (2020), pp. 1–3. DOI: 10.18416/IJMPI.2020.2009001.

[11] A. Antonelli, C. Sfara, J. Rahmer, B. Gleich, J. Borgert, and M. Magnani. “Red Blood Cells as Carriers in Magnetic Particle Imaging”. *Biomedizinische Technik/Biomedical Engineering* 58.6 (Jan. 2013). DOI: 10.1515/bmt-2012-0065.

[12] A. Antonelli, P. Szwargulski, E. S. Scarpa, F. Thieben, G. Cordula, G. Ambrosi, L. Guidi, P. Ludewig, T. Knopp, and M. Magnani. “Development of Long Circulating Magnetic Particle Imaging Tracers: Use of Novel Magnetic Nanoparticles and Entrapment into Human Erythrocytes”. *Nanomedicine* 15.8 (Apr. 2020), pp. 739–753. DOI: 10.2217/nnm-2019-0449.

[13] H. Arami, A. P. Khandhar, A. Tomitaka, E. Yu, P. W. Goodwill, S. M. Conolly, and K. M. Krishnan. “In Vivo Multimodal Magnetic Particle Imaging (MPI) with Tailored Magneto/Optical Contrast Agents”. *Biomaterials* 52 (June 2015), pp. 251–261. DOI: 10.1016/j.biomaterials.2015.02.040.

[14] H. Arami, E. Teeman, A. Troksa, H. Bradshaw, K. Saatchi, A. Tomitaka, S. S. Gambhir, U. O. Häfeli, D. Liggitt, and K. M. Krishnan. “Tomographic Magnetic Particle Imaging of Cancer Targeted Nanoparticles”. *Nanoscale* 9.47 (2017), pp. 18723–18730. DOI: 10.1039/c7nr05502a.

[15] H. Bagheri, C. A. Kierans, K. J. Nelson, B. A. Andrade, C. L. Wong, A. L. Frederick, and M. E. Hayden. “A Mechanically Driven Magnetic Particle Imaging Scanner”. *Applied Physics Letters* 113.18 (Oct. 2018), p. 183703. DOI: 10.1063/1.5052646.

[16] A. C. Bakenecker, J. Schumacher, P. Blümler, K. Gräfe, M. Ahlborg, and T. M Buzug. “A Concept for a Magnetic Particle Imaging Scanner with Halbach Arrays”. *Physics in Medicine & Biology* 65.19 (Sept. 2020), p. 195014. DOI: 10.1088/1361-6560/ab7e7e.

[17] A. C. Bakenecker, M. Ahlborg, C. Debbeler, C. Kaethner, T. M. Buzug, and K. Lüdtke-Buzug. “Magnetic Particle Imaging in Vascular Medicine”. *Innovative Surgical Sciences* 3.3 (Oct. 2018), pp. 179–192. DOI: 10.1515/iss-2018-2026.

[18] A. C. Bakenecker, A. von Gladiss, T. Friedrich, U. Heinen, H. Lehr, K. Lüdtke-Buzug, and T. M. Buzug. “Actuation and Visualization of a Magnetically Coated Swimmer with Magnetic Particle Imaging”. *Journal of Magnetism and Magnetic Materials*. Vol. 473. 2019, pp. 495–500.

[19] A. C. Bakenecker, A. Von Gladiss, H. Schwenke, A. Behrends, T. Friedrich, K. Lüdtke-Buzug, A. Neumann, J. Barkhausen, F. Wegner, and T. M. Buzug. “Navigation of a Magnetic Micro-Robot through a Cerebral Aneurysm Phantom with Magnetic Particle Imaging”. *Scientific Reports* 11.1 (July 2021), p. 14082. DOI: 10.1038/s41598-021-93323-4.

[20] S. Bakhshandeh. “Magnetic Particle Imaging Scanning at the Bedside”. *Nature Reviews Bioengineering* (Apr. 2024). DOI: 10.1038/s44222-024-00186-1.

[21] I. M. Baltruschat, P. Szwargulski, F. Griese, M. Grosser, R. Werner, and T. Knopp. “3d-SMRnet: Achieving a New Quality of MPI System Matrix Recovery by Deep Learning”. *arXiv*. 2019, pp. 109–110.

[22] E. L. Barbier, L. Lamalle, and M. Décorps. “Methodology of Brain Perfusion Imaging: Methodology of Brain Perfusion Imaging”. *Journal of Magnetic Resonance Imaging* 13.4 (Apr. 2001), pp. 496–520. DOI: 10.1002/jmri.1073.

[23] L. M. Bauer, S. F. Situ, M. A. Griswold, and A. C. S. Samia. “Magnetic Particle Imaging Tracers: State-of-the-Art and Future Directions”. *Journal of Physical Chemistry Letters* 6.13 (2015), pp. 2509–2517. DOI: 10.1021/acs.jpclett.5b00610.

[24] L. M. Bauer, S. F. Situ, M. A. Griswold, and A. C. S. Samia. “High-Performance Iron Oxide Nanoparticles for Magnetic Particle Imaging-Guided Hyperthermia (hMPI)”. *Nanoscale* 8.24 (2016), pp. 12162–12169. DOI: 10.1039/c6nr01877g.

[25] K. Bente, M. Weber, M. Graeser, T. F. Sattel, M. Erbe, and T. M. Buzug. “Electronic Field Free Line Rotation and Relaxation Deconvolution in Magnetic Particle Imaging”. *IEEE Transactions on Medical Imaging* 34.2 (2015), pp. 644–651. DOI: 10.1109/TMI.2014.2364891.

[26] S. Biederer, T. Knopp, T. F. Sattel, K. Lüdtke-Buzug, B. Gleich, J. Weizenecker, J. Borgert, and T. M. Buzug. “Magnetization Response Spectroscopy of Superparamagnetic Nanoparticles for Magnetic Particle Imaging”. *Journal of Physics D: Applied Physics* 42.20 (Oct. 2009), p. 205007. DOI: 10.1088/0022-3727/42/20/205007.

[27] C. Billings, M. Langley, G. Warrington, F. Mashali, and J. A. Johnson. “Magnetic Particle Imaging: Current and Future Applications, Magnetic Nanoparticle Synthesis Methods and Safety Measures”. *International Journal of Molecular Sciences* 22.14 (July 2021), p. 7651. DOI: 10.3390/ijms22147651.

[28] M. Boberg, T. Knopp, and M. Möddel. “Analysis and Comparison of Magnetic Fields in MPI Using Spherical Harmonic Expansions.” *8th International Workshop on Magnetic Particle Imaging (IWMPI 2018)* (2018), pp. 159–160.

[29] M. Boberg, T. Knopp, and M. Möddel. “Reducing Displacement Artifacts by Warping System Matrices in Efficient Joint Multi-Patch Magnetic Particle Imaging”. *International Journal on Magnetic Particle Imaging* 6.2 (2020), pp. 1–3. DOI: 10.18416/IJMPI.2020.2009030.

[30] M. Boberg, N. Gdaniec, P. Szwargulski, F. Werner, M. Möddel, and T. Knopp. “Simultaneous Imaging of Widely Differing Particle Concentrations in MPI: Problem Statement and Algorithmic Proposal for Improvement”. *Physics in Medicine & Biology* 66.9 (Apr. 2021), p. 095004. DOI: 10.1088/1361-6560/abf202.

[31] M. Boberg, J. Hunecke, F. Thieben, M. Graeser, and T. Knopp. "MPI Transfer-Function Estimation with Receive-Coil Coupling". *International Journal on Magnetic Particle Imaging IJMPI* (Mar. 2023), Vol 9 No 1 Suppl 1 (2023). DOI: 10.18416/IJMPI.2023.2303053.

[32] M. Boberg, T. Knopp, and M. Möddel. *Unique Compact Representation of Magnetic Fields Using Truncated Solid Harmonic Expansions*. Feb. 2023. arXiv: 2302.07591 [physics].

[33] M. Boberg, T. Knopp, P. Szwargulski, and M. Moddel. "Generalized MPI Multi-Patch Reconstruction Using Clusters of Similar System Matrices". *IEEE Transactions on Medical Imaging* 39.5 (2020), pp. 1347–1358. DOI: 10.1109/tmi.2019.2949171.

[34] J. Bohnert, B. Gleich, J. Weizenecker, J. Borgert, and O. Dössel. "Evaluation of Induced Current Densities and SAR in the Human Body by Strong Magnetic Fields around 100 kHz". *IFMBE Proceedings*. Vol. 22. 2008, pp. 2532–2535. DOI: 10.1007/978-3-540-89208-3_607.

[35] J. Borgert, J. D. Schmidt, I. Schmale, C. Bontus, B. Gleich, B. David, J. Weizenecker, J. Jockram, C. Lauruschkat, O. Mende, M. Heinrich, A. Halkola, J. Bergmann, O. Woywode, and J. Rahmer. "Perspectives on Clinical Magnetic Particle Imaging". *Biomedizinische Technik/Biomedical Engineering* 58.6 (Jan. 2013), pp. 551–556. DOI: 10.1515/bmt-2012-0064.

[36] G. Bringout, W. Erb, and J. Frikel. "A New 3D Model for Magnetic Particle Imaging Using Realistic Magnetic Field Topologies for Algebraic Reconstruction". *Inverse Problems* 36.12 (Dec. 2020), p. 124002. DOI: 10.1088/1361-6420/abb446.

[37] O. Buchholz, K. Sajjamark, J. Franke, H. Wei, A. Behrends, C. Münkel, C. Grüttner, P. Levan, D. Von Elverfeldt, M. Graeser, T. Buzug, S. Bär, and U. G. Hofmann. "In Situ Theranostic Platform Combining Highly Localized Magnetic Fluid Hyperthermia, Magnetic Particle Imaging, and Thermometry in 3D". *Theranostics* 14.1 (2024), pp. 324–340. DOI: 10.7150/thno.86759.

[38] M. P. Bui, T.-A. Le, and J. Yoon. "A Magnetic Particle Imaging-Based Navigation Platform for Magnetic Nanoparticles Using Interactive Manipulation of a Virtual Field Free Point to Ensure Targeted Drug Delivery". *IEEE Transactions on Industrial Electronics* 68.12 (Dec. 2021), pp. 12493–12503. DOI: 10.1109/TIE.2020.3039219.

[39] M. P. Bui, M. Park, T.-A. Le, and J. Yoon. "A Development of 3D Navigation System for Micro-Nano Robot Based on a Magnetic Particle Imaging System". *International Journal on Magnetic Particle Imaging IJMPI* (Mar. 2023), Vol 9 No 1 Suppl 1 (2023). DOI: 10.18416/IJMPI.2023.2303046.

[40] C. T. Chan and S. S. Gambhir. "Indirect Imaging". *Encyclopedia of Diagnostic Imaging*. Ed. by A. L. Baert. Berlin, Heidelberg: Springer Berlin Heidelberg, 2008, pp. 950–954. DOI: 10.1007/978-3-540-35280-8_1246.

[41] P. Chandrasekharan et al. "Using Magnetic Particle Imaging Systems to Localize and Guide Magnetic Hyperthermia Treatment: Tracers, Hardware, and Future Medical Applications". *Theranostics* 10.7 (2020), pp. 2965–2981. DOI: 10.7150/thno.40858.

[42] X. Chen, M. Graeser, A. Behrends, A. von Gladiss, and T. M. Buzug. "First Measurement Results of a 3D Magnetic Particle Spectrometer". *International Journal on Magnetic Particle Imaging* 4.1 (2018). DOI: 10.18416/ijmpi.2018.1810001.

[43] S. H. Choi, T.-A. Le, B. Son, and J. Yoon. "A Portable Single-Sided Magnetic Particle Imaging Concept Using Amplitude Modulation for Breast Conserving Sugery". *International Journal on Magnetic Particle Imaging* (Mar. 2022), Vol 8 No 1 Suppl 1 (2022). DOI: 10.18416/IJMPI.2022.2203024.

[44] W. T. Coffey and Y. P. Kalmykov. "Thermal Fluctuations of Magnetic Nanoparticles: Fifty Years after Brown". *Journal of Applied Physics* 112.12 (Dec. 2012), p. 121301. DOI: 10.1063/1.4754272.

[45] S. C. Cripps. *RF Power Amplifiers for Wireless Communications*. Second edition. Boston: Artech House, 2006.

[46] L. R. Croft, P. Goodwill, M. Ferguson, K. Krishnan, and S. Conolly. "Relaxation in X-Space Magnetic Particle Imaging". *Springer Proceedings in Physics* 140.12 (2012), pp. 149–153. DOI: 10.1007/978-3-642-24133-8_24.

[47] L. R. Croft, P. W. Goodwill, J. J. Konkle, H. Arami, D. A. Price, A. X. Li, E. U. Saritas, and S. M. Conolly. "Low Drive Field Amplitude for Improved Image Resolution in Magnetic Particle Imaging: Low Drive Field Amplitude for Improved Image Resolution". *Medical Physics* 43.1 (Dec. 2015), pp. 424–435. DOI: 10.1118/1.4938097.

[48] M. Dadkhah, N. Kumar, and J. Yoon. "Design and Simulation of a 3D Actuation System for Magnetic Nano-Particles Delivery System". *Intelligent Robotics and Applications*. Ed. by D. Hutchison et al. Vol. 8102. Berlin, Heidelberg: Springer Berlin Heidelberg, 2013, pp. 177–187. DOI: 10.1007/978-3-642-40852-6_20.

[49] R. J. Deissler, Y. Wu, and M. A. Martens. "Dependence of Brownian and Néel Relaxation Times on Magnetic Field Strength". *Medical Physics* 41.1 (Jan. 2014), p. 012301. DOI: 10.1118/1.4837216.

[50] S. Dittmer, T. Kluth, M. T. R. Henriksen, and P. Maass. "Deep Image Prior for 3D Magnetic Particle Imaging: A Quantitative Comparison of Regularization Techniques on Open MPI Dataset". *International Journal on Magnetic Particle Imaging* (Mar. 2021), Vol 7 No 1 (2021). DOI: 10.18416/IJMPI.2021.2103001.

[51] S. Draack, M. Schilling, and T. Viereck. "Magnetic Particle Imaging of Particle Dynamics in Complex Matrix Systems". *Physical Sciences Reviews* 8.2 (Feb. 2023), pp. 213–237. DOI: 10.1515/psr-2019-0123.

[52] D. Eberbeck, C. L. Dennis, N. F. Huls, K. L. Krycka, C. Gruttner, and F. Westphal. “Multicore Magnetic Nanoparticles for Magnetic Particle Imaging”. *IEEE Transactions on Magnetics* 49.1 (Jan. 2013), pp. 269–274. DOI: `10.1109/TMAG.2012.2226438`.

[53] D. Eberbeck, F. Wiekhorst, S. Wagner, and L. Trahms. “How the Size Distribution of Magnetic Nanoparticles Determines Their Magnetic Particle Imaging Performance”. *Applied Physics Letters* 98.18 (May 2011), p. 182502. DOI: `10.1063/1.3586776`.

[54] M. Erbe, T. Knopp, T. F. Sattel, S. Biederer, and T. M. Buzug. “Experimental Generation of an Arbitrarily Rotated Field-Free Line for the Use in Magnetic Particle Imaging”. *Medical Physics* 38.9 (2011), pp. 5200–5207. DOI: `10.1118/1.3626481`.

[55] R. Evens. “The Economic Impact of Technology on Diagnostic Imaging at a University Medical Center”. *American Journal of Roentgenology* 153.1 (July 1989), pp. 179–183. DOI: `10.2214/ajr.153.1.179`.

[56] M. Exner. “Perfusionsbildgebung anhand positiver und negativer Bolusanwendung in der Magnetpartikelbildgebung” (July 2022). DOI: `10.15480/882.5075`.

[57] R. M. Ferguson, A. P. Khandhar, S. J. Kemp, H. Arami, E. U. Saritas, L. R. Croft, J. Konkle, P. W. Goodwill, A. Halkola, J. Rahmer, J. Borgert, S. M. Conolly, and K. M. Krishnan. “Magnetic Particle Imaging With Tailored Iron Oxide Nanoparticle Tracers”. *IEEE Transactions on Medical Imaging* 34.5 (May 2015), pp. 1077–1084. DOI: `10.1109/TMI.2014.2375065`.

[58] R. M. Ferguson, K. R. Minard, and K. M. Krishnan. “Optimization of Nanoparticle Core Size for Magnetic Particle Imaging”. *Journal of Magnetism and Magnetic Materials* 321.10 (May 2009), pp. 1548–1551. DOI: `10.1016/j.jmmm.2009.02.083`.

[59] D. Finas, K. Baumann, L. Sydow, K. Heinrich, K. Gräfe, T. Buzug, and K. Lüdtke-Buzug. “Detection and Distribution of Superparamagnetic Nanoparticles in Lymphatic Tissue in a Breast Cancer Model for Magnetic Particle Imaging”. *Biomedizinische Technik*. Vol. 57. Springer, 2012, pp. 81–83. DOI: `10.1515/bmt-2012-4158`.

[60] D. Finas, K. Baumann, L. Sydow, K. Heinrich, A. Rody, K. Gräfe, T. M. Buzug, and K. Ludtke-Buzug. “SPIO Detection and Distribution in Biological Tissue - A Murine MPI-SLNB Breast Cancer Model”. *IEEE Transactions on Magnetics* 51.2 (2015), pp. 1–4. DOI: `10.1109/TMAG.2014.2358272`.

[61] F. Foerger, M. Graeser, and T. Knopp. “Iron Core Coil Designs for MPI”. *International Journal on Magnetic Particle Imaging* 6.2 (2020), pp. 1–3. DOI: `10.18416/IJMPI.2020.2009042`.

[62] F. Foerger, M. Boberg, M. Möddel, J.-P. Scheel, M. Graeser, and T. Knopp. “Low-Power Iron Selection and Focus Field Generator”. *International Journal on Magnetic Particle Imaging* (Mar. 2022), Vol 8 No 1 Suppl 1 (2022). DOI: `10.18416/IJMPI.2022.2203065`.

[63] J. Franke, U. Heinen, H. Lehr, A. Weber, F. Jaspard, W. Ruhm, M. Heidenreich, and V. Schulz. “System Characterization of a Highly Integrated Preclinical Hybrid MPI-MRI Scanner”. *IEEE Transactions on Medical Imaging* 35.9 (2016), pp. 1993–2004. DOI: `10.1109/TMI.2016.2542041`.

[64] H. Gavilán et al. “Colloidal Flower-Shaped Iron Oxide Nanoparticles: Synthesis Strategies and Coatings”. *Particle & Particle Systems Characterization* 34.7 (July 2017), p. 1700094. DOI: `10.1002/ppsc.201700094`.

[65] L. B. Gerson, J. L. Fidler, D. R. Cave, and J. A. Leighton. “ACG Clinical Guideline: Diagnosis and Management of Small Bowel Bleeding”. *American Journal of Gastroenterology* 110.9 (Sept. 2015), pp. 1265–1287. DOI: `10.1038/ajg.2015.246`.

[66] J. Gevaert, K. Van Beek, O. C. Sehl, and P. J. Foster. “VivoTrax+ Improves the Detection of Cancer Cells with Magnetic Particle Imaging”. *International Journal on Magnetic Particle Imaging* (Oct. 2022), Vol 8 No 2 (2022). DOI: `10.18416/IJMPI.2022.2210001`.

[67] J. I. Gittleman, B. Abeles, and S. Bozowski. “Superparamagnetism and Relaxation Effects in Granular Ni-Si O 2 and Ni- Al 2 O 3 Films”. *Physical Review B* 9.9 (May 1974), pp. 3891–3897. DOI: `10.1103/PhysRevB.9.3891`.

[68] B. Gleich. “Verfahren Zur Ermittlung Der Räumlichen Verteilung Magnetischer Partikel”. DE10151778A1. 2001.

[69] B. Gleich, J. Weizenecker, H. Timminger, C. Bontus, I. Schmale, J. Rahmer, J. Schmidt, J. Kanzenbach, and J. Borgert. “Fast MPI Demonstrator with Enlarged Field of View”. *Proceedings of the International Society for Magnetic Resonance in Medicine (ISMRM)*. Vol. 18. Stockholm, May 2010, p. 218.

[70] B. Gleich and J. Weizenecker. “Tomographic Imaging Using the Nonlinear Response of Magnetic Particles”. *Nature* 435.7046 (2005), pp. 1214–1217. DOI: `10.1038/nature03808`.

[71] B. B. GmbH. “Bruker Announces the World’s First Preclinical Magnetic Particle Imaging (MPI) System.” *https://www.bruker.com/en/products-and-solutions/preclinical-imaging/mpi.html* (Sept. 2013).

[72] P. W. Goodwill and S. M. Conolly. “The X-space Formulation of the Magnetic Particle Imaging Process: 1-D Signal, Resolution, Bandwidth, SNR, SAR, and Magnetostimulation”. *IEEE Transactions on Medical Imaging* 29.11 (2010), pp. 1851–1859. DOI: `10.1109/TMI.2010.2052284`.

[73] P. W. Goodwill and S. M. Conolly. “Multidimensional X-space Magnetic Particle Imaging”. *IEEE Transactions on Medical Imaging* 30.9 (2011), pp. 1581–1590. DOI: `10.1109/TMI.2011.2125982`.

[74] P. W. Goodwill, J. J. Konkle, B. Zheng, E. U. Saritas, and S. M. Conolly. “Projection X-space Magnetic Particle Imaging”. *IEEE Transactions on Medical Imaging* 31.5 (2012), pp. 1076–1085. DOI: `10.1109/TMI.2012.2185247`.

[75] M. Graeser, P. Szwargulski, A. von Gladiss, F. Förger, F. Thieben, P. Ludewig, and T. Knopp. “Receive Path Calibration to Exchange System Matrix Data of Different Receivers”. *International Journal on Magnetic Particle Imaging* 6.2 (2020), pp. 1–3. DOI: `10.18416/IJMPI.2020.2009044`.

[76] M. Graeser, F. Thieben, P. Szwargulski, F. Werner, N. Gdaniec, M. Boberg, F. Griese, M. Möddel, P. Ludewig, D. van de Ven, O. M. Weber, O. Woywode, B. Gleich, and T. Knopp. “Human-Sized Magnetic Particle Imaging for Brain Applications”. *Nature Communications* 10.1 (2019). DOI: `10.1038/s41467-019-09704-x`.

[77] M. Graeser, T. Knopp, M. Grüttner, T. F. Sattel, and T. M. Buzug. “Analog Receive Signal Processing for Magnetic Particle Imaging”. *Medical Physics* 40.4 (2013), p. 42303. DOI: `10.1118/1.4794482`.

[78] M. Graeser, T. Knopp, P. Szwargulski, T. Friedrich, A. Von Gladiss, M. Kaul, K. M. Krishnan, H. Ittrich, G. Adam, and T. M. Buzug. “Towards Picogram Detection of Superparamagnetic Iron-Oxide Particles Using a Gradiometric Receive Coil”. *Scientific Reports* 7.1 (2017), p. 6872. DOI: `10.1038/s41598-017-06992-5`.

[79] M. Graeser, P. Ludewig, P. Szwargulski, F. Foerger, T. Liebing, N. D. Forkert, F. Thieben, T. Magnus, and T. Knopp. “Design of a Head Coil for High Resolution Mouse Brain Perfusion Imaging Using Magnetic Particle Imaging”. *Physics in Medicine & Biology* 65.23 (Dec. 2020), p. 235007. DOI: `10.1088/1361-6560/abc09e`.

[80] C. Greiner, M. A. Rückert, T. Kampf, V. C. Behr, and P. Vogel. “Traveling Wave MPI Utilizing a Field-Free Line”. *International Journal on Magnetic Particle Imaging* (Mar. 2022), Vol 8 No 1 Suppl 1 (2022). DOI: `10.18416/IJMPI.2022.2203027`.

[81] F. Griese, T. Knopp, C. Gruettner, F. Thieben, K. Müller, S. Loges, P. Ludewig, and N. Gdaniec. “Simultaneous Magnetic Particle Imaging and Navigation of Large Superparamagnetic Nanoparticles in Bifurcation Flow Experiments”. *Journal of Magnetism and Magnetic Materials* 498 (2020), p. 166206. DOI: `10.1016/j.jmmm.2019.166206`.

[82] F. Griese, S. Latus, M. Schlüter, M. Graeser, M. Lutz, A. Schlaefer, and T. Knopp. “In-Vitro MPI-guided IVOCT Catheter Tracking in Real Time for Motion Artifact Compensation”. *arXiv* 20.3 (2019), e0230821. DOI: `10.1371/journal.pone.0230821`.

[83] M. Grosser and T. Knopp. “Low Rank Approach to Sparse System Matrix Recovery for MPI”. *9th International Workshop on Magnetic Particle Imaging (IWMPI 2019)*. 2019, pp. 31–32.

[84] M. Grosser. “Compressed Sensing and Experiment Design in Magnetic Field Based Imaging” (2023). DOI: `10.15480/882.8925`.

[85] M. Grosser, M. Boberg, M. Bahe, and T. Knopp. “Enhanced Compressed Sensing Recovery of Multi-Patch System Matrices in MPI”. *International Journal on Magnetic Particle Imaging* (Sept. 2020), Vol 6 No 2 Suppl. 1 (2020). DOI: `10.18416/IJMPI.2020.2009035`.

[86] M. Gruettner, M. Graeser, S. Biederer, T. F. Sattel, H. Wojtczyk, W. Tenner, T. Knopp, B. Gleich, J. Borgert, and T. M. Buzug. “1D-image Reconstruction for Magnetic Particle Imaging Using a Hybrid System Function”. *IEEE Nuclear Science Symposium Conference Record*. 2011, pp. 2545–2548. DOI: `10.1109/NSSMIC.2011.6152687`.

[87] M. Grüttner, T. Knopp, J. Franke, M. Heidenreich, J. Rahmer, A. Halkola, C. Kaethner, J. Borgert, and T. M. Buzug. “On the Formulation of the Image Reconstruction Problem in Magnetic Particle Imaging”. *Biomedizinische Technik* 58.6 (2013), pp. 583–591. DOI: `10.1515/bmt-2012-0063`.

[88] A. Gungor, B. Aşkın, D. Alptekin Soydan, E. U. Saritas, C. B. Top, and T. Çukur. “A Denoiser Scaling Technique for Plug-and-Play MPI Reconstruction”. *International Journal on Magnetic Particle Imaging IJMPI* (Mar. 2023), Vol 9 No 1 Suppl 1 (2023). DOI: `10.18416/IJMPI.2023.2303041`.

[89] N. Hackelberg, J. Schumacher, J. Ackers, M. Möddel, F. Förger, M. Graeser, and T. Knopp. “MPIMeasurements.Jl: An Extensible Julia Framework for Composable Magnetic Particle Imaging Devices”. *International Journal on Magnetic Particle Imaging IJMPI* (Mar. 2023), Vol 9 No 1 Suppl 1 (2023). DOI: `10.18416/IJMPI.2023.2303069`.

[90] N. Hackelberg, J. Schumacher, M. Graeser, and T. Knopp. “A Flexible High-Performance Signal Generation and Digitization Plattform Based on Low-Cost Hardware”. *International Journal on Magnetic Particle Imaging* (Mar. 2022), Vol 8 No 1 Suppl 1 (2022). DOI: `10.18416/IJMPI.2022.2203063`.

[91] J. Haegele, N. Panagiotopoulos, S. Cremers, J. Rahmer, J. Franke, R. L. Duschka, S. Vaalma, M. Heidenreich, J. Borgert, P. Borm, J. Barkhausen, and F. M. Vogt. “Magnetic Particle Imaging: A Resovist Based Marking Technology for Guide Wires and Catheters for Vascular Interventions”. *IEEE Transactions on Medical Imaging* 35.10 (2016), pp. 2312–2318. DOI: `10.1109/TMI.2016.2559538`.

[92] J. Haegele, J. Rahmer, B. Gleich, J. Borgert, H. Wojtczyk, N. Panagiotopoulos, T. M. Buzug, J. Barkhausen, and F. M. Vogt. “Magnetic Particle Imaging: Visualization of Instruments for Cardiovascular Intervention”. *Radiology* 265.3 (2012), pp. 933–938. DOI: `10.1148/radiol.12120424`.

[93] J. Haegele, S. Vaalma, N. Panagiotopoulos, J. Barkhausen, F. M. Vogt, J. Borgert, and J. Rahmer. “Multi-Color Magnetic Particle Imaging for Cardiovascular Interventions”. *Physics in Medicine & Biology* 61.16 (2016), N415–N426. DOI: `10.1088/0031-9155/61/16/N415`.

[94] A. Halkola, T. Buzug, J. Rahmer, B. Gleich, and C. Bontus. “System Calibration Unit for Magnetic Particle Imaging: Focus Field Based System Function”. *Springer Proceedings in Physics*. Vol. 140. Springer, 2012, pp. 27–31. DOI: 10.1007/978-3-642-24133-8_5.

[95] K. Harini, K. Girigoswami, P. Pallavi, P. Gowtham, A. D. Prabhu, and A. Girigoswami. “Advancement of Magnetic Particle Imaging in Diagnosis and Therapy”. *Advances in Natural Sciences: Nanoscience and Nanotechnology* 15.2 (June 2024), p. 023002. DOI: 10.1088/2043-6262/ad3b7a.

[96] M. G. Harisinghani, J. Barentsz, P. F. Hahn, W. M. Deserno, S. Tabatabaei, C. H. van de Kaa, J. de la Rosette, and R. Weissleder. “Noninvasive Detection of Clinically Occult Lymph-Node Metastases in Prostate Cancer”. *New England Journal of Medicine* 348.25 (2003), pp. 2491–2499. DOI: 10.1056/nejmoa022749.

[97] F. Harris. “On the Use of Windows for Harmonic Analysis with the Discrete Fourier Transform”. *Proceedings of the IEEE* 66.1 (1978), pp. 51–83. DOI: 10.1109/PROC.1978.10837.

[98] V. Hartung, J. Günther, A. M. Augustin, T. Reichl, P. Gruschwitz, M. Rückert, T. A. Bley, V. Behr, S. Herz, and P. Vogel. “Resotran® Meets MPI – Clinically Approved Ferucarbotran Reintroduced: A Major Leap towards MPI in Humans”. *International Journal on Magnetic Particle Imaging IJMPI* (Mar. 2023), Vol 9 No 1 Suppl 1 (2023). DOI: 10.18416/IJMPI.2023.2303058.

[99] S. Harvell-Smith, L. D. Tung, and N. T. K. Thanh. “Magnetic Particle Imaging: Tracer Development and the Biomedical Applications of a Radiation-Free, Sensitive, and Quantitative Imaging Modality”. *Nanoscale* 14.10 (2022), pp. 3658–3697. DOI: 10.1039/D1NR05670K.

[100] S. Healy, A. F. Bakuzis, P. W. Goodwill, A. Attaluri, J. W. M. Bulte, and R. Ivkov. “Clinical Magnetic Hyperthermia Requires Integrated Magnetic Particle Imaging”. *WIREs Nanomedicine and Nanobiotechnology* 14.3 (May 2022). DOI: 10.1002/wnan.1779.

[101] M. Heideman, D. Johnson, and C. Burrus. “Gauss and the History of the Fast Fourier Transform”. *IEEE ASSP Magazine* 1.4 (Oct. 1984), pp. 14–21. DOI: 10.1109/MASSP.1984.1162257.

[102] D. Hensley, P. Goodwill, L. Croft, and S. Conolly. “Preliminary Experimental X-space Color MPI”. *2015 5th International Workshop on Magnetic Particle Imaging (IWMPI)*. Istanbul, Turkey: IEEE, Mar. 2015, pp. 1–1. DOI: 10.1109/IWMPI.2015.7106993.

[103] S. Herz, P. Vogel, P. Dietrich, T. Kampf, M. A. Rückert, R. Kickuth, V. C. Behr, and T. A. Bley. “Magnetic Particle Imaging Guided Real-Time Percutaneous Transluminal Angioplasty in a Phantom Model”. *CardioVascular and Interventional Radiology* 41.7 (2018), pp. 1100–1105. DOI: 10.1007/s00270-018-1955-7.

[104] S. Herz, P. Vogel, T. Kampf, P. Dietrich, S. Veldhoen, M. A. Rückert, R. Kickuth, V. C. Behr, and T. A. Bley. “Magnetic Particle Imaging–Guided Stenting”. *Journal of Endovascular Therapy* 26.4 (Aug. 2019), pp. 512–519. DOI: 10.1177/1526602819851202.

[105] H. Hui, J. Liu, H. Zhang, J. Zhong, J. He, B. Zhang, H. Zhang, Q. Li, H. Li, and J. Tian. “*In Vivo* Measurement of Cerebral SPIO Concentration in Nonhuman Primate Using Magnetic Particle Imaging Detector”. *IEEE Magnetics Letters* 14 (2023), pp. 1–5. DOI: 10.1109/LMAG.2023.3281933.

[106] Q. Huynh, O. Doyle, K. B. Fung, C. Saayujya, and S. Conolly. “Active Cancellation of Direct Feedthrough Enables 100-Fold More Sensitive Mass-Limited Detection in Magnetic Particle Sensing Systems”. *2023 IEEE Biomedical Circuits and Systems Conference (BioCAS)*. Toronto, ON, Canada: IEEE, Oct. 2023, pp. 1–5. DOI: 10.1109/BioCAS58349.2023.10388568.

[107] M. A. Ibrahim, B. Hazhirkarzar, and A. B. Dublin. “Gadolinium Magnetic Resonance Imaging”. *StatPearls*. Treasure Island (FL): StatPearls Publishing, 2024.

[108] Institut für Theoretische Elektrotechnik. *CONCEPT-II V12.0*. TET. Hamburg, Germany, 2023.

[109] W. Irnich and F. Schmitt. “Magnetostimulation in MRI”. *Magnetic Resonance in Medicine* 33.5 (May 1995), pp. 619–623. DOI: 10.1002/mrm.1910330506.

[110] A. Izadian. *Fundamentals of Modern Electric Circuit Analysis and Filter Synthesis: A Transfer Function Approach*. Second edition. Cham: Springer, 2023.

[111] J. D. Jackson. *Classical Electrodynamics*. 3. ed., repr. 2013, student ed. Hoboken, NY: Wiley, 2013.

[112] W. R. Johnson. *Filtering Techniques for Noise Suppression in Quasi-Balanced Circuits*. Technical Report No. 32-945. Jet Propulsion Laboratory, 1966.

[113] A. Jordan, P. Wust, H. Fähling, W. John, A. Hinz, and R. Felix. “Inductive Heating of Ferrimagnetic Particles and Magnetic Fluids: Physical Evaluation of Their Potential for Hyperthermia”. *International Journal of Hyperthermia* 25.7 (2009), pp. 499–511. DOI: 10.3109/02656730903287790.

[114] A. Jordan, R. Scholz, P. Wust, H. Fähling, and Roland Felix. “Magnetic Fluid Hyperthermia (MFH): Cancer Treatment with AC Magnetic Field Induced Excitation of Biocompatible Superparamagnetic Nanoparticles”. *Journal of Magnetism and Magnetic Materials* 201.1-3 (July 1999), pp. 413–419. DOI: 10.1016/S0304-8853(99)00088-8.

[115] S. Kaczmarz. “Angenäherte Auflösung von Systemen Linearer Gleichungen”. *Bulletin of the International Academy Polonica Sciences Letters A* 35 (1937), pp. 355–357.

[116] H. Kaden. “Wirbelströme Und Schirmung in Der Nachrichtentechnik”. *Wirbelströme und Schirmung in der Nachrichtentechnik* (1959). DOI: `10.1007/978-3-540-32570-3`.

[117] C. Kaethner, W. Erb, M. Ahlborg, P. Szwargulski, T. Knopp, and T. M. Buzug. “Non-Equispaced System Matrix Acquisition for Magnetic Particle Imaging Based on Lissajous Node Points”. *IEEE Transactions on Medical Imaging* 35.11 (2016), pp. 2476–2485. DOI: `10.1109/TMI.2016.2580458`.

[118] T. Kang, F. Li, S. Baik, W. Shao, D. Ling, and T. Hyeon. “Surface Design of Magnetic Nanoparticles for Stimuli-Responsive Cancer Imaging and Therapy”. *Biomaterials* 136 (Aug. 2017), pp. 98–114. DOI: `10.1016/j.biomaterials.2017.05.013`.

[119] P. Karp and D. Duret. “Unidirectional Magnetic Gradiometers”. *Journal of Applied Physics* 51.3 (Mar. 1980), pp. 1267–1272. DOI: `10.1063/1.327819`.

[120] M. G. Kaul, J. Salamon, T. Knopp, H. Ittrich, G. Adam, H. Weller, and C. Jung. “Magnetic Particle Imaging for in Vivo Blood Flow Velocity Measurements in Mice”. *Physics in Medicine & Biology* 63.6 (2018), p. 64001. DOI: `10.1088/1361-6560/aab136`.

[121] M. G. Kaul, T. Mummert, C. Jung, J. Salamon, A. P. Khandhar, R. M. Ferguson, S. J. Kemp, H. Ittrich, K. M. Krishnan, G. Adam, and T. Knopp. “In Vitro and in Vivo Comparison of a Tailored Magnetic Particle Imaging Blood Pool Tracer with Resovist”. *Physics in Medicine and Biology* 62.9 (Apr. 2017), pp. 3454–3469. DOI: `10.1088/1361-6560/aa5780`.

[122] A. P. Khandhar, R. M. Ferguson, H. Arami, S. J. Kemp, and K. M. Krishnan. “Tuning Surface Coatings of Optimized Magnetite Nanoparticle Tracers for In Vivo Magnetic Particle Imaging”. *IEEE Transactions on Magnetics* 51.2 (2015), pp. 1–4. DOI: `10.1109/TMAG.2014.2321096`.

[123] G. Kim, J. A. Soto, and T. Morrison. “Radiologic Assessment of Gastrointestinal Bleeding”. *Gastroenterology Clinics of North America* 47.3 (Sept. 2018), pp. 501–514. DOI: `10.1016/j.gtc.2018.04.003`.

[124] W. T. Kimberly, A. J. Sorby-Adams, A. G. Webb, E. X. Wu, R. Beekman, R. Bowry, S. J. Schiff, A. De Havenon, F. X. Shen, G. Sze, P. Schaefer, J. E. Iglesias, M. S. Rosen, and K. N. Sheth. “Brain Imaging with Portable Low-Field MRI”. *Nature Reviews Bioengineering* 1.9 (July 2023), pp. 617–630. DOI: `10.1038/s44222-023-00086-w`.

[125] C. Kittel. *Introduction to Solid State Physics*. 8th ed. Hoboken, NJ: Wiley, 2005.

[126] T. Kluth, P. Szwargulski, and T. Knopp. “Towards Accurate Modeling of the Multidimensional Magnetic Particle Imaging Physics”. *New Journal of Physics* 21.10 (Oct. 2019), p. 103032. DOI: `10.1088/1367-2630/ab4938`.

[127] T. Kluth. “Mathematical Models for Magnetic Particle Imaging”. *Inverse Problems* 34.8 (Aug. 2018), p. 083001. DOI: `10.1088/1361-6420/aac535`.

[128] T. Knopp, S. Biederer, T. Sattel, J. Weizenecker, B. Gleich, J. Borgert, and T. M. Buzug. “Trajectory Analysis for Magnetic Particle Imaging”. *Physics in Medicine & Biology* 54.2 (Dec. 2008), pp. 385–397. DOI: `10.1088/0031-9155/54/2/014`.

[129] T. Knopp, M. Erbe, T. F. Sattel, S. Biederer, and T. M. Buzug. “A Fourier Slice Theorem for Magnetic Particle Imaging Using a Field-Free Line”. *Inverse Problems* 27.9 (2011), p. 95004. DOI: `10.1088/0266-5611/27/9/095004`.

[130] T. Knopp, N. Gdaniec, and M. Möddel. “Magnetic Particle Imaging: From Proof of Principle to Preclinical Applications”. *Physics in Medicine & Biology* 62.14 (2017), R124–R178. DOI: `10.1088/1361-6560/aa6c99`.

[131] T. Knopp, N. Gdaniec, R. Rehr, M. Graeser, and T. Gerkmann. “Correction of Linear System Drifts in Magnetic Particle Imaging”. *Physics in Medicine & Biology* 64.12 (June 2019), p. 125013. DOI: `10.1088/1361-6560/ab2480`.

[132] T. Knopp and M. Hofmann. “Online Reconstruction of 3D Magnetic Particle Imaging Data”. *Physics in Medicine & Biology* 61.11 (2016), N257–N267. DOI: `10.1088/0031-9155/61/11/N257`.

[133] T. Knopp, J. Rahmer, T. F. Sattel, S. Biederer, J. Weizenecker, B. Gleich, J. Borgert, and T. M. Buzug. “Weighted Iterative Reconstruction for Magnetic Particle Imaging”. *Physics in Medicine & Biology* 55.6 (2010), pp. 1577–1589. DOI: `10.1088/0031-9155/55/6/003`.

[134] T. Knopp, T. F. Sattel, S. Biederer, and T. M. Buzug. “Field-Free Line Formation in a Magnetic Field”. *Journal of Physics A: Mathematical and Theoretical* 43.1 (2010), 9pp. DOI: `10.1088/1751-8113/43/1/012002`.

[135] T. Knopp, T. F. Sattel, S. Biederer, and T. M. Buzug. “Limitations of Measurement-Based System Functions in Magnetic Particle Imaging”. *Medical Imaging 2010: Biomedical Applications in Molecular, Structural, and Functional Imaging*. Vol. 7626. San Diego, 2010, 76261F. DOI: `10.1117/12.844181`.

[136] T. Knopp, K. Them, M. Kaul, and N. Gdaniec. “Joint Reconstruction of Non-Overlapping Magnetic Particle Imaging Focus-Field Data”. *Physics in Medicine & Biology* 60.8 (2015), pp. L15–L21. DOI: `10.1088/0031-9155/60/8/L15`.

[137] T. Knopp. *Effiziente Rekonstruktion Und Alternative Spulentopologien Für Magnetic-Particle-Imaging*. Vieweg+Teubner, 2011. DOI: `10.1007/978-3-8348-8129-8`.

[138] T. Knopp. *https://github.com/MagneticParticleImaging/MPIUI.jl - An Interactive GUI in the Julia Programming Language.* 2024.

[139] T. Knopp, H. Albers, M. Grosser, M. Möddel, and T. Kluth. “Exploiting the Fourier Neural Operator for Faster Magnetization Model Evaluations Based on the Fokker-Planck Equation”. *International Journal on Magnetic Particle Imaging IJMPI* (Mar. 2023), Vol 9 No 1 Suppl 1 (2023). DOI: `10.18416/IJMPI.2023.2303003`.

[140] T. Knopp, S. Biederer, T. Sattel, and T. M. Buzug. “Singular Value Analysis for Magnetic Particle Imaging”. *IEEE Nuclear Science Symposium Conference Record*. 2008, pp. 4525–4529. DOI: `10.1109/NSSMIC.2008.4774296`.

[141] T. Knopp, M. Erbe, S. Biederer, T. F. Sattel, and T. M. Buzug. “Efficient Generation of a Magnetic Field-Free Line”. *Medical Physics*. Vol. 37. Stockholm, May 2010, pp. 3538–3540. DOI: `10.1118/1.3447726`.

[142] T. Knopp, M. Erbe, T. F. Sattel, S. Biederer, and T. M. Buzug. “Generation of a Static Magnetic Field-Free Line Using Two Maxwell Coil Pairs”. *Applied Physics Letters* 97.9 (2010), pp. 92503–92505. DOI: `10.1063/1.3486118`.

[143] T. Knopp, M. Grosser, M. Graeser, T. Gerkmann, and M. Moddel. “Efficient Joint Estimation of Tracer Distribution and Background Signals in Magnetic Particle Imaging Using a Dictionary Approach”. *IEEE Transactions on Medical Imaging* 40.12 (Dec. 2021), pp. 3568–3579. DOI: `10.1109/TMI.2021.3090928`.

[144] T. Knopp, M. Möddel, F. Griese, F. Werner, P. Szwargulski, N. Gdaniec, and M. Boberg. “MPIFiles.Jl: A Julia Package for Magnetic Particle Imaging Files”. *Journal of Open Source Software* 4.38 (2019), p. 1331. DOI: `10.21105/joss.01331`.

[145] T. Knopp, T. F. Sattel, and T. M. Buzug. “Efficient Magnetic Gradient Field Generation with Arbitrary Axial Displacement for Magnetic Particle Imaging”. *IEEE Magnetics Letters* 3 (2012), p. 6500104. DOI: `10.1109/LMAG.2011.2181341`.

[146] T. Knopp, T. F. Sattel, and T. M. Buzug. “Efficient Positioning of the Field-Free Point in Magnetic Particle Imaging”. *Springer Proceedings in Physics*. Vol. 140. 2012, pp. 161–165. DOI: `10.1007/978-3-642-24133-8_26`.

[147] T. Knopp, P. Szwargulski, F. Griese, and M. Gräser. “OpenMPIData: An Initiative for Freely Accessible Magnetic Particle Imaging Data”. *Data in Brief* 28 (2020), p. 104971. DOI: `10.1016/j.dib.2019.104971`.

[148] T. Knopp, P. Szwargulski, F. Griese, M. Grosser, M. Boberg, and M. Möddel. “MPIReco.Jl: Julia Package for Image Reconstruction in MPI”. *International Journal on Magnetic Particle Imaging* 5.1 (2019). DOI: `10.18416/ijmpi.2019.1907001`.

[149] T. Knopp, T. Viereck, G. Bringout, M. Ahlborg, A. von Gladiss, C. Kaethner, A. Neumann, P. Vogel, J. Rahmer, and M. Möddel. “MDF: Magnetic Particle Imaging Data Format” (2016). DOI: `10.48550/ARXIV.1602.06072`.

[150] T. Knopp and A. Weber. “Sparse Reconstruction of the Magnetic Particle Imaging System Matrix”. *IEEE Transactions on Medical Imaging* 32.8 (2013), pp. 1473–1480. DOI: `10.1109/TMI.2013.2258029`.

[151] J. Konkle, P. Goodwill, and S. Conolly. “Development of a Field Free Line Magnet for Projection MPI”. *SPIE Medical Imaging*. Ed. by J. B. Weaver and R. C. Molthen. Lake Buena Vista, Florida, Mar. 2011, p. 79650X. DOI: `10.1117/12.878435`.

[152] J. J. Konkle, P. W. Goodwill, D. W. Hensley, R. D. Orendorff, M. Lustig, and S. M. Conolly. “A Convex Formulation for Magnetic Particle Imaging X-space Reconstruction”. *PLoS ONE* 10.10 (2015), e0140137. DOI: `10.1371/journal.pone.0140137`.

[153] H.-J. Krause, N. Wolters, Y. Zhang, A. Offenhäusser, P. Miethe, M. H. Meyer, M. Hartmann, and M. Keusgen. “Magnetic Particle Detection by Frequency Mixing for Immunoassay Applications”. *Journal of Magnetism and Magnetic Materials* 311.1 (Apr. 2007), pp. 436–444. DOI: `10.1016/j.jmmm.2006.10.1164`.

[154] K. M. Krishnan. “Biomedical Nanomagnetics: A Spin through Possibilities in Imaging, Diagnostics, and Therapy”. *IEEE Transactions on Magnetics* 46.7 (2010), pp. 2523–2558. DOI: `10.1109/TMAG.2010.2046907`.

[155] T. Kuboyabu, A. Ohki, N. Banura, and K. Murase. “Usefulness of Magnetic Particle Imaging for Monitoring the Effect of Magnetic Targeting”. *Open Journal of Medical Imaging* 06.02 (2016), pp. 33–41. DOI: `10.4236/ojmi.2016.62004`.

[156] S. Latus, F. Griese, M. Schlüter, C. Otte, M. Möddel, M. Graeser, T. Saathoff, T. Knopp, and A. Schlaefer. “Bimodal Intravascular Volumetric Imaging Combining OCT and MPI”. *Medical Physics* 46.3 (2019), pp. 1371–1383. DOI: `10.1002/mp.13388`.

[157] R. Lawaczeck, H. Bauer, T. Frenzel, M. Hasegawa, Y. Ito, K. Kito, N. Miwa, H. Tsutsui, H. Vogler, and H. J. Weinmann. “Magnetic Iron Oxide Particles Coated with Carboxydextran for Parenteral Administration and Liver Contrasting: Pre-clinical Profile of SH U555A”. *Acta Radiologica* 38.4 (1997), pp. 584–597. DOI: `10.1080/02841859709174391`.

[158] T.-A. Le, X. Zhang, A. K. Hoshiar, and J. Yoon. “Real-Time Two-Dimensional Magnetic Particle Imaging for Electromagnetic Navigation in Targeted Drug Delivery”. *Sensors* 17.9 (Sept. 2017), p. 2050. DOI: `10.3390/s17092050`.

[159] R. F. Lee, R. O. Giaquinto, and C. J. Hardy. "Coupling and Decoupling Theory and Its Application to the MRI Phased Array". *Magnetic Resonance in Medicine* 48.1 (July 2002), pp. 203–213. DOI: `10.1002/mrm.10186`.

[160] M. M. Lell, K. Anders, M. Uder, E. Klotz, H. Ditt, F. Vega-Higuera, T. Boskamp, W. A. Bautz, and B. F. Tomandl. "New Techniques in CT Angiography". *RadioGraphics* 26.suppl_1 (Oct. 2006), S45–S62. DOI: `10.1148/rg.26si065508`.

[161] F. Lieb and T. Knopp. "A Wavelet-based Sparse Row-action Method for Image Reconstruction in Magnetic Particle Imaging". *Medical Physics* 48.7 (July 2021), pp. 3893–3903. DOI: `10.1002/mp.14938`.

[162] E. Lin and A. Alessio. "What Are the Basic Concepts of Temporal, Contrast, and Spatial Resolution in Cardiac CT?" *Journal of Cardiovascular Computed Tomography* 3.6 (Nov. 2009), pp. 403–408. DOI: `10.1016/j.jcct.2009.07.003`.

[163] K. Lu, P. W. Goodwill, E. U. Saritas, B. Zheng, and S. M. Conolly. "Linearity and Shift Invariance for Quantitative Magnetic Particle Imaging". *IEEE Transactions on Medical Imaging* 32.9 (2013), pp. 1565–1575. DOI: `10.1109/TMI.2013.2257177`.

[164] P. Ludewig, M. Graeser, N. D. Forkert, F. Thieben, J. Rández-Garbayo, J. Rieckhoff, K. Lessmann, F. Förger, P. Szwargulski, T. Magnus, and T. Knopp. "Magnetic Particle Imaging for Assessment of Cerebral Perfusion and Ischemia". *WIREs Nanomedicine and Nanobiotechnology* 14.1 (Jan. 2022). DOI: `10.1002/wnan.1757`.

[165] P. Ludewig et al. "Magnetic Particle Imaging for Real-Time Perfusion Imaging in Acute Stroke". *ACS Nano* 11.10 (2017), pp. 10480–10488. DOI: `10.1021/acsnano.7b05784`.

[166] K. Lüdtke-Buzug, J. Haegele, S. Biederer, T. F. Sattel, M. Erbe, R. L. Duschka, J. Barkhausen, and F. M. Vogt. "Comparison of Commercial Iron Oxide-Based MRI Contrast Agents with Synthesized High-Performance MPI Tracers". *Biomedizinische Technik* 58.6 (2013), pp. 527–533. DOI: `10.1515/bmt-2012-0059`.

[167] M. Lustig, D. Donoho, and J. M. Pauly. "Sparse MRI: The Application of Compressed Sensing for Rapid MR Imaging". *Magnetic Resonance in Medicine* 58.6 (2007), pp. 1182–1195. DOI: `10.1002/mrm.21391`.

[168] S. Lyer, T. Knopp, F. Werner, J. Zaloga, R. Friedrich, L. Trahms, F. Wiekhorst, T. Struffert, T. Engelhorn, A. Dörfler, T. Baeuerle, M. Uder, R. Tietze, C. Janko, and C. Alexiou. "Multifunctional SPIONs for Theranostics in Cancer". *International Journal on Magnetic Particle Imaging* 4.1 (Aug. 2018), pp. 1–5. DOI: `10.18416/IJMPI.2018.1808001`.

[169] A. Mahmood, M. Dadkhah, M. O. Kim, and J. Yoon. "A Novel Design of an MPI-Based Guidance System for Simultaneous Actuation and Monitoring of Magnetic Nanoparticles". *IEEE Transactions on Magnetics* 51.2 (Feb. 2015), p. 8000305. DOI: `10.1109/TMAG.2014.2358252`.

[170] K. Maier-Hauff, R. Rothe, R. Scholz, U. Gneveckow, P. Wust, B. Thiesen, A. Feussner, A. Von Deimling, N. Waldoefner, R. Felix, and A. Jordan. "Intracranial Thermotherapy Using Magnetic Nanoparticles Combined with External Beam Radiotherapy: Results of a Feasibility Study on Patients with Glioblastoma Multiforme". *Journal of Neuro-Oncology* 81.1 (Jan. 2007), pp. 53–60. DOI: `10.1007/s11060-006-9195-0`.

[171] A. V. Makela, M. A. Schott, C. S. Madsen, E. M. Greeson, and C. H. Contag. "Magnetic Particle Imaging of Magnetotactic Bacteria as Living Contrast Agents Is Improved by Altering Magnetosome Arrangement". *Nano Letters* 22.12 (June 2022), pp. 4630–4639. DOI: `10.1021/acs.nanolett.1c05042`.

[172] A. Malhotra, K. Lüdtke-Buzug, and Hendrik. "A Synthesis Apparatus for the Continuous Flow Synthesis of Magnetic Nanoparticles". *International Journal on Magnetic Particle Imaging* (Mar. 2022), Vol 8 No 1 Suppl 1 (2022). DOI: `10.18416/IJMPI.2022.2203072`.

[173] E. E. Mason, E. Barcikowski, J. Carl, M. Chandeeing, B. Davison, B. Fellows, W. Fetsch, K. Fields, J. Greve, J. J. Konkle, et al. "Preliminary Results: Large Bore Clinical MPI System Imaging Human Head-Sized Fovs". *International Journal on Magnetic Particle Imaging IJMPI*. Vol. 10. 2024, 1 Suppl 1.

[174] E. E. Mason, C. Z. Cooley, S. F. Cauley, M. A. Griswold, S. M. Conolly, and L. L. Wald. "Design Analysis of an MPI Human Functional Brain Scanner." *International Journal on Magnetic Particle Imaging* 3.1 (2017). DOI: `10.18416/ijmpi.2017.1703008`.

[175] E. E. Mason, E. Mattingly, K. Herb, M. Śliwiak, S. Franconi, C. Z. Cooley, P. J. Slanetz, and L. L. Wald. "Concept for Using Magnetic Particle Imaging for Intraoperative Margin Analysis in Breast-Conserving Surgery". *Scientific Reports* 11.1 (June 2021), p. 13456. DOI: `10.1038/s41598-021-92644-8`.

[176] E. Mattingly, E. Mason, K. Herb, M. Śliwiak, J. Drago, M. Graeser, and L. Wald. "A Sensitive, Stable, Continuously Rotating FFL MPI System for Functional Imaging of the Rat Brain". *International Journal on Magnetic Particle Imaging* (Dec. 2022), Vol 8 No 2 (2022). DOI: `10.18416/IJMPI.2022.2212001`.

[177] E. Mattingly, E. Mason, M. Sliwiak, and L. L. Wald. "Drive and Receive Coil Design for a Human-Scale MPI System". *International Journal on Magnetic Particle Imaging* (Mar. 2022), Vol 8 No 1 Suppl 1 (2022). DOI: `10.18416/IJMPI.2022.2203075`.

[178] M. Mauerer, A. Tuysuz, and J. W. Kolar. "Distortion Analysis of Low-THD/High-Bandwidth GaN/SiC Class-D Amplifier Power Stages". *2015 IEEE Energy Conversion Congress and Exposition (ECCE)*. Montreal, QC, Canada: IEEE, Sept. 2015, pp. 2563–2571. DOI: `10.1109/ECCE.2015.7310020`.

[179] J. C. Maxwell. "VIII. A Dynamical Theory of the Electromagnetic Field". *Philosophical Transactions of the Royal Society of London* 155 (Dec. 1865), pp. 459–512. DOI: `10.1098/rstl.1865.0008`.

[180] J. C. Maxwell. "A Treatise on Electricity and Magnetism". *Nature* 7.182 (Apr. 1873), pp. 478–480. DOI: 10.1038/007478a0.

[181] M. H. Mazurek et al. "Detection of Intracerebral Hemorrhage Using Low-Field, Portable Magnetic Resonance Imaging in Patients With Stroke". *Stroke* 54.11 (Nov. 2023), pp. 2832–2841. DOI: 10.1161/STROKEAHA.123.043146.

[182] V. Mecea. "Loaded Vibrating Quartz Sensors". *Sensors and Actuators A: Physical* 40.1 (Jan. 1994), pp. 1–27. DOI: 10.1016/0924-4247(94)85026-7.

[183] S. A. Mirbozorgi, H. Bahrami, M. Sawan, and B. Gosselin. "A Smart Multicoil Inductively Coupled Array for Wireless Power Transmission". *IEEE Transactions on Industrial Electronics* 61.11 (Nov. 2014), pp. 6061–6070. DOI: 10.1109/TIE.2014.2308138.

[184] L. Mirzojan, M. A. Rückert, C. Greiner, A. V. Böhn, T. Kampf, V. C. Behr, and P. Vogel. "Fully Mechanical Driven Traveling Wave MPI". *International Journal on Magnetic Particle Imaging* (Mar. 2022), Vol 8 No 1 Suppl 1 (2022). DOI: 10.18416/IJMPI.2022.2203011.

[185] M. Möddel, F. Griese, T. Kluth, and T. Knopp. "Estimating Orientation Using Multi-Contrast MPI". *International Journal on Magnetic Particle Imaging* 6.2 (2020), pp. 1–3. DOI: 10.18416/IJMPI.2020.2009023.

[186] M. Möddel, C. Meins, J. Dieckhoff, and T. Knopp. "Viscosity Quantification Using Multi-Contrast Magnetic Particle Imaging". *New Journal of Physics* 20.8 (Aug. 2018), p. 83001. DOI: 10.1088/1367-2630/aad44b.

[187] I. Molwitz, H. Ittrich, T. Knopp, T. Mummert, J. Salamon, C. Jung, G. Adam, and M. G. Kaul. "First Magnetic Particle Imaging Angiography in Human-Sized Organs by Employing a Multimodal Ex Vivo Pig Kidney Perfusion System". *Physiological Measurement* 40.10 (2019), p. 105002. DOI: 10.1088/1361-6579/ab4436.

[188] K. Murase, M. Aoki, N. Banura, K. Nishimoto, A. Mimura, T. Kuboyabu, and I. Yabata. "Usefulness of Magnetic Particle Imaging for Predicting the Therapeutic Effect of Magnetic Hyperthermia". *Open Journal of Medical Imaging* 05.02 (2015), pp. 85–99. DOI: 10.4236/ojmi.2015.52013.

[189] L. Nawwas, M. Möddel, T. Knopp, and C. Brandt. "Bias-Reduction for Sparsity Promoting Regularization in Magnetic Particle Imaging". *International Journal on Magnetic Particle Imaging* 6.2 (2020), pp. 1–3. DOI: 10.18416/IJMPI.2020.2009041.

[190] L. Nawwas, C. Brandt, P. Szwargulski, T. Knopp, and M. Möddel. "Reduction of Bias for Sparsity Promoting Regularization in MPI". *International Journal on Magnetic Particle Imaging* (Dec. 2021), Vol 7 No 2 (2021). DOI: 10.18416/IJMPI.2021.2112002.

[191] L. Nawwas, M. Möddel, and T. Knopp. "Influence of the System Matrix on Channel Leakage Artifacts in Multi-Contrast MPI" (Mar. 2024). DOI: 10.18416/IJMPI.2024.2403033.

[192] L. Nawwas, M. Möddel, and T. Knopp. "Multi-Contrast MPI Channel Leakage Reduction Using a Two-Step Measurement and Reconstruction Method" (Mar. 2024). DOI: 10.18416/IJMPI.2024.2403029.

[193] L. Néel. "Thermoremanent Magnetization of Fine Powders". *Reviews of Modern Physics* 25.1 (Jan. 1953), pp. 293–295. DOI: 10.1103/RevModPhys.25.293.

[194] A. Neumann, K. Gräfe, A. Von Gladiss, M. Ahlborg, A. Behrends, X. Chen, J. Schumacher, Y. Blancke Soares, T. Friedrich, H. Wei, A. Malhorta, E. Aderhold, A. C. Bakenecker, K. Lüdtke-Buzug, and T. M. Buzug. "Recent Developments in Magnetic Particle Imaging". *Journal of Magnetism and Magnetic Materials* 550 (May 2022), p. 169037. DOI: 10.1016/j.jmmm.2022.169037.

[195] D. Niculaes, A. Lak, G. C. Anyfantis, S. Marras, O. Laslett, S. K. Avugadda, M. Cassani, D. Serantes, O. Hovorka, R. Chantrell, and T. Pellegrino. "Asymmetric Assembling of Iron Oxide Nanocubes for Improving Magnetic Hyperthermia Performance". *ACS Nano* 11.12 (Dec. 2017), pp. 12121–12133. DOI: 10.1021/acsnano.7b05182.

[196] P. I. Nikitin, P. M. Vetoshko, and T. I. Ksenevich. "New Type of Biosensor Based on Magnetic Nanoparticle Detection". *Journal of Magnetism and Magnetic Materials* 311.1 (Apr. 2007), pp. 445–449. DOI: 10.1016/j.jmmm.2006.10.1180.

[197] N. Nothnagel, J. Rahmer, B. Gleich, A. Halkola, T. M. Buzug, and J. Borgert. "Steering of Magnetic Devices with a Magnetic Particle Imaging System". *IEEE Transactions on Biomedical Engineering*. Vol. 63. Nov. 2016, pp. 2286–2293. DOI: 10.1109/TBME.2016.2524070.

[198] H. Nyquist. "Certain Topics in Telegraph Transmission Theory". *Transactions of the American Institute of Electrical Engineers* 47.2 (Apr. 1928), pp. 617–644. DOI: 10.1109/T-AIEE.1928.5055024.

[199] A. A. Ozaslan, A. Alacaoglu, O. B. Demirel, T. Cukur, and E. U. Saritas. "Fully Automated Gridding Reconstruction for Non-Cartesian x-Space Magnetic Particle Imaging". *Physics in Medicine & Biology* 64.16 (2019), p. 165018. DOI: 10.1088/1361-6560/ab3525.

[200] A. A. Ozaslan, M. Utkur, U. Canpolat, M. A. Tuncer, K. Karli Oguz, and E. U. Saritas. "PNS Limits for Human Head-Size MPI Systems: Preliminary Results". *International Journal on Magnetic Particle Imaging* (Mar. 2022), Vol 8 No 1 Suppl 1 (2022). DOI: 10.18416/IJMPI.2022.2203028.

[201] M. H. Pablico-Lansigan, S. F. Situ, and A. C. S. Samia. "Magnetic Particle Imaging: Advancements and Perspectives for Real-Time in Vivo Monitoring and Image-Guided Therapy". *Nanoscale* 5.10 (2013), p. 4040. DOI: `10.1039/c3nr00544e`.

[202] D. Pantke, N. Holle, A. Mogarkar, M. Straub, and V. Schulz. "Multifrequency Magnetic Particle Imaging Enabled by a Combined Passive and Active Drive Field Feed-through Compensation Approach." *Medical physics* 46.9 (Sept. 2019), pp. 4077–4086. DOI: `10.1002/mp.13650`.

[203] H. Paysen, O. Kosch, J. Wells, N. Loewa, and F. Wiekhorst. "Characterization of Noise and Background Signals in a Magnetic Particle Imaging System". *Physics in Medicine & Biology* 65.23 (Dec. 2020), p. 235031. DOI: `10.1088/1361-6560/abc364`.

[204] H. Paysen, J. Wells, O. Kosch, U. Steinhoff, J. Franke, L. Trahms, T. Schaeffter, and F. Wiekhorst. "Improved Sensitivity and Limit-of-Detection Using a Receive-Only Coil in Magnetic Particle Imaging". *Physics in Medicine & Biology* 63.13 (July 2018), 13NT02. DOI: `10.1088/1361-6560/aacb87`.

[205] C. Pestana. *Fluids and Electrolytes in the Surgical Patient*. 5th ed. Philadelphia: Lippincott Williams & Wilkins, 2000.

[206] J. L. Prince and J. M. Links. *Medical Imaging Signals and Systems*. 2., [updated] ed. Boston: Pearson, 2015.

[207] H. Radermacher, F. Schrank, D. Pantke, F. Mueller, M. Peters, and V. Schulz. "Highly Flexible Gradiometer Coil Arrangement Offering Improved Passive Compensation for Multi-Frequency MPI". *International Journal on Magnetic Particle Imaging IJMPI* (Mar. 2023), Vol 9 No 1 Suppl 1 (2023). DOI: `10.18416/IJMPI.2023.2303030`.

[208] J. Radon. "Über Die Bestimmung von Funktionen Durch Ihre Integralwerte Längs Gewisser Mannigfaltigkeiten". *Berichte der Sächsischen Akademie der Wissenschaft* 69 (1917), pp. 71–86. DOI: `10.1090/psapm/027/692055`.

[209] J. Rahmer, A. Halkola, B. Gleich, I. Schmale, and J. Borgert. "First Experimental Evidence of the Feasibility of Multi-Color Magnetic Particle Imaging". *Physics in Medicine & Biology* 60.5 (2015), p. 1775.

[210] J. Rahmer, B. Gleich, C. Bontus, I. Schmale, J. Schmidt, J. Kanzenbach, O. Woywode, J. Weizenecker, and J. Borgert. "Results on Rapid 3D Magnetic Particle Imaging with a Large Field of View". *Proc. ISMRM*. Vol. 19. 2011, p. 629.

[211] J. Rahmer, D. Wirtz, C. Bontus, J. Borgert, and B. Gleich. "Interactive Magnetic Catheter Steering with 3-D Real-Time Feedback Using Multi-Color Magnetic Particle Imaging". *IEEE Transactions on Medical Imaging* 36.7 (2017), pp. 1449–1456. DOI: `10.1109/TMI.2017.2679099`.

[212] J. Rahmer, C. Stehning, and B. Gleich. "Spatially Selective Remote Magnetic Actuation of Identical Helical Micromachines". *Science Robotics* 2.3 (2017). DOI: `10.1126/scirobotics.aal2845`.

[213] J. Rahmer, C. Stehning, and B. Gleich. "Remote Magnetic Actuation Using a Clinical Scale System". *PLoS ONE* 13.3 (2018), e0193546. DOI: `10.1371/journal.pone.0193546`.

[214] J. Rahmer, J. Weizenecker, B. Gleich, and J. Borgert. "Signal Encoding in Magnetic Particle Imaging: Properties of the System Function". *BMC Medical Imaging* 9.4 (2009). DOI: `10.1186/1471-2342-9-4`.

[215] J. Rahmer, J. Weizenecker, B. Gleich, and J. Borgert. "Analysis of a 3-D System Function Measured for Magnetic Particle Imaging". *IEEE Transactions on Medical Imaging* 31.6 (2012), pp. 1289–1299. DOI: `10.1109/TMI.2012.2188639`.

[216] B. Ramlawi. "The Era of Catheter-Based and Minimally Invasive Cardiac Surgery". *Methodist DeBakey Cardiovascular Journal* 12.1 (Jan. 2016), p. 3. DOI: `10.14797/mdcj-12-1-3`.

[217] A. M. Rauwerdink, E. W. Hansen, and J. B. Weaver. "Nanoparticle Temperature Estimation in Combined Ac and Dc Magnetic Fields". *Physics in Medicine & Biology* 54.19 (2009), p. L51. DOI: `10.1088/0031-9155/54/19/L01`.

[218] A. M. Rauwerdink and J. B. Weaver. "Measurement of Molecular Binding Using the Brownian Motion of Magnetic Nanoparticle Probes". *Applied Physics Letters* 96.3 (2010), 3pp. DOI: `10.1063/1.3291063`.

[219] A. M. Rauwerdink and J. B. Weaver. "Viscous Effects on Nanoparticle Magnetization Harmonics". *Journal of Magnetism and Magnetic Materials* 322.6 (2010), pp. 609–613. DOI: `10.1016/j.jmmm.2009.10.024`.

[220] P. Reimer and T. Balzer. "Ferucarbotran (Resovist): A New Clinically Approved RES-specific Contrast Agent for Contrast-Enhanced MRI of the Liver: Properties, Clinical Development, and Applications". *European Radiology* 13.6 (2003), pp. 1266–1276. DOI: `10.1007/s00330-002-1721-7`.

[221] A. Remmo, N. Löwa, O. Kosch, D. Eberbeck, A. Ludwig, L. Kampen, C. Grüttner, and F. Wiekhorst. "Cell Tracking by Magnetic Particle Imaging: Methodology for Labeling THP-1 Monocytes with Magnetic Nanoparticles for Cellular Imaging". *Cells* 11.18 (Sept. 2022), p. 2892. DOI: `10.3390/cells11182892`.

[222] F. Rentzeperis, D. Rivera, J. Y. Zhang, C. Brown, T. Young, B. Rodriguez, A. Schupper, G. Price, J. Gomberg, T. Williams, A. Bouras, and C. Hadjipanayis. "Recent Developments in Magnetic Hyperthermia Therapy (MHT) and Magnetic Particle Imaging (MPI) in the Brain Tumor Field: A Scoping Review and Meta-Analysis". *Micromachines* 15.5 (Apr. 2024), p. 559. DOI: `10.3390/mi15050559`.

[223] K. Riahi, M. M. Van De Loosdrecht, L. Alic, and B. Ten Haken. “Magnetic Performance of Synomag® Nanoparticles in Various Environments”. *International Journal on Magnetic Particle Imaging* (Sept. 2020), Vol 6 No 2 Suppl. 1 (2020). DOI: 10.18416/IJMPI.2020.2009022.

[224] P. B. Roemer, W. A. Edelstein, C. E. Hayes, S. P. Souza, and O. M. Mueller. “The NMR Phased Array”. *Magnetic Resonance in Medicine* 16.2 (Nov. 1990), pp. 192–225. DOI: 10.1002/mrm.1910160203.

[225] T. J. Rouphael. *Wireless Receiver Architectures and Design: Antennas, RF, Synthesizers, Mixed Signal, and Digital Signal Processing*. Burlington: Elsevier Science, 2014.

[226] J. Salamon, J. Dieckhoff, M. G. Kaul, C. Jung, G. Adam, M. Möddel, T. Knopp, S. Draack, F. Ludwig, and H. Ittrich. “Visualization of Spatial and Temporal Temperature Distributions with Magnetic Particle Imaging for Liver Tumor Ablation Therapy”. *Scientific Reports* 10.1 (2020), pp. 1–11. DOI: 10.1038/s41598-020-64280-1.

[227] J. Salamon, M. Hofmann, C. Jung, M. G. Kaul, F. Werner, K. Them, R. Reimer, P. Nielsen, A. Vom Scheidt, G. Adam, T. Knopp, and H. Ittrich. “Magnetic Particle / Magnetic Resonance Imaging: In-Vitro MPI-Guided Real Time Catheter Tracking and 4D Angioplasty Using a Road Map and Blood Pool Tracer Approach”. *PLOS ONE* 11.6 (June 2016). Ed. by M. Yamamoto, e0156899. DOI: 10.1371/journal.pone.0156899.

[228] S. Salamzadeh, E. Krooshoop, B. Ten Haken, and L. Alic. “DiffMag Handheld Probe for Perioperative Lymph Node Harvesting”. *International Journal on Magnetic Particle Imaging IJMPI* (Mar. 2023), Vol 9 No 1 Suppl 1 (2023). DOI: 10.18416/IJMPI.2023.2303052.

[229] E. U. Saritas, P. W. Goodwill, and S. M. Conolly. “Effects of Pulse Duration on Magnetostimulation Thresholds”. *Medical Physics* 42.6 (2015), pp. 3005–3012. DOI: 10.1118/1.4921209.

[230] E. U. Saritas, P. W. Goodwill, G. Z. Zhang, and S. M. Conolly. “Magnetostimulation Limits in Magnetic Particle Imaging”. *IEEE Transactions on Medical Imaging* 32.9 (2013), pp. 1600–1610. DOI: 10.1109/TMI.2013.2260764.

[231] T. F. Sattel, S. Biederer, T. Knopp, K. Lüdtke-Buzug, B. Gleich, J. Borgert, and T. M. Buzug. “Hand-Held Concept of a Magnetic Particle Imaging Device”. *Suppl. Mol. Imaging Biol.* Vol. 11. Montreal, Sept. 2009, J521.

[232] T. F. Sattel, S. Biederer, T. Knopp, K. Lüdtke-Buzug, B. Gleich, J. Weizenecker, J. Borgert, and T. M. Buzug. “Single-Sided Coil Configuration for Magnetic Particle Imaging”. *IFMBE Proceedings*. Vol. 25. Munich, Sept. 2009, pp. 281–284. DOI: 10.1007/978-3-642-03885-3_78.

[233] T. F. Sattel, O. Woywode, J. Weizenecker, J. Rahmer, B. Gleich, and J. Borgert. “Setup and Validation of an MPI Signal Chain for a Drive Field Frequency of 150 kHz”. *IEEE Transactions on Magnetics* 51.2 (Feb. 2015), pp. 1–3. DOI: 10.1109/TMAG.2014.2326256.

[234] J.-P. Scheel, J. Ackers, and M. Graeser. “Influence of Switched-Mode Power Supplies in an Arbitrary Waveform Magnetic Particle Spectroscope”. *International Journal on Magnetic Particle Imaging IJMPI* 10.1 Suppl 1 (2024).

[235] K. Scheffler, M. Boberg, and T. Knopp. “Boundary Artifact Reduction by Extrapolating System Matrices Outside the Field-of-View in Joint Multi-Patch MPI”. *International Journal on Magnetic Particle Imaging* (Mar. 2022), Vol 8 No 1 Suppl 1 (2022). DOI: 10.18416/IJMPI.2022.2203019.

[236] K. Scheffler, M. Boberg, and T. Knopp. “Hands-Free Reconstruction for MPI”. *International Journal on Magnetic Particle Imaging IJMPI* (Mar. 2023), Vol 9 No 1 Suppl 1 (2023). DOI: 10.18416/IJMPI.2023.2303025.

[237] K. Scheffler, M. Boberg, and T. Knopp. “Solving the MPI Reconstruction Problem with Automatically Tuned Regularization Parameters”. *Physics in Medicine & Biology* 69.4 (Feb. 2024), p. 045024. DOI: 10.1088/1361-6560/ad2231.

[238] K. Scheffler, L. Meyn, F. Foerger, M. Boberg, M. Martin, and T. Knopp. “Ellipsoidal Harmonic Expansions for Efficient Approximation of Magnetic Fields in Medical Imaging”. *International Journal on Magnetic Particle Imaging IJMPI* 10.1 Suppl 1 (Mar. 2024). DOI: 10.18416/IJMPI.2024.2403006.

[239] B. Schiek, I. Rolfes, and H. J. Siweris. *Noise in High-Frequency Circuits and Oscillators*. Hoboken, N.J: Wiley-Interscience, 2006.

[240] I. Schmale, B. G. J. Borgert, and J. Weizenecker. “Noise within Magnetic Particle Imaging”. *Magnetic Nanoparticles*. Institute of Medical Engineering, University of Lübeck, Germany: WORLD SCIENTIFIC, Aug. 2010, pp. 154–161. DOI: 10.1142/9789814324687_0022.

[241] I. Schmale, B. Gleich, O. Mende, and J. Borgert. “On the Design of Human-Size MPI Drive-Field Generators Using RF Litz Wires”. *2015 5th International Workshop on Magnetic Particle Imaging (IWMPI)*. Istanbul, Turkey: IEEE, Mar. 2015, pp. 1–1. DOI: 10.1109/IWMPI.2015.7107071.

[242] I. Schmale, B. Gleich, J. Rahmer, C. Bontus, J. Schmidt, and J. Borgert. “MPI Safety in the View of MRI Safety Standards”. *IEEE Transactions on Magnetics* 51.2 (Feb. 2015), pp. 1–4. DOI: 10.1109/TMAG.2014.2322940.

[243] I. Schmale, B. Gleich, J. Schmidt, J. Rahmer, C. Bontus, R. Eckart, B. David, M. Heinrich, O. Mende, O. Woywode, J. Jokram, and J. Borgert. “Human PNS and SAR Study in the Frequency Range from 24 to 162 kHz”. *2013 International Workshop on Magnetic Particle Imaging, IWMPI 2013*. 2013, p. 1. DOI: 10.1109/IWMPI.2013.6528346.

[244] O. C. Sehl and P. J. Foster. “The Sensitivity of Magnetic Particle Imaging and Fluorine-19 Magnetic Resonance Imaging for Cell Tracking”. *Scientific Reports* 11.1 (Nov. 2021), p. 22198. DOI: `10.1038/s41598-021-01642-3`.

[245] O. C. Sehl, J. J. Gevaert, K. P. Melo, N. N. Knier, and P. J. Foster. “A Perspective on Cell Tracking with Magnetic Particle Imaging”. *Tomography* 6.4 (Dec. 2020), pp. 315–324. DOI: `10.18383/j.tom.2020.00043`.

[246] C. Shasha and K. M. Krishnan. “Nonequilibrium Dynamics of Magnetic Nanoparticles with Applications in Biomedicine”. *Advanced Materials* 33.23 (June 2021), p. 1904131. DOI: `10.1002/adma.201904131`.

[247] C. Shasha, E. Teeman, K. M. Krishnan, P. Szwargulski, T. Knopp, and M. Möddel. “Discriminating Nanoparticle Core Size Using Multi-Contrast MPI”. *Physics in Medicine & Biology* 64.7 (2019), p. 74001. DOI: `10.1088/1361-6560/ab0fc9`.

[248] M. I. Shliomis and V. I. Stepanov. “Theory of the Dynamic Susceptibility of Magnetic Fluids”. *Advances in Chemical Physics*. Ed. by W. Coffey. Hoboken, NJ, USA: John Wiley & Sons, Inc., Mar. 2007, pp. 1–30. DOI: `10.1002/9780470141465.ch1`.

[249] D. Shmilovitz. “On the Definition of Total Harmonic Distortion and Its Effect on Measurement Interpretation”. *IEEE Transactions on Power Delivery* 20.1 (Jan. 2005), pp. 526–528. DOI: `10.1109/TPWRD.2004.839744`.

[250] N. Singh, G. J. Jenkins, R. Asadi, and S. H. Doak. “Potential Toxicity of Superparamagnetic Iron Oxide Nanoparticles (SPION)”. *Nano Reviews* 1.1 (Jan. 2010), p. 5358. DOI: `10.3402/nano.v1i0.5358`.

[251] G. Song, M. Chen, Y. Zhang, L. Cui, H. Qu, X. Zheng, M. Wintermark, Z. Liu, and J. Rao. “Janus Iron Oxides @ Semiconducting Polymer Nanoparticle Tracer for Cell Tracking by Magnetic Particle Imaging”. *Nano Letters* 18.1 (Jan. 2018), pp. 182–189. DOI: `10.1021/acs.nanolett.7b03829`.

[252] P. R. Stauffer, T. C. Cetas, and R. C. Jones. “Magnetic Induction Heating of Ferromagnetic Implants for Inducing Localized Hyperthermia in Deep-Seated Tumors”. *IEEE Transactions on Biomedical Engineering* BME-31.2 (Feb. 1984), pp. 235–251. DOI: `10.1109/TBME.1984.325334`.

[253] C. Stehning, B. Gleich, and J. Rahmer. “Simultaneous Magnetic Particle Imaging (MPI) and Temperature Mapping Using Multi-Color MPI”. *International Journal on Magnetic Particle Imaging* 2.6 (2016), pp. 1–6.

[254] E. M. Stein and R. Shakarchi. *Fourier Analysis: An Introduction*. Princeton Lectures in Analysis 1. Princeton: Princeton University Press, 2003.

[255] J. Stelzner, A. Bakenecker, A. Behrends, G. Bringout, X. Chen, A. Von Gladiss, K. Gräfe, J. Schumacher, and T. Buzug. “Implementation and Imaging with a Versatile 180 Mm Magnetic-Particle-Imaging Field-Generator”. *Journal of Magnetism and Magnetic Materials* 559 (Oct. 2022), p. 169509. DOI: `10.1016/j.jmmm.2022.169509`.

[256] J. Stelzner, M. Graeser, A. Bakenecker, A. von Gladiss, G. Bringout, and T. M. Buzug. “Measurements Inside a Rabbit Sized FFL-MPI Device Using a Gradiometric Receive Coil”. *International Journal on Magnetic Particle Imaging* 3.1 (2017), pp. 1–5. DOI: `10.18416/ijmpi.2017.1703012`.

[257] M. Storath, C. Brandt, M. Hofmann, T. Knopp, J. Salamon, A. Weber, and A. Weinmann. “Edge Preserving and Noise Reducing Reconstruction for Magnetic Particle Imaging”. *IEEE Transactions on Medical Imaging* 36.1 (2017), pp. 74–85. DOI: `10.1109/TMI.2016.2593954`.

[258] C. Sullivan. “Optimal Choice for Number of Strands in a Litz-Wire Transformer Winding”. *IEEE Transactions on Power Electronics* 14.2 (Mar. 1999), pp. 283–291. DOI: `10.1109/63.750181`.

[259] C. Sun, J. S. Lee, and M. Zhang. “Magnetic Nanoparticles in MR Imaging and Drug Delivery”. *Advanced Drug Delivery Reviews* 60.11 (Aug. 2008), pp. 1252–1265. DOI: `10.1016/j.addr.2008.03.018`.

[260] P. Szwargulski and T. Knopp. “Influence of the Receive Channel Number on the Spatial Resolution in Magnetic Particle Imaging”. *International Journal on Magnetic Particle Imaging* Vol.3 (2017), 7 pages. DOI: `10.18416/IJMPI.2017.1703014`.

[261] P. Szwargulski, M. Moddel, N. Gdaniec, and T. Knopp. “Efficient Joint Image Reconstruction of Multi-Patch Data Reusing a Single System Matrix in Magnetic Particle Imaging”. *IEEE Transactions on Medical Imaging* 38.4 (Apr. 2019), pp. 932–944. DOI: `10.1109/TMI.2018.2875829`.

[262] P. Szwargulski, M. Wilmes, E. Javidi, F. Thieben, M. Graeser, M. Koch, C. Gruettner, G. Adam, C. Gerloff, T. Magnus, T. Knopp, and P. Ludewig. “Monitoring Intracranial Cerebral Hemorrhage Using Multicontrast Real-Time Magnetic Particle Imaging”. *ACS Nano* 14.10 (2020), pp. 13913–13923. DOI: `10.1021/acsnano.0c06326`.

[263] E. T. Tan, Y. Hua, E. W. Fiveland, M. E. Vermilyea, J. E. Piel, K. J. Park, V. B. Ho, and T. K. F. Foo. “Peripheral Nerve Stimulation Limits of a High Amplitude and Slew Rate Magnetic Field Gradient Coil for Neuroimaging”. *Magnetic Resonance in Medicine* 83.1 (Jan. 2020), pp. 352–366. DOI: `10.1002/mrm.27909`.

[264] B. Tasdelen, M. Utkur, E. Atalar, and E. U. Saritas. “Vector Modulator Based Automated Active Compensation of Direct Feedthrough in Magnetic Particle Imaging”. *29th International Society for Magnetic Resonance in Medicine (ISMRM),(Online)* (2021), No. 4266.

[265] A. Tateo, A. Iurino, G. Settanni, A. Andrisani, P. F. Stifanelli, P. Larizza, F. Mazzia, R. M. Mininni, S. Tangaro, and R. Bellotti. “Hybrid X-Space: A New Approach for MPI Reconstruction”. *Physics in Medicine & Biology* 61.11 (2016), pp. 4061–4077. DOI: `10.1088/0031-9155/61/11/4061`.

[266] Z. W. Tay, P. Chandrasekharan, A. Chiu-Lam, D. W. Hensley, R. Dhavalikar, X. Y. Zhou, E. Y. Yu, P. W. Goodwill, B. Zheng, C. Rinaldi, and S. M. Conolly. “Magnetic Particle Imaging-Guided Heating in Vivo Using Gradient Fields for Arbitrary Localization of Magnetic Hyperthermia Therapy”. *ACS Nano* 12.4 (2018), pp. 3699–3713. DOI: `10.1021/acsnano.8b00893`.

[267] Z. W. Tay, P. Chandrasekharan, X. Y. Zhou, E. Yu, B. Zheng, and S. Conolly. “In Vivo Tracking and Quantification of Inhaled Aerosol Using Magnetic Particle Imaging towards Inhaled Therapeutic Monitoring”. *Theranostics* 8.13 (2018), pp. 3676–3687. DOI: `10.7150/thno.26608`.

[268] Z. W. Tay, P. W. Goodwill, D. W. Hensley, L. A. Taylor, B. Zheng, and S. M. Conolly. “A High-Throughput, Arbitrary-Waveform, MPI Spectrometer and Relaxometer for Comprehensive Magnetic Particle Optimization and Characterization”. *Scientific Reports* 6 (2016). DOI: `10.1038/srep34180`.

[269] Z. W. Tay, D. Hensley, J. Ma, P. Chandrasekharan, B. Zheng, P. Goodwill, and S. Conolly. “Pulsed Excitation in Magnetic Particle Imaging”. *IEEE Transactions on Medical Imaging* 38.10 (Oct. 2019), pp. 2389–2399. DOI: `10.1109/tmi.2019.2898202`.

[270] Z. W. Tay, D. W. Hensley, E. C. Vreeland, B. Zheng, and S. M. Conolly. “The Relaxation Wall: Experimental Limits to Improving MPI Spatial Resolution by Increasing Nanoparticle Core Size”. *Biomedical Physics & Engineering Express* 3.3 (May 2017), p. 035003. DOI: `10.1088/2057-1976/aa6ab6`.

[271] Z. W. Tay, S. Savliwala, D. W. Hensley, K. B. Fung, C. Colson, B. D. Fellows, X. Zhou, Q. Huynh, Y. Lu, B. Zheng, P. Chandrasekharan, S. M. Rivera-Jimenez, C. M. Rinaldi-Ramos, and S. M. Conolly. “Superferromagnetic Nanoparticles Enable Order-of-Magnitude Resolution & Sensitivity Gain in Magnetic Particle Imaging”. *Small Methods* 5.11 (Nov. 2021), p. 2100796. DOI: `10.1002/smtd.202100796`.

[272] K. Them, M. G. Kaul, C. Jung, M. Hofmann, T. Mummert, F. Werner, and T. Knopp. “Sensitivity Enhancement in Magnetic Particle Imaging by Background Subtraction”. *IEEE Transactions on Medical Imaging*. 3rd ser. 35 (2016), pp. 893–900. DOI: `10.1109/TMI.2015.2501462`.

[273] F. Thieben, M. Boberg, P. Szwargulski, M. Graeser, and T. Knopp. “Gradient Power Reducing Using Pulsed Selection-Field Sequences”. *International Journal on Magnetic Particle Imaging* 6.2 (2020), pp. 1–3. DOI: `10.18416/IJMPI.2020.2009054`.

[274] F. Thieben, M. Boberg, M. Graeser, and T. Knopp. “Efficient 3D Drive-Field Characterization for Magnetic Particle Imaging Systems”. *International Journal on Magnetic Particle Imaging* (Mar. 2022), Vol 8 No 1 Suppl 1 (2022). DOI: `10.18416/IJMPI.2022.2203015`.

[275] F. Thieben, F. Foerger, M. Boberg, T. Liebing, M. Graeser, M. Möddel, and T. Knopp. “Algorithmic Channel Decoupling for Misaligned Receive Coils in Magnetic Particle Imaging”. *International Journal on Magnetic Particle Imaging* (Mar. 2022), Vol 8 No 1 Suppl 1 (2022). DOI: `10.18416/IJMPI.2022.2203029`.

[276] F. Thieben, T. Knopp, M. Boberg, F. Foerger, M. Graeser, and M. Möddel. “On the Receive Path Calibration of Magnetic Particle Imaging Systems”. *IEEE Transactions on Instrumentation and Measurement* 72 (2023), pp. 1–15. DOI: `10.1109/TIM.2022.3219461`.

[277] F. Thieben, F. Mickoleit, S. Tessaro, P. Ludewig, D. Schüler, J. R. Garbayo, R. Uebe, and T. Knopp. “Development of Optimized Magnetic Particle Imaging Tracers Utilizing Genetically Engineered Magnetosomes”. *International Journal on Magnetic Particle Imaging IJMPI* (Mar. 2023), Vol 9 No 1 Suppl 1 (2023). DOI: `10.18416/IJMPI.2023.2303066`.

[278] C. B. Top, A. Güngör, S. Ilbey, and H. E. Güven. “Trajectory Analysis for Field Free Line Magnetic Particle Imaging”. *Medical Physics* 46.4 (2019), pp. 1592–1607. DOI: `10.1002/mp.13411`.

[279] A. Tsanda, P. Jürß, N. Hackelberg, M. Grosser, M. Möddel, and T. Knopp. “Extension of the Kaczmarz Algorithm with a Deep Plug-and-Play Regularizer” (Mar. 2024). DOI: `10.18416/IJMPI.2024.2403010`.

[280] M. Utkur, Y. Muslu, and E. U. Saritas. “Relaxation-Based Color Magnetic Particle Imaging for Viscosity Mapping”. *Applied Physics Letters* 115.15 (2019), p. 152403. DOI: `10.1063/1.5110475`.

[281] M. Utkur and E. U. Saritas. “Simultaneous Temperature and Viscosity Estimation Capability via Magnetic Nanoparticle Relaxation”. *Medical Physics* 49.4 (Apr. 2022), pp. 2590–2601. DOI: `10.1002/mp.15509`.

[282] S. Vaalma, J. Rahmer, N. Panagiotopoulos, R. L. Duschka, J. Borgert, J. Barkhausen, F. M. Vogt, and J. Haegele. “Magnetic Particle Imaging (MPI): Experimental Quantification of Vascular Stenosis Using Stationary Stenosis Phantoms”. *PLoS ONE* 12.1 (2017), e0168902. DOI: `10.1371/journal.pone.0168902`.

[283] S. Valtchev, E. Baikova, and L. Jorge. “Electromagnetic Field as the Wireless Transporter of Energy”. *Facta universitatis - series: Electronics and Energetics* 25.3 (2012), pp. 171–181. DOI: `10.2298/FUEE1203171V`.

[284] O. Veiseh, J. W. Gunn, and M. Zhang. “Design and Fabrication of Magnetic Nanoparticles for Targeted Drug Delivery and Imaging”. *Advanced Drug Delivery Reviews* 62.3 (2010), pp. 284–304. DOI: `10.1016/j.addr.2009.11.002`.

[285] T. Viereck, C. Kuhlmann, S. Draack, M. Schilling, and F. Ludwig. “Dual-Frequency Magnetic Particle Imaging of the Brownian Particle Contribution”. *Journal of Magnetism and Magnetic Materials* 427 (2017), pp. 156–161. DOI: `10.1016/j.jmmm.2016.11.003`.

[286] P. Vogel, T. Kampf, M. Rückert, C. Grüttner, A. Kowalski, H. Teller, and V. Behr. "Synomag®: The New High-Performance Tracer for Magnetic Particle Imaging". *International Journal on Magnetic Particle Imaging* (Mar. 2021), Vol 7 No 1 (2021). DOI: 10.18416/IJMPI.2021.2103003.

[287] P. Vogel, M. A. Rückert, C. Greiner, J. Günther, T. Reichl, T. Kampf, T. A. Bley, V. C. Behr, and S. Herz. "iMPI: Portable Human-Sized Magnetic Particle Imaging Scanner for Real-Time Endovascular Interventions". *Scientific Reports* 13.1 (June 2023), p. 10472. DOI: 10.1038/s41598-023-37351-2.

[288] P. Vogel, M. A. Rückert, S. J. Kemp, A. P. Khandhar, R. M. Ferguson, S. Herz, A. Vilter, P. Klauer, T. A. Bley, K. M. Krishnan, and V. C. Behr. "Micro-Traveling Wave Magnetic Particle Imaging - Sub-Millimeter Resolution with Optimized Tracer LS-008". *IEEE Transactions on Magnetics* 55.10 (2019), pp. 1–7. DOI: 10.1109/TMAG.2019.2924198.

[289] P. Vogel, S. Herz, T. Kampf, M. A. Rückert, T. A. Bley, and V. C. Behr. "Low Latency Real-time Reconstruction for MPI Systems". *International Journal on Magnetic Particle Imaging* Vol.3 (2017), 8 pages. DOI: 10.18416/IJMPI.2017.1707002.

[290] P. Vogel, S. Lother, M. A. Ruckert, W. H. Kullmann, P. M. Jakob, F. Fidler, and V. C. Behr. "MRI Meets MPI: A Bimodal MPI-MRI Tomograph". *IEEE Transactions on Medical Imaging* 33.10 (2014), pp. 1954–1959. DOI: 10.1109/TMI.2014.2327515.

[291] P. Vogel, J. Markert, M. A. Rückert, S. Herz, B. Keßler, K. Dremel, D. Althoff, M. Weber, T. M. Buzug, T. A. Bley, W. H. Kullmann, R. Hanke, S. Zabler, and V. C. Behr. "Magnetic Particle Imaging Meets Computed Tomography: First Simultaneous Imaging". *Scientific Reports* 9.1 (Sept. 2019), p. 12627. DOI: 10.1038/s41598-019-48960-1.

[292] P. Vogel, M. A. Rückert, P. Klauer, W. H. Kullmann, P. M. Jakob, and V. C. Behr. "Traveling Wave Magnetic Particle Imaging". *IEEE Transactions on Medical Imaging* 33.2 (2014), pp. 400–407. DOI: 10.1109/TMI.2013.2285472.

[293] P. Vogel, M. A. Rückert, B. Friedrich, R. Tietze, S. Lyer, T. Kampf, T. Hennig, L. Dölken, C. Alexiou, and V. C. Behr. "Critical Offset Magnetic PArticle SpectroScopy for Rapid and Highly Sensitive Medical Point-of-Care Diagnostics". *Nature Communications* 13.1 (Nov. 2022), p. 7230. DOI: 10.1038/s41467-022-34941-y.

[294] A. Von Gladiss, M. Graeser, P. Szwargulski, T. Knopp, and T. M. Buzug. "Hybrid System Calibration for Multidimensional Magnetic Particle Imaging". *Physics in Medicine & Biology* 62.9 (2017), pp. 3392–3406. DOI: 10.1088/1361-6560/aa5340.

[295] A. Von Gladiss, M. Ahlborg, T. Knopp, and T. M. Buzug. "Compressed Sensing of the System Matrix and Sparse Reconstruction of the Particle Concentration in Magnetic Particle Imaging". *IEEE Transactions on Magnetics* 51.2 (2015), pp. 1–4. DOI: 10.1109/TMAG.2014.2326432.

[296] A. von Gladiss, M. Graeser, A. Behrends, X. Chen, and T. M. Buzug. "Efficient Hybrid 3D System Calibration for Magnetic Particle Imaging Systems Using a Dedicated Device". *Scientific Reports* 10.1 (Oct. 2020), pp. 1–12. DOI: 10.1038/s41598-020-75122-5.

[297] A. Von Gladiss, M. Graeser, A. Cordes, A. C. Bakenecker, A. Behrends, X. Chen, and T. M. Buzug. "Investigating Spatial Resolution, Field Sequences and Image Reconstruction Strategies Using Hybrid Phantoms in MPI". *International Journal on Magnetic Particle Imaging* (Mar. 2020), Vol 6 No 1 (2020). DOI: 10.18416/IJMPI.2020.2003004.

[298] A. Von Gladiss, I. Kramer, N. Theisen, R. Memmesheimer, A. C. Bakenecker, T. M. Buzug, and D. Paulus. "Data Augmentation for Training a Neural Network for Image Reconstruction in MPI". *International Journal on Magnetic Particle Imaging* (Mar. 2022), Vol 8 No 1 Suppl 1 (2022). DOI: 10.18416/IJMPI.2022.2203058.

[299] Y.-X. J. Wang. "Superparamagnetic Iron Oxide Based MRI Contrast Agents: Current Status of Clinical Application". *Quantitative Imaging in Medicine and Surgery* 1.1 (Dec. 2011), pp. 35–40. DOI: 10.3978/j.issn.2223-4292.2011.08.03.

[300] J. B. Weaver, A. M. Rauwerdink, C. R. Sullivan, and I. Baker. "Frequency Distribution of the Nanoparticle Magnetization in the Presence of a Static as Well as a Harmonic Magnetic Field". *Medical Physics* 35.5 (2008), pp. 1988–1994. DOI: 10.1118/1.2903449.

[301] A. Weber and T. Knopp. "Reconstruction of the Magnetic Particle Imaging System Matrix Using Symmetries and Compressed Sensing". *Advances in Mathematical Physics* 2015 (2015). DOI: 10.1155/2015/460496.

[302] A. Weber and T. Knopp. "Symmetries of the 2D Magnetic Particle Imaging System Matrix". *Physics in Medicine & Biology* 60.10 (Apr. 2015), pp. 4033–4044. DOI: 10.1088/0031-9155/60/10/4033.

[303] M. Weber, J. Beuke, A. Von Gladiss, K. Gräfe, P. Vogel, V. C. Behr, and T. M. Buzug. "Novel Field Geometry Using Two Halbach Cylinders for FFL-MPI". *International Journal on Magnetic Particle Imaging* Vol 4 (Mar. 2019), No 2 (2018). DOI: 10.18416/IJMPI.2018.1811004.

[304] F. Wegner, T. Friedrich, A. von Gladiss, U. Grzyska, M. M. Sieren, K. Lüdtke-Buzug, A. Frydrychowicz, T. M. Buzug, J. Barkhausen, and J. Haegele. "Magnetic Particle Imaging: Artifact-Free Metallic Stent Lumen Imaging in a Phantom Study". *CardioVascular and Interventional Radiology* 43.2 (Oct. 2019), pp. 331–338. DOI: 10.1007/s00270-019-02347-x.

[305] F. Wegner, A. Von Gladiss, J. Haegele, U. Grzyska, M. M. Sieren, E. Stahlberg, T. H. Oechtering, K. Lüdtke-Buzug, J. Barkhausen, T. M. Buzug, and T. Friedrich. "Magnetic Particle Imaging: In Vitro Signal Analysis and Lumen Quantification of 21 Endovascular Stents". *International Journal of Nanomedicine* Volume 16 (Jan. 2021), pp. 213–221. DOI: `10.2147/IJN.S284694`.

[306] I. N. Weinberg, P. Y. Stepanov, S. T. Fricke, R. Probst, M. Urdaneta, D. Warnow, H. Sanders, S. C. Glidden, A. McMillan, P. M. Starewicz, and J. P. Reilly. "Increasing the Oscillation Frequency of Strong Magnetic Fields above 101 kHz Significantly Raises Peripheral Nerve Excitation Thresholds". *Medical Physics* 39.5 (May 2012), pp. 2578–2583. DOI: `10.1118/1.3702775`.

[307] R. Weissleder, D. D. Stark, B. L. Engelstad, B. R. Bacon, C. C. Compton, D. L. White, P. Jacobs, and J. Lewis. "Superparamagnetic Iron Oxide: Pharmacokinetics and Toxicity". *American Journal of Roentgenology* 152.1 (1989), pp. 167–173. DOI: `10.2214/ajr.152.1.167`.

[308] J. Weizenecker, J. Borgert, and B. Gleich. "A Simulation Study on the Resolution and Sensitivity of Magnetic Particle Imaging". *Physics in Medicine & Biology* 52.21 (2007), pp. 6363–6374. DOI: `10.1088/0031-9155/52/21/001`.

[309] J. Weizenecker, B. Gleich, J. Rahmer, H. Dahnke, and J. Borgert. "Three-Dimensional Real-Time in Vivo Magnetic Particle Imaging". *Physics in Medicine & Biology* 54.5 (2009), pp. L1–L10. DOI: `10.1088/0031-9155/54/5/L01`.

[310] J. Weizenecker, B. Gleich, and J. Borgert. "Magnetic Particle Imaging Using a Field Free Line". *Journal of Physics D: Applied Physics* 41.10 (2008), 3pp. DOI: `10.1088/0022-3727/41/10/105009`.

[311] D. Weller, J. M. Salamon, A. Frölich, M. Möddel, T. Knopp, and R. Werner. "Combining Direct 3D Volume Rendering and Magnetic Particle Imaging to Advance Radiation-Free Real-Time 3D Guidance of Vascular Interventions". *CardioVascular and Interventional Radiology* 43.2 (2020), pp. 322–330. DOI: `10.1007/s00270-019-02340-4`.

[312] J. Wells, H. Paysen, O. Kosch, L. Trahms, and F. Wiekhorst. "Temperature Dependence in Magnetic Particle Imaging". *AIP Advances* 8.5 (2018), p. 56703. DOI: `10.1063/1.5004506`.

[313] F. Werner, M. Graeser, F. Thieben, P. Szwargulski, N. Gdaniec, M. Boberg, F. Griese, M. Möddel, P. Ludewig, D. van de Ven, O. M. Weber, O. Woywode, B. Gleich, and T. Knopp. "Stroke Detection Using Magnetic Particle Imaging: A Phantom Study Using a Human-sized Brain Phantom". *International Workshop on Magnetic Particle Imaging*. 2019, pp. 141–142.

[314] F. Werner, N. Gdaniec, and T. Knopp. "Improving the Spatial Resolution of Bidirectional Cartesian MPI Data Using Fourier Techniques". *International Journal on Magnetic Particle Imaging* Vol.3 (2017), 6 pages. DOI: `10.18416/IJMPI.2017.1703007`.

[315] A. B. Williams and F. J. Taylor. *Electronic Filter Design Handbook: LC, Active, and Digital Filters*. 2nd ed. New York: McGraw-Hill, 1988.

[316] J. L. Winer, C. Y. Liu, and M. L. Apuzzo. "The Use of Nanoparticles as Contrast Media in Neuroimaging: A Statement on Toxicity". *World Neurosurgery* 78.6 (Dec. 2012), pp. 709–711. DOI: `10.1016/j.wneu.2011.08.013`.

[317] L. Wöckel, J. Wells, O. Kosch, S. Lyer, C. Alexiou, C. Grüttner, F. Wiekhorst, and S. Dutz. "Long-Term Stable Measurement Phantoms for Magnetic Particle Imaging". *Journal of Magnetism and Magnetic Materials* 471 (Feb. 2019), pp. 1–7. DOI: `10.1016/j.jmmm.2018.09.012`.

[318] J. Yang, Y. Shi, W. Y. Wei, and H. Shen. "A Wireless Power Transfer System Based on Impedance Matching Network". *International Journal of RF and Microwave Computer-Aided Engineering* 30.12 (Dec. 2020). DOI: `10.1002/mmce.22437`.

[319] X. Yang, G. Shao, Y. Zhang, W. Wang, Y. Qi, S. Han, and H. Li. "Applications of Magnetic Particle Imaging in Biomedicine: Advancements and Prospects". *Frontiers in Physiology* 13 (July 2022), p. 898426. DOI: `10.3389/fphys.2022.898426`.

[320] K. B. Yesin, K. Vollmers, and B. J. Nelson. "Modeling and Control of Untethered Biomicrorobots in a Fluidic Environment Using Electromagnetic Fields". *The International Journal of Robotics Research* 25.5-6 (May 2006), pp. 527–536. DOI: `10.1177/0278364906065389`.

[321] L. Yin, W. Li, Z. Bian, Z. Chen, Y. Liu, J. Zhong, S. Zhang, Y. Du, H. Hui, and J. Tian. "A Streamlined 3-D Magnetic Particle Imaging System With a Two-Stage Excitation Feed-Through Compensation Strategy". *IEEE Transactions on Instrumentation and Measurement* 72 (2023), pp. 1–10. DOI: `10.1109/TIM.2023.3328682`.

[322] T. Yoshida, N. B. Othman, and K. Enpuku. "Characterization of Magnetically Fractionated Magnetic Nanoparticles for Magnetic Particle Imaging". *Journal of Applied Physics* 114.17 (Nov. 2013), p. 173908. DOI: `10.1063/1.4829484`.

[323] T. Yoshida, T. Nakamura, O. Higashi, and K. Enpuku. "Magnetic Fractionation and Characterization of Magnetic Nanoparticles for Magnetic Particle Imaging". *Japanese Journal of Applied Physics* 57.8 (Aug. 2018), p. 080302. DOI: `10.7567/JJAP.57.080302`.

[324] E. Y. Yu, M. Bishop, B. Zheng, R. M. Ferguson, A. P. Khandhar, S. J. Kemp, K. M. Krishnan, P. W. Goodwill, and S. M. Conolly. "Magnetic Particle Imaging: A Novel in Vivo Imaging Platform for Cancer Detection". *Nano Letters* 17.3 (2017), pp. 1648–1654. DOI: `10.1021/acs.nanolett.6b04865`.

[325] E. Y. Yu, P. Chandrasekharan, R. Berzon, Z. W. Tay, X. Y. Zhou, A. P. Khandhar, R. M. Ferguson, S. J. Kemp, B. Zheng, P. W. Goodwill, M. F. Wendland, K. M. Krishnan, S. Behr, J. Carter, and S. M. Conolly. "Magnetic Particle Imaging for Highly Sensitive, Quantitative, and Safe in Vivo Gut Bleed Detection in a Murine Model". *ACS Nano* 11.12 (2017), pp. 12067–12076. DOI: `10.1021/acsnano.7b04844`.

[326] P. Zacharias. *Magnetic Components: Basics and Applications*. Wiesbaden: Springer Fachmedien Wiesbaden, 2022. DOI: `10.1007/978-3-658-37206-4`.

[327] X. Zhang, T. A. Le, and J. Yoon. "Development of a Real Time Imaging-Based Guidance System of Magnetic Nanoparticles for Targeted Drug Delivery". *Journal of Magnetism and Magnetic Materials* 427 (2017), pp. 345–351. DOI: `10.1016/j.jmmm.2016.10.056`.

[328] B. Zheng, P. W. Goodwill, N. Dixit, D. Xiao, W. Zhang, B. Gunel, K. Lu, G. C. Scott, and S. M. Conolly. "Optimal Broadband Noise Matching to Inductive Sensors: Application to Magnetic Particle Imaging". *IEEE Transactions on Biomedical Circuits and Systems* 11.5 (Oct. 2017), pp. 1041–1052. DOI: `10.1109/TBCAS.2017.2712566`.

[329] B. Zheng, T. Vazin, P. W. Goodwill, A. Conway, A. Verma, E. Ulku Saritas, D. Schaffer, and S. M. Conolly. "Magnetic Particle Imaging Tracks the Long-Term Fate of in Vivo Neural Cell Implants with High Image Contrast". *Scientific Reports* 5.1 (Sept. 2015), p. 14055. DOI: `10.1038/srep14055`.

[330] B. Zheng, W. Yang, T. Massey, P. W. Goodwill, and S. M. Conolly. "High-Power Active Interference Suppression in Magnetic Particle Imaging". *2013 International Workshop on Magnetic Particle Imaging, IWMPI 2013*. 2013, p. 1. DOI: `10.1109/IWMPI.2013.6528381`.

[331] J. Zhong, M. Schilling, and F. Ludwig. "Simultaneous Imaging of Magnetic Nanoparticle Concentration, Temperature, and Viscosity". *Physical Review Applied* 16.5 (Nov. 2021), p. 054005. DOI: `10.1103/PhysRevApplied.16.054005`.

[332] X. Y. Zhou, K. E. Jeffris, E. Y. Yu, B. Zheng, P. W. Goodwill, P. Nahid, and S. M. Conolly. "First in Vivo Magnetic Particle Imaging of Lung Perfusion in Rats". *Physics in Medicine & Biology* 62.9 (2017), pp. 3510–3522. DOI: `10.1088/1361-6560/aa616c`.

List of Figures

List of Tables